DOCTORAT MATIERE BRETAGNE MOLECULES LOIRE ET MATERIAUX

UNIVERSITÉ DE NANTES

THESE DE DOCTORAT DE

L'UNIVERSITE DE NANTES
COMUE UNIVERSITE BRETAGNE LOIRE

ECOLE DOCTORALE N° 596
Matière Molécules et Matériaux
Spécialité : Sciences des Matériaux

Par
Anthony IMPELLIZZERI

Atomic-Scale Modelling of Folding and Filling in 2D Nanostructures

Modélisation à l'échelle atomique du pliage et du remplissage dans des nanostructures 2D

Thèse présentée et soutenue à Nantes, le 15 Décembre 2020
Unité de recherche : UMR6502
Thèse N° : (10)

Rapporteurs avant soutenance

Elena BESLEY
Professeur, Université de Nottingham (UK)
Raul ARENAL
Directeur de Recherche, Université de Zaragoza (ES)

Composition du Jury

Président
Florent BOUCHER
CNRS Directeur de Recherche
Directeur de l'Institut des Matériaux Jean Rouxel (IMN)

Isabelle BRAEMS CNRS Chargé de Recherche, Institut des Matériaux Jean Rouxel (IMN)
Alfonso SAN-MIGUEL Professeur, Université de Lyon (FR)
Irene SUAREZ-MARTINEZ, Senior Lecturer, University of Curtin (AU)
Elena BESLEY Professeur, Université de Nottingham (UK)
Raul ARENAL Directeur de Recherche, Université de Zaragoza (ES)

Directeur de thèse
Chris EWELS CNRS Directeur de Recherche Institut des Matériaux Jean Rouxel (IMN)

Co-directeur de thèse
Dmitry RYBKOVSKIY Researcher, Skolkovo Institute of Science & Technology (RU)

Résumé étendu en Français

Cette thèse explore les implications de la courbure locale dans les nanomatériaux basés sur les couches de carbone et de nitrure de bore, en utilisant principalement la théorie fonctionnelle de la densité (DFT) avec des fonctions semi-locales et hybrides.

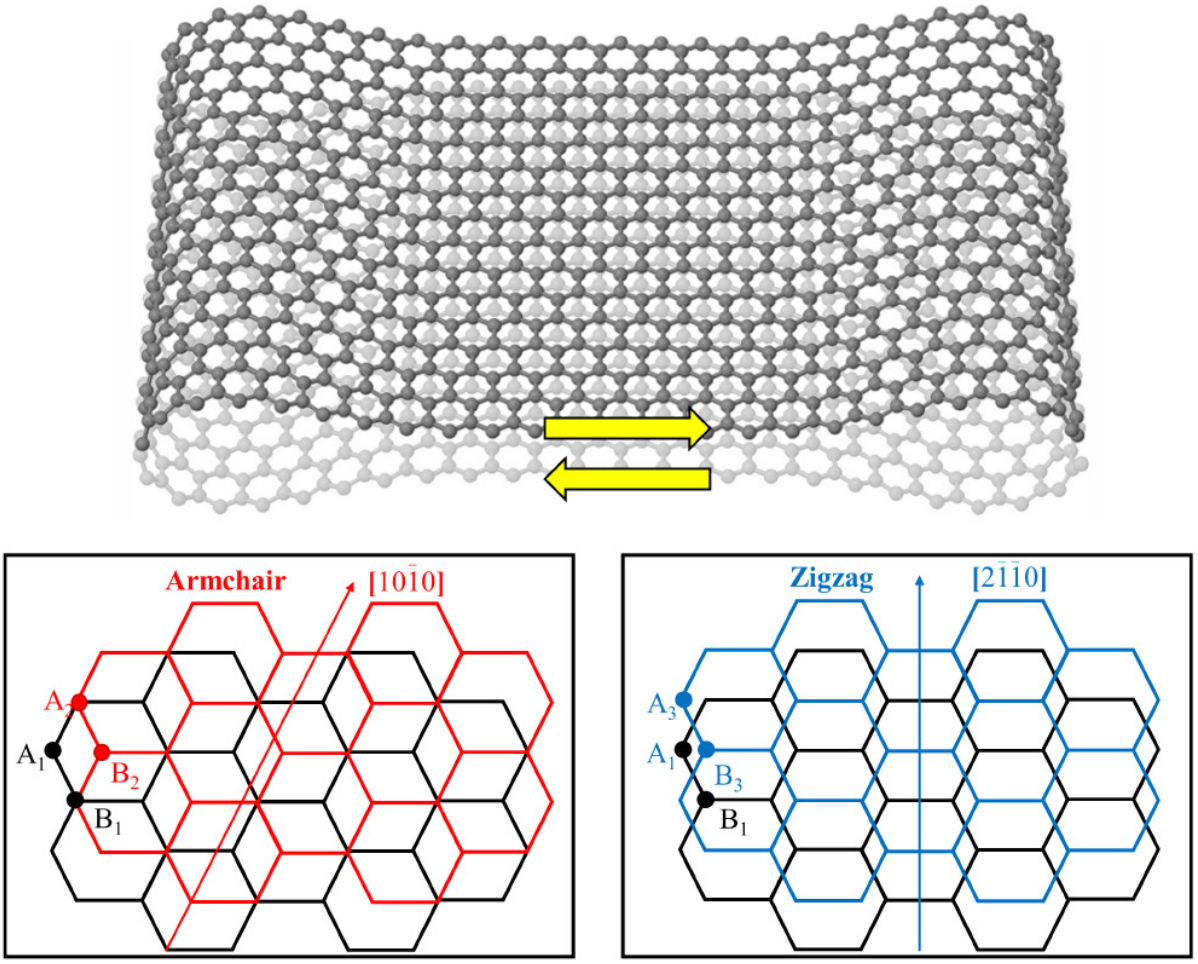

Figure : Géométrie de l'effondrement du nanotube de carbone mono-feuille. Les flèches jaunes indiquent le mode de cisaillement intercouche. Bas : Déplacements le long du « armchair » [10-10]et motifs en « zigzag » [2-1-10] des structures en treillis des couches adhérentes formant la section centrale en graphène bicouche des tubes aplatis. Les atomes de carbone du (noir) inférieur et du (rouge/bleu) couches supérieures sont respectivement intitulées $A_{1(2/3)}$ et $B_{1(2/3)}$.

Nous avons théoriquement admis que les nanotubes de carbone à paroi simple s'effondrent au-delà du diamètre seuil de 5.1 nm en utilisant le DFT en combinaison avec les corrections de Van der Waals, en excellent accord avec le résultat expérimental le plus plausible. Nous avons démontré que tous les nanotubes considérés (armchair, zig-zag et chiral), y compris toutes les sous-familles deviennent semi-conductrices, exposant l'ouverture d'un petit gap énergétique lors de l'effondrement. Cette transition métal-semiconducteur est une conséquence de la localisation de la courbure qui brise la symétrie du treillis. L'impact des légers déplacements entre les couches adhérentes dans cette topologie tubulaire est d'un grand intérêt pour concevoir des bandes interdites appropriées pour des applications telles que les interconnexions.

Nous avons également confirmé la tendance générale des liaisons intercouches à former des dislocations prismatiques entre les plans de base du graphite, qui se produisent généralement dans les échantillons fortement endommagés et irradiés. Cette analyse pourrait suggérer la formation de nanostructures, ressemblant à des nanotubes effondrés intercalés entre des couches de carbone. Les calculs de structure électronique ont montré l'apparition d'états de bord dans la région de la monocouche ainsi que des bords fermés. Les bandes de basse énergie au niveau de Fermi dépendent fortement du couplage entre les couches de la région bicouche, tandis que l'ouverture d'une bande interdite est due à la rupture de symétrie dérivée de la courbure locale. L'apparition d'états de bord est importante pour étudier le magnétisme au niveau des noyaux reconstruits. Ils sont considérés comme candidats pour la magnétisation habituellement observée dans le graphite endommagé et irradié.

L'application de haute pression dans des nanotubes de nitrure de bore à parois multiples conduit à la formation de nouvelles morphologies par rapport à la famille des carbones, notamment les bambous, les alvéoles de taille irrégulière et l'apparition de bords repliés, comme l'a montré l'analyse avec le microscope de transmission électronique. La formation de cet ensemble de nouvelles configurations peut être attribuée à la fracture des tubes internes polygonés en réponse à la pression appliquée, conduisant à des arrangements différents. Nos calculs théoriques ont révélé que les nanotubes de nitrure de bore à paroi simple effondrés sont énergétiquement favorisés par rapport à leur homologue cylindrique pour une valeur seuil de diamètre de 3.0 nm. La formation de morphologies différentes de cas du carbone ainsi qu'un diamètre critique d'effondrement inférieur représente une signature claire de la nature ionique du bore et de l'azote aussi.
L'analyse des propriétés électroniques a révélé que la déformation par pliage mécanique dans les nanotubes BN diminue la bande interdite au niveau des cavités des bords, se comportant comme une homojonction de type II.
Cette étude met en évidence l'aspect surprenant de la façon dont la déformation structurelle locale peut induire de fortes modifications des propriétés physiques de matériaux stratifiés de taille micrométrique à l'échelle « macro ». Ça donne une piste intéressant, pour utiliser les systèmes à bords étroits pour différentes applications, y compris les dispositifs accordés électro-optiques et même la spintronique.

Nous avons mis en œuvre la formulation semi-classique de Placzek de la théorie Raman pour simuler les spectres vibrationnels avec une précision DFT-D2. L'idée de base de cette approche est la relation directe entre la section transversale Raman et la première dérivée du tenseur de polarisation

par rapport aux coordonnées vibratoires. L'approximation de Placzek a permis d'analyser et de différencier une grande variété de nanomatériaux de carbone, tels que le graphène, le fullerène et les SWCNT cylindriques. La méthode que nous avons proposée a montré l'activation de la bande D induite par le désordre pour les nanotubes et les nanorubans, où les défauts ponctuels et les arêtes sont tous responsables de la rupture de la symétrie hexagonale, selon des travaux expérimentaux antérieurs.

De plus, l'analyse d'images par microscopie a permis d'identifier clairement des tubes isolés qui se sont effondrés. En comparant les spectres Raman entre des tubes cylindriques et des tubes effondrés ayant une densité de défauts négligeable comparable, nous avons observé l'absence et la présence d'une bande D intense et étroite, respectivement. Ainsi, nous avons démontré que la bande D représente une propriété intrinsèque des nanotubes effondrés, qui est due à la ligne de changement d'hybridation le long des cavités de bord, plutôt qu'une conséquence de défauts structurels. Ce résultat est d'un intérêt fondamental puisque l'intensité de la bande D est historiquement utilisée pour quantifier la quantité totale de désordre dans les nanomatériaux de carbone, alors que nous avons détecté la présence d'une bande sans défaut, qui est activée par la rupture de symétrie dérivée de la présence simultanée de feuilles aplaties et de bords courbés ultra-lisses.

Cette bande D induite par le pliage sert à revisiter la caractérisation Raman de cette classe de systèmes, dont la symétrie est rompue par un changement local de courbure, notamment : le graphène plié et défilé, le flambage du graphite nucléaire recuit, les nanofibres de carbone en plaquettes, les cristaux polyédriques graphéniques en forme de cône, etc.

En outre, les principes qui sous-tendent la méthode multi-longueurs d'onde présentée sont plus généraux et ne se limitent pas aux seuls systèmes à base de carbone étudiés ici.

Nous avons analysé la stabilité énergétique de nombreuses configurations de phosphore, en constatant que le phosphore (P) noir n'est pas l'état de base omniprésent, mais qu'il est dégénéré avec une structure rouge-V. Ensuite, nous avons exploré le passage de la phase 3D en vrac (macro-échelle) à la phase 1D (nano-échelle) du P rouge après son encapsulation dans des nanotubes par analyse microscopique et caractérisation Raman. Nous avons simulé les spectres Raman de chaînes simples, doubles et sept P en utilisant la méthode Placzek de premier ordre au niveau de précision DFT-D2, précédemment utilisée pour la famille des carbones. Nos résultats semblent suggérer que les signaux P à basse fréquence enregistrés dans l'expérience correspondent à des paquets composés par différents poids de chaînes P2P8 et P2P9. Ces deux chaînes peuvent être considérées comme des variantes défectueuses l'une de l'autre. Cette étude a révélé la formation de nouvelles allotropies de phosphore utilisant des nanotubes de carbone comme modèles, ce qui pourrait ouvrir la voie à ces nouvelles nanostructures de phosphore vers d'autres applications.

Par la suite, nous avons systématiquement étudié la tendance des atomes d'iode confinés à l'intérieur des nanotubes de carbone à se polymériser dans des structures en chaîne en utilisant des méthodes de recherche de structure aléatoire et de compression. En augmentant la concentration d'iode, nous avons observé une séquence de transitions de phase allant d'une configuration de chaîne simple, puis double à triple. Le transfert de charge et le déplacement d'énergie de Fermi ont prouvé que les ions poly iodures

sont les dopants dominants, ce qui suffit à expliquer l'amélioration de la conductivité des nanotubes observée dans la littérature antérieure.

Il a également été constaté que le remplissage d'iode dans les nanotubes à multi paroi hautement cristallins entraîne l'intercalation d'iode entre les parois concentriques des nanotubes. Ce mécanisme de remplissage est favorisé par la dilatation thermique des couches intermédiaires entre les noyaux des tubes à haute température, ce qui induit une déformation par flambage. Nos calculs avec DFT-D2 ont démontré que l'iode intercalé dépend principalement de l'espacement entre les parois des tubes et est stabilisé pour une valeur de 0.681 nm.

Enfin, nous avons présenté une nouvelle approche pour obtenir des nanotubes de carbone stables et effondrés à des diamètres inférieurs à 5.1 nm en remplissant les cavités avec d'autres matériaux comme l'iode, comme le montre la microscopie électronique à transmission par balayage. Plus surprenant encore, le remplissage local des bords permet de régler les propriétés électroniques de l'ensemble des tubes effondrés pour obtenir des semi-conducteurs dopés *n* et *p* en fonction du matériau encapsulé. Ce résultat stimule l'intérêt pour la fabrication de nanotubes effondrés et rempli pour les applications de dispositifs électroniques, en remplacement des tubes circulaires et des rubans de graphène plus conventionnels.

UNIVERSITÉ DE NANTES
Institut des Matériaux Jean Rouxel

Anthony Impellizzeri

ATOMIC-SCALE MODELLING OF FOLDING AND FILLING IN 2D NANOSTRUCTURES

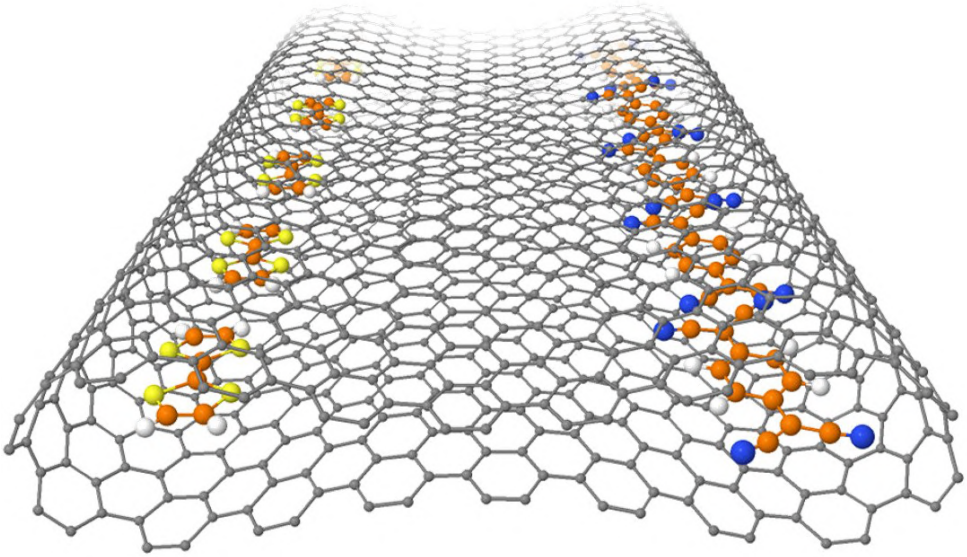

PhD Thesis

Supervisors:

Dr. C. P. Ewels
Dr. D.V. Rybkovskiy

CSI-Advisors:

Prof. X. Roquefelte
Dr. C. Bousige

academic year 2020/2021

This is the fight of our lives.
And we're gonna win.
Whatever it takes.
Steve Rogers

Contents

Preface

This thesis is submitted in fulfillment of the requirements for the PhD degree set by the University of Nantes (France). All the results presented in this work have been collected from 1^{st} September 2017 to 10^{th} October 2020, working under the supervision of the Research Director Christopher Paul Ewels belonging to the Physics and Materials Nanostructures (PMN) group at the Institut des Matériaux Jean Rouxel of Nantes (IMN).
I acknowledge funding from the Agence Nationale de la Recherche (ANR), namely the project ANR-16-CE24-0008-01 "EdgeFiller". Over the entire period 2017-2020 I have been affiliated with the Centre National de la Recherche Scientifique (CNRS). My PhD project has been supervised by Director of Research Christopher P. Ewels together with Dr. Dmitry V. Rybkovskiy during the final year. This national project boasts a prestigious partnership with chemists of the Centre de Recherche Paul Pascal (CRPP) of Bordeaux along with microscopists and Ramanists of the Centre d'élaboration de matériaux et d'études structurales (CEMES) of Toulouse.
Some of the results have been obtained in the context of one short external research stay spent from 4^{th} November 2019 to 2^{nd} December 2019 at the Skolkovo Institute of Science and Technology (Skoltech) of Moscow (Russia) working with my adjoint supervisor Dr. Dmitry V. Rybkovskiy. In the 3° PhD year, the partnership network expanded further since I worked on several external projects including notably: (*i*) Department of Chemistry of Loughborough (United Kingdom), (*ii*) Institut Lumiére Matiére of Lyon (France), (*iii*) Laboratoire de Physique des Solides (LPS) of Paris (France), and (*iv*) Novosibirsk State University of Siberia (Russian Federation).

First and firemost I would like thank my PhD supervisor Christopher P. Ewels with all my heart. With his immense enthusiasm, kindness, care, and patience, I realised I met one of the most amazing supervisors aroung the world. By providing exhaustive and very clear explanations to the dumbest of my questions and most articulated debates in all possible modes (face-to-face, e-mail and Slack chats) and teaching me the basics of Fortran programming, he has made my PhD experience so awesome, evolving beyond the brightest of my initial expectations. Thank you very much, Chris, for always treating me with trust and respect, both as a scientist and as a friend. I am truly honored to worked under your supervision.
I basically owe my two most important PhD achievements to Dmitry V. Rybkovskiy. He developed one of the calculation approaches that I have widely used in the thesis. He mentored me with patience and enthusiasm. He always supported me with expertise and experience, always ready to debug new features to make my 'computational' life easier. I feel extremely lucky to worked under his guidance.
A very special thanks goes to chemists Emmanuel Picheau, Ferdinand Hof, and Alain Pénicaud of CRPP institute and then physicists Abraao Cefas Torres-Dias, Pascal Puech and Marc Monthioux of CEMES institute. It is because of all them that I

was able satisfy my desire to combine theory and experiments within my project. I am so glad of the cooperative spirit showed during every EdgeFiller meeeting and mainly for the enthusiasm with which all of you have taken on board my computational contributions to your really exciting projects. I want to thank experts Alain, Marc and Pascal for your constructive criticism which always stimulated me towards on achieving the targets and especially for their dynamic attitude towards science. I am sincerely grateful to Emmanuel and Abraao for their passionate and friendly collaborative spirit. In particular, I would like to thank Emmanuel for teaching me how to synthesise experimental nanotubes and the use of electron microscopy during my stay in Bordeaux. It was awesome to feel that adrenaline typical of experimentalists, moving quickly from one laboratory to another and walking up and down stairs as athletes.
A huge thanks goes all the people with whom I have had the pleasure to share intriguing scientific projects: (*i*) the experimentalists working in my laboratory: Bernard Humbert, Maxime Bayle, Jean-Yves Mevellec and Jean-Luc Duvail. In particular, I am grateful to Bernard who helped me in the interpretation of some results and Jean-Luc for his active interest and stimulating discussions, (*ii*) James McHugh and Paul Mouratidis from Loughborough, who included me in the dislocation project; (*iii*) Italian guys Michele Amato and Alberto Zobelli, who participated with much enthusiasm in the project proposed by us. Michele kindly produced results in a very short time and the observations of a real expert like Alberto significantly helped me to better understand and improve the quality of our shared work; (*iv*) the Russian guys Viktor Korootev, Alexander Okotrub and Lyuba Bulusheva for their incredible speed in obtaining reliable results.
A special thanks goes to experts Alfonso San-Miguel and Raul Arenal, who shared with me without any hesitation your experimental results on the basis of total trust and confidence. Especially, I am truly grateful to Alfonso for including in your nice project.
I am thankful to all the theoreticians at the IMN for all the stimulating discussions had during every brainstorming, especially Adrien Stoliaroff, Camille Latouche, Isabelle Breams, and Eric Faulques. Also, I want to thank Eric Gautron for his immense availability in observing samples using the renowned microscopy of IMN, which is called "Nanth'emis".
A well deserved thanks goes to the administration of IMN, in particular Elodie, Isabelle, Murielle, Catherine and Richard, who have always taken care of the bureaucratic issues related to my PhD.

I want to thank Florent Boucher, Isabelle Breams, Alfonso San Miguel, Irene Suarez-Martinez for all the stimulating and interesting discussions during my PhD defence. In particular, Raul Arenal and Elena Besley, who gave me very useful suggestions to greatly improve the contents reported in this thesis. I was really honored to share and discussed all my work with these people so strong of nanoscience community.

A heartfelt thank you for my colleagues and friends at the IMN Angélique, Danilo, Jeremy, Patricia and Xiaoyang. I want to sincerely thank Yuman, Daniel, Raquel (with whom I learned to speak Spanish too), and Maria, who have been there for me since the beginning of my PhD experience, including all funny moments spent in caféteria or at lunch time.

Outside France, a huge thanks goes to my dear professor and friend professor Giuseppe Anglilella, which always believed in me and supported during my path. Of course, I wish to thank my friend Gaetano Calogero together, with whom I had the pleasure to publish my first work during my 1^{st} PhD year. In the last context, I would to thank José Caridad, Mads Brandbyge, and Peter Boggild.
I am extremely thankful to my beloved brothers, Salvo, Ciccio, and Pippo, who are always there for me every time I need them, despite the huge distance that sets us apart. I would like also thank my dear friends: Nino, Vera, Ryan, and Giusy, that I always see once back in Sicily.
I want to say thanks my parents which supported me with all their love and all their packages filled with "Sicilian" food. I will never forget when my mom dedicated the Andrea Bocelli's song "All'alba vinceró" wishing "Good luck" for my adventure in Nantes.
Another special thanks goes to my grandparents and then Privitera's family, who usually call me to find out if I am fine and if I always eat.
Last but not least, my beloved girlfriend Valentina. She has tirelessly endured every joy and satisfaction, every struggle and distress that I have had during my PhD, including all those times I was speaking using Italian, English, Spanish, and French simultaneously, resembling a sort of "Minions"-like language at the end of every day. I am deeply grateful to her for encouraging me more than anybody else, with an infinite source of love and endless patience. Our love is something that does not fear thousand miles of distance and cannot be explained by physics. So, it is simply the "true love".
This whole work is dedicated to my girlfriend and parents.

Abstract

This thesis explores the implications of local curvature in layered carbon and boron-nitride nanomaterials, using primarily density functional theory (DFT) with semi-local and hybrid functionals. Carbon and boron-nitride nanotubes are not stable above a certain diameter but spontaneously collapse. Fascinating electronic phenomena can emerge in these radially deformed nanosystems, such as a metal-semiconductor transition for carbon, and gap reduction in the case of insulating hBN. I compare this with the structure and electronic properties of prismatic edge dislocations in bulk graphite. The so-called "D-band" in Raman spectroscopy is typically assigned to point defects, I demonstrate here that its intense presence in clean collapsed carbon nanotubes is instead related to symmetry breaking induced by localization of curvature along the collapsed edge. Elements such as iodine and phosphorus can be encapsulated inside carbon nanotubes or the edge cavities of collapsed tubes, forming 1D-like chains whose structures may not exist if considered free-standing, and facilitating nanotube collapse through charge transfer. I propose a simple and efficient method based on quantum mechanical DFT and semiclassical Placzek approximation to characterize the Raman features of large systems such as collapsed nanotubes and phosphorus chains with high accuracy. These results demonstrate how local deformations can completely modify the properties of nanomaterials, pushing them towards novel and unexpected applications.

Keywords: Graphene, Boron Nitride, Folding, Filling, Density Functional Theory, Placzek approximation.

Resumé (Summary in French)

Cette thèse explore les implications de la courbure locale dans les nanomatériaux basé sur les couches de carbone et de nitrure de bore, en utilisant principalement la théorie fonctionnelle de la densité (DFT) avec des fonctions semi-locales et hybrides. Les nanotubes de carbone et de nitrure de bore ne sont pas stables au-dessus d'un certain diamètre mais s'effondrent spontanément. Des phénomènes électroniques fascinants peuvent apparaître dans ces nanosystèmes déformés radialement, tels qu'une transition métal-semiconducteur pour le carbone, et une réduction du gap électronique dans le hBN isolant. Je compare ces phénomènes à la structure et aux propriétés électroniques des dislocations prismatiques des bords du graphite massif. La "bande D" en spectroscopie Raman est généralement attribuée à des défauts ponctuels. Je démontre ici que sa présence intense dans des nanotubes de carbone propres et effondrés est plutôt liée à la rupture de symétrie induite par la localisation de la courbure le long du bord effondré. Des éléments tels que l'iode et le phosphore peuvent être encapsulés à l'intérieur de nanotubes de carbone ou dans les cavités du bord des tubes effondrés, formant des chaînes de type 1D dont les structures peuvent ne pas exister si elles sont considérées comme autonomes, et facilitant l'effondrement des nanotubes par transfert de charge. Je propose une méthode simple et efficace basée sur la DFT, la mécanique quantique et l'approximation semi-classique de Placzek pour caractériser les caractéristiques Raman de grands systèmes tels que les nanotubes effondrés et les chaînes de phosphore avec une grande précision. Ces résultats démontrent comment des déformations locales peuvent modifier complètement les propriétés des nanomatériaux, les poussant vers des applications nouvelles et inattendues.

Keywords: Graphène, Nitrure de bore, Pliage, Remplissage, Théorie Fonctionnelle de la Densité, Approximation de Placzek.

List of contributions

This thesis is based on the published contributions listed below.

I A. Impellizzeri, P. Briddon and C.P. Ewels. *Stacking- and chirality-dependent collapse of single-walled carbon nanotubes: A large-scale density-functional study.* In: *Phys. Rev. B* **100** (11), 115410 (2019).

II A. Impellizzeri, M. Amato, A. Zobelli and C.P. Ewels. *Band gap reduction at edge folds in hexagonal boron nitride.* submitted (2020).

III E. Picheau, A. Impellizzeri, D.V. Rybkovskiy, M. Bayle, J.-Y. Mevellec, F. Hof, H. Saadaoui, L. Noé, A. C. Torres-Dias, J.-L. Duvail, M. Monthioux, B. Humbert, P. Puech, C.P. Ewels and A. Pénicaud. *Intense Raman D band without disorder in flattened carbon nanotubes.* In: *ACS Nano, accepted* (2020).

IV D.V. Rybkovskiy, A. Impellizzeri, E.D. Obraztsova and C.P. Ewels. *Polyiodide structures in thin single-walled carbon nanotubes: A large-scale density-functional study.* In: *Carbon* **142**, 123-130 (2019).

Other published articles by the author (not covered in this thesis):

I J.M. Caridad, G. Calogero, P. Pedrinazzi, J.E. Santos, A. Impellizzeri, T. Gunst, T.J. Booth, R. Sordan, P. Boggild and M. Brandbyge. *A Graphene-Edge Ferroelectric Molecular Switch.* In: *Nano Lett.* **18** (8), 4675-4683 (2018).

II A. Yaya, A. Impellizzeri, F. Massuyeau, J.L. Duvail, P. Briddon and C.P. Ewels. *Mapping the stacking interaction of triphenyl vinylene oligomers with graphene and carbon nanotubes.* In: *Carbon* **141**, 274-282 (2019).

List of conference contributions for the period 2017-2020:

- Talk:

  1. A. Impellizzeri, C. P. Ewels, E. Picheau, A. Pénicaud, A. C. Torres-Dias and M. Monthioux. *Modelisation des nanotubes de carbone dogbones avec techniques ab initio.*
     In: **SFEC 2019** (April 23-26, 2019 - Toulouse, France).
  2. A. Impellizzeri, C. P. Ewels, A. C. Torres-Dias, M. Monthioux, E. Picheau and A. Pénicaud. *Selective edge filling of collapsed carbon nanotubes for nanoelectronics: an ab-initio study.*
     In: **SFP 2019** (July 08-12, 2019 - Nantes, France).

3. A. Impellizzeri, D.V. Rybkovskiy, E. Picheau, M. Bayle, B. Humbert, J.-L. Duvail, C. P. Ewels, F. Hof, A. Pénicaud, A. C. Torres-Dias, M. Monthioux and P. Puech. *Development of ab-initio method to multi-wavelength dependent Raman spectroscopy of 2D-nanomaterials.*
   In: **Graphene** & **2DM 2020** (July 07, 2020 - Madrid, Spain).
4. A. Impellizzeri, D.V. Rybkovskiy, V. Koroteev, A. Okotrub, L. Bulusheva and C. P. Ewels. *Encapsulated phosphorus packings in single-walled carbon nanotube: a Raman spectroscopy investigation.*
   In: **NanoteC 2020** (August 25, 2020 - Surrey, United Kingdom).
5. A. Impellizzeri, M. Amato, A. Zobelli and C. P. Ewels. *Impact of mechanical deformation on the electronic properties of 2D nanomaterials.*
   In: **CMD2020GEFES** (August 31 - September 4, 2020 - Madrid, Spain).

- Poster:

1. A. Impellizzeri, C. P. Ewels, M. Monthioux and A. Pénicaud. *Determination of phase transition in filled collapsed carbon nanotubes: a first-principle investigation.*
   In: **ChemOnTubes 2018** (April 22-26, 2018 - Biarritz, France).
2. A. Impellizzeri, C. P. Ewels, M. Monthioux and A. Pénicaud. *Phase transition and charge density in filled collapsed carbon nanotubes: an ab-initio study.*
   In: **NanoteC 2018** (August 29 - September 1, 2018 - Sussex, United Kingdom).
3. A. Impellizzeri, C. P. Ewels, E. Picheau, A. Pénicaud, A. C. Torres-Dias and M. Monthioux. *Selective edge filling of collapsed carbon nanotubes for field effect transistors.*
   In: **Chem2DMat 2019** (September 03-06, 2019 - Dresden, Germany).

Chapter1

Introduction

In the last fifty or more years, scientists over the world have made achievements so revolutionary, from the existence of the Higgs Boson (also known as "God particle") [1, 2] to "Mars 2020" mission [3], they can be considered milestones of human history. All of this is possible because of important advances in scalable manufacturing of nanostructures to build super-computers used by groups of CERN and NASA in these two cases.
In the field of nanotechnology, two other examples of scientific progress are: *(i)* the realization of quantum computers capable of running enormous computational tasks in order of a few seconds, which current state-of-the-art classical versions would take 10,000 years to perform [4]; *(ii)* mobile phones able to fit around the wrist of our hand, with really high memory capacity. The performance of these technological innovations are due to the prominent properties of semiconductor devices and integrated circuits made by silicon and carbon. For this reason the Si and C industries are 10^{12} dollar industry in the world, whose technology lies at the core of the majority commercial electronic applications in use today. Their impact on modern society is so huge it is hard to quantify.
To this point in history, we have to be grateful for uncountable efforts made by scientists on the front of materials science, which opened up the doors to an era where technological progress is rapidly evolving.

1.1 The new horizons of nanomaterials

One-atom-thick crystals, more commonly known as two-dimensional (2D) materials, have totally revolutionized multiple industries [5]. Soon after Geim and Novoselov isolated graphene [6], considered the "thinnest known material in the universe" but also the strongest ever measured [7], 2D nanomaterials became the subject of extensive research and millions-worth investments. The objective of this section is

to provide the main properties, progress and challenges of three 2D nanomaterials made from light elements and their derivatives that will be discussed in this thesis.

Graphene. The reasons why a simple nanosheet of sp^2-like hybridized carbon atoms arranged in a honeycomb-like lattice has prompted extensive research and media attention are manifold. First, graphene science relies on one of the most abundant elements on the Earth, carbon [8]. It represents a strong economical benefit in terms of industrial production. Second, in band theory graphene is a zero-gap semiconductor with electrons (and holes) that behave as massless particles and obey the relativistic Dirac equation [9, 10]. This is the root of fascinating properties for graphene transistors, like ballistic transport obtained for channel length values roughly equal to 50 nm [11] and electron-optics (a phase shift observed in the quantum conductance oscillations at low magnetic fields $\sim$ 0.3 T) [12]. Third, another benefit of its unique electronic structure is the capacity to absorb a large fraction ($\sim$ 2.3%) of incident white light [13], which makes graphene an excellent transparent conductor for use in solar photovoltaic applications [14]. Fourth, an intriguing property is the high mechanical flexibility which stimulated the minds of scientists to theorize and generate novel carbon-based on architectures with different dimensionality. Indeed, the universe of carbon nanoscale structures has expanded exponentially over the last 30 years, resulting in a 'plethora' of nanoforms (see Fig. 1.1), some of which either have grown bottom-up directly from gas precursors or through chemical vapour deposition (CVD) synthesis (Fig. 1.1(a)-(g)), while other configurations still remain hypothetical and need to be found (Fig. 1.1(m)-(p)) [15]. Among discovered sp^2 hybridized carbon nanostructures, the formation of C_{60} fullerene [16] and then the detection of a nanotubular graphene phase [17] by transmission electron microscopy (TEM) have represented landmark progress in carbon nanoscience.
Single-walled carbon nanotube (SWCNT) structure corresponds to the rolling of the hexagonal lattice of a graphene sheet in a specific direction resulting in seamless carbon cylinders. The chirality (also known as helicity) of rolled-up nanotube is determined by the chiral angle ϑ, which can be defined by a pair of indices (n,m), corresponding to multiples of the graphene unit cell vectors [18]. Nanotubes with ϑ = 0° and 30° are called zig-zag ($m = 0$) and armchair ($n = m$), respectively, while all others with different angles are called chiral SWCNTs ($n \neq m$). The electronic properties of SWCNTs is uniquely defined by their chirality because of band folding of graphene: zig-zag nanotubes can be either unidimensional metals or semiconductors depending on their diameter according to Clar's textet scheme, while armchair ones are metallic regardless of the diameter [11, 19]. In addition, carbon nanotubes possess other exceptional properties, such as high strength ($\sim$37 GPa), themal conductivity ($\sim$3500 W/m/K) and ballistic transport [11, 20]. Given their outstanding performance, techonologies based on individual tubes, bundles and composites have been developed in the last two decades receiving a lot of attention [20]. These

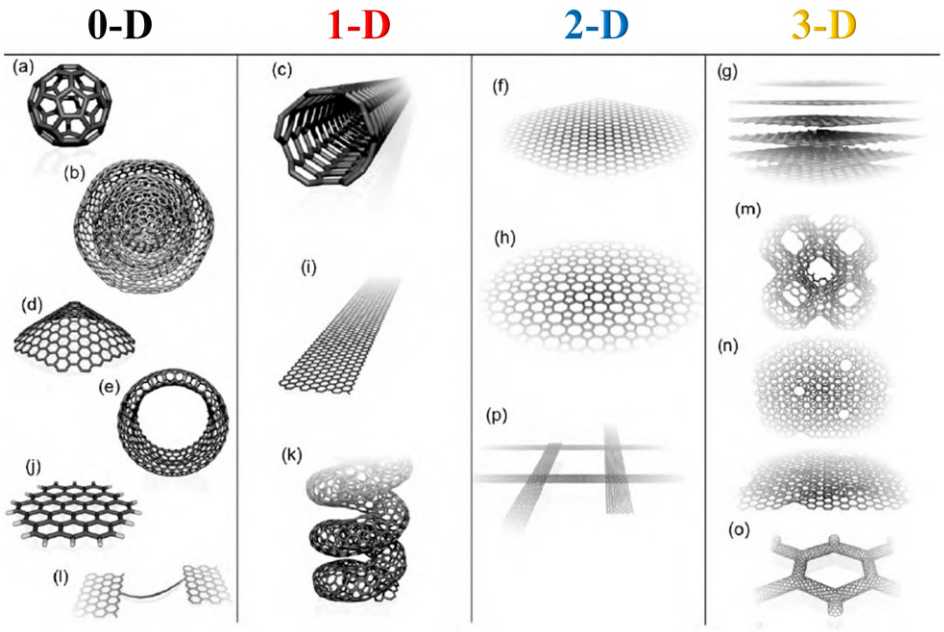

Figure 1.1: Schematic representation of sp^2-like carbon nanoforms exhibiting different dimensionalities: 0D [(a) C_{60} molecule, (b) graphitic nano-onions, (c) carbon nanohorns, (e) nanotoroids, (j) graphene clusters, (l) carbon chains], 1D [(c) single-walled carbon nanotubes, (i) graphene nanoribbons, (k) helicoidal nanotubes], 2D [(f) graphene, (h) Haeckelite surface, (p) 2D nanoribbons network], and 3D [(g) graphite, (m) 3D Schwarzite crystals, (n) carbon nanofoams, (o) 3D nanotube network]. Figure taken from [15].

progress paved the way to a whole new chemistry and physics of carbon, such as the synthesis of hybrid structures composed by nanotubes interconnected with graphene sheets named 'rebar' graphene [21].

The chirality-dependent electronic behavior of carbon nanotubes attracted the interest of many groups to explore the properties of flat carbon strips of finite-size with non-three coordinated atoms at the edges, now termed *graphene nanoribbons* (GNRs). Theoretical calculations have been showed that graphitic ribbons with zig-zag edges are metallic conductors, while armchair morphology can exhibit both metallic and semiconducting transport depending on the width W [11, 15]. More interestingly, previous theoretical and experimental works have been confirmed that narrow GNRs ($W < 10$ nm) behave as semiconductors independently of their edge configurations [22, 23]. For this reason ultrasmooth graphene ribbons have been considered excellent candidates for use in nanoelectronics, such as field-effect transistors, unlike SWCNTs. However, the presence of structural defects, which may appear during growth process, drastically deteriorate the electrical transport properties of systems under discussion [24]. A wide spectrum of methods has been

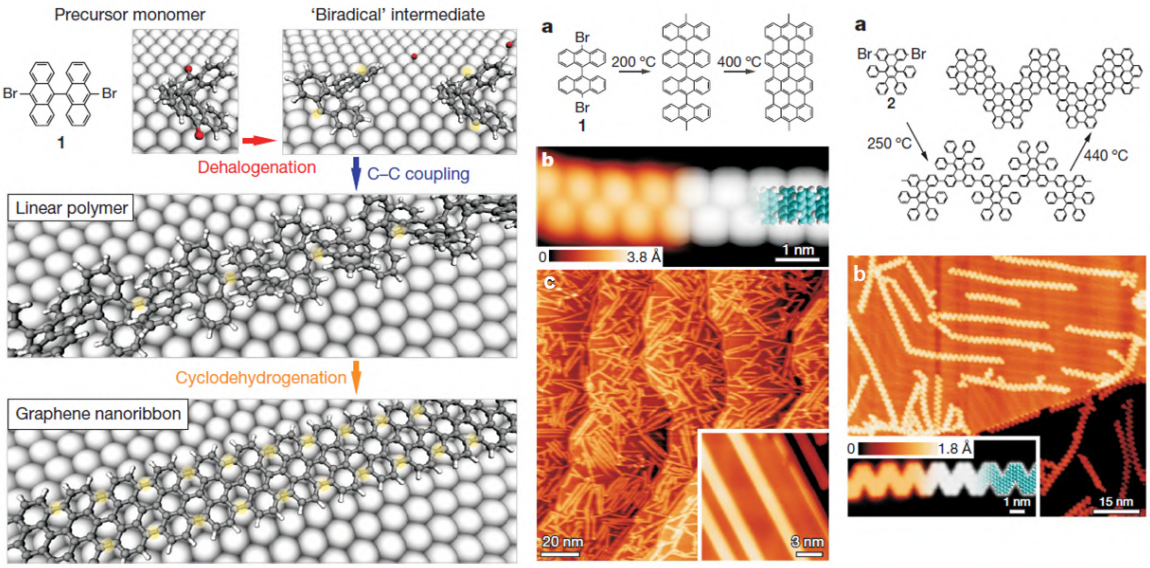

Figure 1.2: (Left) Illustration of main steps for surface-supported GNR synthesis using 10,10′-dibromo-9,9′-bianthryl monomers as precursor. Reaction schemes to obtain straight N=7 (middle) and chevron (right) GNRs, using different precursors. Resulting scanning transmission microscopy images are shown below. Images adapted from [28].

proposed with the goal to yield highly crystalline GNRs: exfoliation of a layered crystal [23], CVD [25, 26], and chemical synthesis [27].
Fasel and co-workers have been used an ingenious bottom-up approach based on the deposition of a given cluster of carefully chosen monomers either on Au(111) or on Ag(111) surfaces with subsequent removal of all halogens, formation of single C-C bonds between monomers and cyclodehydrogenation in the end (see Fig. 1.2) [28]. Other groups obtained graphene nanoribbons by unzipping multi-walled carbon nanotubes, through intercalation-exfoliation, introduction of catalytic metal nanoparticles, plasma etching of initial samples embedded in a polymer matrix, or by passing an electric current [15, 29, 30]. In all cases, the resulting ribbons are characterized by ultra-high quality, smooth edges, and controllable widths.
Thus, given the high control in manipulating carbon architectures, it is opened an avenue for the large-scale production of novel nanoforms useful in nanoelectronics, such as ultra-smooth graphene ribbons exhibiting electrical conductivity and mobility suitable for room-temperature transistor applications.

Hexagonal Boron Nitride. Like its isostructural carbon counterpart, the hexagonal boron nitride (h-BN) monolayer consists of a honeycomb-like network of sp^2 covalent bonds, except with alternating boron and nitrogen atoms in the hexagons [31–

33]. This analogy has also been found for BN nanotubes (BNNTs) first synthesized in 1995 [34], whose chiralities are defined exactly like its sister carbon system. A few scientists have successfully fabricated BN nanoribbons (BNNRs) by unwrapping multi-walled tube samples [35], as already noted in carbon case [30]. For these reasons h-BN is also referred in literature as "white-graphene". Interestingly, boron-nitride nanosystems are electrical insulators with a wide optical band gap. The estimated energy gap of both nanotubes and nanoribbons is around 6.20 eV [36–38], although corresponding excitation peaks are slightly different [37].
All these characteristics make h-BN an ideal substrate for graphene able to keep and improve its electrical performance, such as the opening of a band gap, reducing or even eliminating environmental influence [39, 40]. This is an important benefit of h-BN in comparison to other surfaces characterized by either dangling bonds or charge traps like SiO_2, which usually reduce the intrinsic properties of graphene, such as the suppression of its carrier mobility [39–41]. The ability to assemble different 2D crystalline materials generating multilayer heterostructures in a controlled way opened new opportunities in the direction of transistor design at the atomic scale, whose properties can be tailored for specific applications [41, 42]. In addition, h-BN exhibits other outstanding properties such as chemical inertness, low dielectric constant, and high thermal conductivity [41, 43].
Although h-BN is very promising for a plethora of applications, the basic question about the real intrinsic band gap nature has been object of controversy and therefore of intense investigations. Previous optical measurements made on h-BN crystal samples have shown a dominant luminescence peak at $\sim$ 5.76 eV (or 215.0 nm) in the ultraviolet (UV) region, providing a reliable proof on its direct-like behavior [43]. However, first theoretical calculations have been predicted an indirect band gap nature [44, 45]. This strong constrast has been successfully resolved by Cassabois and co-workers by using two-photon exciton spectroscopy. They confirmed that the single particle energy gap is indirect with a value of 6.08 $\pm$ 0.015 eV and in parallel unraveled the existence of phonon-assisted optical transitions in the emission spectrum of h-BN [46]. Last point demonstrates how h-BN and derived nanoforms can be considered as a promising candidates for optoelectronic applications in the far UV region, overcoming the limits found in other large band-gap materials like GaN and AlN [47].
Another largely unexplored aspect would be the variation of quasiparticle band gap for layered h-BN having different stackings. Inspired by last issue, one of the purposes of this thesis will be provide a comprehensive theoretical demonstration on how layer registry can modify the band gap behavior of BN, i.e. from direct to indirect and vice-versa.

Phosphorus. Elemental solid phosphorus (P) have been triggering enormous attention for chemists and physicists given its large versatility in a variety of technological fields, although much less explored than graphene and h-BN. One reason why of such

intense interest is because it displays a fascinating structural diversity resulting in a 'plethora' of allotropic configurations, including white, black, red, and their derivatives [48].
In this context, the determination of the most stable form of phosphorus at low pressures and temperatures represented a long-debated point, which is why exhaustive thermodynamics and energy stability analysis were needed [48, 49]. White phosphorus (sometimes also known as yellow) represents the most common form and it is a polymorphic crystal composed by P_4 molecules, whose arrangement is highly sensitive to temperature (T) obtaining several phases. At room temperature there is the α-phase, which transforms reversibly into β- and γ-forms at T = 196.15 K and 88.15 K, respectively[1]. The P tetrahedra of β configuration are arranged in the triclinic configuration, while the γ-phase is characterized by a monoclinic crystal structure [49, 50].
Then, it has been observed that white phosphorus changes into the new phase of orthorhombic black phosphorus under atmospheric pressure [51]. This new family of phosphorus possesses high carrier mobility and in-plane anisotropic physical properties [52]. In addition, the layered 3D black P can be mechanically exfoliated in order to obtain the corresponding 2D counterpart, which is called phosphorene. Unlike the carbon case, the direct band gap of black P is thickness dependent ranging from 0.3 to 1.5 eV (bulk to monolayer) [53]. Such prominent properties potentially make black phosphorus a suitable semiconductor material in a variety of applications, such as batteries, optoelectronics, photonics, sensors and transistors [52].
The third and most complex family is red-phosphorus and it can be synthesized in many modifications numbered from I to V [48]. The first three species have never been observed in pure form and hence the corresponding crystalline configurations are still the focus of on-going investigations [48, 49, 54]. The formation of triclinic IV-phase is obained by keeping the temperature in the range $\sim$ 750-800 K [48]. The red-V structure emerged at higher temperature T $\sim$ 823 K or through the crystallization from liquid [48, 54, 55]. The latter phase is characterized by a monoclinic crystal structure comprised of covalently linked pentagonal P tubes [48, 49], whick are held together by van der Waals interactions. After a few decades, it was realised that the red-IV form exactly matches the fibrous-red crystal structure, whereas the red-V phase corresponds to the configuration observed by Hittorf, also known as violet phosphorus [56].
Surprisingly, Häser and co-worker predicted novel tubular modifications of red P [57], which were then experimentally discovered by Pfitzner et al. through the extraction of parallel sets of 1D tubular phosphorus nanorods from $(CuI)_nP_{12}$ matrices with n = 2, 3, and 8 [58]. This basically results in changes of the rod packings where van der Waals forces play a dominant role. The existence of isolated tubular units was further confirmed by the analysis of corresponding diffraction patterns [58, 59]. These results represent a crucial advancement towards a better understanding of

[1]The $\beta \rightarrow \gamma$ phase transition or vice-versa has never been observed.

phosphorus physics, because they permit to classify P nanorods between molecular (0D), layered (2D) and covalently linked (3D) structures, exactly like carbon family. Initial geometries of all P allotropes here discussed reported in the Inorganic Crystal

Table 1.1: Allotropes of phosphorus and nanorods after removing CuI compounds with well-defined crystal structures and space groups available in ICSD [60]. Z is the total number of atoms in the primitive unit cell.

P allotrope	Z	Space group	ICSD No.
Black	4	$Cmca$	23836
γ-white	8	$C2/m$	154318
β-white	24	$P\bar{1}$	68326
Red-IV	42	$P\bar{1}$	391323
Red-V	84	$P2/m$	29273
P2[P8]P2[P9]P2[	24	m-P, t-P	202051
[P8]P4(4)[	15	$P2_1/c$	400984
[P10]P2[	24	$P2_1$	401755
[P12]P2[	28	$P2_1/c$	404896

Structure Database (ICSD) [60] are shown in Fig.1.3 with all details listed in Table 1. Phosphorus structures were visualized using the software VESTA [61]. Among all P configurations here discussed, the β-white phosphorus is accepted as the most common and reference state at low temperature. The most thermodynamically stable phase at room temperature and pressure is currently supposed to be the black phosphorus, as evidenced by previous theoretical calculations [49, 59].
In this thesis, we will provide an accurate study about the energy stability of all P structures with well-known crystal structure taking van der Waals interactions into account in order to create an exhaustive hierarchical scale, whose configurations with lowest energy are accepted as most favorable ones to find in experiment.

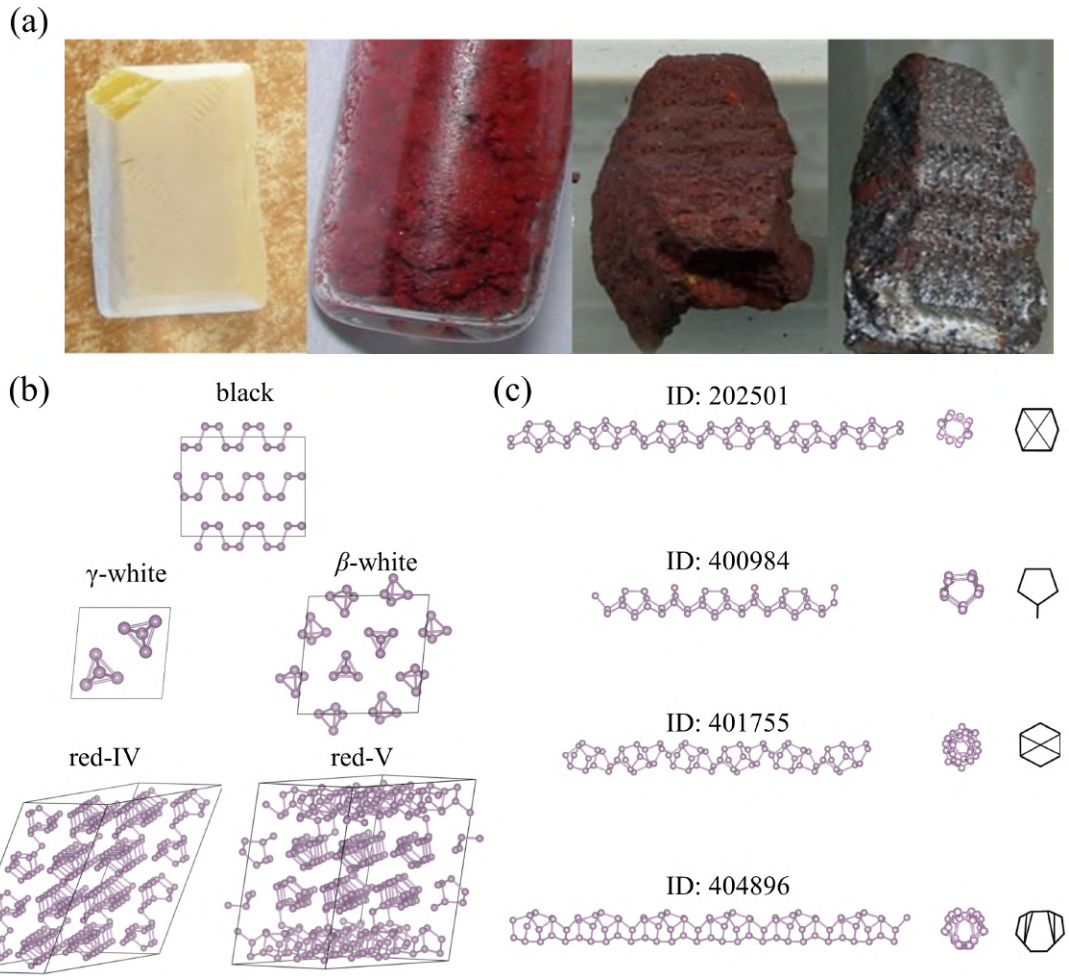

Figure 1.3: (a) Samples of phosphorus families: white (left), red granules (centre left), red chunk (centre right), and violet (right). (b) Crystal structures of black (orthorhombic), γ-white (monoclinic), β-white (triclinic), red-IV (triclinic), and red-V (monoclinic). (c) Phosphorus nanorods after removal of CuI matrices with corresponding schematic representations indicated by black solid lines. Images (a) and (b) taken from [49, 62].

1.2 Novel class of collapsed nanostructures

As illustrated before, one-dimensional sub-10-nm GNRs are supposed to be excellent candidates to extend the range of application of 2D graphene in nanoelectronics, sensors, memory and processing devices, given the opening of a band gap.
However, a systematic theoretical investigation predicted that the ribbon width must range between 2-3 nm in order to obtain an appreciable band gap ~ 0.7 eV, nearly close to Ge or InI [63]. Larger values of energy gap (1.1-1.4 eV, such as Si, InP, or GaAs) can be reached by further reducing the width of the ribbon towards 1-2 nm [63]. For ultra-narrow GNRs (W = 1-3 nm), even single atom variations in width, crystallographic orientation, or different edge-functionalizations are sufficient to cause significant band gap oscillations [63, 64]. Nowadays, a very wide sprectrum of different techniques is available to shift the Fermi level and increase its own carrier concentration, such as the introduction of scattering centres, substitutional doping, molecules adsorbed on the surface, coupling with substrates. Unfortunately, all mentioned approaches significantly destroy the intrinsic properties of graphene, just like the degradation of electron mobility.
Thus, it is clear that other approaches or even novel structures are needed in order to overcome the limitations of simple graphene and carbon nanoribbons with very short widths.

1.2.1 Collapsed carbon nanotubes as graphene nanoribbons

An original and promising alternative has been proposed in 1995. The pioneering work published by Chopra et al. reported a series of TEM images, which showed a novel class of stacked bilayer graphene nanoribbons with chemical bonding at the edges defined as close-edged bilayer GNRs (CE-BGNRs) [65]. This carbon nanostructure is obtained after radial deformation of large-diameter SWCNT, whose original cylindrical shape is broken resulting into a collapsed cross-section. CE-BGNRs consist of two highly strained edge bulbs (resembling small radius 1D circular nanotubes), bridged by a central flat region similar to 2D bilayer graphene (see Fig. 1.4(a)). For this reason such overlaid nanoribbons with folded edges are usually referred in the literature as "fully collapsed (sometimes also flattened) carbon nanotubes" [65] or "dogbone nanotubes" [66]. The thermodynamic driving force for collapse is given by a competitive process between the energy gain of attractive vdW interactions (E_{vdW}) in the central graphene-like zone [67, 68], against the energy loss for repulsive strain (E_{strain}) due to the presence of localizing curvature at each edge side [69, 70], as follows:

$$\Delta E_{\mathrm{eq}} = W_{\mathrm{flat}} E_{\mathrm{vdW}} - 2E_{\mathrm{strain}}. \tag{1.1}$$

Since the surface interactions between facing layers of the central region are width dependent, the structural transition from circular to collapsed shape is a function of the

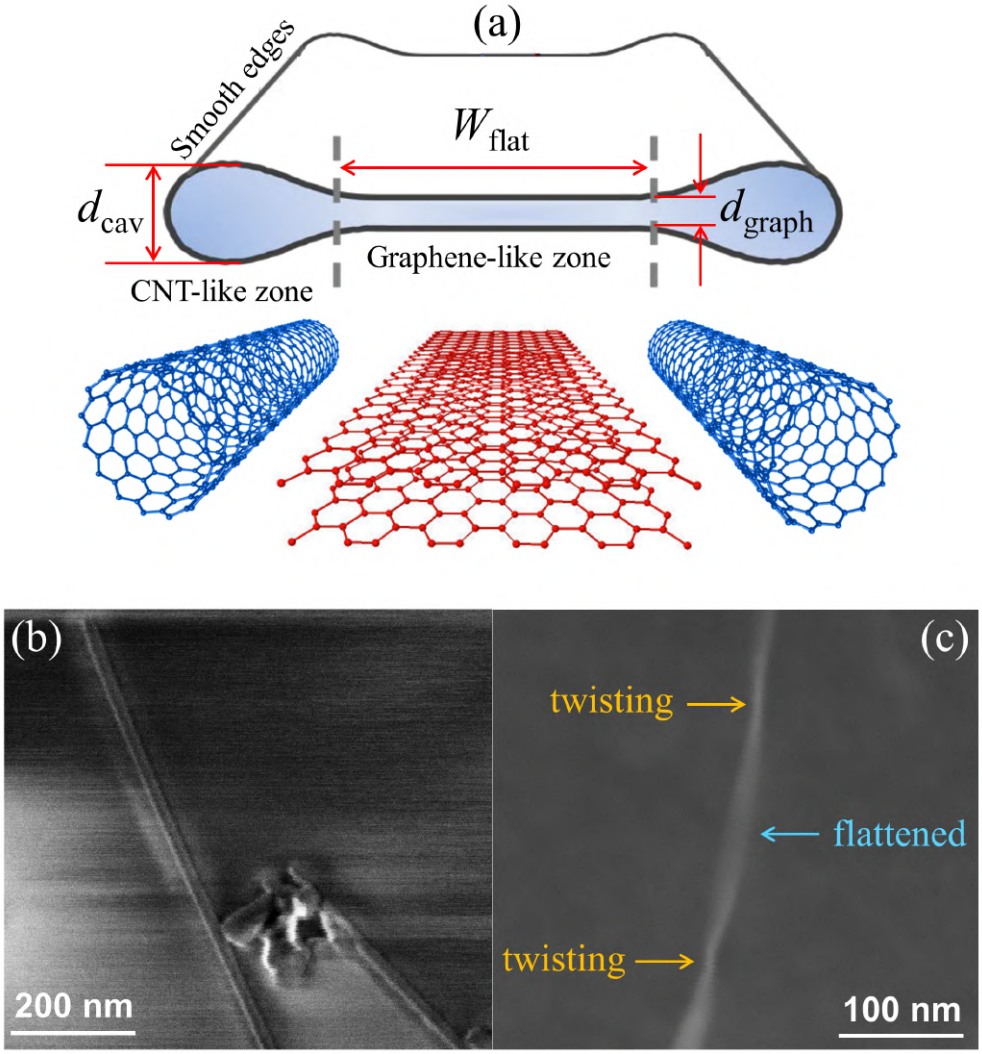

Figure 1.4: Top: (a) Schematic illustration of hybrid geometry of fully collapsed SWCNT obtained by merging bilayer graphene (red) with two circular tubes-like edges (blue). Labels indicate main geometry parameters used throughout the thesis: W_{flat} = width of central flattened region, d_{graph} = interlayer distance of graphene-like zone, and d_{cav} = diameter of edge cavities. Bottom: Scanning electron microscopy (SEM) images of flattened carbon nanotubes without (b) and with (c) evidence of twisting. Images (b)-(c) were obtained by partner CEMES. Credits: A. C. Torres-Dias.

nanotube diameter and is energetically favored above a given threshold D_{cross} [65,71]. Since then, collapsed carbon nanotubes have attracted worldwide attention, investigating: *(i)* factors that can induce the self-flattening deformation, *(ii)* experimental methods for large-scale fabrication, and *(iii)* precise determination of the threshold diameter for SWCNTs to spontaneously collapse.

Several possibilities have been reported to explain and even favour the tendency for single- and multi-walled nanotubes to collapse: the twisting deformation [65,72,73], irradiation with 800 keV electron beam of a TEM [74–76], ball milling process under ambient conditions [77,78] and temperature [79]. The structural flattening deformation is also further favoured by the interaction with different substrates [80,81] and bundling-like arrangement [66,82,83]. Additionally, the pressure-dependent collapse has been a focus of many investigations. San-Miguel and his group have explored the collapse of few-wall (single, double and triple) bundled CNTs under high-pressure using a resonant Raman scattering approach joint with different levels of theoretical methods [84–87]. They demonstrated how the radial collapse pressure P_c can be evaluated as a function of innermost tube diameter d_{in} with distinct deviations from the Lévi-Carrier law ($P_c \propto d_{in}^3$) originally proposed [71,84]. Noteworthy in this regard is that the thermodynamic stability of bundled collapsed nanotubes may be attributed to the mechanical screening between inner and outer nanotubes [84,87]. A range of synthesis routes for collapsed tubes have been developed, such as arc discharge [65,88–91], laser vaporization [92] and chemical synthesis using precusors at high pressure [93]. A popular approach is the chemical vapour deposition. For example, Campos-Delgado and co-workers have synthesized well-ordered separate planes of graphene nanoribbons, where heat treatments up to 2273.15 K lead to the annealing of point defects and interstitials with covalent bonding between reactive edges resulting into the formation of cavities [94,95]. The same type of bulb-like morphology can be obtained for stacked cup nanofibers at temperatures from 2073.15 to 3273.15 K [96].

Although the above-mentioned approaches are promising for the large-scale production of multi-walled collapsed nanotubes, the growth of single-walled ones remains quite challenging. For this reason, novel routes for the fabrication of flattened CBGNRs have been proposed. Firstly, Dai and colleagues isolated bilayer ribbons with folded edges by unwrapping gas-phase oxidized multi-walled nanotubes using an ultrasonic sonicator, despite resulting samples were erroneously identified as GNRs with dangling bonds [97]. Secondly, fully collapsed SWCNTs can be extracted from large-diameter MWNTs[2] via sonication in the presence of carefully chosen surfactants [98]. In this thesis, dog-bone nanotubes will be obtained using this method within our partnership with chemists at CRPP institute of Bordeaux (see Fig. 1.5). A fundamental basic point was to determine the collapse threshold diameter for SWCNTs. It represents a delicate and controversial point, since previous TEM images showed flattened samples having D_{cross} values significant different from each other [66,81]. This discrepancy may be attributed to the influence of external factors mentioned before. He et al. were able to chemically synthesize free-standing dog-bone SWCNTs on catalyst Au nanoparticles. They unambiguously demonstrated that the threshold diameter (labelled as D_{cross}) for single-walled tubes to collapse is

[2]Prior to the extraction phase, closed edges at both ends of MWNTs were removed by a thermal oxidation reaction.

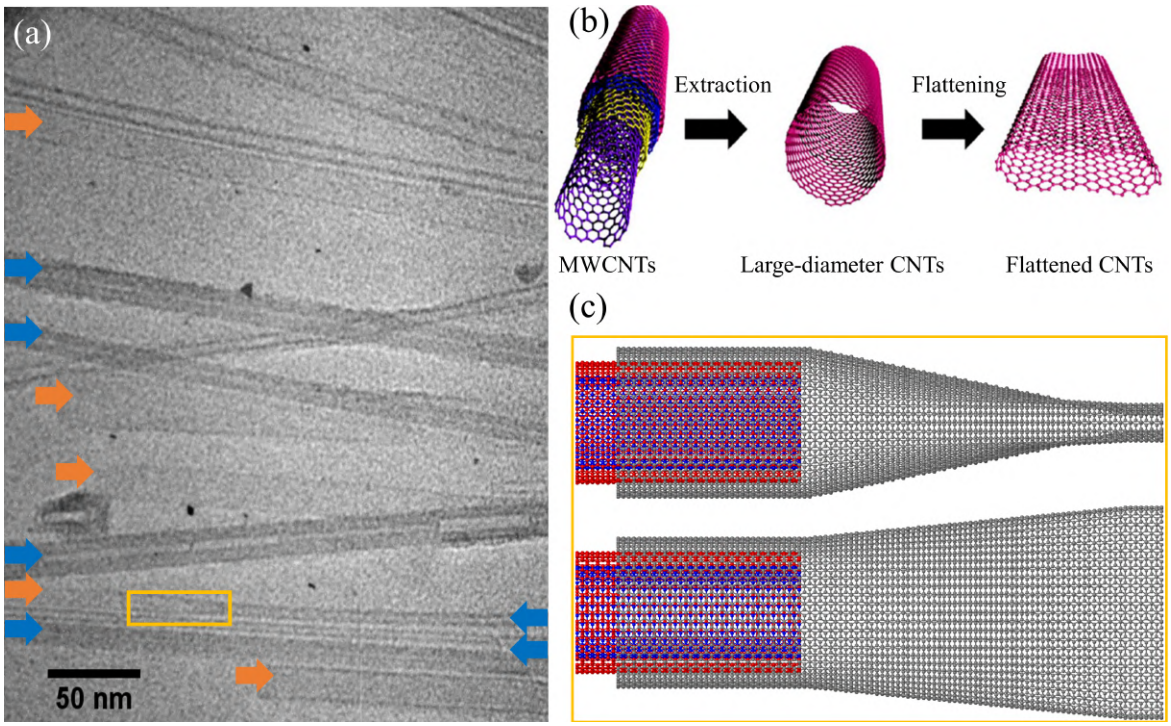

Figure 1.5: (a) TEM image showing MWCNTs (blue arrows) and fully collapsed carbon nanotubes (orange arrows). (b) Schematic illustration of preparation procedure of flattened nanotubes. (c) Atomistic representation of the extraction process via sonication to obtain spontaneously collapsed nanotubes. Images (a)-(c) are taken from Paper III, while image (b) is taken from [98].

5.1 nm [99]. In this specific context, the decision to use gold nanoparticles properly treated with air calcination has proved pivotal by overcoming the usual tendency of catalyst particles to nucleate double- and even multi-walled nanotubes instead of single-walled ones [100–102].
Surprisingly, this novel class of hybrid systems between circular nanotubes and bilayer graphene exhibited both highest mobility and lowest resistivity of any free-standing GNR samples produced to date [97, 98, 103, 104]. Latest observation further confirms the considerable impact of this new carbon nanostructure along the horizon of nanoelectronics.
Despite the remarkable progress, there are still other aspects that remain unexplored: i) the lattice registry effect on the determination of D_{cross} value for collapsed tubes, since stacking order cannot be well controlled; ii) the impact of different chiralities on the electrical properties; iii) the effects of molecules encapsulated inside these deformed carbon nanostructures; iv) the signature of local folding with respect to other topological defects. In this thesis we aim to address all of these points.

1.2.2 Evidence of folding in boron nitride

As aforementioned, boron nitride nanostructures are isostructural to corresponding carbon family. Given the analogue property of high flexibility, the following basic question arises: "*Is there any evidence for edge folding deformation for layered BN?*".

High-resolution TEM (HRTEM) characterization revealed that parallel planes of BN crystal in cubic form (properly treated at high pressures and temperatures) show the tendency to bend back and join in pairs with spontaneous formation of bulb-like structures at the edges [105]. Additionally, hBN samples obtained by chemical exfoliation [33] or chemical vapour deposition [106–108] can be characterized by the same type of mechanical deformation (see Fig. 1.6).

The formation of closed edges was originally attributed to intense electron beam irradiation [109]. However, this hypothesis was then proved wrong, since prolonged exposure tend to destroy the edge cavities with transition into amorphous phase [105]. A possible simple explanation is that dangling bonds resulting from induced-disorder treatment are stabilized with covalent bonding. This process is favoured by the turbostratic arrangement between different sheets of BN along the out-of-plane direction [33, 105]. Indeed, HRTEM imaging has clearly revealed the BN basal planes can assume different stacking combinations [105].

Although the absence of dangling bonds is very common in BN, the impact of such mechanical deformation on their main properties has remained much less explored compared to their carbon counterparts. This is primarily due to the fact the well-defined synthesis of folded-induced BN-based on nanostructures constitutes a much more challenging task. For this reason, we will investigate the electronic properties of hBN with closed edges in order to unravel its potential impact on different applications, such as optics.

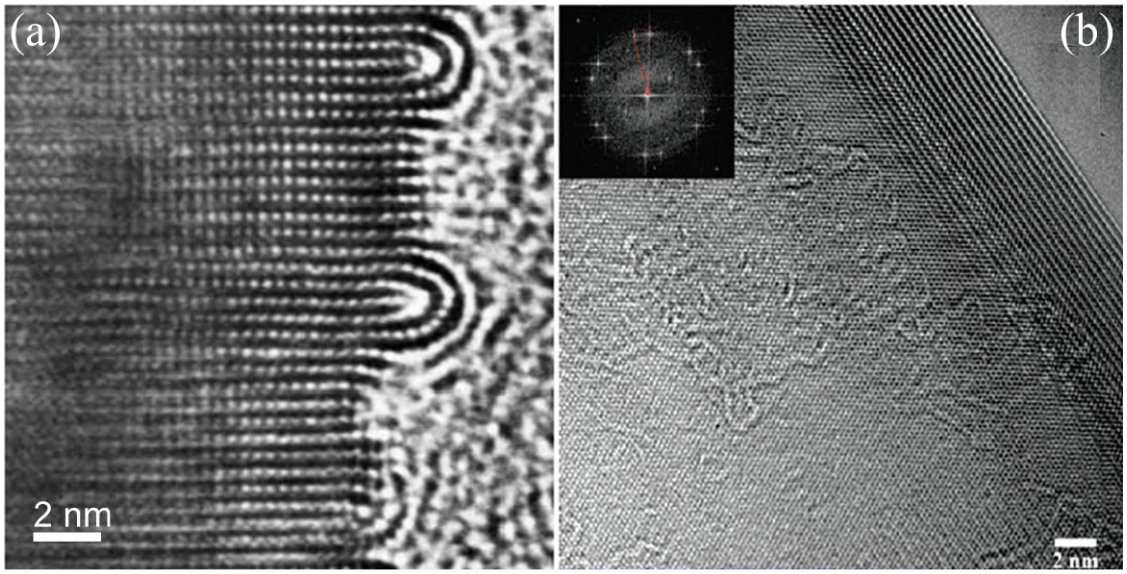

Figure 1.6: HRTEM images of: (a) formation of edge bulbs in bulk BN crystals. (b) exfoliated hBN sheets with folded edges, where inset represents the corresponding 2D fast Fourier transform. Images are taken from [33, 105].

1.3 Polystructures encapsulated inside SWCNTs

A great deal of the SWCNTs success stems from the ability to control and tune their electronic properties through different functionalization methods. An effective way to gain such control is to dope the structure with selected atoms and molecules. Several approaches have been developed for this purpose, such as the introduction of molecules in the hollow of the core tube (endohedral doping) [110], iodine species trapped within bundles intercalated between the outer shells of the tubes (also known as exohedral doping) [111]. In all cases, the doping with electron donors and acceptors induces a sensitive Fermi level shift with consequent conductivity improvement, thus making CNTs suitable for applications in nanoelectronics [111].
During studies of nanotube properties after interaction with atoms and molecules, TEM investigations revealed a surprising aspect. The atomic arrangement of encapsulated polystructures inside narrow nanotubes ($D < 2$ nm) can change, obtaining unique 1D systems [112–116], which may not exist as free-standing configurations. Despite evidence of structural transitions from 3D bulk to 1D phases for materials confined inside nanotubes, their complete identification may be quite complicated since microscopy imaging just provided a 2D projection of a 3D structure plus further distortions due to the electron beam application [117, 118]. For this reason, theoretical support to determine the equilibrium crystal structure of materials in a confined nanospace on the basis of energy stability is strongly required [118].

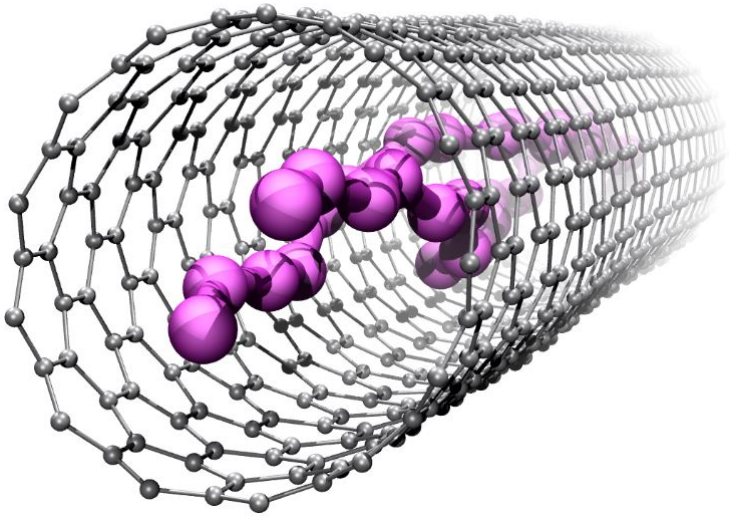

Figure 1.7: Schematic illustration of iodine in double-helical arrangement after encapsulation inside single-walled carbon nanotube. In this thesis, we explain how to obtain this kind of configurations using *ab-initio* random structure searching (AIRSS) method. This figure is adapted from Paper IV. Credits: D.V. Rybkovskiy.

In this thesis we will combine state-of-the-art microscopy characterization with total energy calculations of atomic geometries predicted by random structure searching methods [119] or extracted from ICSD [60] data set in order to interpret the unusual dynamical behaviour of those configurations grown inside narrow SWCNTs (see Fig. 1.7). This investigation is of fundamental importance for understanding the basic principles for atomic structures design at the nanolevel when the experimental data is not sufficient.

1.4 Atomistic modelling

Nowadays the use of computational tools to simulate and study the structural, electronic, and magnetic properties of nanostructures is essential for researchers working in a wide variety of technological contexts [120]. Generally, theoretical modelling represents a formidable asset to explore the potential of new materials and provide a complementary and valid support for the interpretation and/or benchmark of experimental results.
A fully-fledged encyclopedia of methods is available today, spanning from *ab-initio* methods able to capture the quantum-mechanical nature of systems at atomic scale to empirical models needed to explore the global behavior of nanostructures in determined processes or chemical reactions. Depending on the target in terms of accuracy and computational resources, the choice of the investigation method remains crucial.

All nanomaterials involved in this thesis will be addressed by employing atomistic simulations, i.e. modelling atom-by-atom, using very popular methods in the computational community of materials science [120], namely density functional theory (DFT) and molecular dynamics (MD) with empirical potentials.
In particular, along the line of emerging class of carbon- and phosphorus-based nanostructures, we will present a new methodology to simulate their Raman spectra, considered one of the most powerful and sensitive tools, to probe modifications induced in a given nanoscale system [121].

1.5 Outline of the thesis

The thesis is structured as follows.

- In Chapter 2 we present the quantum-mechanical and classical methods adopted throughout the thesis, namely DFT and MD, along with the various implementations used. We illustrate how to simulate Raman spectra in DFT, explaining also how to include the dependence from the excitation wavelength with the benefit to qualitatively capture the resonance condition.

- In Chapter 3, based on Papers I and II, we describe the thermodynamic stability and electronic properties of closed-edges bilayer graphene and boron nitride nanoribbons, exploring the impact of the curvature. Attention will also be paid to a related not-well explored type of basal dislocation, where bulk graphite is affected by interlayer displacements and chemical bonding due to the introduction/removal of half a single graphene layer. It is called a 'prismatic' edge dislocation, which resembles in some aspects the folding deformation.

- In Chapter 4, partly based on Paper III, we present a novel interpretation of the intense defect-free Raman 'D'-band by analyzing both experimental evidence and theoretical computations made on fully collapsed carbon nanotubes. We then generalize it by investigating systems mechanically deformed by the curvature, such as folded and scrolled graphene.

- In Chapter 5, partly based on Paper IV, we explore the change of electronic and vibrational properties for SWCNTs filled with polystructures, such as iodine and phosphorus. Not only that, we also propose a novel route of nanoribbon doping via filling the enlarged cavities of collapsed carbon nanotubes, with supporting experimental verification.

Chapter2

Computational methods

Computational chemistry offers a large variety of possible atomistic approaches to investigate the properties of nanomaterials. In this chapter, we introduce the basic formalism of the theory adopted throughout the rest of the thesis, i.e. density functional theory (DFT).

2.1 Overview of Density Functional Theory

Following the publications of P. Hohenberg, W. Kohn and L.J. Sham [122, 123], DFT quickly become one of the most ambitious and popular approaches to better describe the quantum behavior of atoms and molecules useful in several application fields, such as physics, chemistry, materials science, geology and even biology [124]. Such popularity is due to the following reason: when we apply well-known wave-function methods on systems composed with many particles, like organic molecules, large solids or condensed systems, their investigation is limited by poor scaling, resulting in very huge computational costs and indeed rapidly become intractable [125]. For example, the computational time scaling of Hartree Fock (HF) calculations is $\mathcal{O}(N^4)$, with N represents the number of electrons, while post-HF methods scale like $\mathcal{O}(N^5)$, allowing us to describe simulated systems composed by only decades of atoms [126]. Kohn-Sham DFT can be considered as a complementary method from a different perspective [122, 123]. Instead working with a 3N-dimensional space of single-particle states, all physical quantities of interest here are defined by the local three-dimensional electron density, $\rho(\mathbf{r})$, while the basis set is defined using a set of functions such as plane-waves (PW), or linear combination of atomic orbitals (LCAO) or even relativistic Gaussians (RG). Large and computationally expansive LCAO and RG basis sets usually describe all occupied bands of a given system at the same level as PWs but with lower computational cost. Main speed gain is because they are *local*, so e.g. do not describe vacuum and are good for local defects [127].

Although the default scaling law of DFT is $\mathcal{O}(N^3)$, many computational physicists and chemists worked to further optimize diagonalization algorithms, reaching time scaling like $\mathcal{O}(N^2 \log N)$[1] [128]. Compared to other *ab-initio* methods, this represents a better compromise between scalability and time savings. Furthermore, DFT is especially suitable to provide a complementary reliable support to experiments involving defects, disorder, interfaces, electron-phonon coupling and spin-orbit coupling and much more.
The implementation of current DFT codes enables to perform electronic structure computations of systems composed by several hundreds of atoms within a reasonable human time. Despite ever-increasing improvements mentioned above, it is known that the system size intrinsically accessible by DFT remains still limited to isolated portions of realistic bulk, locally perturbed regions and nanodevices.
In the next sections we briefly provide a quick primer of DFT fundamentals, emphasizing its advantages and limitations, so to acquire more familiarity with the theoretical background of this work. Of course DFT is a much larger subject: we invite the interested reader to refer to the several books [122, 129] available on this field, as well as the *Perspective* published by Axel D. Becke [123], where the state-of-the-art of DFT is outlined very clearly[2].

2.1.1 DFT in a nutshell

The theory developed by L. H. Thomas, E. Fermi, and P. A. M. Dirac in 1926 explained that the exchange and kinetic energies of a many-electron system can be locally approximated by their one-electron ground-state density, $\rho(\mathbf{r})$ [131]. The limitation of the proposed approach is the inability to reproduce atomic shell structures. Thus, it results quite poorly in the description of binding molecules [132].
The Hartree-Fock (HF) model combined with Slater formulation provided the first model of the electronic structure of complex condensed-matter systems, although electronic correlations were completely neglected [133]. Some fundamental properties of solid-stated physics cannot be reproduced in this way.
A significant advancement was reached in 1964 with the first published paper on DFT by Hohenberg and Kohn (HK) [122]. Given a system of N interacting electrons characterized by an electronic wave function[3] in an external nuclear potential V_{e-n}, described by the following Hamiltonian:

$$\hat{H}_e(\mathbf{R}) = \hat{T}_e + \hat{V}_{e-e} + \hat{V}_{e-n} = \tag{2.1}$$

[1] The actual purpose is the implementation of massively parallel methods, which enable reductions down to $\mathcal{O}(N)$.

[2] For people interested in a more formal approach, it is useful to refer to E. Engel's and R.M. Dreizel's *Density Functional Theory: an advanced course* [130].

[3] The electronic wave function can be separated from that of the nuclei within the Born-Oppenheimer approximation.

$$= -\sum_i \frac{\hbar^2}{2m_e}\nabla_i^2 + \sum_{i\neq j}\frac{e^2}{2|\mathbf{r}_i - \mathbf{r}_j|} + \sum_i V_{e-n}(\mathbf{r}_i), \tag{2.2}$$

they demonstrated that:

Theorem 2.1.1. *The ground-state energy of a many-electron system from Schrödinger's equation is a unique functional of the electron density ρ.*

Theorem 2.1.2. *The electron density that minimizes the energy of the overall functional is the true electron density corresponding to the full solution of the Schrödinger equation.*

The 1st theorem establishes a 1:1 mapping between the ground-state properties of a given system and its electron density, which indeed is considered as the key variable in DFT. This point is really important, because we can completely determine all properties of interest on the basis of a function of four variables (three spatial plus spin), rather than a function on $3N$ variables (like the wave function). Thus, the "power" of this theorem consists in the reducing of dimension of the problem under consideration. With the 2nd theorem, once the energy functional is specified and minimized, we can find the ground-state of the system. The HK theorems may be considered as the formal exactification of the Thomas-Fermi model.
On the basis of results published by Kohn and Sham [123], the energy functional introduced can be written as follows:

$$E[\rho(\mathbf{r})] = E_{\text{known}}[\rho(\mathbf{r})] + E_{\text{xc}}[\rho(\mathbf{r})], \tag{2.3}$$

where $E_{\text{xc}}[\rho(\mathbf{r})]$, called the exchange-correlation functional, is defined to include all the quantum mechanical effects that are not included in the "known" terms[4].
By using the variational principle, Kohn and Sham showed the decomposition of N-electron Schrödinger equation into a set of single-electron equations:

$$-\frac{1}{2}\nabla_i^2\psi_i^{\text{KS}} + V_{\text{eff}}(\mathbf{r})\psi_i^{\text{KS}} = \varepsilon_i\psi_i, \tag{2.4}$$

where: $\{\psi_i^{\text{KS}}\}$ represents a set of single-particle orbitals whose electron density is defined to be exactly that of the real system, while $V_{\text{eff}}(\mathbf{r})$ is a new effective external potential[5], which includes the effects of exchange and correlation incorporated in

[4]The term E_{known} in eq. (2.3) includes the electron kinetic energies, the Coulomb interactions between the electrons and the nuclei, and then those between pairs of electrons and those between pairs of nuclei.

[5]In addition to its standard definition in terms of the functional derivative of $E_{\text{xc}}[\rho(\mathbf{r})]$, the exchange-correlation potential $V_{xc}[\rho(\mathbf{r})]$ constitutes a mean-field mechanical interaction potential between the electrons.

$E_{\rm xc}[\rho(\mathbf{r})]$. The expression of the resulting total energy is determined by performing a summation over only the occupied states, as follows:

$$E_{\rm tot}[\rho(\mathbf{r})] = \sum_{occ} \varepsilon_i - \frac{1}{2}\int d\mathbf{r}d\mathbf{r}' \frac{\rho(\mathbf{r})\rho(\mathbf{r}')}{|\mathbf{r}-\mathbf{r}'|} - \int d\mathbf{r} V_{\rm xc}[\rho(\mathbf{r})]\rho(\mathbf{r}) + E_{\rm xc}[\rho(\mathbf{r})], \quad (2.5)$$

Thus, we can summarize the essence of the Kohn-Sham ansatz: electrons in atoms, molecules and solids can be described as independent particles moving in this effective potential. As a result, Kohn-Sham DFT can be considered an independent-particle theory, in fact it may be regarded as the formal advancement of Hartree theory.
The KS equations require to be solved self-consistently due to the density dependence on the one-electron effective potential. Thus, the key point here is the functional E_{XC}: once its analytical form is specified, the main DFT computational problem comes down to a self-consistent numerical solution of the KS equations, carried out as outlined in the following algorithm [134]:

1. Define an initial, trial electron density, $\rho(\mathbf{r})$.

2. Solve the KS equations defined using $\rho(\mathbf{r})$ to find the single-particle wave functions, $\psi_i(\mathbf{r})$.

3. Determine the electron density defined through the KS single-particle wave functions: $\rho^{\rm KS}(\mathbf{r}) = 2\sum_i \psi_i^*(\mathbf{r})\psi_i(\mathbf{r})$.

4. Compare the calculated electron density, $\rho^{\rm KS}(\mathbf{r})$, with the electron density used in solving the KS equations, $\rho(\mathbf{r})$. If the two densities match between themselves, then this is the ground-state electron density and it can be used to compute the total energy. If the two densities are different, then the trial electron density must be updated in some way. Once it is done, the process restarts again from step 2.

Once the self-consistent loop illustrated above is converged for a fixed configuration of nuclei, the forces acting on each of them can be evaluated, invoking the Hellmann-Feynman theorem [129]. This procedure can be iterated until a (local) energy minimum is achieved, corresponding to a stable configuration of the system. This optimization problem, usually referred to as a geometry relaxation, can be solved by employing several proper numerical methods [129], such as the quasi-Newton method, or the conjugate gradient method used in the current study.

2.1.2 Our DFT toolbox

DFT is now implemented in a plethora of commercial and open-source codes, each one with its own benefits and limitations. In this thesis we will use two implementations of DFT, namely Ab Initio Modeling Program (AIMPRO) [135–138] and

QUANTUM-ESPRESSO [139, 140]. These software packages mainly differ in the type of basis set adopted to approximate KS wave-functions. At the same time we hope to provide a general perspective of the numerical accuracy of our calculations.

- **Exchange-correlation functionals**:
  Once the exact exchange-correlation functional ($E_{\rm xc}$) is available, the electron density and corresponding total energy can be computed within the DFT code. Unfortunately, the $E_{\rm xc}$ cannot be found exactly and it has to be substituted by an approximate form. The simplest is the local-density approximation (LDA), where the real original inhomogeneous system is assumed to be composed of infinitesimal volumes, within which each density is constant. We are basically assuming that the exchange-correlation energy per electron at a given point $\mathbf{r}$ in the electron gas is equal to the exchange-correlation energy per electron in a *homogeneous* electron gas that has the same electron density as the electron gas at the same point $\mathbf{r}$. As is well known, the exchange ($E_{\rm x}$) and correlation ($E_{\rm c}$) functionals in LDA tend to overestimate and underestimate almost all interactions, respectively. But, the resulting $E_{\rm xc}$ functional involves a cancellation of errors coming from previous two contributions. The latter point explains why: despite its seemingly inaccurate nature, LDA has been remarkably successful for many systems, such as diamond-structure silicon [11]. For this reason, $E_{\rm xc}^{\rm LDA}$ values are really close to those obtained by more sophisticated Quantum Monte Carlo (QMC) approach with respect to other methods. It was later demonstrated how this approximation is not reasonable to describe non-covalent forces, i.e. hydrogen bonding and vdW interactions, which are crucial for the formation, stability, and function of molecules and materials, like transition metal oxides [11]. Given this limitation, attempts to find better approximations were performed. The subsequent approximate functional generalizes the basic idea of the previous one by taking into account the local uniform density ρ together with its gradient term ($\Delta\rho$). Given their dependence on the gradient of the charge density, the DFT functionals based on this generalized gradient approximation (GGA) are also called "semi-local", typically yielding better results than the LDA, for geometries and ground state energies of molecules and solids [11]. The main difference and accuracy among GGA functionals is given by the choice of the exchange enhanced factor ($F_{\rm x}^{\rm GGA}(s)$) used to define the exchange energy:

$$E_{\rm x}^{\rm GGA}[\rho(\mathbf{r})] = \int d\mathbf{r}\ \varepsilon_{\rm x}[\rho(\mathbf{r})]\, F_{\rm x}^{\rm GGA}(s). \tag{2.6}$$

  The most common parametrizations for the $F_{\rm x}^{\rm GGA}(s)$ functional were provided by Perdew and Wang and then by Perdew, Burke and Ernzerhof (PBE) [11, 141].

- **Dispersion correction**:
  If LDA tends to underestimate lattice parameters of layered nanostructures characterized by weak van der Waals (vdW) interactions, on the other hand GGA-PBE computations overestimate these values (e.g. graphene unbound). Therefore, many approaches have been developed to accurately model these long-range interactions, which play a significant role in interlayer binding between different layers. These are commonly included in the GGA through the semi-empirical corrections developed by Grimme, namely D2 [142] and D3 [143]. The vdW corrections (also termed dispersive corrections) add an additional term E_{vdW} to the DFT total energy E_{DFT}, as follows:

$$E_{\mathrm{DFT-D}} = E_{\mathrm{DFT}} + E_{\mathrm{vdW}}, \tag{2.7}$$

$$E_{\mathrm{vdW}} = -\frac{1}{2}\sum_{A,B} f_{\mathrm{damp}}(R_{AB}, R_A^0, R_B^0) C_{6,AB} R_{AB}^{-6}, \tag{2.8}$$

  where the D2 and D3 corrections differ in the tractation of the dispersion coefficient $C_{6,AB}$. These two corrections cannot properly quantify long-range interactions described through C_6 terms. Regarding this point, Tkatchenko and Scheffler proposed a method to determine these dispersion coefficients accurately. The underlying idea consists of using the ground-state electron density to compute the C_6 coefficients as a function of *relative* polarizability for atoms in a given system [11]. Thus, the description of weakly bonded systems in DFT is greatly improved.
  Subsequent works have mainly focused on how to improve the description of the repulsive behavior of the exchange-correlation functional carried out by a damping factor f_{damp}. The version proposed by Becke and Johnson (BJ) leads to a constant contribution of E_{vdW} to the total correlation energy from each pair of atoms directly bonded with the consequent benefit to avoiding artificial repulsive interatomic forces at shorter distances [144]. To gauge the performance of the BJ damping factor, it has been tested on selected molecules using a long list of different exchange-correlation functionals. This benchmark widely demonstrated that DFT-vdW coupled with BJ damping factor provides more reliable results on the thermodynamic properties of strongly bound molecules [144].

- **DFT functionals beyond GGA**:
  As introduced before, the vdW interactions are critical to better investigate a plethora of systems, including bulk solids, surface phenomena, or even biostructures. However, the vdW forces depend also on non-local charge events, which correlate different sub-regions of the entire system under analysis. LDA and GGA functionals give no account of the fully non-local vdW interaction. It represented the motivation to implement a fully-fledged class

of van der Waals density functionals (vdW-DFs) scheme [11]. This novel theory level is based on the inclusion of a non-local correlation functional of the density ρ, described as follows:

$$E_c^{nl}[\rho] = \int d^3\mathbf{r} \int d^3\mathbf{r}' \ \rho(\mathbf{r})\phi(\mathbf{r},\mathbf{r}')\rho(\mathbf{r}'). \tag{2.9}$$

In this context, C09, revPBE and PW86 functionals have been proposed. Langreth and co-workers tested these functionals on 22 weakly-bonded molecules, observing that equilibrium spacings, hydrogen-bond strengths, and interlayer potentials predicted by PW86 are really improved and even close to those of accurate quantum chemical calculations [11].
The electronic band gaps of semiconductors and insulators are one of the most important quantities investigated for electronics, spintronics, and optoelectronics applications. The electronic energy gap is simply defined as the difference between the conduction band minimum (CBM) and valence band maximum (VBM). It is well-known that standard DFT woefully underestimates band gap value, due to a missing contribution by an amount nearly equal to a derivative discontinuity of the exact E_{xc} [145].
More sophisticated approximated forms for the exchange-correlation functional are needed. One possible solution consists in using so-called hybrid functionals based on a mix of HF and DFT exchange, which significantly reduces the discrepancy between DFT predicted and experimentally estimated values. However, the integration of the HF exchange significantly increases the computational costs. A solution has been proposed by Heyd *et al.*, where the full Coulomb operator is replaced by an error function-screened version, whose short-range (SR) and long-range (LR) components are well-separated [146]. This formulation takes into account only the SR part of the HF exchange, since the LR one is completely screened with resulting lowering of the computational demand for calculations. The hybrid exchange-correlation functional developed by Heyd, Scuseria and Ernzerhof (HSE) is defined as follows:

$$E_{\mathrm{xc}}^{\mathrm{HSE}} = \alpha E_{\mathrm{x}}^{\mathrm{HF,SR}}(\omega) + (1-\alpha)E_{\mathrm{x}}^{\mathrm{PBE,SR}}(\omega) + E_{\mathrm{x}}^{\mathrm{PBE,LR}}(\omega) + E_{\mathrm{c}}^{\mathrm{PBE}}, \tag{2.10}$$

where: the parameter ω defines the separation between long and short range interactions, while α corresponds to the Fock exchange.
In the original parametrization for HSE06 proposed in Ref. [146], the parameters ω and α are set to 0.106 a.u. (atomic units = a.u.) and 0.25, respectively. Although the HSE06 version excels for semiconductors with band gaps in the range 1-5 eV [147], it has been demonstrated that an appropriate parametrization should be done when pronounced changes in screening are considered [148, 149]. This is particularly true for wide band gap materials such as h-BN, which will be described in the results section.

- **Basis set**:
  In codes like QUANTUM-ESPRESSO the KS wave-functions are expanded in terms of plane waves, as follows:

$$\phi_{\mathbf{k}}(\mathbf{r}) = \frac{1}{\sqrt{\Omega}} \sum_{\mathrm{G}} c_{(\mathrm{k+G})} e^{i(\mathrm{k+G})\mathrm{r}}, \tag{2.11}$$

  where Ω represents the unit cell volume and the summation is over all reciprocal lattice vectors G. These functions can be obtained by diagonalizing the Hamiltonian matrix elements of the Schrödinger equation. Just as for a Fourier transform in practice, the exact solution evaluated in even a single point in k-space would require a summation over an infinite number of possible values of G. The infinite sum shown in eq. (2.11) is truncated to include terms characterized by a kinetic energy $E = (\hbar^2/2m)|\mathrm{k} + \mathrm{G}|^2$ only up a finite cutoff value. However, such a truncation to a finite basis set will lead to a source of inaccuracy in the computed total energy and its derivatives[6]. Therefore, appropriate convergence tests are necessary in order to find a cutoff energy with the required accuracy level.

  In AIMPRO instead the wave-functions are described via a set of localised Cartesian Gaussian orbitals (COGs), defined by the product of Gaussian exponents with polynomial functions centered on atoms [150]:

$$\phi_{i,n_1,n_2,n_3}(\mathbf{r}) = x^{n_1} y^{n_2} z^{n_3} e^{-\alpha_i r^2}, \tag{2.12}$$

  where $x^{n_1} y^{n_2} z^{n_3}$ and α_i define the angular (together with magnetic quantum numbers) and spatial dependence of the functions, respectively. The mix of Gaussian exponents and angular momentum makes the current basis set more flexible and accurate than PW one in the description of systems with broken lattice symmetry, e.g. defective regions in a crystal. Additionaly, the choice of the total number of polynomial functions including all angular momenta up to s ($l = 0$), p ($l = 0{-}1$), d ($l = 0{-}2$) and so on in a given COG can influence the accuracy of ground-state energy computations. It is noted that angular momentum up to s, p, d results in 1, 4, and 10 independent functions, respectively [150]. For example, a simple basis set composed of four p-functions gives rise to 16 functions per atom, and could result in quite poor reproduction of the system of interest. On the other hand, a larger basis set with four d-type functions resulting in 40 functions provides a lower and more reliable total

[6]For this reason PW-DFT codes are not the suggested preference to investigate the properties of systems whose wave-functions vary rapidly, and therefore a large number of plane-waves is required. They also insufficient for systems with significant amounts of vacuum, which has to be treated at the same level of precision as the rest of the computed cell.

energy, however, the size of the full Hamiltonian increases and in turn the computational cost. For this reason, it is important to choose a set of basis with an appropriate combination of p- and d-type functions which represents a reasonable trade-off between accuracy and computational time savings.
When dealing with carbon-based systems, the main "focus" of this thesis, accurate benchmark studies are crucial to select the appropriate basis set for the investigated problem. For example, the *pdpp* basis set composed by 22 independent functions is widely used for carbon nanostructures with defects and reproduces well intra-system bonding [150, 151]. However, this basis set usually fails in the prediction of inter-system longer range properties, such as the interlayer binding energy of bulk graphite. Therefore, a heavier basis set composed by two p-functions combined to three d-type ones resulting in 38 independent functions in total (referred to as *pdddp* for simplicity) was developed with the aim of matching as far as possible with the experimental value estimated by Zacharia and co-workers: 52 ± 5 meV/atom [152].
Although the stacking of the basal plane of graphene sheets to form a 3D carbon solid can arrange in different configurations, the Bernal (AB) stacking represents the preference. Fig. 2.1 shows the impact of various basis sets on the interlayer potentials of AB-stacked graphite with lowest binding energies and interlayer distances listed in Table 2.1. This performance study of various basis sets was carried out within AIMPRO code using DFT-GGA/PBE approximation coupled with Grimme D3 dispersion correction. The binding energies predicted by *pdpp* basis set is larger by $\sim 25\%$ than the *pdddp* value and it is about twice as large as the result obtained by quantum MC [153]. It demonstrates that a smaller basis set certainly overestimates the vdW interaction, like optB86b-vdW approach [154]. The larger *pdddp* basis set gives a reliable binding energy in very good agreement with more sophisticated random phase approximation (RPA) calculations [155] and experiment [152]. These results clearly indicate that: once the level of DFT theory is selected (LDA, GGA, and so on), the proper choice of basis-exponents represents an important preliminary step before starting the real computations of interest.
All main results reported in this thesis are produced by the *pdddp* basis set. However, if *pdddp* computations should be too computationally huge for large size-systems, then the smaller *pdpp* basis set will be adopted.

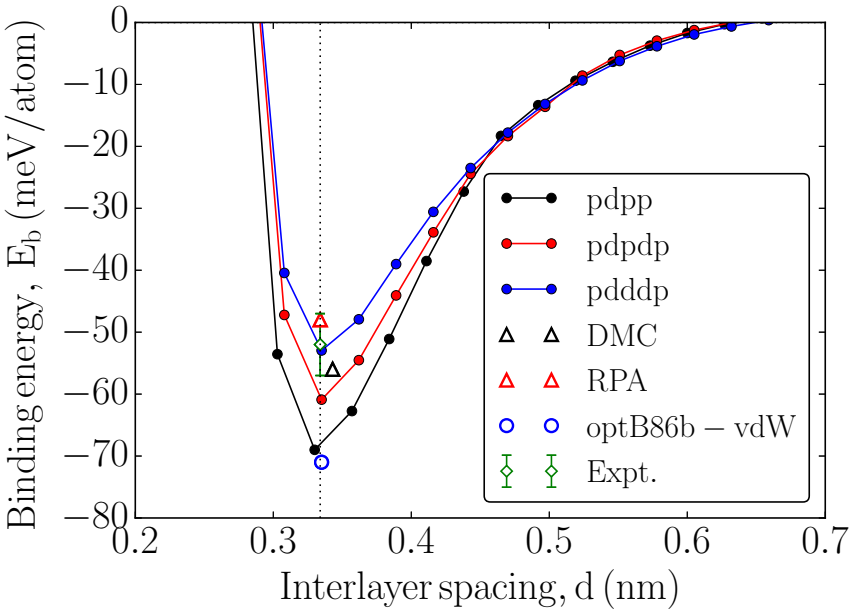

Figure 2.1: (Color line) DFT-GGA+D3 calculated interlayer binding energy of graphite by changing basis set: *pdpp* (black line), *pdpdp* (red line), *pdddp* (blue line) in comparison with experiment and different theoretical methods: DMC, RPA, and optB86b-vdW.

Table 2.1: Interlayer spacings and binding energies of graphite in AB-stacking by increasing the number of functions involved in each basis set and their comparison with the experiment.

DFT-D3			
Basis set	No. functions	d_{in} [nm]	E_b [meV/atom]
pdpp	22	0.330	−68.94
pdpdp	32	0.333	−60.83
pdddp	38	0.335	−52.91
Experiment	-	0.334	-52 ± 5

2.2 Modelling of Raman Spectroscopy

As discussed previously, Raman spectroscopy represents a powerful and nondestructive tool to differentiate related nanomaterials. Since the physics behind Raman spectroscopy is a very large subject, a full exhaustive explanation has resulted in some excellent books [156,157]. However, the modelling of Raman spectra is always quite challenging for computational physicists, generating criticism concerning the validity of each proposed methodology, especially in the resonance regime. In this section we provide a quick primer of theoretical background of Raman spectroscopy together with similitaries and differences of implemented methods used to simulate vibrational spectra.

2.2.1 Raman background theory

The Raman effect is defined as the inelastic scattering process of light when a given system of initial energy E_i absorbs a photon of energy $\hbar\omega_L$ with incident polarization $\mathbf{u}_L$ exciting up to a virtual state of energy E_f and emitting a photon with energy $\hbar\omega_S$ and scattered polarization $\mathbf{u}_S$ [158, 159]. The scattered Raman intensity I_s is defined as follows:

$$I_s = I_0 \frac{d\sigma}{d\Omega}, \tag{2.13}$$

which increases linearly with the incident intensity I_0. The differential cross section of this process can be expressed in the following form:

$$\frac{d\sigma}{d\Omega} = \frac{\omega_L \omega_s^3}{(4\pi\varepsilon_0)^2 c^4} |V_{if}|^2 \delta(E_i + \hbar\omega_L - E_f - \hbar\omega_S), \tag{2.14}$$

where: Ω is a solid angle, the δ function ensures energy conservation, while the term V_{if} represents the 2^{nd} order matrix element for light scattering derived under Kramers, Heisenberg, and Dirac formalism [160, 161]. Since all states involved in the latter matrix element depend from nuclear as well as electronic degrees of freedom, the corresponding calculation is analytically demanding. By using the Born-Oppenheimer approximation, it is possible to separate the two contributions mentioned above, obtaining the following simplified expression:

$$V_{if} = \mathbf{u}_L \cdot \sum_{e,k} \left[\frac{\langle i^0 | D_e | k^e \rangle \langle k^e | D_e^* | f^0 \rangle}{E_e - E_0 + \varepsilon_k^e - \varepsilon_i^0 - \hbar\omega_L} + \frac{\langle k^e | D_e^* | f^0 \rangle \langle i^0 | D_e | k^e \rangle}{E_e - E_0 + \varepsilon_k^e - \varepsilon_i^0 + \hbar\omega_S} \right] \cdot \mathbf{u}_S^{\mathrm{T}}, \tag{2.15}$$

where: D_e is the dipole transition matrix element, the electronic energies of ground and excited states are labelled as E_0 and E_e, respectively, while their corresponding vibrational parts are indicated as ε_i^0 and ε_k^e. The energies E_0 and E_e are independent of the nuclear coordinates and represent the minima of the harmonic curves

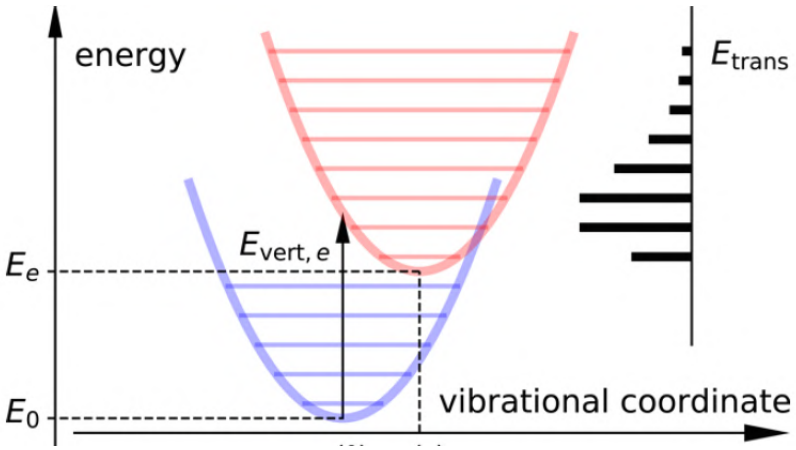

Figure 2.2: Schematic representation of the displaced harmonic oscillator model for the electronic ground (blue) and excited (red) state. Figure taken from [162].

within the displaced harmonic oscillator approximation, as depicted in Fig. 2.2. The energy difference between incident and scattered photon corresponds to the energy difference of vibrational states as follows:

$$\hbar\omega_L - \hbar\omega_S = E_f - E_i = \varepsilon_f^0 - \varepsilon_i^0 \begin{cases} > 0, & \text{Stokes} \\ < 0, & \text{anti} - \text{Stokes} \end{cases} \tag{2.16}$$

One may derive Raman intensities starting from Eq. (2.15) by using appropriate approximations [162].

2.2.2 Placzek Approximation

Although the electronic and vibrational motions are decoupled in Eq. (2.15), the determination of vibrational states and corresponding eigenvalues for a multidimensional electronic surface still remains a formidable task. For this reason, the following approximations are typically applied:

1. Under the semi-classical approximation [162,163], the energy terms $E_e - E_0 + \varepsilon_k^e - \varepsilon_i^0$ in the denominators of Eq. (2.15) are replaced by their main contribution, i.e. the vertical transition energy to the electronic state represented in Fig.2.2:

$$E_e - E_0 + \varepsilon_k^e - \varepsilon_i^0 \approx E_{vert,e}. \tag{2.17}$$

Once Eq. (2.17) is applied to Eq. (2.15), the dependence on k of denominators is removed and it is possible to apply the closure relation:

$$\sum_k |k^e\rangle\langle k^e| = 1. \tag{2.18}$$

For real and symmetric wave functions (for those systems where the magnetic field is supposed to be absent), the following condition is valid: $\omega_L \approx \omega_S \approx \omega$. With all these assumptions, the new expression for V_{if} is further simplified as:

$$V_{if} = \mathbf{u}_L \cdot \langle i^0|\alpha(\omega)|f^0\rangle \cdot \mathbf{u}_S^{\mathrm{T}}, \tag{2.19}$$

where the term $\alpha(\omega)$ represents the polarizability tensor in its electronic ground state:

$$\alpha(\omega) = \sum_e \frac{2E_{vert,e}D_eD_e}{E_{vert,e}^2 - \hbar^2\omega^2}, \tag{2.20}$$

2. In classical Raman theory [162, 163], the complex polarizability tensor $\alpha(\omega)$ can be expanded in a Taylor series in terms of normal vibrational coordinates:

$$\alpha(\omega, \mathrm{q}_l) = \underbrace{\alpha(\omega, \mathrm{q}_l^0)}_{\text{Rayleigh}} + \underbrace{\left.\frac{\partial\alpha(\omega, \mathrm{q}_l)}{\partial \mathrm{q}_l}\right|_{\mathrm{q}_l=\mathrm{q}_l^0} \cdot (\mathrm{q} - \mathrm{q}_l^0) + ...}_{\text{Raman}}, \tag{2.21}$$

where $\mathrm{q}_l = \mathrm{q}_l(\nu)$ is the position of the atom ν^{th} along a given direction ($l = x$, y or z). In the harmonic approximation, the first term corresponds to Rayleigh scattering (f=i), while the first-order derivative of the polarizability tensor with respect to the atomic displacements represents the Raman contribution (f=$i\pm1$). The latter term is used to compute the Raman tensor $\tilde{R}$ for phonon mode j at incident excitation energy E_{exc} [164], as follows:

$$\tilde{R}(j, E_{\text{exc}}) = \sum_{\nu=1}^{N}\sum_{l=1}^{3} \frac{\partial\alpha(E_{\mathrm{L}})}{\partial \mathrm{q}_l(\nu)} \frac{e_l^j(\nu)}{\sqrt{m_\nu}}, \tag{2.22}$$

where: $e_l^j(\nu)$ corresponds to the eigen-vector of the dynamic matrix, while m_ν is mass of the ν^{th} atom. Their ratio represents the eigen-displacement along the direction l in the j^{th} phonon mode.
The limitation involving first derivatives is that quadratic or mixed modes cannot be included at this approximation level, since only one vibrational quantum is excited.

The methodology described here, where the scattered Raman intensity is proportional to the energy-dependent Raman tensors for each of the phonon modes j from the dielectric function derivatives at energies E_{exc}, is known as the Placzek approximation [162]. It can be summarized as follows:

$$I_s \propto \left| \mathbf{u}_L \cdot \tilde{R}(j, E_{\text{exc}}) \cdot \mathbf{u}_S^{\text{T}} \right|^2 . \tag{2.23}$$

The chemistry community used this powerful approximation widely, although one takes care on the exact expression of the Raman intensity to use depending on the system under investigation, i.e. molecules or well-oriented solids [162].
For the most common experimental setup, the Raman intensity is expressed as [162]:

$$I_s = 45a^2 + 7\gamma^2 + 5\delta^2, \tag{2.24}$$

where a, γ and δ represent the Raman invariants and are the mean polarizability, the anisotropy and the asymmetric anisotropy, respectively [156]. According to the Placzek approximation, all three quantities are defined as a function of Raman tensor components.
Once determined the matrix elements $\tilde{R}(j, E_{\text{exc}})$ and averaging over incoming and scattered light polarizations in all planes of the nanostructure of interest, the Raman intensities can be calculated as:

$$I_s = \begin{cases} \frac{1}{4}\frac{n_j+1}{\omega_j}(|\tilde{R}_{xx}|^2 + |\tilde{R}_{xy}|^2 + |\tilde{R}_{yx}|^2 + |\tilde{R}_{yy}|^2), & xy \text{ plane} \\ \frac{1}{4}\frac{n_j+1}{\omega_j}(|\tilde{R}_{xx}|^2 + |\tilde{R}_{xz}|^2 + |\tilde{R}_{zx}|^2 + |\tilde{R}_{zz}|^2), & xz \text{ plane} \\ \frac{1}{4}\frac{n_j+1}{\omega_j}(|\tilde{R}_{yy}|^2 + |\tilde{R}_{yz}|^2 + |\tilde{R}_{zy}|^2 + |\tilde{R}_{zz}|^2), & yz \text{ plane} \end{cases}, \tag{2.25}$$

where: $n_j = [\exp(\hbar\omega_j/k_B T) - 1]^{-1}$ is the Boltzmann distribution function at a given temperature T expressed in K and ω_j is the frequency of the j^{th} phonon mode.
Having described this theoretical approach, I now describe how to implement its key points from a computational point of view as outlined in Fig. 2.3: after performing structural relaxation, the phonon frequencies and eigen-vectors at the Γ point of a given system were calculated. After the diagonalization of the dynamical matrix, all atomic coordinates are displaced along each of the phonon eigen-vectors, considering both positive and negative displacements. For each of these displaced structures, we compute both real and immaginary parts of the polarizability tensors within the sum over states approach from corresponding electronic band structure at energies close to the experimental excitation energies. We next evaluated Raman tensors for each of the phonon modes from the energy-dependent polarizability derivatives. The resulting matrix elements have been then used to determine Raman intensities. The final Raman spectra are obtained after Lorentzian broadening. While phonon frequencies and polarizability α were directly extracted from DFT computations using AIMPRO software package, Raman tensors $\tilde{R}$ and intensities I_s were computed using the Placzek approximation implemented in the algorithm, which we have developed during an intense training at the Skoltech Institute.
We will mostly use the set of Eq. (2.25) to reproduce the Raman spectra of the carbon nanostructures investigated in this thesis.

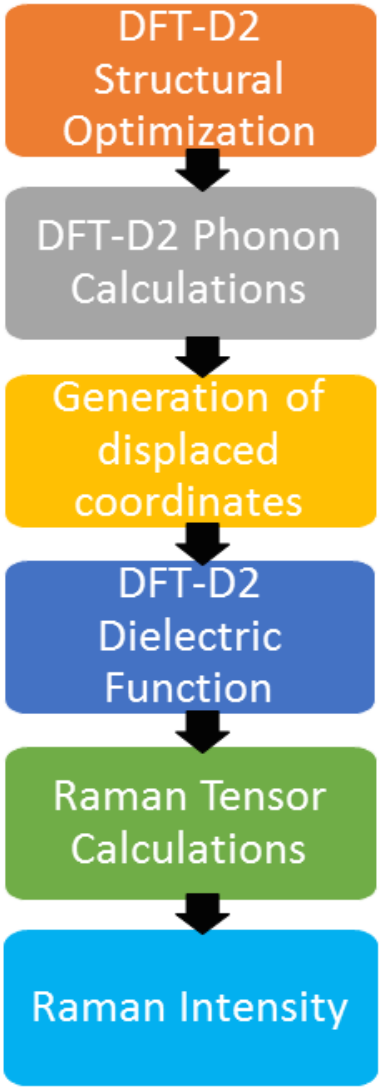

Figure 2.3: Workflow scheme of the Raman-Placzek approximation. The atomic coordinates of a given system are allowed to fully relax without any constraint. The corresponding phonon frequencies and eigen-vectors for the optimized configuration with the finite atomic displacements of 0.106 Å. Then, a set of displaced coordinates along each phonon mode is generated. Real and imaginary parts of the dielectric tensor are computed for each displaced configuration within DFT level. The resulting matrix elements are then used to evaluate Raman tensors, which represent the main components in order to determine the Raman cross-section.

2.2.3 Approximation beyond semi-classical approach

As seen above, physicists and chemists widely use the semi-classical Placzek approximation to reproduce the Raman intensities of those molecules having an electronic gap so large that the experimental wavelength of incident photon ω_L is far from any electronic resonance. In the non-resonant Raman scattering regime, the dependence on the excitation wavelength ($\omega_L \to 0$) is neglected and the polarizability tensor $\alpha(\omega_L)$ is replaced by its static version $\alpha(0)$ derived by calculations with applied electric fields. This last assumption is not valid for studying and characterizing solids, since transitions involving multiple vibrational quanta are absent in Placzek [162].
To go beyond the semi-classical approach in order to take multiple vibrational excitations into account, where only energy transitions from the vibrational ground state depend on the nuclear coordinates, Albrecht proposed an alternative formulation [162, 165]. If all energy terms in the denominators of Eq. (2.15) exhibit the same dependence, then one may expand all matrix elements in terms of vibrational coordinates. In such a way, the resulting expression for V_{if} would be composed by a sum of three terms as:

$$V_{if} = V_{if}^{\mathrm{A}} + V_{if}^{\mathrm{B}} + V_{if}^{\mathrm{C}}, \tag{2.26}$$

where just the first term labelled A gives a dominant contributation close to the resonance regime[7]. It is also known as the Frank-Condon term and represents the key quantity to differentiate Raman intensities obtained by Placzek and Albrecht approaches [162, 166].
Interestingly, it has been observed that the Placzek approximation agrees qualitatively with the Albrecht one in the near-resonant regime for the excitation of single vibrational quanta[8]. This was particularly double-checked for the *trans*-butadiene compound [162], as shown in Fig. 2.4. In the region below 2000 cm^{-1}, the Placzek spectrum qualitatively matches with Albrecht despite its much lower absolute intensity [161]. The peaks at higher vibrational frequencies due to the multiple excitations are absent in the Placzek version given the limitation to neglect derivatives of higher-order, which are instead well-reproduced within the Albrecht approach. Although the resonance Raman intensities obtained under the Albrecht approximation are remarkably similar to those of molecules investigated in the experiments, this method is computationally demanding for large-size systems. Depending on the target, the choice of method is driven by the balance between accuracy and computational cost. Since in this thesis we will investigate nanostructures with hundreds of atoms, our

[7] Prior theoretical literature showed that Raman intensities obtained when taking into account only the Albrecht A term are comparable to that full Albrecht. In cases where we observe visible differences, it may be due to phenomena of destructive interference described by the sum of Albrecht BC terms, which is also called the Herzberg-Teller term [166]. For interested readers, the full detailed tractation about the role of each Albrecht term is found in [162].

[8] An approximate equality between the two proposed approaches is obtained in the limit of very small excitation energies, formally described by: $\hbar\omega_L / E_{vert,e} \to 0$.

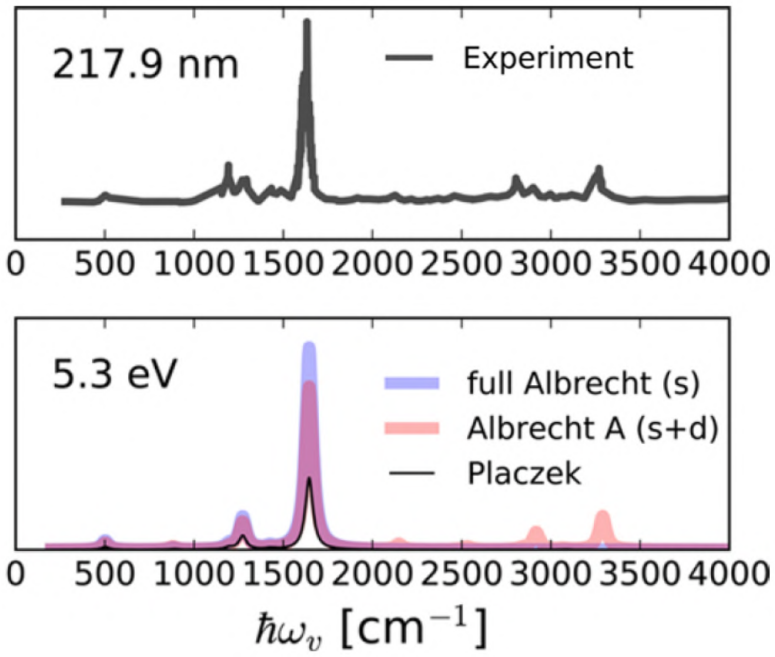

Figure 2.4: Top: Experimental near-resonant Raman spectrum for *trans*-butadiene recorded at excitation energy 5.3 eV (at 217.9 nm, equivalently). Bottom: Simulated Raman spectra by comparing different theory levels: Placzek (black solid line), full Albrecht with single (cyan) and double (pink) vibrational excitations. The asymmetric anisotropy was set to 0.2 (Albrecht) and 0.4 eV (Placzek). Figure taken from [162].

multi-wavelength method based on the Placzek approximation represents a reliable compromise.

2.3 Reactive empirical potential for carbon-based system

Soon after Brenner introduced a classical potential energy function to describe bond making and breaking of diamond films in chemical vapour deposition [167], there was intense interest in developing empirical potentials to calculate the structural properties and energetics of a wide range of other carbon structures. These include fullerenes [168], carbon melts [169], hydrogenated diamond-like carbon [170], amorphous carbon [171], nanocones and screw dislocations [172], and processes associated with nanoindentation [173, 174] or friction between layered materials [175].
The benefit of using empirical potentials is the possibility to investigate large systems composed by hundreds of thousands of atoms, which would be not feasable

with quantum mechanical approaches[9]. The basic concept of the classical approach consists in using an interatomic potential $E(\{r\})$, which expresses the total energy of a given system as a function of the set $\{r\}$ of particle coordinates. In this context, one must takes care about the expression of the potential energy to describe the type of bond order, which is highly sensitive to the local portions of the geometry system under consideration [176].
In the last decades, the description of intermolecular interactions in condensed-phase hydrocarbon systems (like graphite, polymers and liquids) related to chemical bonding variation has been the object of debate and hereby of intense work. For example, the Abell-Tersoff potential does not permit to simultaneously evaluate equilibirium distances, energies, force constants for C-C bonds and it only has limited capacity to describe energetics atomic collisions [176, 177]. A similar situation exists for the reactive empirical bond-order (REBO) potential developed by Brenner, which only describes shorter-range interactions ($r < 2$ Å) between C-C, C-H, and H-H atoms [178]. Although it has been widely used to model different carbon nanosystems, such as fullerenes, carbon nanotubes, tribology and tribochemistry of diamond interfaces, the absence of non-bonded or longer-range interaction terms makes this potential quite poor to analyze hydrocarbon systems with important longer range bonding effects such as vdW. Consequently, this creates a strong challenge for the determination of a unified empirical potential.
A solution to this problem has been proposed by Stuart *et al.* [179] and it is based on an improved version of the REBO potential with additional energy terms as follows:

$$E = \frac{1}{2}\sum_{i}\sum_{j\neq i}\left[E_{ij}^{\mathrm{REBO}} + E_{ij}^{\mathrm{LJ}} + \sum_{k\neq i}\sum_{l\neq i,j,k} E_{ijkl}^{\mathrm{tors}}\right]. \tag{2.27}$$

Here: the second energy term (E_{ij}^{LJ}) represents the Lennard-Jones potential, which includes all longer-range interactions. The last term (E_{ijkl}^{tors}) is the torsional interaction potential and describes the dihedral angle behaviour of systems under analysis. This complementary formulation of the REBO potential, which permits to evaluate the non-bonded interactions through an adaptive intermolecular treatment, is called the AIREBO potential. It represents a useful addition to the arsenal of computational chemistry to provide valid results about hydrocarbon liquids, thin films, and other materials dominated by covalent interactions [179].
We gauge the performance of the classical AIREBO potential against the accuracy of quantum mechanical DFT computations to investigate one of the key points of the thesis, i.e. the determination of the threshold diameter for single-walled carbon nanotubes to collapse. All simulations are performed using the large-scale atomic molecular massively parallel simulator code (LAMMPS) [180].

[9]Despite the advantage to analyze complex physical systems and chemical reactions, methods based on empirical potentials permit to investigate only energetics and mechanical properties, while those electronic and magnetic ones need an *ab-initio* approach.

Chapter3

DFT analysis of closed-edged nanomaterials

Many outstanding properties of nanostructures are reliant on the presence of structural defects. Deviations from the perfectly flat infinite hexagonal lattice turn out to be essential to achieve specific functionalites for desired applications, such as chemical reactivity and doping. For this reason, the influence of point and line defects on the properties of carbon [11, 15, 24, 181–184] and boron nitride [33, 105, 185–187] hexagonal lattices has been well-documented, forming a fully-fledged encyclopedia. However, relatively few of these studies have addressed possible out-of-plane deformations, adopted by carbon and boron nitride sheet edges, such as folding, scrolling, buckling, rippling, and wrinkling [188,189]. These topological distortions lead to the formation of local curvature along the surface and interlayer bonding, resulting in a mixture of sp^2-sp^3 rehybridization of atoms with consequent changes of corresponding electronic structure.
In this chapter, our main focus is to explore the stability of closed-edged graphene and boron nitride nanostructures with their new and distinct properties. Same attention will also be paid to the formation of prismatic edge dislocations, a form of "internal edge", on highly damaged graphite by particle irradiation. Prismatic edges are also common during growth.

3.1 Chirality and stacking effects in collapsed CNTs

Fully collapsed (or flattened) carbon nanotubes become energetically favored with respect to their cylindrical counterparts above a certain diameter [190, 191]. In the present section, we determine the precise value of diameter for SWCNTs with different chiralities to spontaneously collapse.
Besides helicity dependence, collapsed tubes are also structurally defined by another

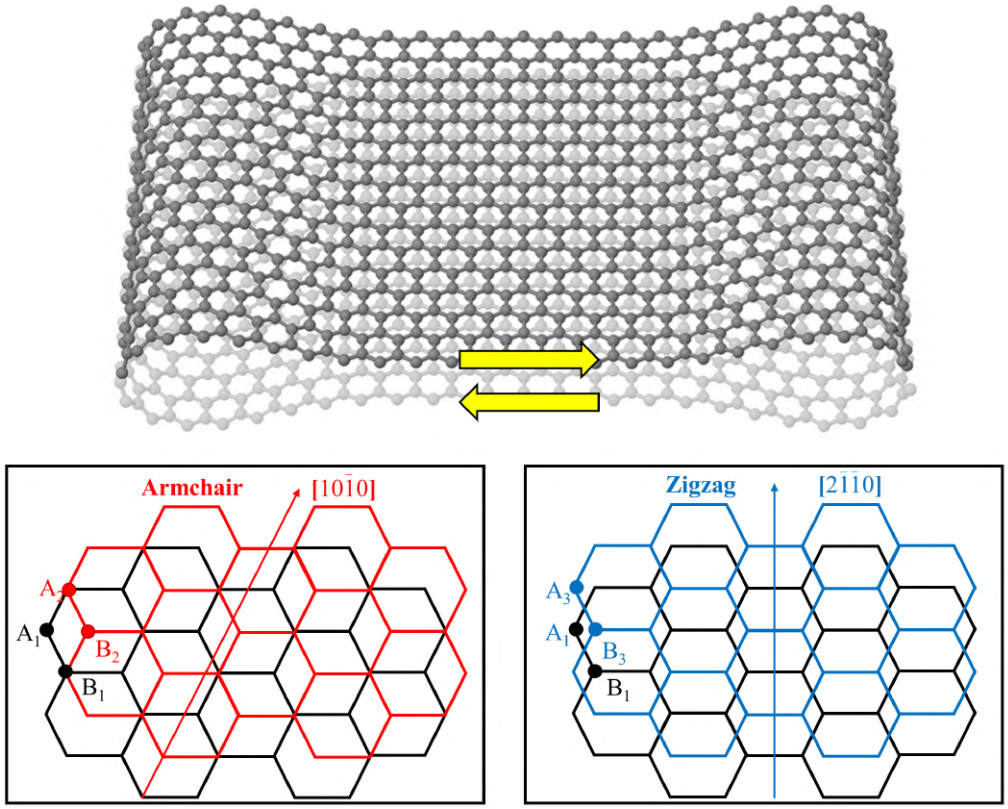

Figure 3.1: Top: Geometry of collapsed SWCNT. Yellow arrows show interlayer shear mode. Bottom: Displacements along the armchair [10$\bar{1}$0] and zig-zag [2$\bar{1}$ $\bar{1}$0] patterns of the lattice structures of adhering layers forming bilayer graphene-like central section of flattened tubes. Carbon atoms of the (black) lower and (red/blue) upper layers are labelled as $A_{1(2/3)}$ and $B_{1(2/3)}$, respectively. Bottom image taken from Paper I.

parameter, namely the interlayer shear between facing layers of the flat middle section and that can consequently change its stacking combination (see Fig. 3.1). Despite increasing interest in the physics of folded graphene edges, the role of interlayer registry effects still remains largely unexplored since stacking order is turbostratic and not controllable in collapsed tubes experimentally [192, 193]. We will address the structural transition from circular to dog-bone shape taking also the effect of lattice registry into account.

The electronic structure of flattened nanotubes are analyzed showing a band gap emergence due to the presence of uniform smooth edges and its sensitivity to the chirality and stacking sequence. This study fully described in Paper I constitutes a solid benchmark for the on-going development of an atomistic model that can be harnessed to realize electronic devices having enhanced conductivity [29,97,98,103,104].

3.1.1 Geometry of collapsed SWCNTs

The formation of collapsed tubes via radial deformation and spontaneous collapse of free-standing SWCNTs has been studied extensively using a plethora of experimental and theoretical methods. Given the nanotube diameter D, it was widely demonstrated that the structural circular-collapsed transition can be described in function of two threshold diameters D_{meta} and D_{cross} [81, 99, 154, 193], as follows:

1. $D < D_{\text{meta}}$: collapsed deformed nanotubes cannot be stabilized and only circular configuration stays in equilibrium;

2. $D_{\text{meta}} \leq D < D_{\text{cross}}$: the collapsed configuration can be in equilibrium, but it is thermodynamically unfavorable (metastable) compared to circular one;

3. $D \geq D_{\text{cross}}$: collapsed tubes are energetically more stable (absolute stability), while nanotubes with circular cross section become metastable.

Electron microscopy studies show that free-standing chiral SWCNTs collapse when their diameter exceeds a threshold $D_{\text{cross}} = 5.1$ nm [99]. Since the metastable threshold diameter D_{meta} lies below D_{cross}, it cannot be experimentally observable. Previous theoretical investigations have been mostly made using empirical models, such as molecular dynamics, molecular mechanics, and continuum elasticity supplemented with vdW interaction, mainly because atomistic scale methods based on DFT are computationally demanding in simulating large-size collapsed CNTs [65, 81, 99, 154, 194–205]. Classical methods give the D_{meta} values in 1.4-3.2 nm range, however, the prediction of stable collapse threshold diameter D_{cross} shows a much larger variation among calculated values from 2.0-8.8 nm, implying their limited usefulness.
Our empirical AIREBO computations underestimate the experimental collapse threshold diameter by ∼1.0 nm compared to experiments, while other potentials show the opposite effect, e.g. 6.2 nm using Tersoff-Brenner and LJ potentials [202]. This lack in achieving of the experimental threshold diameter is attributed to the difficulty of classical potentials to properly estimate the vdW interactions between facing graphene layers taking stacking and thermal effects at room temperature into account [99]. It suggests that empirical potentials are not well adapted to quantitatively describe collapsed deformation and so a more accurate atomistic model is recommended, like DFT.
In order to fix this discrepancy, we make a detailed *ab-initio* investigation of self-collapse deformation of isolated SWCNTs, employing several levels of DFT approximation with the software AIMPRO (see Table 3.1). Initially, we calculated the total energy difference between AB-stacked collapsed ($E_{\text{tot}}^{\text{collapsed}}$) and circular ($E_{\text{tot}}^{\text{circular}}$) of armchair ($n$,$n$) nanotubes to determine above which flattened tubes become the most stable configurations (see Fig. 3.2(a)). Both crossing diameter and optimized parameters of dog-bone structure, notably the interlayer spacing in the central flat

Table 3.1: Summary of threshold metastable (D_{meta}) and stable (D_{cross}) diameters (in nm) between circular and collapsed free-standing SWCNTs provided in literature and in Paper I. The methodologies adopted to obtain these results are also given.

Ref.	D_{meta} [nm]	D_{cross} [nm]	Methodology
[194]	-	2.000	MD: REBO + LJ potentials
[195]	1.400	2.000	Continuum model verified by MD
[65]	-	2.600	Simple model using curvature and vdW energies
[81]	-	2.600	MD: AIREBO potential without torsion term
[196]	1.000	3.000	MD and molecular mechanics simulations
[197]	2.700	3.3-8.8	Continuum elasticity (CE) model verified by DFT
[198]	-	3.400	Tight binding method and MD: LJ potential
[199]	2.100	3.800	Atomic-scale finite-element (AFEM) and CE methods
[99]	1.800	4.100	MD: AIREBO + LJ potentials
[200]	-	4.100	AFEM method and MD: Tersoff + LJ potentials
[154]	2.200	4.300	DFT calculations with optB86b-vdW
[201]	2.200	4.500	CE model using strain and vdW energies
[99]	1.800	5.100	MD results corrected by DFT-vdW
[154]	2.200	5.180	DFT with GGA-PBE+D2 in AB-stacking
[202]	2.400	6.200	MD: 2$^{\text{nd}}$-generation Tersoff-Brenner and LJ potentials
[203]	3.200	6.400	Finite-deformation model
[204, 205]	2.5,2.1	7.000	CE shell model using DFT results for strain energy
[99]	-	5.100	Experiment: CVD and TEM image analysis
Our work	1.800	4.075	MD: AIREBO potential with torsion term
Our work	3.497	-	DFT with GGA-PBE in AB-stacking
Our work	1.904	5.141	DFT with GGA-PBE+D2 in AB-stacking
Our work	1.904	5.337	DFT with GGA-PBE+D3(BJ) in AB-stacking
Our work	2.987	7.256	DFT with LDA in AB-stacking

graphene-like zone (d_{graph}), the diameter of edge cavity (d_{cav}) are strongly sensitive to the type of approximation used in the calculations.

First of all, our GGA+D2 calculated threshold diameter ($D_{\text{cross}} = 5.141$ nm) exactly matches with experimentally measured value (~ 5.1 nm) [99] for collapsed tubes with stacking close to AB and agrees with prior literature at the same level of approximation [154], whereas, D3(BJ) version exhibits a slightly higher value of 5.337 nm. Another small difference between D2 and D3(BJ) corrections is the predicted interlayer spacing in the central flattened zone $d_{\text{graph}} = 0.327$ and 0.334 nm, respectively. Dispersion-corrected GGA gives edge cavity diameter d_{cav} of 0.780 nm independent of vdw correction implemented in the calculations. This is very close to the diameter of (6,6) nanotube (0.814 nm) and slightly larger than the diameter of C_{60} fullerene (~ 0.7 nm) [16]. Although the calculated interlayer spacing of central flat section for collapsed tubes ($d_{\text{graph}} = 0.333$ nm) using LDA agrees with experiments (0.334 nm) and most reliable calculations recently collected [152,206], it overestimates both collapse threshold diameter (7.256 nm) and size of edge cavities (0.878 nm). Due to its weakest interlayer binding, the GGA approximation without vdW correction predicts the largest edge cavity equal to 1.060 nm. Indeed the stable threshold diameter cannot be ever reached, despite the attempts to simulate large-width collapsed tubes resulting computationally quite huge.

The radial collapse represents the trade-off between interlayer coupling vs localisation of curvature, and hence interlayer binding energy will be critical. In fact, there is a direct correlation between threshold diameters of collapsed SWCNTs and binding energy minima of bilayer graphene (see Fig. 3.2(b)). The binding energies predicted by DFT+D are somewhat larger (in magnitude) than those obtained using diffusive QMC approach [153, 207], while they are very close with the long-range van der Waals density functional (vdW-DF) and many body-dispersion (MBD) methods referred to in Ref. [153]. In addition, they finally match with the most recent density functional calculations within the Grimme scheme using either projector-augmented wave (GGA+D2-PAW) [154] or pseudopotentials proposed by Burkatzki, Filippi, and Dolg (GGA+D2-BFD) [208]. This excellent agreement provided for interlayer interaction further confirms that GGA+D2 scheme matches well the experimental threshold to nanotube collapse. LDA significantly underestimates the interlayer binding of bilayer graphene compared to GGA+D method ($> 30\%$) and hence overestimates the collapse threshold. Underestimation of the interlayer potential of GGA without vdW corrections is so high that collapsed nanotubes will never be energetically stable.

In summary, these results demonstrate that: *(i)* proper treatment of the vdW interaction plays a crucial role for the thermodynamic stability of flattened SWCNTs, whose layered structures resemble those of bilayer graphene and even graphite; *(ii)* while LDA and GGA show significant deviations from the experiment, the dispersion correction GGA (DFT-D2) show the best agreement with both available experimental data and most common theoretical methods reported in literature.

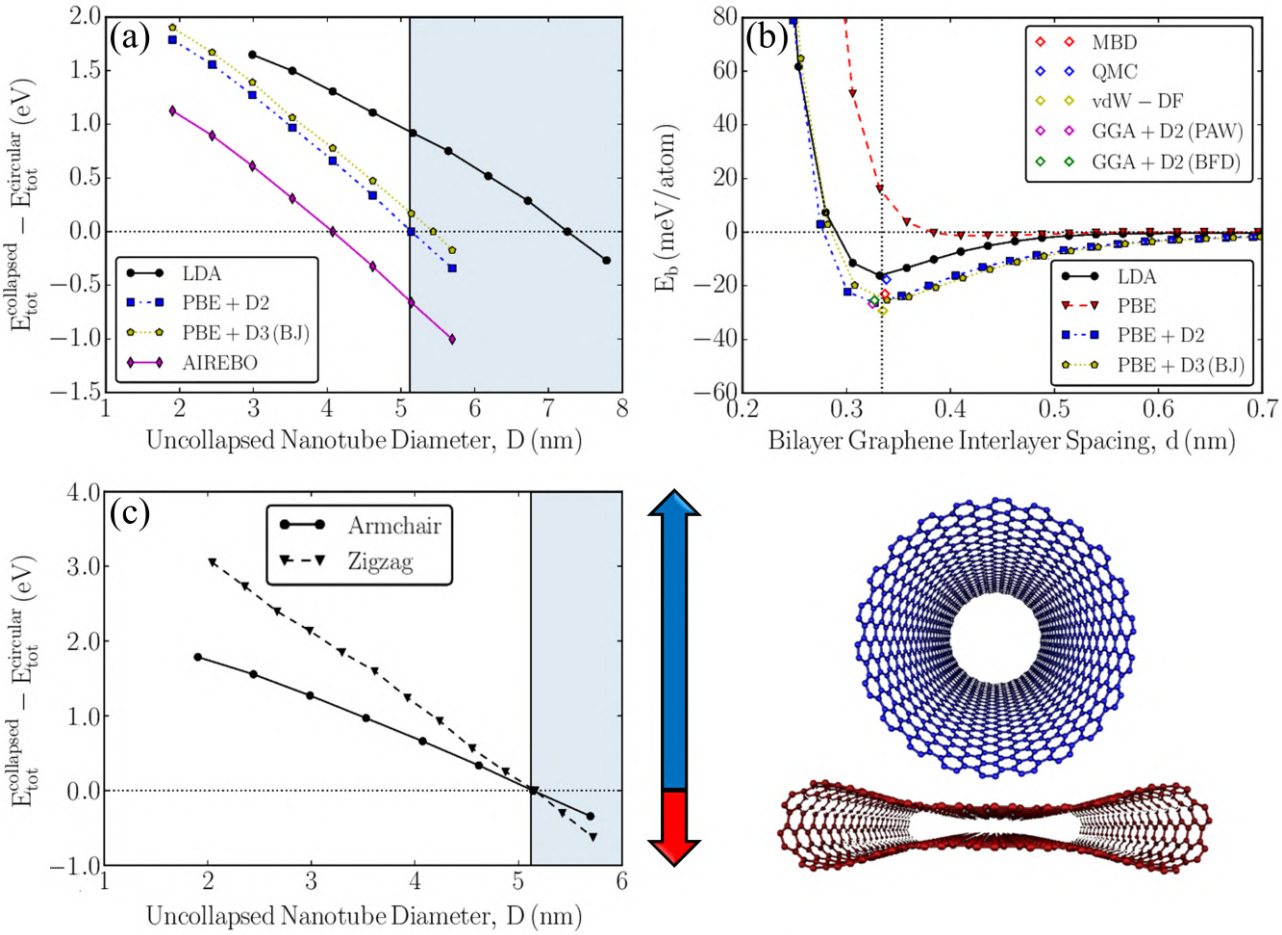

Figure 3.2: (a) Total energy difference between free-standing AB-stacked collapsed ($E_{\rm tot}^{\rm collapsed}$) and circular ($E_{\rm tot}^{\rm circular}$) armchair ($n$,$n$) SWCNTs versus uncollapsed tube diameter D (nm) changing level of theory. The intersection point at $\Delta E_{tot} = 0.0$ eV represents the threshold diameter for isolated nanotubes to collapse. Shaded section indicates diameters for which collapse is observed experimentally [99]. DFT calculated interlayer binding energies for AB-stacked bilayer graphene in comparison with different theoretical methods: MBD [153], QMC [153, 207], vdW-DF [153], GGA+D2 (PAW) [154], and GGA+D2 (BFD) [208], respectively. Vertical dashed line represents interlayer distance of bilayer graphene and graphite obtained in the experiment [152, 206]. (c) DFT-D2 calculated deformation energy of collapsed nanotubes at different diameters with armchair (solid line) and zigzag (dashed line) chirality. Magenta section represents diameters for which collapse is observed [99]. The threshold diameter for SWCNTs to collapse is essentially chirality independent (5.141 and 5.154 nm for armchair and zigzag, respectively). All DFT calculations are carried out with a large *pdddp* basis set. Image taken from Paper I.

Having tested the performance of DFT exchange-correlation functionals for interlayer interaction in collapsed SWCNTs, we extend this energy stability study to the zigzag (n,0) nanotubes. Using the DFT-D2 scheme, the collapse threshold diameter for both armchair and zigzag nanotube is 5.1 nm (see Fig. 3.2(c)), confirming that the structural phase transition is largely independent of tube chirality. Zig-zag collapsed tubes have edge cavities slightly smaller than the diameter of a (11,0) nanotube (0.862 nm).
Interestingly, zigzag SWCNTs naturally collapse with a resulting stacking sequence slightly different to AB, which is usually labeled as AB′ [209]. Radial collapsed zigzag nanotubes can be recognized as an analog of bilayer armchair GNRs with closed edges, where AB-stacking is geometrically incompatible upon the formation of the cavities [210].
The effects of stacking and lattice registry on flattening deformation is described in detail in the next section.

3.1.2 Impact of interlayer shearing

The self-collapse process lowers the symmetry of a SWCNT and introduces an additional structural modification respect to circular nanotubes, named the interlayer shear of the layers that changes the stacking between adhering flat regions (see Fig. 3.1). However, microscopy imaging combined with electron diffraction pattern analysis suggests no apparent link between chiral angle and threshold diameter for collapse [99].
Having established the validity of the PBE+D2 approach for the description of the interlayer coupling, we now apply it in order to unravel the features of this *translational shearing*. We first analyzed the interlayer binding of infinite bilayer graphene with various stacking sequences (see Fig. 3.3(b)), obtained by sliding top layer with respect to bottom one along [10$\bar{1}$0] direction (see Fig. 3.3(a)). The AB (Bernal) stacking is the most stable configurations with lowest binding minimum. Additional translational shifts along [10$\bar{1}$0] lead to the formation of other stackings labeled as AB′, A′A, and AA stackings, whose relative binding energy increases by $\sim$ 1, 6, to 10 meV/atom, respectively.
The nature of translational intermediates (AB′ and AA′) is further investigated using the nudged elastic band (NEB) reaction-pathway sampling scheme [211]. Starting from the AB-stacking mode, we performed a set of lateral shifts of one graphene layer parallel to the basal plane of the other. At each transition state we calculated the total energy of the bilayer system. The resulting sliding energy landscape is presented in Fig. 3.3(c). As expected, the strongest coupling is obtained for AB stacking. Two saddle points were found, which correspond to intermediate AB′ and AA stackings. The first case possesses little higher energy compared to AB and there is experimental evidence of its existence provided by TEM imaging [212]. Instead, the AA-stacking is characterized by the highest barrier height of 10 meV/atom,

confirming that bilayer graphene behaves like turbostratically stacked (decoupled) material. The remaining intermediate case between AA and AB stacking (labeled AA′) cannot transform without barrier to AB. Hence, it is not even a local minimum and will be not observable in experiments.
Changing the stacking in the collapsed armchair nanotubes, we observed a similar trend in the collapse diameter threshold, which increases from 5.141 nm (AB and AB′ stacked, since the interlayer binding energy difference is only 1 meV/atom) to 5.337 nm (AA′ stacked), reaching 5.699 nm when the overlapping layers of central flat zone are arranged in AA stacking mode (see Fig. 3.3(d)). Last result clearly shows that the AB stacking mode is the suggested preference. However, the energy balance difference (defined in Eq. (1.1)) between AB ($\vartheta = 60°$) and AA ($\vartheta = 0°$) is just ~ 9 meV/atom, and this indicates that two faceted graphene plane in collapsed SWCNTs may even translate and/or rotate towards non-AB stacking[1]. Besides larger diameter tubes have random chirality distributions, and then in general when they collapse they will produce turbostratic stacking, and hence intermediate translations AA′ and AB′ represent a better general model of collapsed carbon nanotubes than two extreme stacking limits AA or AB.
While the thermodynamic stability of carbon nanotubes to collapse is weakly dependent by lattice registry, the corresponding electronic behavior can significantly change depending on stacking feature [212,213]. For example, the effect of layer registry is reflected at the energy dispersive electronic structure of infinite flat bilayer graphene (see Fig. 3.4). For AB stacking, the interlayer coupling shows a parabolic dispersion of the π bands with a small overlap at Fermi level $E_{\mathrm{F}} = 0$, in the vicinity of Dirac points ($k \sim 2/3$). In AA stacking mode, two pairs of bands cross at E_{F} having a linear relation dispersion. For an intermediate shift between AA and AB stacking (see Fig. 3.4(b)), the conduction and valence bands show the opening of two band gaps of around 0.17 eV. For another shift (see Fig. 3.4(d)), there is a crossing of two bands above Fermi level with an energy gap of 0.2 eV.
This analysis reveals the distinct signature of different stackings, which can imply some consequences on the governing physical properties of fully collapsed CNTs described in the next section, as already observed on folded graphene [214].

[1]In current DFT calculations thermal effects at finite temperature have been completely neglected, since it is widely accepted they play a marginal role ($< 5\%$) compared to the impact of stacking variation about the estimation of vdW interaction [99].

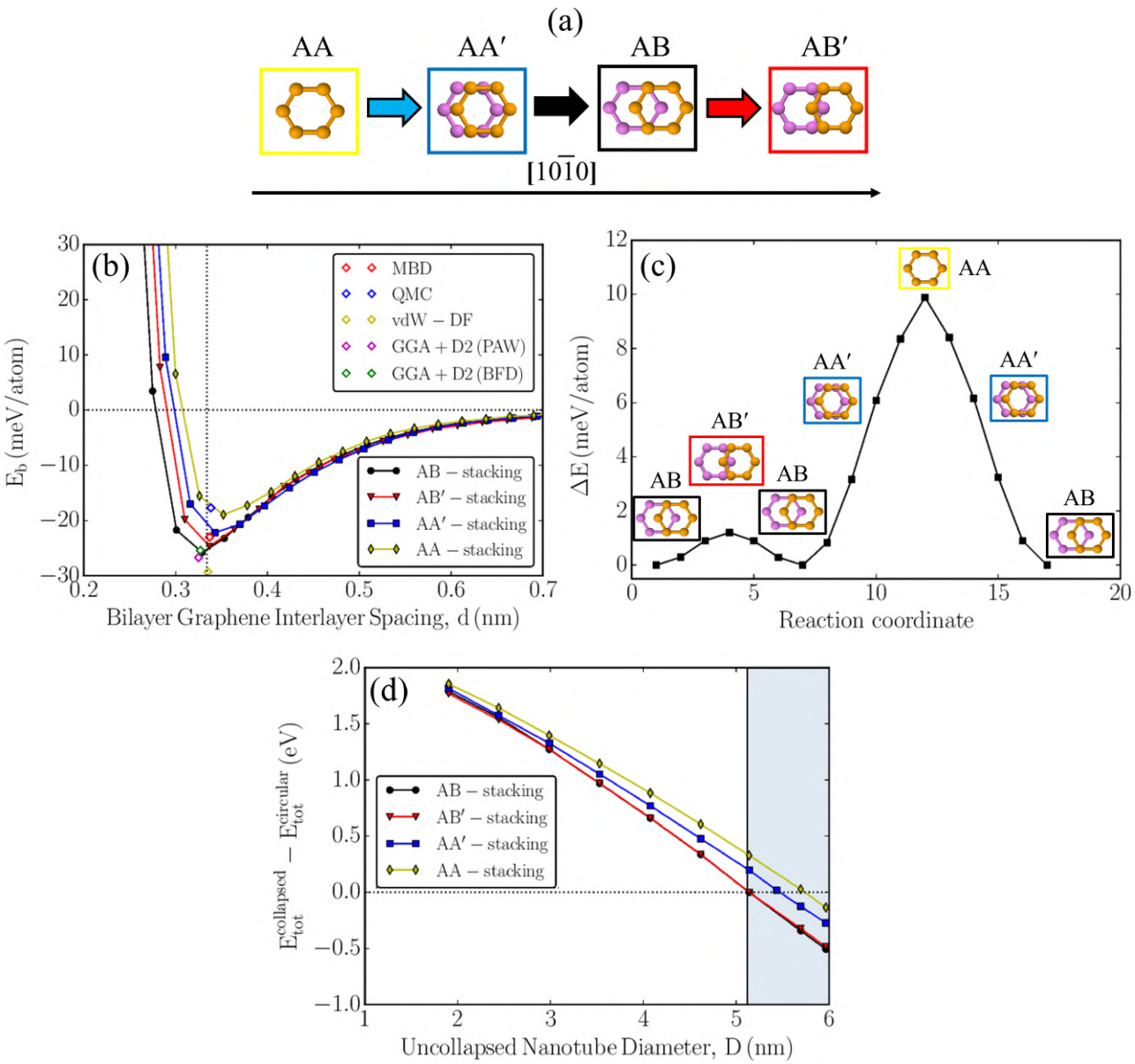

Figure 3.3: (a) Structural scheme of [10$\bar{1}$0] interlayer shear showing AA (yellow), AA′ (blue), AB (black), and AB′ (red). (b) DFT-D2 calculated binding energies for bilayer graphene. Vertical line represents average interlayer distance of bilayer graphene obtained in experimental studies [152, 206], while isolated points indicate different theoretical methods: MBD [153], QMC [153,207], vdW-DF [153], GGA+D2 (PAW) [154], and GGA+D2 (BFD) [208], respectively. (c) Energy reaction pathway of infinite bilayer graphene for the sliding of one layer with respect to another one along [10$\bar{1}$0]. (d) Total energy difference between free-standing collapsed ($E_{\rm tot}^{\rm collapsed}$) and circular ($E_{\rm tot}^{\rm circular}$) armchair ($n$,$n$) SWCNTs versus tube diameter D (nm). The intersection point at $\Delta E_{tot} = 0.0$ eV represents the threshold diameter for nanotubes to collapse. Magenta section indicates diameters for which collapse is observed experimentally [99]. Images (a), (b) and (d) taken from Paper I.

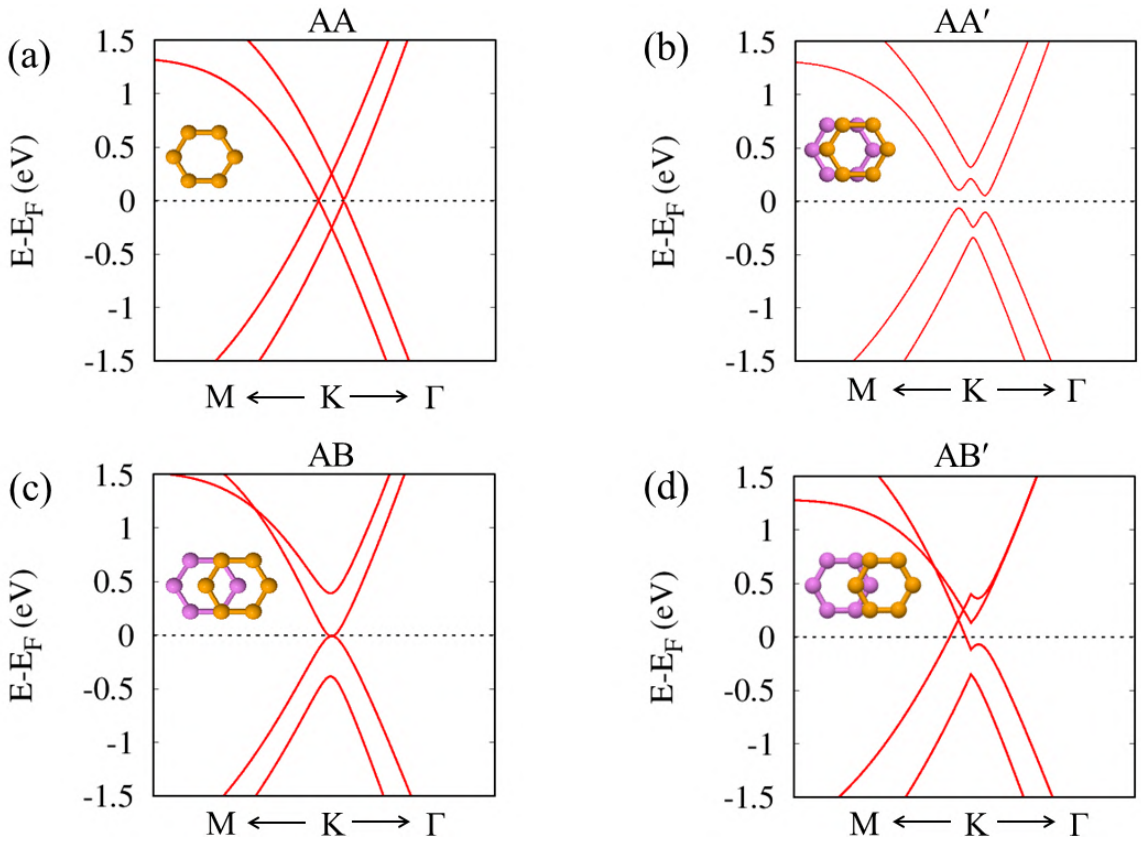

Figure 3.4: DFT-D2 computed electronic band structures of shifted (as indicated by insets) infinite bilayer graphene along the M → K → Γ direction. (a) and (c) indicates the extreme limits of AA and AB stackings, while (b) and (d) represent the intermediate translations labeled as AA′ and AB′. In (a) two pairs of energy bands cross the E_F characterized by a linear relation dispersion. In (c) the lowest conduction and highest valence bands touch the E_F, showing a quadratic relation dispersion. The interlayer coupling of (b) case induces the opening of an energy gap with two pairs of band extrema in each conduction and valence regime. In the second intermediate case (d), two bands cross above the E_F with the apparition of a small gap.

3.1.3 Electronic structures of collapsed SWCNTs

Previous electrical measurements of fully collapsed double- and multi-walled CNTs revealed an unusual physical property. The rehybridization due to the local curvature at the edge induces a metal-semiconductor phase transition in overall system, opening a small band gap without the need to introduce topological defects, molecular adsorption or stretching. Direct observations of this electronic change for metallic nanotubes in response to collapse deformation were obtained using several tools, including scanning tunnelling spectroscopy [215, 216], atomic force microscopy [217], and temperature-dependent conductance measurements [98]. A clear proof is represented by the variation of the conductance profile between the flat graphene-like zone at the center and other various locations of the tube. This result would drive carbon nanotubes physics towards new levels of sensitivity, which could make them suitable for example for nanoswitching applications [216, 217].

3.1.3.1 Stacking-dependent band gap of achiral SWCNTs

Fig. 3.5 shows the electronic band structures of a collapsed armchair (26,26) SWCNT, as an example, compared to those of bilayer zig-zag graphene nanoribbon (B-ZGNR) with hydrogen edge passivation. The intermediate is a bilayer ribbon where one of the two edges is closed with interlayer bonding (like collapsed tubes), while the other passivated by hydrogen (referred as 1-CE-BGNRs, to simplicity), which can also be seen as a folded ribbon. In these calculations, we adopted both AB- (in α-edge alignment[2]) and AA-stacked systems to see the effects of different interlayer coupling on the electronic structures.
Both B-ZGNR and 1-CE-B-ZGNRs show localized edge states (marked with orange lines) that are associated to the breakdown of sp^2-network induced by hydrogen passivated carbon atoms [218]. In addition, the behavior of bands at the charge neutrality point is highly sensitive to the interlayer arrangement between faceted graphene layers. For AB stacking, the two parabolic bands with minima/maxima at $k \sim 2/3$ never touch at the Fermi level (unlike bilayer graphene) giving rise to small band gap. In the AA-stacking, one pair of linear band approaches E_F at $k \sim 16/25$ (similar to bilayer graphene), while another one exhibits a quadratic relation dispersion leading to the formation of a wider energy gap towards $k \sim 17/25$, in contrast to bilayer graphene with the same stacking order.
In contrast, collapsed armchair SWCNTs show no edge-related states around Fermi level in comparison to edge passivated structures, band structures are still character-

[2]Two edge alignments can be defined for B-ZGNRs, named α and β. The α-edge alignment is obtained by translating one graphene basal plane by 0.142 nm along ribbon length, while the β arrangement is given by rotation of one layer around z-axis followed by interlayer shift of 0.142 nm. DFT energy stability calculations have proven that B-ZGNRs edges prefer to be arranged in α mode, resulting to a shorter interlayer spacing for the edge part compared to the central section due to the attractive interaction [218].

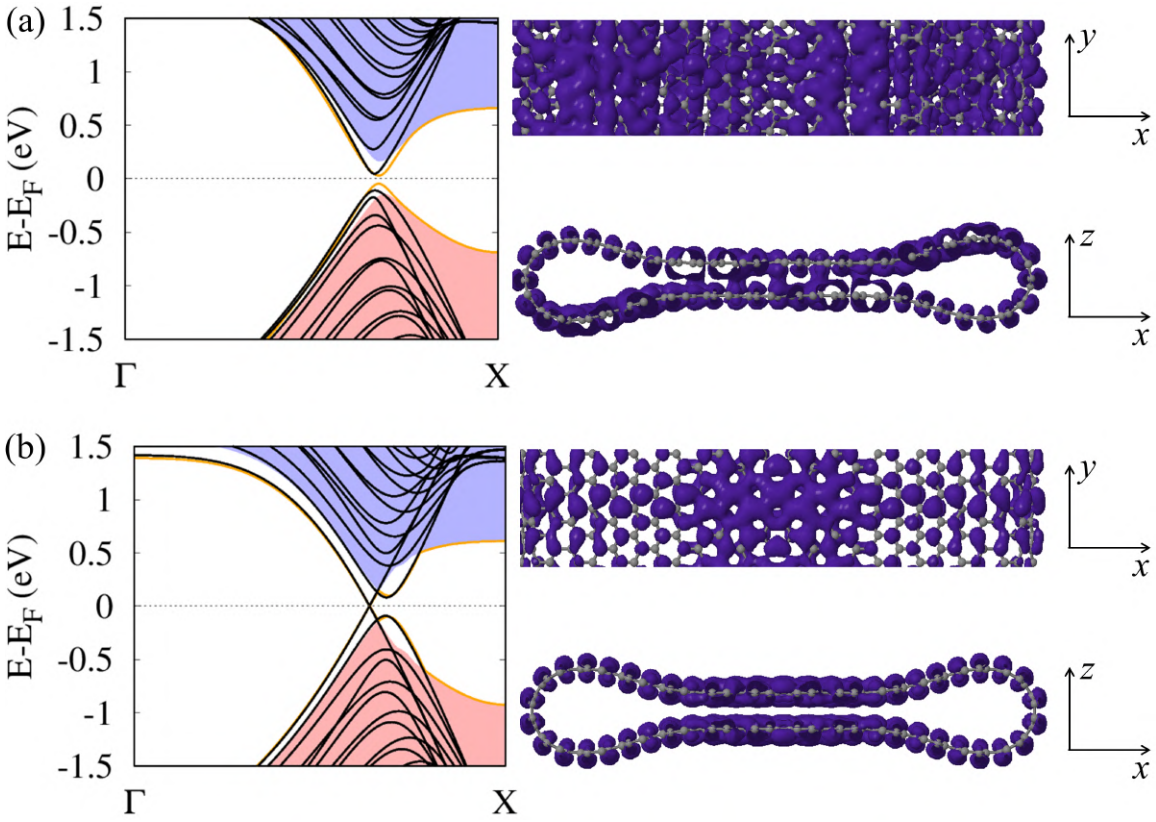

Figure 3.5: (Left) DFT-D2 spin averaged electronic band structures of collapsed armchair (26,26) SWCNT (black solid lines) in comparison with B-ZGNR and 1-CE-B-ZGNR (coloured filled space), whose highest valence and lowest conduction edge bands are represented by orange solid lines. Horizontal dotted line indicates the Fermi level E_F. (Right) Square of the wave-function distribution for the occupied state in proximity to the charge neutrality point both in lateral and top view. (a) AB and (b) AA stacking modes are assumed here. Image taken from Paper I.

ized by the opening of a stacking-dependent band gap. In the AB-stacked collapsed tubes the parabolic bands lead to the formation of a higher energy gap ($\sim$ 180 meV) than B-ZGNR ($\sim$ 89 meV) and 1-CE-B-ZGNR ($\sim$ 95 meV) with comparable widths. The collapsed nanotubes in AA-stacking are semimetallic with a tiny gap of $\sim$ 15 meV at $k \sim 16/25$, but a wide gap ($\sim$ 300 meV) opens for the higher k ($\sim 17/25$) exactly like B-ZGNR and 1-CE-B-ZGNR. Thus, the opening of a band gap is uniquely due to the local perturbations of flat geometric graphene structure, which breaks the original hexagonal symmetry with consequent rehybridization, as evidenced by corresponding wave function distributions. This important result demonstrates how metal-semiconductor transition can be achieved by tube collapse, without introducing defects or different passivated edges, which act like scattering centers near the Fermi level.

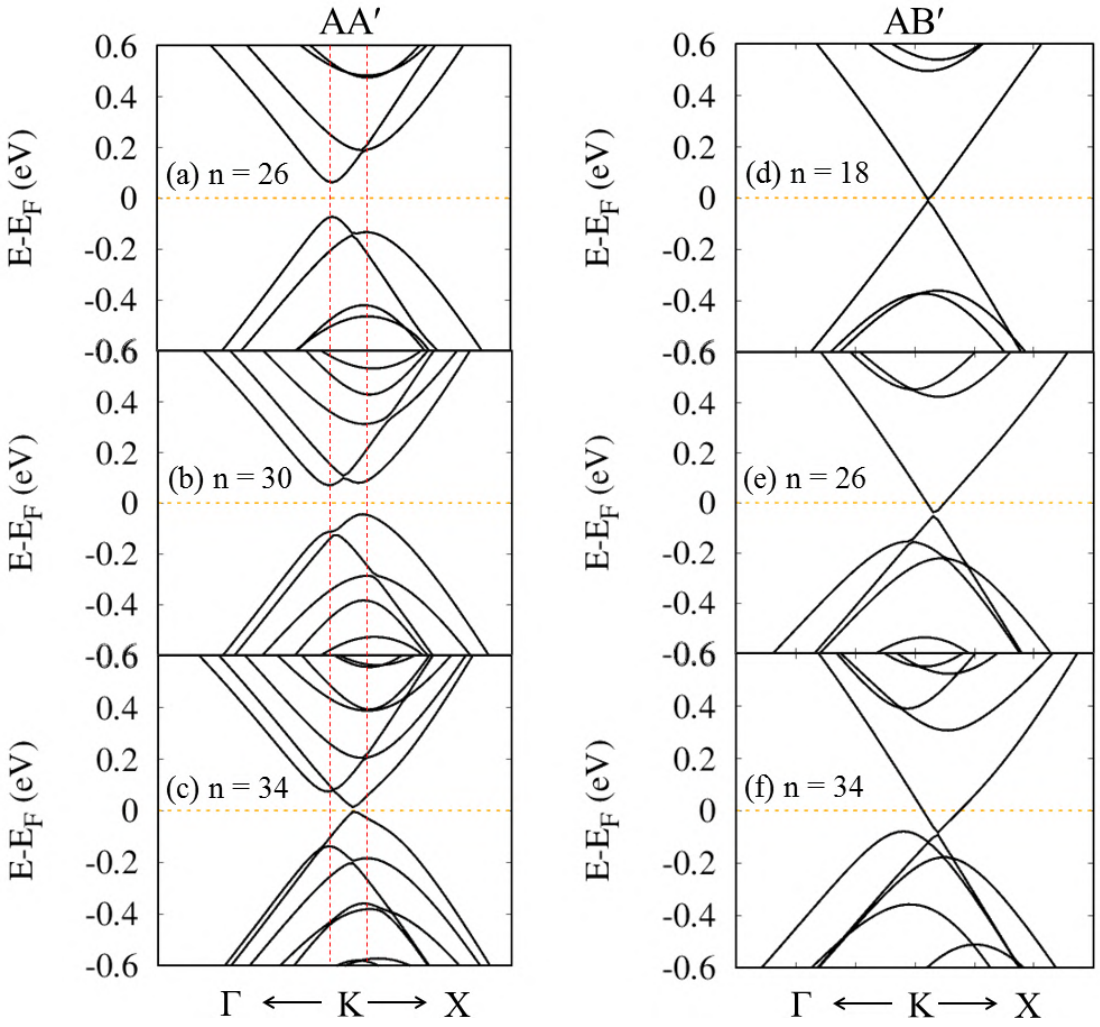

Figure 3.6: DFT-D2 spin averaged electronic band structures of armchair (n,n) collapsed carbon nanotubes in intermediate AA′ stacking (left column, with n = 26, 30, 34) and AB′ stacking (right column, with n = 18, 26, 34). Horizontal orange dotted line is the Fermi level E_F, while vertical red dashed line indicates positions of highest valence and lowest conduction bands to define energy gaps for AA′-stacked collapsed tubes. Image taken from Paper I.

The electronic structure of collapsed armchair nanotubes with intermediate stackings are shown in Fig. 3.6. For the intermediate case between AA and AB (denoted as AA′), there are two pairs of parabolic bands (like AB case), each with an associated band gap (as we seen for infinite bilayer graphene at the same stacking order). Interestingly, these band gaps vary differently with nanotube width: while the band gap at lower k increases by increasing the tube size, that at higher k show the opposite variation with values approaching those obtained for AA-stacking case.

In the second intermediate case AB′, the system is semimetallic showing two size-dependent effect: *(i)* the lowest conduction band drops below E_{F} when exceeds a given width of around 5.06 nm and continues to drop for wider sizes; *(ii)* the electron-hole asymmetry of all states below and above valence maximum and conduction minimum, respectively, which is generally detected in quantum Hall regime transport measurements [219].
In summary, the conduction and valence states around the Fermi level and hence the energy gap of collapsed armchair CNTs depend on the interlayer translation and associated stacking between the top and bottom layer.
We next extend this analysis to zig-zag collapsed carbon nanotubes. Like their circular counterpart [220], zig-zag SWCNTs with collapsed cross-sectional shape can be also classified in three distinct families as a function of the diameter (see Fig. 3.7), with one relevant difference. While ($3n$,0) circular nanotubes show metallic conductivity (similar to graphite), the equivalent collapsed configuration exhibits a small diameter-dependent energy gap. This is analogous with the corresponding armchair case, demonstrating that metallic circular nanotubes change to semiconductors upon collapse regardless of chirality. The ($3n$+1,0) and ($3n$+2,0) nanotubes remain semiconducting, with gaps comparable to those of cylindrical tubes. The energy gap variation of both circular and collapsed CNTs can be summarized with following scaling rules:

$$E_{\mathrm{g}}^{n+2} > E_{\mathrm{g}}^{n+1} > E_{\mathrm{g}}^{n} \begin{cases} = 0 & \text{(circular)} \\ \neq 0 & \text{(collapsed)} \end{cases} \quad \text{for all } n$$

We compared the electronic structures of collapsed zig-zag nanotubes with mono- and bi-layer armchair graphene nanoribbons, which have also three distinct sets of energy gaps scaling as a function on the ribbon width as follows [221, 222]:

$$E_{\mathrm{g}}^{p+1} > E_{\mathrm{g}}^{p} > E_{\mathrm{g}}^{p+2} \neq 0,$$

where $3p + x$ represents the number of carbon dimer lines along the ribbon. If the ribbon is considered as an unzipped nanotube[3], then $p = n/2$. It was found that the energy bands of collapsed zig-zag around E_{F} are largely linear like their circular counterpart but exhibiting smooth curvature somewhere, similar to armchair ribbons[4].

[3]The classifications of both zig-zag tubes and armchair ribbons can be expressed in terms of their aromaticity, which is introduced in Clar's theory. The proposed scheme is based on the formal arrangement of localized π electrons in aromatic sextets [11, 223].

[4]For people interested in a more exhaustive comparative analysis, it is useful to refer to Paper I: A. Impellizzeri, P. Briddon, and C. P. Ewels. "Stacking- and chirality-dependent collapse of single-walled carbon nanotubes: A large-scale density-functional study". *Phys. Rev. B* **100** (2019), pp. 115410-17.

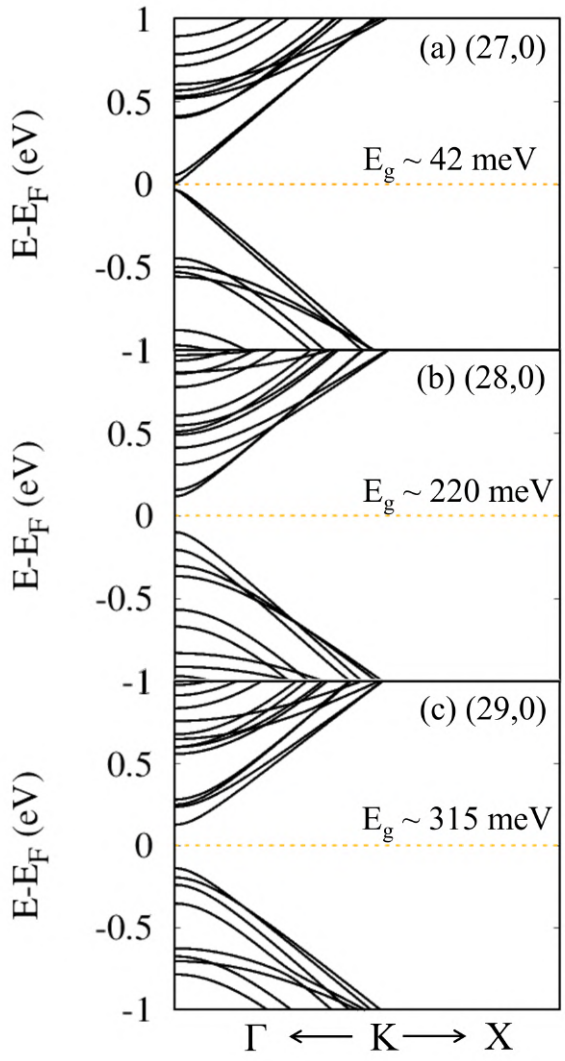

Figure 3.7: DFT-D2 spin averaged electronic band structures of zig-zag $(n,0)$ collapsed SWCNTs in intermediate AB′ stacking with $n = 27, 28, 29$. Fermi level E_F is indicated by horizontal orange dotted line. Image taken from Paper I.

3.1.3.2 Energy bands of chiral collapsed nanotubes

Despite the remarkable progress in the fabrication methods of large-diameter collapsed SWCNTs, the control of chirality distribution for the resulting samples still remains challenging. Generally, the stacking sequence will be turbostratic, as evidenced by He and co-workers. They were in fact the first ones to show TEM images of collapsed nanotubes, where carbon hexagons of faceted layers are rotated with 'well-determined' chiral angle $\vartheta = 6.5°$, $20.4°$, $49.0°$, for example [99].
Thus, a theoretical investigation of collapsed chiral carbon nanotubes in order to better figure out the role of lattice incommensurability is required. For this purpose, we have devised the following strategy: First, using self-consistent density functional based on tight binding (DFTB) with periodic boundary conditions, we collapse a chiral circular SWCNT and started to reduce step-by-step the unit cell height, so that the periodically repeated tube walls pushed each other. Second, the resulting collapsed structure is then re-optimized using DFT-D2 approach (see Fig. 3.8(a)). We chose a (60,15) nanotube with diameter equal to 5.38 nm, above the threshold for stability ($\sim$ 5.1 nm) [99].
We then computed the electronic band structure and associated density of states of this wide collapsed chiral nanotube (see Fig. 3.8(b)). Notice that the highest valence and lowest conduction flat band minima around $k \sim 2/3$ are separated by a tiny energy gap of around 17.3 meV, similar to AA-stacked collapsed armchair nanotubes. However, our predicted band gap could in reality be closer to 35-40 meV, since semilocal exchange-correlation functional GGA-PBE coupled to vdW corrections used in our current study tends to systematically underestimates the semiconducting band gaps by $\sim$50% [145]. All bands immediately below and above are described by parabolic dispersion relation.
This analysis suggests that low-energy bands of collapsed SWCNTs may be highly sensitive to very small variations of the rotational angle between adhering layers of middle flat zone, resembling twisted bilayer graphene (TBG) [224]. By adjusting the twist angle below 10°, the electronic structure of the overall system is determined by the combination of sub-regions with different symmetric stackings (sometimes, also known as moiré patterns, see Fig. 3.8(a)) and weak interlayer coupling [224]. In such a way, chiral collapsed SWCNTs can be proposed as quasi-1D moiré superlattices.
A very intriguing purpose would be to explore the electronic properties of collapsed tubes for rotation angles under 1°, since theoretical studies made on bilayer graphene have proven that Fermi velocity drops to zero, and van Hove singularities are so close to each other. It results in the formation of a unique flat band at the charge neutrality point [224], giving rise to new physics. Our results represent the starting point to spur theoretical and experimental research on chiral collapsed SWCNTs for the implementation of a novel generation of Mott insulators [225, 226] and superconductivity [225, 227] in low dimensions. Therefore, these systems would represent promising platforms for next developments in magic angle physics.

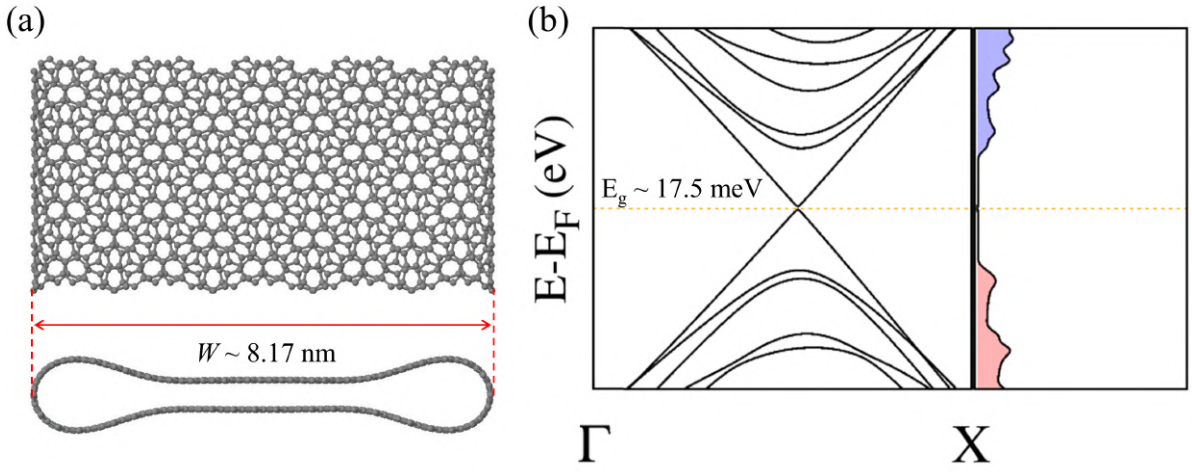

Figure 3.8: (a) 1 × 4 × 1 super cell of a collapsed chiral (60,15) SWCNT in top (upper) and lateral (lower) view. The width of the system is indicated by red double arrow. This nanotube has 420 atoms in the unit cell and a chiral angle $\vartheta = 3.79°$. The repeating "Moiré" sublattice can be seen. (b) Spin averaged Band structure of the (60,15) collapsed nanotube calculated along Γ-X path and associated density of states, showing an electronic band gap equal to 17.5 meV. The Fermi energy is set at 0 eV.

3.1.3.3 Origin of the band gap?

As previously shown, the main electronic structure feature of nanotubes with collapsed cross-sectional shape is the opening of a small band gap in both achiral (armchair, zig-zag) and chiral families. Several proposals have been made to explain its origin, without ever providing a comprehensive explanation. For example, Chang et al. claimed the appearance of a band gap in metallic tubes is solely due to the mirror symmetry breaking (MSB) provoked by the radial deformation [228], as found for monolayer graphene epitaxially grown on SiC substrates [229]. However, this argument proved to be insufficient, because DFTB calculations made on a squashed armchair carbon nanotube with a distance between top and bottom sides of ∼0.29 nm, showed that the band gap is zero [230]. Thus, the *physical* distinction of the two nanotube sublattices in order to induce the metal-semiconductor transition must be driven by MSB combined with an additional process. Tight-binding molecular dynamics (TB-MD) coupled with nonequilibrium Green's function calculations suggested it is induced by a combination of the symmetry breaking at the edges and sufficiently strong interactions between adhering layers [231]. Further tight-binding analysis have shown the opening of a band gap, which is due to the appreciable interaction between the atoms on the opposing sides separated by a distance of ∼0.38 nm [230].
However, all these investigations have been carried out on armchair nanotubes with

diameters in the range of ∼0.8-1.6 nm, which are definitely far from experimental threshold diameter to collapse (∼5.1 nm). That means the previous arguments are not very convincing for stable collapsed SWCNTs with large-area stacked faces connected by the edge cavities.
Now, we are going to provide our explanation on what is causing the opening of the band gap. For collapsed armchair tubes, the shift of the Fermi level is due to charge distribution difference between cavities and flattened bilayer, where σ-π hybridization is enhanced [228]. Fig. 3.9(a) shows the energy gap variation for AB-stacked armchair collapsed nanotubes as a function of their collapsed width, where the dependence by a third new threshold diameter D_{flat} ∼3.5 nm (or width equal to 5.09 nm) is noticeable, such that:

1. $D \leq D_{\text{flat}}$: the energy gap is *inversely* proportional to the width W. The CBM lightly oscillates by 35-40 meV, while the VBM drops forming a gap. This behavior is attributed to the very narrow and poorly defined central region, whose attractive vdW interactions are really small with respect to the repulsive strain of the edge cavities, inducing a geometric distortion on the overall structure. The same direct relationship is found for hydrogen terminated B-ZGNRs for widths < 3.5 nm due to the geometrical deformation caused by the interlayer edge interactions [218].

2. $D = D_{\text{flat}}$: the central region of (26,26) collapsed nanotube is well defined, with the highest bang gap of ∼180 meV. This tube is intrinsically polarized, with partial atomic charges (determined via Mulliken analysisl [232]) higher in the flat middle region than the strained edge cavities (see Fig. 3.9(c)).

3. $D > D_{\text{flat}}$: collapsed nanotubes exhibit energy gaps *directly* proportional to the width, similar to graphene ribbons. This trend comes from quantum confinement and the weak interlayer coupling. The electronic properties of wide semiconducting flattened nanotubes tend towards those of infinite bilayer graphene at the same stacking order. First, both CBM and VBM gradually approach each other but without touching at the Dirac point; the energy gap will never disappear due to the presence of strained edge cavities. Second, while Mulliken charge distribution of cavities remains largely width independent, those of adhering layers approach asymptotically the values of infinite bilayer graphene ($|\delta| = 0.139e^-$) as width goes to infinity (see Fig. 3.9(b)).

This study demonstrates the direct correlation between charge variation and band gap opening, whose origin can be fully explained: the interwall interactions in the strained edge cavities are weaker (with interlayer distance of around 0.778-0.815 nm) than of the bilayer-like region (0.327-0.352 nm). Besides different hybridization of π states between upper and lower layers of folded graphene, they partially confine electrons in the central zone, resulting in a spatial charge separation between the cavities and centre, without impurity doping. This last point might suggest col-

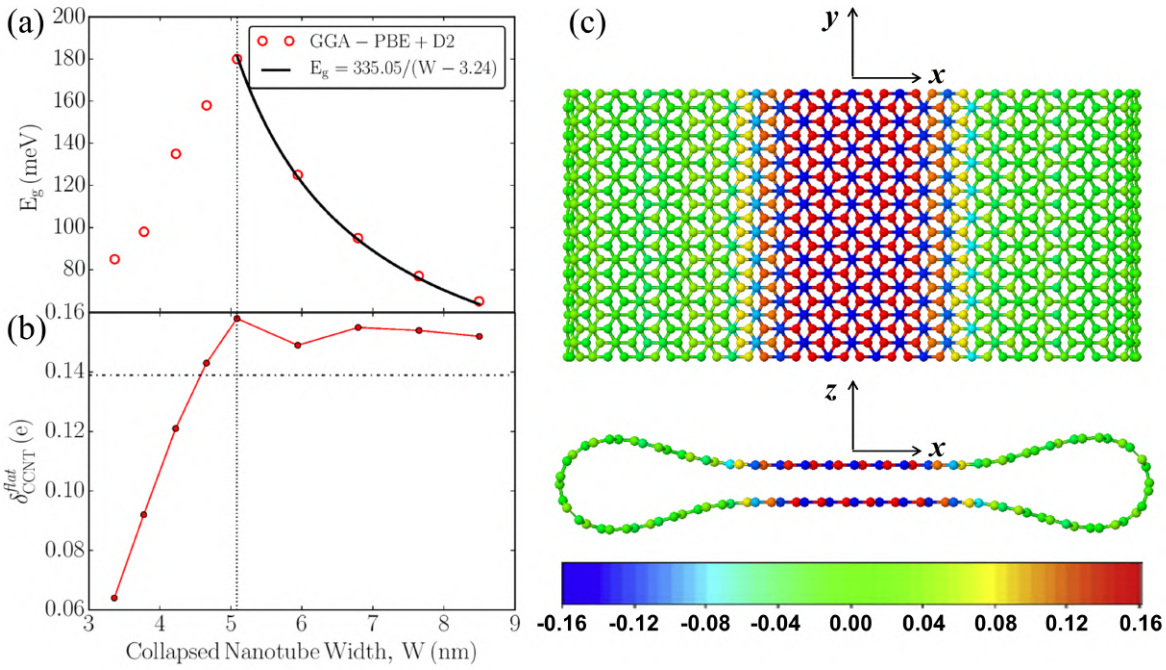

Figure 3.9: DFT-D2 calculated (a) energy gaps (red empty circles) and (b) the maximum Mulliken positive charges located in the central region for AB-stacked flattened armchair (n,n) SWCNTs versus the collapsed nanotube width W. The solid black curve shows the equation: $E_g = 335.05/(W - 3.24)$, fitted to the band gaps of the dogbone nanotubes. The nanotube diameter threshold D_{flat} ~3.51 nm (W_{flat} = 5.09 nm) is indicated by vertical dashed line. (c) Color representation of Mulliken partial charge distribution for a (26,26) AB-stacked collapsed tube with diameter corresponding to $D = D_{flat}$. Image taken from Paper I.

lapsed SWCNTs as a novel type of 'type-II homojunction' with more remarkable and desirable properties as compared to, for example, strained Si nanowires [233], such as high carrier mobility and transparency.

In summary, *quantum confinement* and *local charge* effects due to the collapse deformation induce an interlayer electrostatic polarization such as to break the mirror symmetry, so that the interwall potential generates the band gap opening. This result is qualitatively in agreement with prior analytical calculations of the interwall interactions within the effective-mass scheme [234]. The mechanism of the band gap formation in collapsed nanotubes due to the *internal* polarization is different compared to bilayer graphene devices, where a potential difference can be introduced between layers via an *external* transverse electric field [235, 236].

In general, the gap of parabolic bands around the Fermi level is inversely proportional to the width of the central flat region, which corresponds to the total collapsed tube width minus the cavity widths. The precise scaling rules of armchair and zigzag collapsed tubes depend on stacking style and sub-family, respectively, as shown

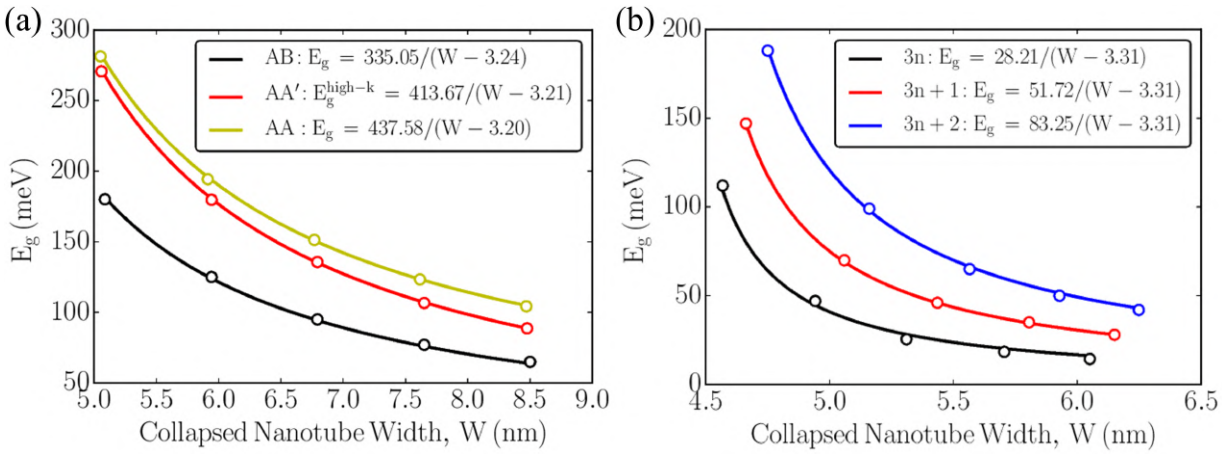

Figure 3.10: DFT-D2 calculated energy gaps of semiconducting (a) armchair and (b) zig-zag collapsed carbon nanotubes (empty circles) versus total width, taking different stackings and sub-families into account. The solid curves show the best-fit equations. Image taken from Paper I.

in Fig. 3.10. The different energy gap variation follows qualitatively that seen in armchair and zig-zag circular nanotubes. It can be ascribed to the different chiralities, associated with 1D-confinement induced band folding of the bilayer graphene band structure. The $1/W$ behavior of E_g is in agreement with prior calculations on hydrogen-edge saturated zig-zag [218] and armchair [222] bilayer GNRs, even using methods beyond DFT such as Green's functions and screened Coulomb interactions [22].
In addition, previous experimental temperature measurements of conductance for ∼20 nm width chiral collapsed tubes have estimated a transport gap of 13.7 meV [98], which lies in the range between our values for armchair (21.2 meV) and zig-zag (3.27 meV) nanotubes, as calculated from our best fit curves[5]. Thus, we demonstrated that all nanotube families become semiconductors upon collapsing, mainly due to the confinement and spatial charge variation between strained edge cavities and flattened central region, which is qualitatively confirmed by electrical transport measurements of collapsed nanotues reported in literature, where they were erroneously identified as graphene nanoribbons [97, 103].

[5]Note that the electronic structures reported here neglect *external* charge transfer process due to substrate interactions, which can show Fermi-level shift depending on the work function difference between the tube and substrate. They also do not incorporate the effect of twisting [73] or kinks [73, 81] that can affect the conductivity, as observed in previous Raman measurements.

3.2 Formation of prismatic edges dislocations

In the last section, we discussed the formation of local edge curvature in closed-edged BGNRs obtained by collapsing SWCNTs. This type of mechanical deformation resembles somewhat one type of line defect commonly observed in turbostratic graphite named *prismatic edge dislocation*. It is the terminating line when one layer of graphene in a bulk graphite terminates abruptly [237, 238]. So it represents an additional partial layer, which can be constructed. Doing this, we obtain a patch of graphene between two layers of graphite and the edge around it is called a *prismatic dislocation loop*.

This type of line defect occurs in highly irradiated and heat treated[6] samples such as graphite and even multi-walled carbon nanotubes (see Fig. 3.11(a)-(d)), observed using STM [237, 239] and TEM [240–242]. Conceptually, core structures involve linear "cutting" of a graphene sheet with consequent formation of dangling bonds. This energetic defect can be stabilised, either through local rehybridisation and edge restructuring (a sort of 'free-standing' edge structure), or through directly bonding into the graphene layer above/below (an 'inter-plane bonded' structure). This second option can disrupt the local resonant π-bonded structure of the sheet above/below, which brings an associated energy cost. Thus, the relative stability of these two structures is not *a priori* obvious and will strongly depend on the local dislocation core structure. For this reason, prismatic edge dislocations are also known as non-basal dislocations with Burgers vectors oriented along the normal direction of layered material[7] [237].

Prior TEM imaging analysis revealed these two distinct types of prismatic edge dislocations: (1) a "sandwich-type", where an extra graphene layer resides between two neighboring graphene layers (see Fig. 3.11(a),(b),(e),(f)) and (2) a "Y-type" where edges of the extra graphene plane bind with a neighboring graphene plane (see Fig. 3.11(c),(d),(g),(h)). They can also be intuitively seen as *unbonded* and *bonded*, respectively. The prismatic core obtained in the second configuration effectively reminds in some aspects to edge cavities formed in collapsed carbon nanotubes.

Despite the large amount of experimental evidence and their implications in conductivity and expansion of carbon based materials, there are very few literature of the physical and electronic structure of prismatic dislocations [238, 242].

In this section, we will explore the energy stability and electronic properties of both bonded and unbonded bond prismatic dislocations, always using DFT-GGA+D2 level with the software AIMPRO.

This study is in collaboration with our colleagues at Loughborough University.

[6]This type of dislocation was observed at high temperatures $T > 0.5\,T_{\mathrm{m}}$, where T_{m} represents the melting temperature.

[7]The twin class of non-basal prismatic dislocation is simply called *basal*, where the material is accomodated within a graphene sheet and corresponding Burgers vectors lie in the out-of-plane of layered structure [237, 238].

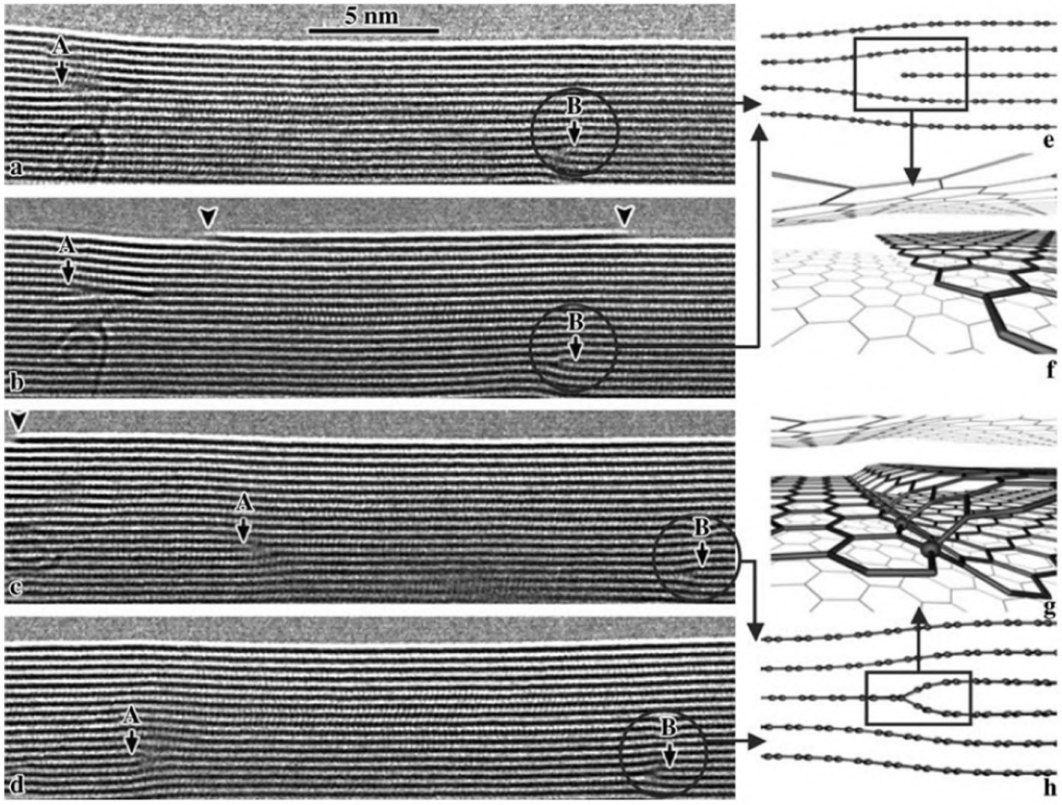

Figure 3.11: Sequence of HRTEM showing the growth process of a nanotube wall on the outer surface (a)-(d). Arrows indicate atomic steps of two detected prismatic edge dislocations: (e),(f) sandwich- and (g),(h) Y-type. Figure taken from [242].

3.2.1 Our DFT approach

Compared to collapsed nanotubes, whose structure is obtained by simply bonding edges between two graphene nanoribbons, the modelling of prismatic edge dislocations may not be so intuitive. Computational details are presented below.

Unit cell. Fig. 3.12(a),(b) schematically depicts the unbonded and bonded configurations modelled by the orthorhombic lattice definition for the unit cell. Dislocations loops, which consist of pairs of dislocations with opposite Burgers vectors, have been constructed in vacuum, and particular attention has been taken to account for finite-size effects. At small widths of formed closed structures (or more precisely, core separations), $W < 2$ nm, it is found that the correct bilayer separation d_{00} is not recovered for most core configurations, therefore all cells employed in this study use a larger inter-core separation of $W \geq 4$ nm to guarantee accurate graphitic interlayer separation. This is consistent with our threshold determined for stable collapsed SWCNTs. In addition, sufficient vacuum space between neighboring species ($\sim$25.0

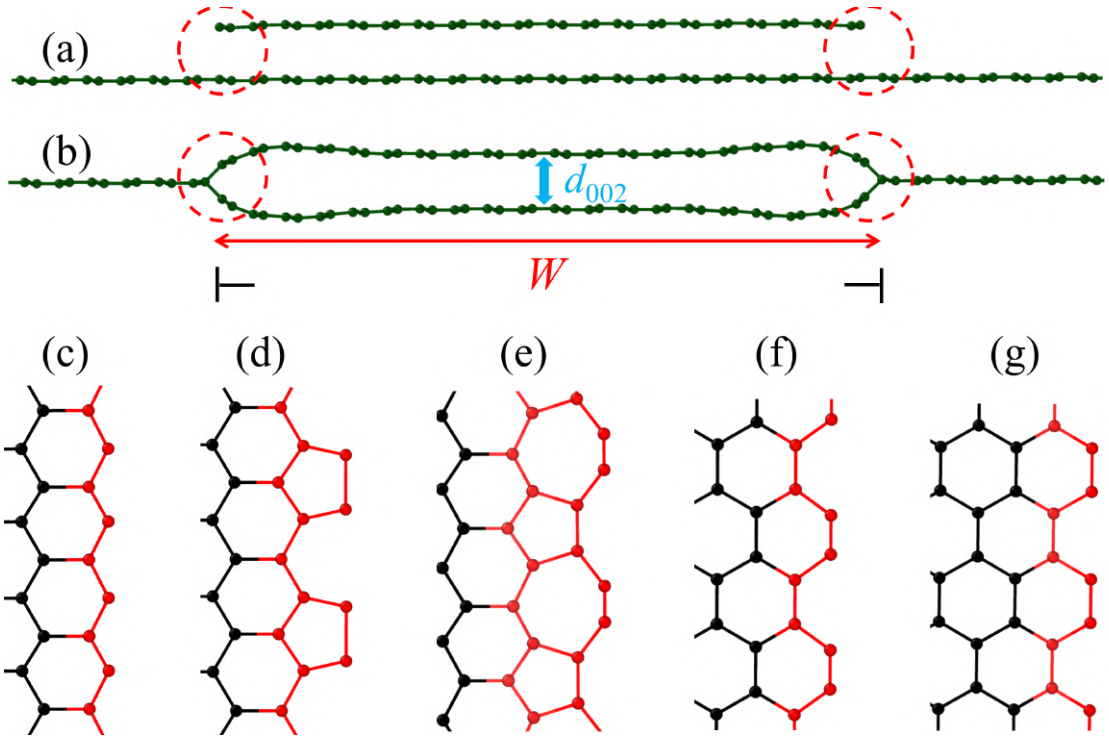

Figure 3.12: (Top) Schematic representation of the isolated prismatic dislocation dipole cores with (a) unbonded and (b) bonded configurations. Labels indicate main geometry parameters used throughout this study: W = width of closed structure or even separation distance between prismatic cores, d_{002} = interlayer spacing between pre-existing graphene plane and new inserted finite-size carbon layer. Dislocations core are marked with red dashed circles together with canonic symbol. (Bottom) Scheme showing the different terminations of graphene edges with a row of single dangling bonds. (c) zig-zag edge, (d) reconstructed Klein edge, (e) 5-7 reconstructed Stone-Wales zig-zag, (f) armchair edge, (g) shifted armchair edge. Red is to highlight the edge to aid the reader.

Å) is set in the direction perpendicular to the graphene sheets to prevent interaction.

Edge geometry. Various core structures can be constructed using the graphene edges. The different edge structures are a function of the crystallographic orientation along the edge, which can be labelled according to whether they fall along the zig-zag $[2\bar{1}\,\bar{1}0]$ and the armchair $[10\bar{1}0]$ direction. Fig. 3.12(c)-(f) shows the different edge terminations: (*i*) the reconstructed Klein type, where the dislocation line lies in the shuffle rather than the glide plane. The dangling bonds along the edge may bond pairwise creating a 2×1 edge reconstruction to reduce energy, which leads to the formation of pentagon structure. (*ii*) Stone-Wales type obtained by bond rotation with consequent formation of alternating sequence of pentagons and heptagons

along the direction parallel at the edges. It is again favoured because rehybridization to spat the heptagon. This latter edge configuration forms dynamically in TEM as follows: the stable hydrogenated edge is the zig-zag, then the e-beam blows off all hydrogens, and we can see it reconstruct in real-time to 5-7 combination, which is lower in energy than the zig-zag when not hydrogenated. The various cores created in the current investigation have then been labelled according to the edge structures in the monolayer (ml) and in the top and bottom of the bilayer (bl) in the core region. Carbon edge's versatile bonding resulted in a wide variety of prismatic core dislocations which surely need a systematic nomenclature:

- the zz-zz-zz structure is obtained when both monolayer and top-bottom sheets of the bilayer core region have zig-zag edges;
- the rk-rk-rk feature represents the other symmetric configuration with all reconstructed Klein-type edges;
- the rk-zz-rk configuration is constructed as an asymmetric combination, with monolayer and bottom sheet of the core characterized by reconstructed Klein edges, while the top in the core region has zig-zag ones;
- the zz-rk-rk structure has zig-zag edges in the monolayer, while top and bottom of bilayer core have reconstructed Klein edges;
- the zz-zz-rk combination is composed by monolayer and top sheet of bilayer-like region with zig-zag edges, while the bottom sheet of the core with reconstructed Klein edges.

These five combinations are depicted in Fig. 3.13. While the first case is entirely formed from undefected hexagonal graphene planes, the other five cores feature lines of pentagon-octagon defects. In addition, prismatic dislocation loops can also be investigated as function of the stacking style between the cores. Two situations are then possible: (*i*) the stacking at the core is locally AA in the transition region and the resulting stacking fault induces a basal dislocation away from the core obtaining the energetically-preferred rhombohedral stacking in the bulk graphite, (*ii*) or the basal component is included directly in the prismatic core through chemical bonding.

Formation energy. Before turning to electronic properties, we investigated the formation energy for the isolated monolayer-bilayer dislocation core, defined as follows:

$$E_{\mathrm{f}} = E_{\mathrm{core}} - N_{\mathrm{ml}}\epsilon_{\mathrm{ml}} - N_{\mathrm{bl}}\epsilon_{\mathrm{bl}}, \tag{3.1}$$

where E_{core} is the total energy of the entire system, N_{ml} and N_{bl} are the numbers of carbon atoms in the monolayer and bilayer-like regions, respectively, while ϵ_{ml} and ϵ_{bl} indicate the calculated energy per carbon atom of the isolated infinite monolayer and bilayer sheets. The total energy per dislocation dipole has then been extracted

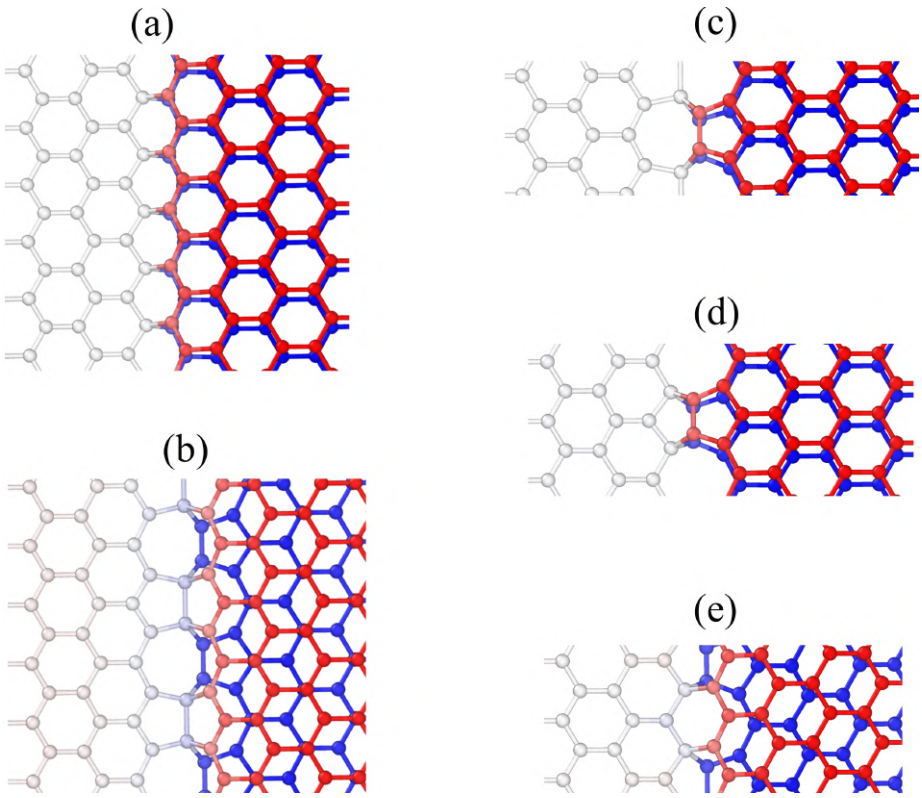

Figure 3.13: DFT-D2 optimized geometries of prismatic zig-zag core dislocations by changing the edge structure among different sub-parts composing the overall system: (a) zz-zz-zz, (b) rk-zz-rk, (c) rk-rk-rk, (d) zz-rk-rk, and (e) zz-zz-rk. Coloured atoms indicate upper (red) and lower (blue) graphene sheets of the bilayer core region. Image Credit: J. G. MacHugh.

from the calculated formation energy. This energy term is of paramount importance in the theory of dislocations, because it constrains their motion in the bulk.

3.2.2 Energy stability of prismatic zig-zag cores

Table 3.2 details the resulting formation energies of the constructed prismatic configurations for the zig-zag cores as well as the resulting stacking order in the bilayer region. The smaller formation energy means that the resulting structure is more stable.

By assuming graphene planes of the core region arranged in AA-stacking, the most stable structure is the symmetric configuration at which all edges are zig-zag (see Fig. 3.13(a)). The next prismatic core structure is the asymmetric combination where the Klein edge bonds into zig-zag one in the core region (see Fig. 3.13(c)). The other AA-stacked configuration, which involve multiple Klein edges meeting in the core (see Fig. 3.13(d)), are much higher in energy and hence energetically less

Table 3.2: DFT-D2 calculated total formation energies (whose superscripts "d" and "c" mean: energy per dislocation and per core, respectively) of the zig-zag prismatic dislocation cores and optimized interlayer spacing of the central region between the two dislocations.

Fig. 3.13	ML	Top	Bottom	Stacking	E_f^d [eV/Å]	E_f^c [eV/Å]	d_{002} [Å]
(a)	zz	zz	zz	AA	1.775	8.875	3.519
(b)	rk	zz	rk	AB	2.387	11.936	3.251
(c)	rk	rk	rk	AA	3.075	15.375	3.973
(d)	zz	rk	rk	AA	3.444	17.219	3.499
(e)	zz	zz	rk	AB′	2.621	13.104	3.252

stable compared to the symmetric configuration without defects.
The only configuration with bilayer like-region arranged in AB stacking is the rk-zz-rk, at which a reconstructed Klein edge in the monolayer shares a zig-zag and another Klein edge (see Fig. 3.13(b)). The resulting core is moderately again higher in energy than the clean configuration with all zig-zag like edges. This energy cost is evidently due to the deviation from perfect graphitic hexagons, since it includes a pentagon at each of the Klein edges, as well as a heptagon where the bottom zig-zag edge meets the defect, leading to 5-7 combination in the core region. The resulting bridging region is strained, since it consists of sp^3-hybridized C-C bonds with bond length of approximately 1.53 Å linking core to the graphene sheet.
This will also have implications for mobility, since it is the only ont that does not involve reconstruction. This matches the structures modelled by Suarez-Martinez and co-workers [238].
It is widely accepted the bulk graphite is predominantly AB stacked, however, regions with AA or even intermediate stackings may easily form due to the relatively low stacking fault penalty of graphite [214]. Given that the formation energy of the basal dislocation in graphite is in the order of 0.1-0.2 eV/Å [238, 243], we may conclude that while a variety of cores are energetically possible, the AA stacked cores are most likely to form and then generate basal dislocations away from the core through basal shear, rather than through the direct incorporation of a basal component at the core as in the case for the zig-zag cores with AB stacking.

3.2.3 Electronic states in zig-zag cores

We next examined the impact of prismatic zig-zag cores on the electronic properties of graphene. Fig. 3.14(a) shows the electronic band structure for the most stable

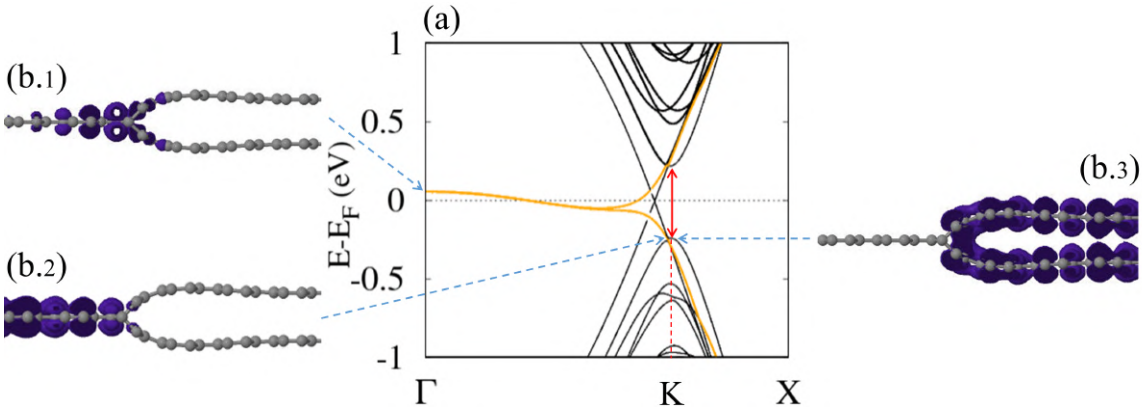

Figure 3.14: (a) DFT-D2 spin averaged band structure of prismatic core dislocation with all zig-zag edges. Edge states are marked with orange solid line, while the opened small band is indicated by red double arrow. The position of Fermi level is set to 0. Isosurface showing the square of the wavefunction distribution (10% maximum value) of edge state at the (b.1) Γ, (b.2) K (∼17/25) points and highest occupied state always at (b.3) K point. Given the symmetric configuration, only half of the supercell is shown here for clarity.

zz-zz-zz symmetric configuration. This shows two interesting features: First, the apparition of two-fold degenerate bands around Fermi level, localized edge states associated with the prismatic cores in each side. Plotting the square of the wavefunction at the Γ point, it is confirmed that these low-energy bands come from edge states located in the monolayer-bilayer bridging region (Fig. 3.14(b.1)), while they are on the whole layer at K point (∼ 17/25), as shown in Fig. 3.14(b.2). Second, the energy bands at the charge neutrality point largely depend from the stacking order of the bilayer-like region. The zz-zz-zz core with AA-stacking remains semimetallic with linear dispersion relation similar to that of AA-stacked infinite flat bilayer graphene at lower k, but a wide gap parabolic state opens for the higher k ∼17/25, which is located along bilayer core region also including closed-edges (Fig. 3.14(b.3)). This subband gap opening is attributed to the combined effect of interlayer coupling and quantum confinement in a manner similar to that of collapsed armchair SWCNTs with the same stacking order, except for the edge states characterizing zig-zag GNRs. Thus, the electronic properties of bonded prismatic dislocations can be viewed as mixed combination of collapsed nanotubes [244] and monolayer graphene ribbons [245].
To better investigate the contribution of prismatic cores, we have projected out the total density of electronic states, along with the position of the Fermi energy for the selected entire system (see Fig. 3.15). The two degenerate edge states are almost absent in the monolayer region, but start to appear with increasingly higher intensity approaching bilayer-like region up to the maximum in monolayer-bilayer transition

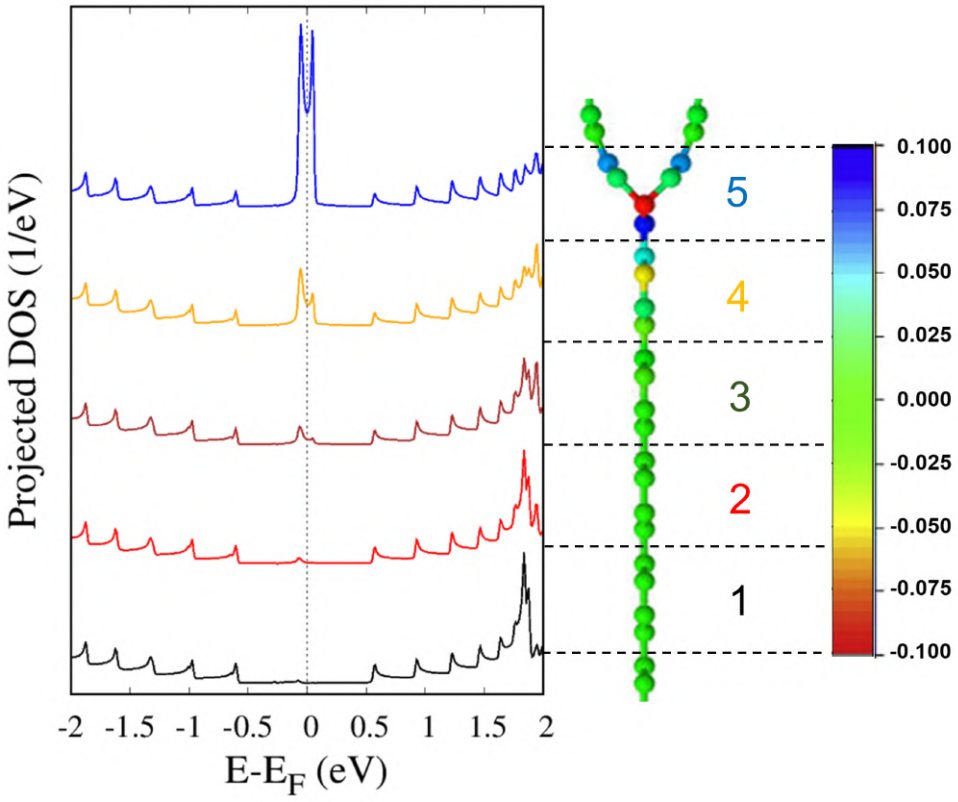

Figure 3.15: (Left) Spin-averaged local density of electronic states of bonded prismatic edge dislocation with zig-zag edges moving from monolayer- to the bilayer-like region. Vertical dashed line indicates Fermi level position set to zero. (Right) Mulliken partial charge analysis of zig-zag core, showing that bridging zone is more higher charged with respect to other sub-regions of the overall system.

area corresponding to the prismatic cores. We note the van Hove singularities visible in the PDOS, more commonly associated with CNTs, occur here because of the 1D confined structures created by dislocation lines. Furthermore, Mulliken population analysis showed local charge difference between sp^3-interlinking bonds and the rest of the hybrid system (see Fig. 3.15). This suggests in the case of the zig-zag cores that induced rehybridization has an insulating effect on dangling bonds along the edge. This will shield the edge states from enviromental influence in a manner similar to nanotube-terminated edges in monolayer graphene [246].
In summary, prismatic edge dislocations show many similarities with graphene nanoribbons and collapsed carbon nanotubes. These include the appearance of localized edge states and the opening of a band gap due to rehybridization effect. Time constraints mean that I have not yet been able to explore the electronic properties of armchair-terminated edge prismatics, but previous literature suggests they are rehybridised and as a result do not have localised edge states.

3.3 Role of folding in hexagonal boron nitride

We learned how folding graphene changes its form into complex shapes with novel physical qualities. However, contrary to the carbon family, boron nitride folded structures or even collapsed nanotubes have rarely been observed. While carbon nanotubes with dog-bone cross section can be reached through a plethora of methods, including acid treatments [15, 29], pressure induced [84–87], or sonication [98], the same range of approaches can be partially successful in BN [247, 248]. Therefore the synthesis of closed-edged bilayer boron nitride nanoribbons is quite challenging and little explored.

Only recently, a few groups have devised ingenious routes for the purpose of interest. Firstly, Zettl and co-workers produced a large fraction of BN nanostructures including collapsed (with spontaneous twisting) nanotubes using a versatile plasma synthesis system [249]. Secondly, tube geometry can be obtained by cutting bilayer h-BN sheets with electron beam irradiation and then spontaneous covalent interconnection between the two layers at open edge [250]. Thirdly, nanotubes with collapsed morphology were synthesized via CVD using $MgCl_2$ as a promoter [251]. Although chemical vapour deposition represents a useful approach towards large-scale production, the resulting samples deteriorated due to the high defect concentration.

In Paper II, on which the first half of this section is based, we present TEM imaging analysis of high-quality boron nitride nanotubes fabricated with another approach, i.e. Boron Oxide CVD (BOCVD) following a catalytic "Vapour-Liquid-Solid mechanism" [252–254]. The grown multi-walled samples then undergo high pressure cycles, where inner nanotubes exhibit peculiar morphologies, including self-folding.

Our first focus is to model from a fully atomistic quantum-mechanical perspective the structure and energetics of single- and double-walled collapsed BN nanotubes using a vdW-inclusive DFT-D scheme. In doing this we will also examine changes of the thermodynamic stability for nanotubes in bundling to corroborate the experimental findings obtained by: S. D. Silva-Santos and A. San-Miguel at Institut Lumière Matière of Lyon (ILM), C. Journet at Laboratoire Multimatériaux et Interfaces (LMI) of Lyon, C. Dalverny at Centre Technologique des Microstructures (CTμ) of Lyon, J.M. De Sousa at Instituto Federal do Piauí (IFPI) of Brazil, and A.L. Aguiar at Departamento de Física do Piauí (DFPI) of Brazil.

Not only that, being an indirect wide gap semiconductor, h-BN presents a strong luminescence in the far UV region (4.4-6.3 eV) [46], which is largely due to exciton-phonon coupling process [255, 256]. It has been observed that its optical spectrum exhibits additional emission peaks associated to folding deformation and changes in stacking order [257]. At folded layers the emission spectrum seems dominated by near band edge emissions, few hundreds of meV below the free exciton energy [257, 258]. Although these spectral features are attributed to phonon assisted inter-valley scattering phenomena [259], the mechanism behind the selection of specific phonon replica at folds remains unclear.

In the second part of this section, based on Paper III, we will investigate the ground state electronic structure of both folded h-BN and collapsed SW- and DW-BNNTs in both armchair and zig-zag orientations, as well as corresponding circular nanotubes. We demonstrate the appearance of additional states associated with local strained edge cavities, leading to a band gap reduction of the overall folded system compared to un-folded counterpart. We reconcile a detailed understanding of electronic properties in these deformed structures with experimental measurements, suggesting the strong impact of the folds for the optical response of the overall system.

3.3.1 Experimental results

Fig. 3.16 shows the TEM morphology evolution of MWBNNTs as a function of applied hydrostatic pressure in cycles of 7, 15, and 36 GPa at 200 kV with specimens rotated from $-60°$ to $+66°$. All of these experimental results were provided by our collaborators from ILM, LMI, and CTμ Institutes of Lyon together with group researchers of IFPI and DFPI in Brazil. First of all, at ambient conditions multi-walled samples exhibit regular patterns associated to the helical polygonization of internal nanotubes [260–262], as further evidenced by the sequence of dark (or bright) spots along the tube axis (see Fig. 3.16(a.1-3)).
At lowest pressure cycle of around 7 GPa, we start to observe the formation of 'bamboo-like' structure (Fig. 3.16(b.1)), which were not seen in pristine samples. In addition, while some tubes show a sort of radial deformation along their axial direction (Fig. 3.16(b.2)), other samples are characterized by a local densification on the tube walls that is associated to the local flattening of all or part of the tube walls (Fig. 3.16(b.3)).
By increasing the pressure to 15 GPa, we observe the same type of structural changes obtained in the previous cycle but more pronounced (see Fig. 3.16(c.1-3)).
At fourth pressure stage of 36 GPa, the resulting samples show much more significant transformations. Although most tubes are extremely damaged (Fig. 3.16(d.2,3)), it is nevertheless possible to observe bamboo- (Fig. 3.16(d.4)) and 'alveoral'-like structure (Fig. 3.16(d.1,5)) with very highly dense tube packings. TEM images of these latter structures at higher magnification show a really novel morphology. Note that the tube wall is divided in two regions (see Fig. 3.16(e.1-2)). The external region is a multi-walled tubular structure made of about 40-50 tubes with an external diameter of about 110-120 nm. Two possible interpretations can be provided to identify the internal one: (*i*) domino stacking of fully collapsed boron nitride nanotubes, or (*ii*) sequence of folds. This point is questionable, since it is hard to follow a single wall/line - to see if at both ends it has strained edge cavity, and whether they are aligned in pairs (i.e. corresponding to close-edged bilayer h-BN ribbons) or offset (i.e. multiply folded h-BN). Regardless of the real geometry in this region, we note that folded structures form an angle $\vartheta \sim 15°$ with respect to the tube axis running all along the tube without interruption.

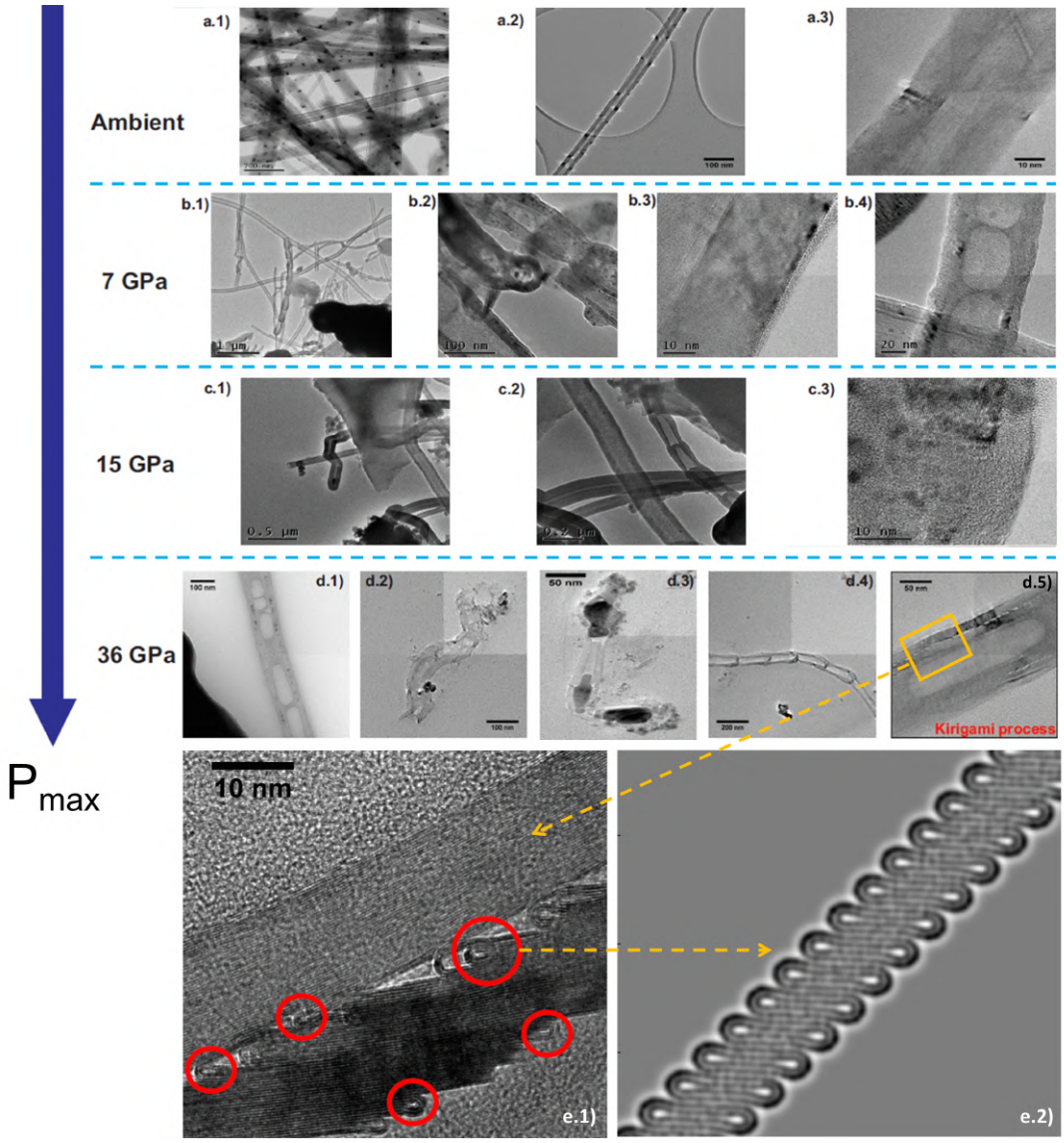

Figure 3.16: HRTEM images of the pristine MWBNNTs sample (ambient) and their structural evolution after pressure cycles up to 7, 15, and 36 GPa performed at 200 kV. BN nanotubes shows bamboo-like configuration for all tested pressure values. At 36 GPa, several microns length tube showing various internal self-organized alveoli of irregular size (e.1), which resemble either collapsed nanotubes in bundling or multiply folds. Credits: S. D. Silva-Santos and experimental co-workers. Simulated TEM image at 200 kV (e.2) is obtained using QSTEM software package. Scales are provided in each image.

3.3.2 Structure and energetics of collapsed h-BN nanotubes

The local curvature at the edge cavities and changes of the stacking order in overlapping flat layers have non-negligible effects on the main properties of collapsed boron nitride nanotubes. However, due to its ionicity the stacking and lattice registry in h-BN is quite different compared to its isostructural counterpart graphite:

- while graphite is well known to crystallize in the AB (Bernal) phase, h-BN favours AA′ stacking [31,263], where nitrogen atoms of one layer all lie directly above boron atoms in the next layer and vice-versa.

- the two most studied stacking patterns for carbon are AB and AA. In the case of h-BN, the alternating sequence of boron and nitrogen atoms leads to the possibility to define more alternative sequences, as observed in samples synthesized by chemical exfoliation [33] and low-pressure CVD [264]. Four high-symmetry stacking configurations can be derived from ground state AA′ through translational sliding or out-of-plane rotation of one of the basal planes in the unit cell. Since a nomenclature consensus is still lacking, we named different stacking sequences with labels used in most recent literature [257,264]. Thus, we refer to these configurations as AA (formed by stacking B to B and N to N in two aligned layers), AB (analogous to AB graphite, with B and N overlapping in neighboring layers), AB_1 and AB_2 (as AB but solely B or N atoms overlapping, respectively). More interestingly, we defined for the first time a further metastable configuration we label AB_3, which can be produced by translating one of the basal plane of the AA-stacking by a vector (0, 1/2, 0). In other words, it corresponds to BN dimers of one layer sitting in the middle of hexagons of the adhering one, analogous to the intermediate AB′-stacking found in carbon [209, 214, 244].

All of these stacking combinations are depicted in Fig. 3.17, while their geometry parameters and resulting DFT-D2 binding energies are summarized in Table 3.3. We note that the binding energy difference between AA′ and AB is only 1.51 (0.92) meV/atom for bulk (bilayer) h-BN. This result is consistent with previous experimental observation of (virtually) pure AB-stacked h-BN flakes [264]. The AB_1-stacking is next closest in energy (+5.22 and +2.37 meV/atom for bulk and bilayer, respectively), while AB_2- and AA-stackings are significantly higher in energy than other sequences. The resulting hierarchical energy scale is in good agreement with most recent calculations carried out via highly advanced methods, such as GGA coupled with vdW forces using Tkatchenko-Scheffler (TS) scheme [264], and hybrid PBE0 functional and local second-order Mϕller-Plesset perturbation [265].
In order to assess the robustsness of our GGA-vdW (Grimme D2) approach, we analyzed the interlayer sliding energy landscape of bilayer h-BN by testing other DFT theory levels, i.e. LDA and GGA without dispersion correction. Starting from ground state AA′ stacking pattern, we perfom a set of lateral shifts of one h-BN

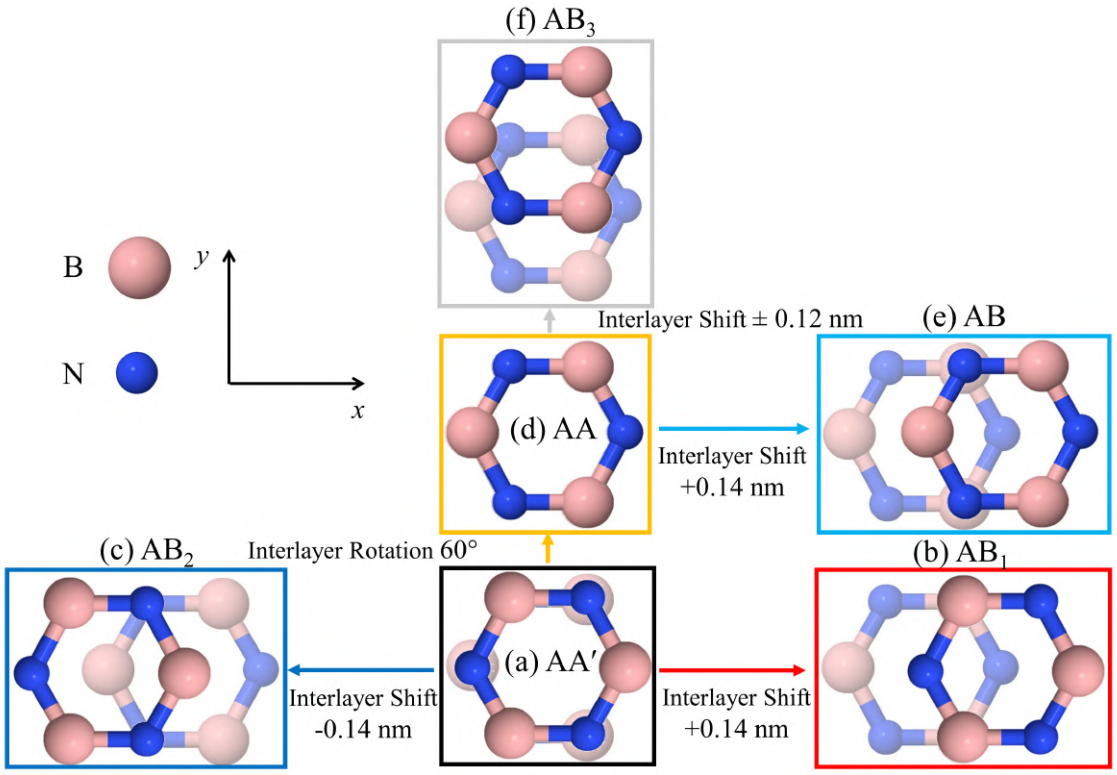

Figure 3.17: Six high-symmetry h-BN stackings linked by interlayer translation and rotation, (a) AA′ is the most stable, and transforms to (b) AB_1 and (c) AB_2 via x-axis translation of one basal plane by ±0.14 nm (red and blue arrows, respectively), or to (d) AA by rotation of one layer around the z-axis (yellow arrow). Subsequent 0.14 nm interlayer shift (purple arrows) gives (e) AB-stacking. A new stacking (f) AB_3 is obtained by translating one layer of AA along the y-axis by ±0.12 nm (pink arrow). Image taken from Paper II.

basal plane by a vector $t\cdot(1/3,\ 3/2,\ 0)$, with t a real number. For example, AB_1- and AB_2- stacking modes are obtained for $t = 1$ and 2, respectively. In this set of calculations, atomic positions and out-of-plane space are allowed to relax. At each shifted configuration we calculated the corresponding total energy. The resulting energy profile is presented in Fig. 3.18. This clearly demonstrates that both LDA and GGA approximations underestimate the interlayer potentials of layered h-BN and hence the implementation of dispersion correction. The DFT-D2 mean-free path matches with those obtained in the accurate theoretical studies referred to in Ref. [265].

Given the impact the layer registry had for infinite flat h-BN, the next step is the investigation of their effects on the energetics of collapsed nanotubes.

Table 3.3: DFT-D2 calculated lattice parameters (in nm) and relative binding energies (in meV/atom) obtained for bulk and bilayer h-BN with different stacking orders. Taken from Paper II.

	Bulk			Bilayer		
	a_0 [nm]	c_0 [nm]	E_b [meV/atom]	a_0 [nm]	c_0 [nm]	E_b [meV/atom]
AA′	0.252	0.315	0	0.251	0.318	0
AB	0.251	0.317	1.51	0.251	0.319	0.92
AB_1	0.251	0.318	5.22	0.250	0.322	2.37
AB_3	0.251	-	-	0.250	-	-
AB_2	0.251	0.333	23.65	0.250	0.335	10.81
AA	0.250	0.337	25.83	0.249	0.341	11.69
Experiment	0.254	0.333	-	0.251	0.325±0.010	-

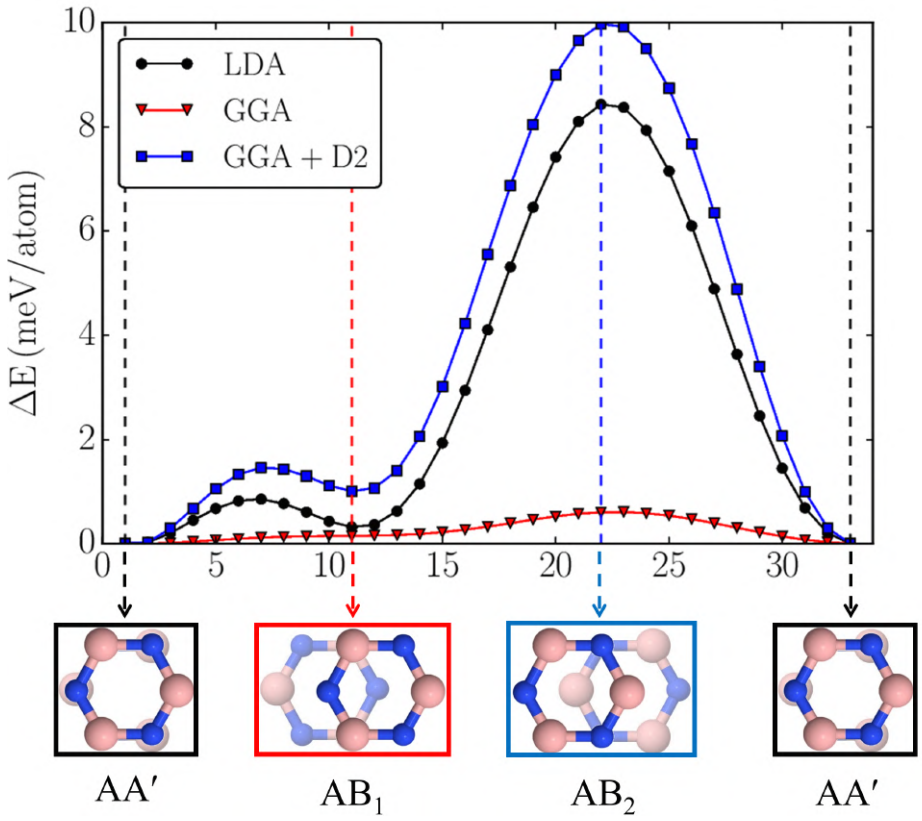

Figure 3.18: Translational energy barrier of bilayer h-BN using following paths obtained by a vector $t\cdot(1/3,\ 3/2,\ 0)$: AA′ --→ AB_1 ($t = 1$) --→ AB_2 ($t = 2$) --→ AA′, at different DFT exchange-correlation functionals: LDA (black), GGA (red) and GGA+D2 (blue). Image taken from Paper II.

3.3.2.1 Energy stability of free-standing BNNTs

Folded h-BN monolayers can be modelled by collapsed boron nitride nanotubes. In doing this, we highlight similarities and differences with its carbon counterpart:

Similarities

- There is a direct relationship between lowest energy stacking and fold high-symmetry orientation. If a fold is not aligned with a high symmetry direction, the two layers lie at an angle to each other, forming a quasi-Moiré pattern whose stacking order is essentially turbostratic [266]. In this case charge localization matching the Moiré lattice spacing is predicted [267].

- The collapse of BN nanotubes is diameter dependent. Following the same strategy used for the carbon case, we have calculated the deformation energy between collapsed and circular configurations in order to determine the threshold, above which the circular cross section spontaneously collapses to a dogbone-like shape consisting of two strained side cavities bridged via a central flat region.

Differences

- When folding along the armchair $[10\bar{1}0]$ direction the most stable stacking is the ground state AA′ for boron nitride (see Fig. 3.19(a.1)), which is in contrast to the AB in carbon. However, folding along the zig-zag $[2\bar{1}\,\bar{1}0]$ direction is equivalent to a basal plane rotation of π and therefore it is not possible to restore the lowest energy AA′ and AB for boron nitride and carbon, respectively. Instead, the lowest energy stacking sequences compatible with a zig-zag fold are labelled AB_3 (see Fig. 3.19(a.2)) for boron nitride and AB′ for carbon.

- While it was proven experimentally and then confirmed theoretically that the carbon collapse threshold is roughly equal to 5.14 nm (see Subsection 3.1.1), we obtained for free-standing SWBNNTs a critical diameter equal to 3.05 nm (see Fig. 3.19(b)). This difference can be understood through the correlation with the interlayer binding of bulk h-BN, which is 25.52 meV/atom higher than graphite, and hence will favour collapse. It is also consistent with the high polar nature of boron nitride [268].

Single-Walled. We then explored the lattice registry effect on the thermodynamic stability of collapsed armchair SWBNNTs (see Fig. 3.19(b)). Changing the stacking fault between overlapping flat regions, we found that both AA′- and AB_1-stacked collapsed nanotubes are stabilized at $D_{\text{cross}} = 3.05$ nm, because the bilayer interlayer binding difference between them is just 2.37 meV/atom. If the middle flat section is arranged in less stable AB_2 stacking, nanotube collapse for a critical diameter value

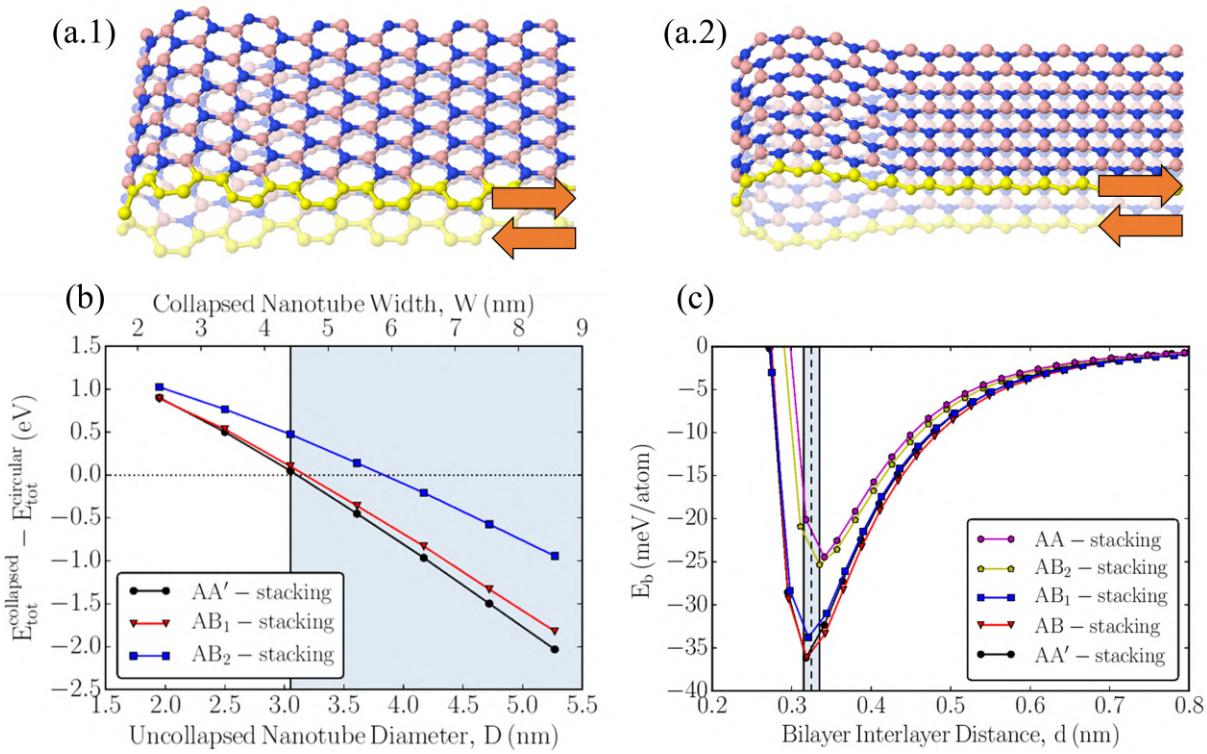

Figure 3.19: (Top) Schematic illustration of folded h-BN with (a.1) armchair and (a.2) zigzag edges, whose most energetically favored central flattened zones are characterized by AA′- and AB_3-stackings, respectively. Yellow balls indicated nanotube orientation, while red arrows show interlayer shearing mode. (Bottom) (b) Total energy difference between free-standing collapsed ($E_{\rm tot}^{\rm collapsed}$) and circular ($E_{\rm tot}^{\rm circular}$) armchair ($n$,$n$) SWCNTs versus tube diameter D (lower x-axis) and equivalent width (upper x-axis). The intersection point at $\Delta E_{tot} = 0.0$ eV indicates the threshold diameter above which collapsed boron-nitride nanotubes become energetically favourable in comparison to circular ones. (c) GGA-D2 calculated binding energies for infinite bilayer h-BN. Vertical dashed line and magenta section represent its average interlayer distance and corresponding uncertainty (0.325 ± 0.01 nm) obtained in prior experimental studies. Image taken from Paper II.

equal to 3.89 nm, since the associated relative binding for infinite bilayer is 10.81 meV/atom. This stacking-dependent collapse of single-walled BNNTs is consistent with the interlayer potential analysis of corresponding infinite bilayer h-BN (see Fig. 3.19(c)).

The small critical diameters obtained for free-standing armchair SWBNNTs seem to confirm the most recent experimental evidence, although our predicted values are somehow larger than those estimated in the experiments (∼0.45 nm) [250]. One possible explanation is that the additional interaction with Cu substrate (not incor-

porated in our study) can induce charge transfer, thus favouring the self-collapsing behaviour [250].
In summary, BN nanotubes can collapse at diameter values lower (3.0-3.9 nm) than carbon family due to the high ionic character of boron and nitrogen.

Double-Walled. Like carbon, studies on growing large diameter collapsed single-walled BN nanotubes have been scarce, while multi-walled samples are more common. Previous theoretical studies showed that the collapse threshold in carbon nanotubes increases by increasing the wall number N. This is because the attractive vdW energy after collapse is largely independent of the number of tube walls, while the curvature energy gain increases with increased wall number. For large experimental DWNTs, turbostratic is most likely. It would be computationally heavy to simulate the large-syze of experimental samples. Thus, we modelled DW tubes using small unit cells with different interlayer couplings.
However, a point that remains unexplored is the variation of the critical diameter for multi-walled nanotubes as a function of registry patterns formed between tube walls. This is important in order to control the interlayer spacing at cavity. To elucidate this we have considered two sets of armchair DWBNNTs with varying both intralayer stackings and distances, including the $(n,n)@(n+4,n+4)$, $(n,n)@(n+5,n+5)$ and $(n,n)@(n+6,n+6)$ combinations (see Fig. 3.20). In this study, the ground state AA′-stacking is used for inner shell.
For $(n,n)@(n+4,n+4)$ and $(n,n)@(n+6,n+6)$ cases all central facing layers are still arranged in AA′-stacking mode, while $(n,n)@(n+5,n+5)$ systems show the following stacking sequence: AA′-AA′-AB_1 between inner and outer tubes. Geometry parameters and critical diameters of collapsed DWBNNTs are listed in Table 3.4. Deformation energy between collapsed and circular double-walled nanotubes indicate that for $(n,n)@(n+4,n+4)$ the collapse threshold is the same of that found in single-walled case. The $(n,n)@(n+5,n+5)$ and $(n,n)@(n+6,n+6)$ systems collapse at diameter values equal to 3.27 nm and 3.51 nm, respectively, which are higher with respect to single-walled case. In order to establish the best size pairings of DWBNNTs, additional parameters are needed. Relative energy calculations carried out on following three cases: (22,22)@(26,26), (22,22)@(27,27) and (22,22)@(28,28), demonstrated that the second case represents the lowest energy configuration. Besides its energy stability, the outer (26,26) tube appears very tight with respect to the inner one. In addition, one cavity of the external (28,28) tube tend to stick with that of the internal (26,26) due to the strong vdW interactions, provoking an increase of the interwall spacing between cavities in the opposide side. These results suggest the $(n,n)@(n+5,n+5)$ combination as the best compromise to simulate collapsed DWBNNTs.

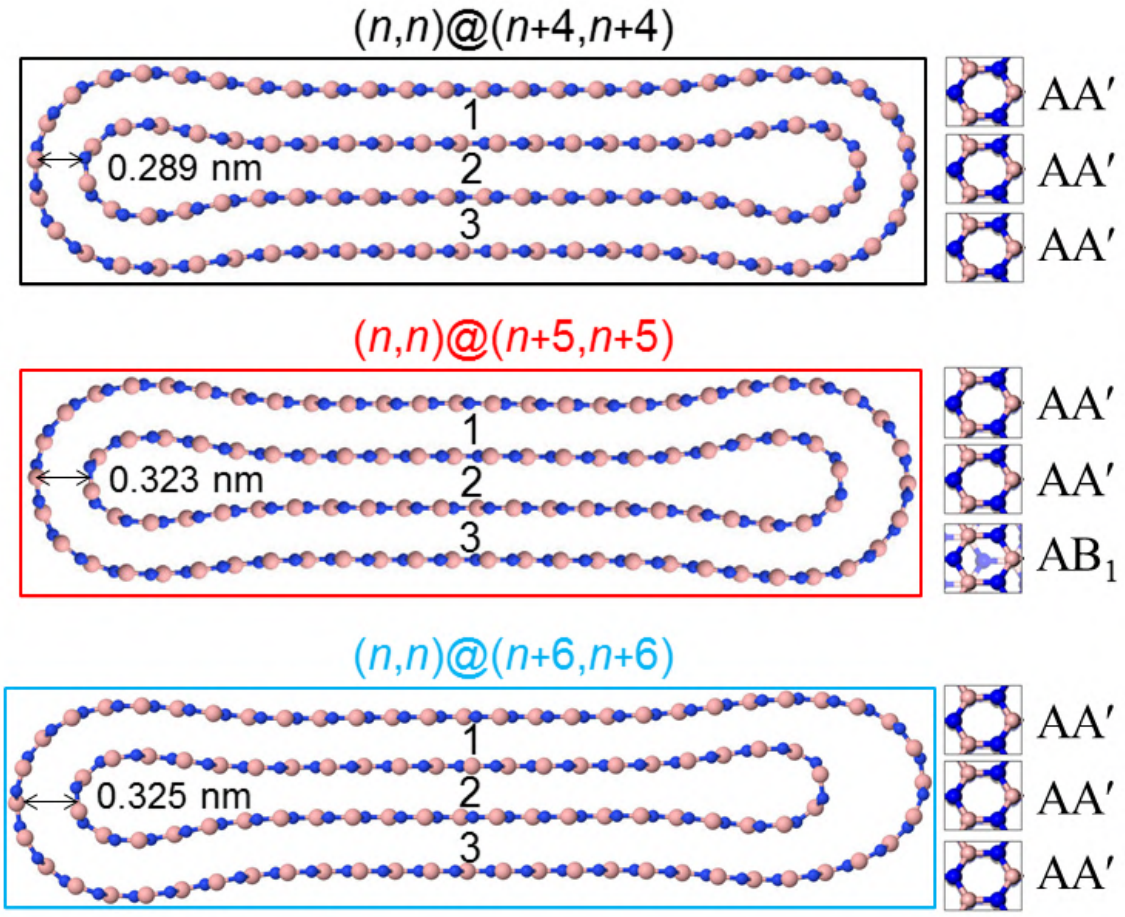

Figure 3.20: Cross-sectional views of double-walled collapsed BNNTs by changing the diameter of the outer tube: (black) (n+4,n+4), (red) (n+5,n+5), and (blue) (n+6,n+6). Stacking orders between tube walls are indicated by black squares.

Table 3.4: Interwall cavity distances, collapse threshold diameters and energy differences (per unit cell) between two sets of free-standing DWBNNTs.

Collapsed DWBNNTs			
Outer tube	d_{in}^{cav} [nm]	D_{cross} [nm]	Relative energy [meV/atom]
(n+4,n+4)	0.289	3.05	0.27
(n+5,n+5)	0.323	3.52	0.00
(n+6,n+6)	0.325	3.27	1.78

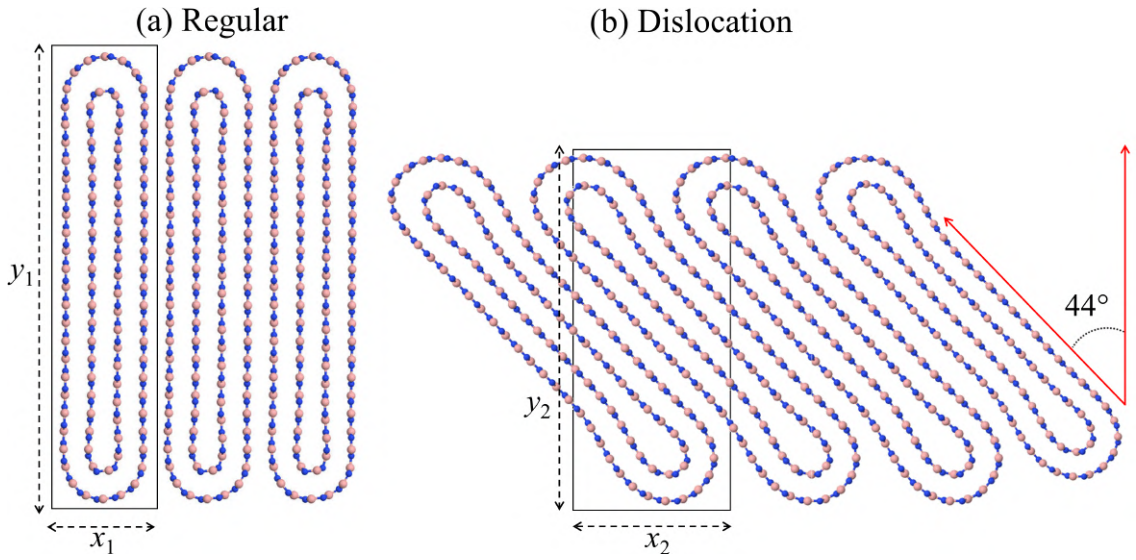

Figure 3.21: Cross-sectional views of packing modes of collapsed (22,22)@(27,27) BNNTs in a stack, as obtained via DFT-D2 structural relaxation. The rectangles with different sizes delineate the computational unit-cells. Two stacking modes considered are: (a) regular and (b) dislocation. The second one is obtained by rotation the overall geometry along tube axis by an angle of 44°, as marked black dotted arc.

3.3.2.2 Bundles of collapsed DWBNNTs

While packings of circular boron nitride nanotubes have been thoroughly investigated [269–271], studies concerning interactions between collapsed BNNTs has not been reported to date.
To this purpose, we extend the concept of balancing the bending energy stored at the edge cavities with the attractive vdW energy exerted in middle flat regions, applied so far to free-standing DWBNNTs, to a system of interacting ones. We considered bundles of collapsed double-walled (n,n)@$(n+5,n+5)$ BNNTs formed by two possible interacting stacking modes (see Fig. 3.21):

- *regular*: BN nanotubes are perfectly aligned along the out-of-plane direction. Notice that the typical dog-bone shape becomes elliptical as a result of induced forces from neighboring tubes (Fig. 3.21(a)).

- *dislocation*: this configuration involves two identical collapsed nanotubes with flat regions on their opposite faces (Fig. 3.21(b)).

We performed relaxation calculations on the translational cell of one individual collapsed DWBNNT under orthorhombic cell. Like the single-walled case, we applied periodic boundary conditions. To enable vdW interaction between neighboring stacks, we reduced the out-of-plane lattice vector obtaining a shell separation

distance approximately equal to that of bulk h-BN (0.325 nm) and keeping large vacuum space (∼20.0 Å) only in one in-plane direction. The dislocation mode can be reached by rotating the entire tube structure along its periodic direction. Angle-dependent test calculations found that the lowest energy configuration is obtained for an angle equal to 44°. DFT-D2 analysis of the total energy (per unit cell) of collapsed DWBNNTs revealed an energetic advantage of regular stacking over dislocation mode, although their relative difference per atom is just 1.8 meV/atom, suggesting the possibility that both configurations may be experimentally observable.
Note that we go from regular (Fig. 3.21(b)) to dislocation (Fig. 3.21(a)) configuration, the cell length increase ($x_1 > x_2$), while the cell height decrease ($y_1 < y_2$). This would be a response to increasing pressure. However, there will be limits to the increase in y which is possible, because it is constrained within a tube (the only way it can increase y is to move into the central cavity space). Once good reason to go from dislocation to stacking mode is if there is intense pressure via the ends of the tubes, which is driving a decrease in x.
In conclusion, our results show that there is a trade-off when tilting such structures, since the tilted structure has more space for formation of larger more stable edge cavities, but this is counteracted by a reduction in the degree of overlap between neighboring structures, and hence vdW interaction. The calculations might suggest that these two effects are largerly balanced, and the degree of tilting is thus likely dependent on the experimental conditions imposed of the unit-cell dimensions.

3.3.3 Gap reduction at edge folds

The next task is the analysis of the electronic properties of h-BN folded nanostructures. However, many effects can contribute simultaneously in determining their ground state electronic structure, such as layer registry, interlayer coupling, curvature, and confinement. This means that we need somehow to take account of the distinctive roles played by the stacked overlapping flat faces and edge cavities. For folded boron nitride systems, their analogies with stacked infinite flat bulk and bilayer h-BN may provide a useful insight into the electronic band gap variation, as we discuss in the following.

Bulk and Bilayer h-BN. Firstly, we calculated the quasiparticle energy gaps of both bulk and bilayer hexagonal boron nitride using different semi-local exchange correlation functionals including corrections for vdW interactions and very accurate post-DFT hybrid functional. The performance of the functionals with respect to the experimentally measurable value (∼5.96 eV) [46] has been compared, as shown in Table 3.5. We note that the general behavior of the electronic band gaps (direct and indirect) matches with prior literature [264, 272]. In addition, our GGA+D2 results are close with previous LDA [273], and GGA+TS [264] calculations.

Despite the good agreement with other theoretical works, the semilocal exchange-correlation functionals used in our current study systematically underestimate the energy gap of h-BN measured in experiment. For this reason, the band gaps of GGA+D2 optimized systems are re-calculated using the hybrid HSE06 functional with QUANTUM-ESPRESSO code by our colleagues M. Amato and A. Zobelli at Laboratoire de Physique des Solides (LPS) of Paris. In order to correctly predict the band gap of AA′-stacked bulk h-BN, we optimized the Fock exchange operator following the approach reported in Ref. [149]. The resulting parameter $\alpha = 0.31$ combined with screening parameter fixed at $\omega = 0.106$ a.u. gives a band gap of 6.09 eV, in excellent agreement with most reliable experiment [46] and recent HSE06 [275] and GW calculations [272, 276, 277].
In principle, the set of parameters used to describe the bulk configuration cannot be applied in the case of bilayer and single-walled nanotubes, because geometric confinement induces changes in screening effect affecting the computed band gaps in a very specific way [149]. As such the parameters are not, in principle, transferable. We addressed this issue double-checking the dependence of the energy gap of both h-BN flat bilayers on the two HSE06 parameters of interest.

Table 3.5: DFT calculated quasiparticle energy gaps (in eV) for the bulk and the bilayer h-BN in their five stacking faults compared with most recent and reliable theoretical calculations. Indirect and direct band gaps are labelled by "(i)" and "(d)", respectively. Taken from Paper II.

h-BN	Method	AA′	AB	AB_1	AB_2	AB_3	AA
Bulk	LDA	4.14 (i)	4.23 (i)	3.42 (d)	3.44 (i)	-	3.50 (d)
	GGA+D2	4.20 (i)	4.35 (i)	3.27 (d)	3.25 (i)	3.13 (d)	3.21 (d)
	HSE ($\alpha = 0.25$)	5.74	5.78	4.70	4.59	4.60	4.52
	HSE ($\alpha = 0.31$)	6.09	6.12	5.15	4.90	4.91	4.83
	HSE ($\alpha = 0.40$)	6.12	6.14	5.08	4.87	4.88	4.80
	GGA+TS [264]	4.29 (i)	4.37 (i)	3.65 (i)	3.62 (i)	-	3.72 (d)
	GW [272]	6.10	6.23	5.30	5.39	-	5.38
	GW [276]	5.73	5.87	5.01	4.96	-	4.96
Bilayer	LDA	4.32 (i)	4.35 (i)	3.98 (d)	4.08 (i)	-	3.97 (d)
	GGA+D2	4.35 (i)	4.39 (i)	3.94 (d)	4.00 (i)	3.94 (d)	3.94 (d)
	HSE ($\alpha = 0.50$)	7.22	7.10	7.16	6.78	7.05	6.82
	LDA [273]	4.34 (i)	4.36 (i)	4.01 (d)	4.08 (i)	-	4.05 (d)
	GGA [274]	4.69	4.60	4.29	4.52	-	4.23
	GGA+TS [264]	4.52 (i)	4.50 (i)	4.14 (d)	4.26 (i)	-	4.20 (d)
	GW [272]	7.10	7.09	6.75	6.84	-	6.80

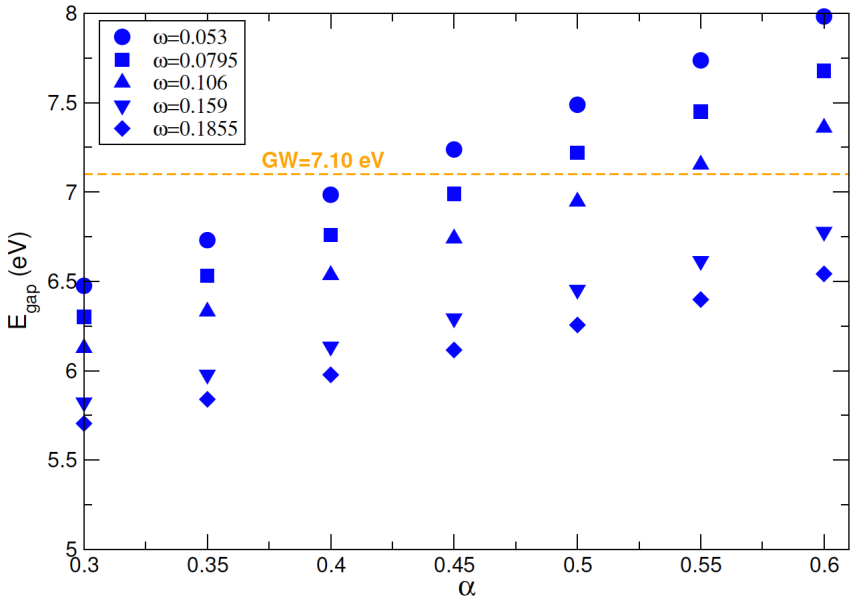

Figure 3.22: Optimization of HSE06 parameters (ω and α) for AA′ h-BN bilayer to better predict corresponding energy gap. Horizontal orange dashed line represents the band gap of h-BN bilayer at the same stacking phase obtained within the GW approach. Image taken from Paper II. Credit: Michele Amato

Fig. 3.22 shows the variation of energy band gap for AA′-stacked h-BN bilayer by varying the couple of optimized HSE06 parameters. It is important to point out that energy gaps of different bilayer stacking phases obtained for a given set of parameters ($\alpha = 0.50$ and $\omega = 0.0795$ a.u.) are very close to GW calculations reported in literature. [149], with the exception of AB_1 sequence. From HSE06 calculations, we can conclude that the set of parameters giving correct values of the bulk band gaps are not able to proper describe the electronic properties of every stacked bilayer-like system, which can be understood through the correlation between screening and confinement explained above.
Despite the GGA+D2 absolute band gaps being underestimated, the *relative* energy gaps between high symmetry configurations are in very good agreement with those obtained with HSE06 using GGA+D2 optmized geometries, as well as GW values [272]. Fig. 3.23 shows the resultant comparative analysis. These preliminary results justify the use of semi-local GGA-vdW to the study of band gap changes in systems characterized by more continuous stacking transformations, such as multilayer wrinkles or folds. Fig. 3.24 shows a 2D map of the band gap variation of different stackings with respect to ground state AA′. Cell dimensions were kept fixed at the relaxed AA′ values, in-plane layer translations are applied and then all atoms are allowed to move freely and independently in the out-of-plane direction. These maps are extrapolated from 60×60 grid of calculations.

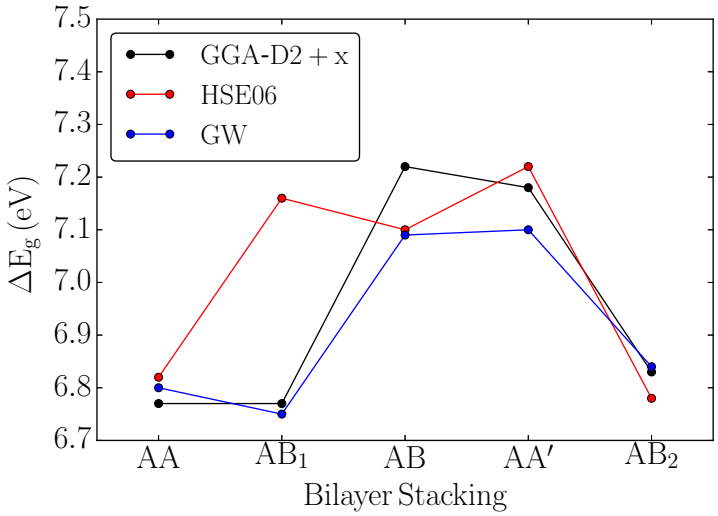

Figure 3.23: Calculated energy gaps of bilayer h-BN in different stacking orders with respect to the ground-state AA′ using different levels of theory: semi-local GGA/PBE+D2, hybrid HSE06, and GW. Image taken from Paper II.

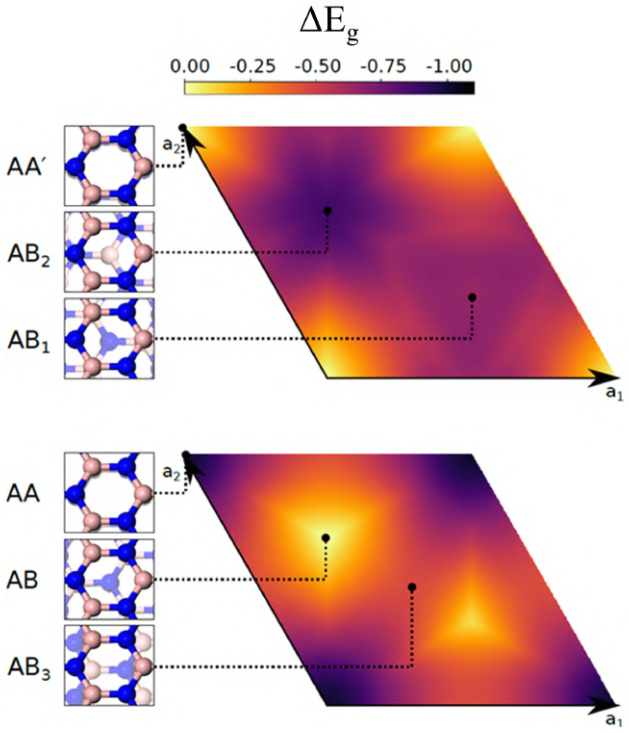

Figure 3.24: Contour plots showing decrease in GGA/PBE+D2 band gap compared to AA′-stacking (eV) of bilayer h-BN linked by interlayer translation and rotation. (Top) Energy gap variation between AA′, AB_1, and AB_2 stackings. (Bottom) Energy gap variation between AA, AB, and AB_3 stackings. Image taken from Paper II.

The resulting energy gaps vary up to 1 eV with stacking transformations, and the most stable stacking symmetries (AA′ and AB) show the largest values.

Collapsed SWBNNTs. We compare here the electronic band structures of collapsed armchair (30,30) and zig-zag (36,0) single-walled BN nanotubes with corresponding infinite flat un-folded bilayer in GGA+D2 with AIMPRO code. As introduced previously, the lowest stacking configuration is fold orientation-dependent. While the central flat region of the armchair nanotube is AA′-stacked with interlayer spacing of 0.32 nm, the adhering flat middle layers of the zig-zag tube are arranged in AB_3-stacking with a separation distance of 0.33 nm. The calculated height of edge cavity for armchair and zig-zag collapsed nanotubes is ∼0.54 nm and 0.62 nm, which are almost identical to the diameters of circular (4,4) and (8,0) nanotubes, respectively. Surprisingly, the electronic properties show relevant differences between two considered tube orientations, as depicted in Fig. 3.25.
The AA′-stacked collapsed armchair SWBNNT is characterized by a wide indirect band gap matching that of infinite bilayer with same stacking order. However, within the gap an additional filled state appears whose maximum lies 0.07 eV above the bilayer valence band (VBM) at 2/3 of the Γ-X path (Fig. 3.25(a)). The integration perpendicular to the cross-section of wave function distribution plotted in Fig. 3.25(b) show that this state corresponds to N atoms situated in the folds also including the line of hybridization change, while the conduction band minimum (CBM) remains "bilayer-like" and is associated with B atoms of the middle flat section, as further evidenced by projecting the electronic density of states at different locations along the cavity (Fig. 3.25(c)). Unlike the armchair case, the AB_3-stacked collapsed zig-zag nanotube exhibits a direct band gap with an additional state 0.37 eV below the CBM that is localized on the B atoms of the edge bulbs, while the valence regime behaves as infinite flat bilayer h-BN (Fig. 3.25(e)-(g)).
We observed therefore a lowering of electronic energy gap associated with the appearance of additional bands either above the valence band or below the conduction for armchair and zig-zag fold orientations, respectively. This is in addition to any gap change imposed by the local stacking. The overall structure of the zig-zag collapsed tube can be interpreted as 'type-II' homojunction between two wide band gap semiconductors: a bulk core with a wider gap and a folded edges region with a gap smaller by 0.37 eV, while armchair folds seem to play no relevant role (a valence band offset of only 0.07 eV). Indeed, we found that the electronic structure is largely independent of the collapsed tube width (unlike carbon nanotubes [244]), as depicted in Fig. 3.26.
The effect of the curvature can also be analyzed using Bader charges as a measure of the local ionicity. The central bilayer-like region show $0.72e^-$ transfer from B to N, slightly higher than the equivalent infinite bilayer ($0.69e^-$), while in the edge cavities this value drops to $0.56e^-$, which is lower than in an equivalent diameter (4,4) circular nanotube ($0.59e^-$).

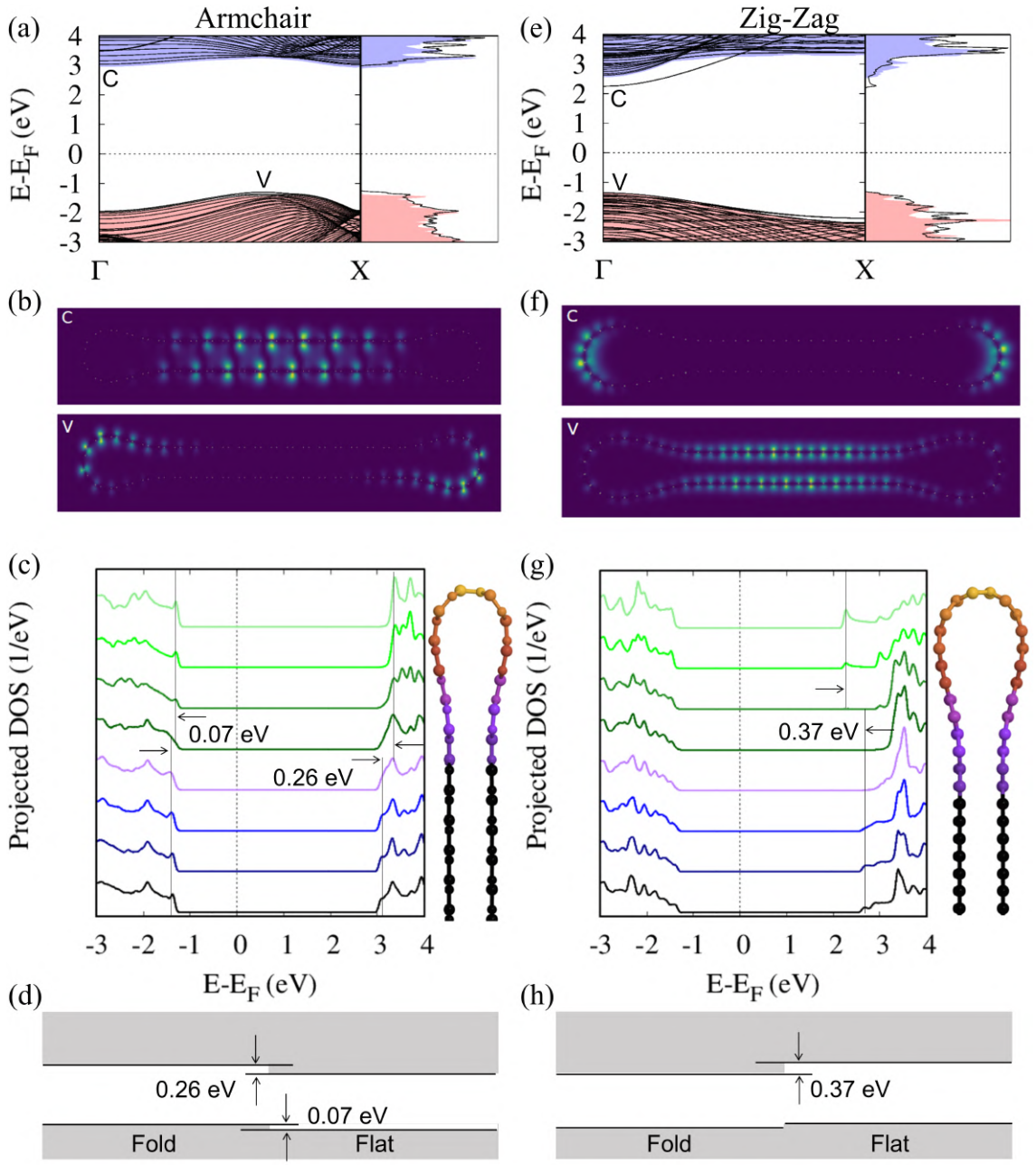

Figure 3.25: (a,e) Electronic band structures and associated density of states of fully collapsed SWBNNTs (black solid line) and corresponding infinite flat bilayer h-BN (filled color). (b,f) Integration perpendicular to the cross-section image of the wave function square. (c,g) Local density of states moving from cavities (light-green line) to the central flat zone (black line), as shown in the inset. (d,h) Qualitative model of the band-alignment. Armchair (left column) and zig-zag (right column) folds in AA′ and AB$_3$-stacked, respectively. Image taken from Paper II.

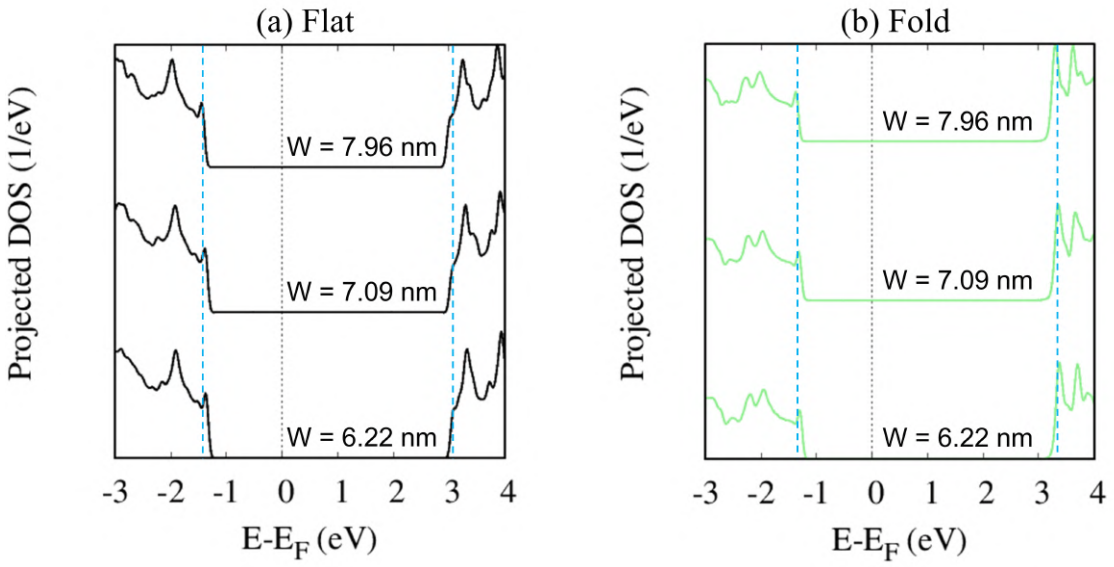

Figure 3.26: Local density of states moving from (a) central flat zone (black lines) and (b) cavities (light-green lines) by increasing the collapsed nanotube width in steps of 0.87 nm: 6.22 nm (bottom), 7.09 nm (middle), and 7.96 nm (top) of (26,26), (30,30), and (34,34) armchair nanotubes, respectively.

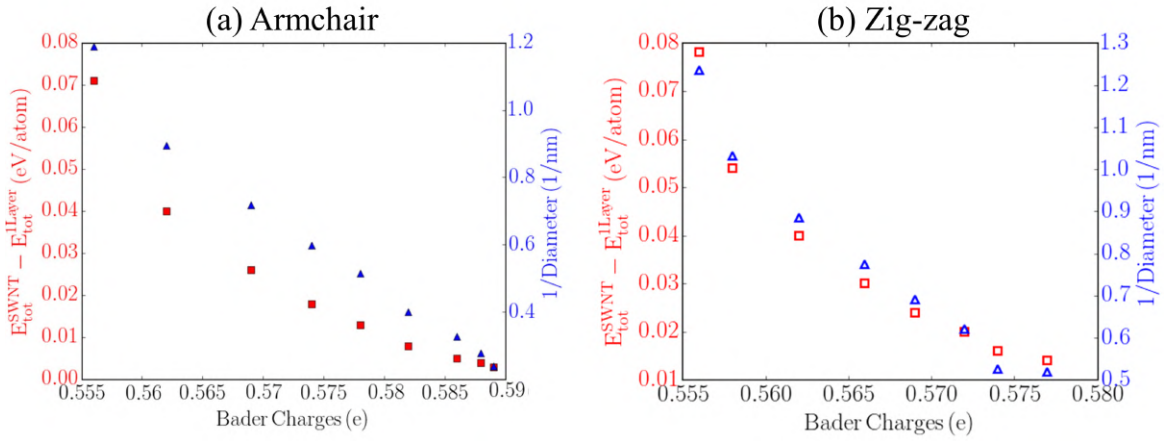

Figure 3.27: Bader charges (red, e) of B and N atoms in circular SWBNNTs are approximately linearly and inversely proportional to the reciprocal of the nanotube diameter (blue, 1/nm) and the formation energy relative to an infinite flat BN monolayer. (a) armchair and (b) zig-zag chirality nanotubes. Image taken from Paper II.

The decreasing in polarization corresponds to the destabilization of the bonding caused by curvature, which can be explained through the correlation of ionicity and

tube radius for circular BN nanotubes (see Fig. 3.27). This result shows that the material becomes slightly less ionic as the curvature increases regardless of tube chirality.
In summary, zig-zag folds appear to be able to act as hole traps in hBN and it will be interesting to correlate this with optical emission studies.

Collapsed DWBNNTs. We extend the study of band gap reduction to double-walled collapsed nanotubes keeping the same theory level. The reason of this other set of computations is twofold: *(i)* to understand the confinement effect on folded BN nanostructures; *(ii)* experiments have shown a larger concentration of multilayer-folds with respect to single-ones. Thus, collapsed double-walled tubes better reflect the structures of samples synthesized experimentally. Since relative energy tests and resulting geometry parameters have indicated (n,n)@(n+5,n+5) as the best combination among three sets of armchair double-walled tubes (see subsubsection 3.3.2.2), we analyzed the electronic structure of collapsed (22,22)@(27,27) DWBNNT, which exhibits the following sequence of stackings after structural optimization: $AA'-AA'-AB_1$.
In order to unravel the distinctive role of edge bulbs and stacked faces, we exploited their analogies and differences to the electronic properties of quadrilayer h-BN with the same stacking sequence. The resultant comparative analysis is shown in Fig. 3.28.
The DWBNNTs is a direct band gap semiconductor due to the presence of AB_1-stacking (see Fig. 3.28(top)). Like the previous single-walled case, an additional gap state appears in the valence band regime due to the end cavities, but with a considerable difference: the valence band maximum of cavity states at $\sim$2/3 of the Γ-X path is higher than that of the quadrilayer one by 0.15 eV. This point is further confirmed by projecting density of states around different regions of the overall system (see Fig. 3.28(bottom)).
This result highlights the key points of the current investigation:

- the VBM of the total density of states matches with that obtained for PDOS at the folds.
- the CBM of the total density of states corresponds to the minimum obtained in the conduction regime of the infinite quadrilayer hBN.
- thus, the energy gap of the overall tube can be interpreted as a result of the combination between VBM and CBM coming from edge folds and flat region, respectively.
- The total band gap is lower of 0.15 eV in comparison to the infinite flat quadrilayer[8].

[8]The quadrilayer case was double-checked with both orthorhombic and hexagonal unit-cells.

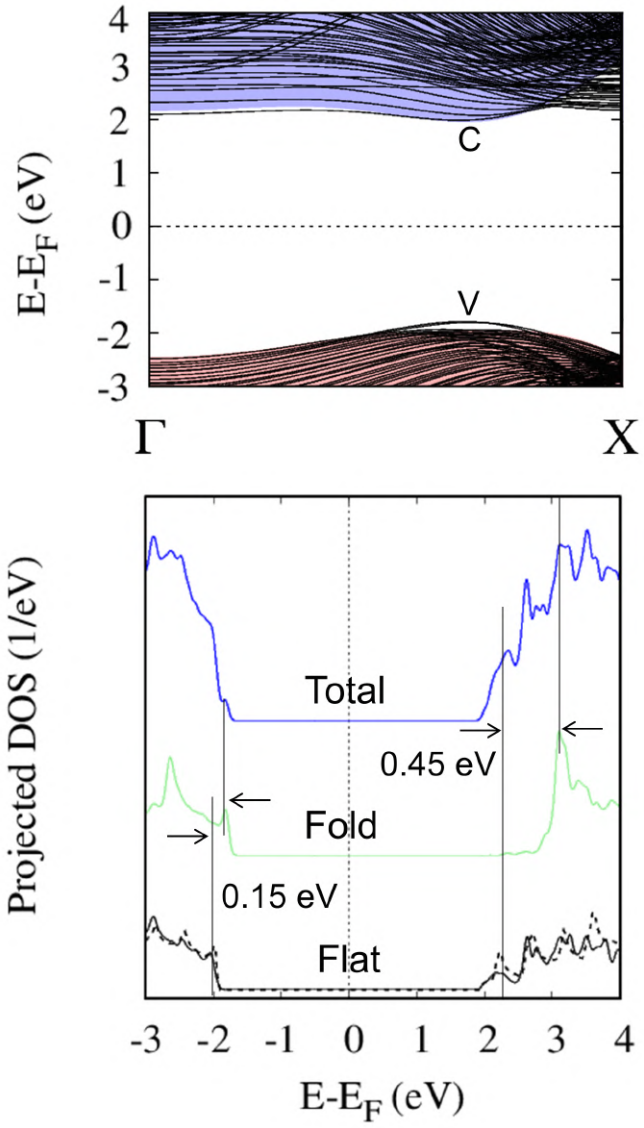

Figure 3.28: (Top) Electronic band structures of fully collapsed DWBNNTs (which black solid line) and corresponding infinite flat quadrilayer h-BN (filled color). (Bottom) Local density of states moving from cavities (light-green line) to the central flat region (black line) compared to the total density of states of the overall structure (blue line) and infinite flat quadrilayer (dashed black line).

Uniform k-point grids were used along in-plane directions for DOS calculations and found no changes for the band gap.

All of these collapsed nanotubes represent the unconstrained limit for h-BN folding, but in folded and pleated mono- and multilayers, on substrates and at folded stacked edges there will be further constraints on the fold.

Multiply folded h-BN. In a last set of computations, we have considered a limit model, where a monolayer has been repeatedly folded to give infnite bulk AA′-stacked h-BN with armchair folds. The interlayer spacing of flattened regions is 0.32 nm, which matches the calculated un-folded bulk h-BN in AA′-stacking value. In this case two edge cavities are observed, one almost free-standing and the other smaller and constrained, characterized by a diameter equal to 0.57 nm and 0.38 nm, respectively (see Fig. 3.29(a)).
The calculated electronic structure show an indirect band gap matching bulk h-BN at the same stacking order (see Fig. 3.29(b)). Compared to single- and double-walled collapsed nanotubes, we observe the appearition of two additional gap states above 0.09 eV and 0.30 eV above bulk VBM. Integration perpendicular to the cross-section image of the wave function square revealed that the shallower gap state corresponds to the smaller constrained cavities, while the second one is associated to the unconstrained larger bulbs (see Fig. 3.29(c)).
These considerations can be extended to the case of more complex multilayer folds, for example reconstructed edges of bulk h-BN, the so-called "nanoarches" [105] The interlayer misalignment due to the differing radius of curvature of folded layers results in a continuous change of the stacking order, which will be essentially turbostratic. Folded h-BN can be interpreted as quasi-1D Moiré superlattice. Indeed, a 1D-equivalent of 2D Moiré pattern band-gap variation has been recently predicted to result in localized charge puddling in misaligned h-BN layers [267].
In summary, we unravelled the effect of edge folds consisting of the introduction of additional gap states that reduce the energy gap of the original infinite un-folded systems. Analysis of both collapsed nanotubes and multi-folded system with armchair folds showed that gap reduction increases by increasing the total number of layers from bilayer up to bulk-like configuration.
Similar qualitative result has been obtained for h-BN with zig-zag folds through the examination of double-walled $(n,0)@(n+8,0)$ collapsed nanotubes and folded bulk[9]. In Table 3.6, we summarize the core of the current investigation.
In general, it is well-known that energy gap of h-BN nanostructures can be modulated by transverse electric fields [278, 279] or uniaxial strain [280]. In this study, we found another way to drammatically modify the electronic structures of defect-free h-BN represented by unusual covalent bonds at its edges.

[9]For readers interested in a more exhaustive analysis to the h-BN systems with zig-zag folds, it is useful to refer to Paper II: A. Impellizzeri, M. Amato, A. Zobelli and C.P. Ewels. "Band gap reduction at edge folds in hexagonal boron nitride". *submitted* (2020).

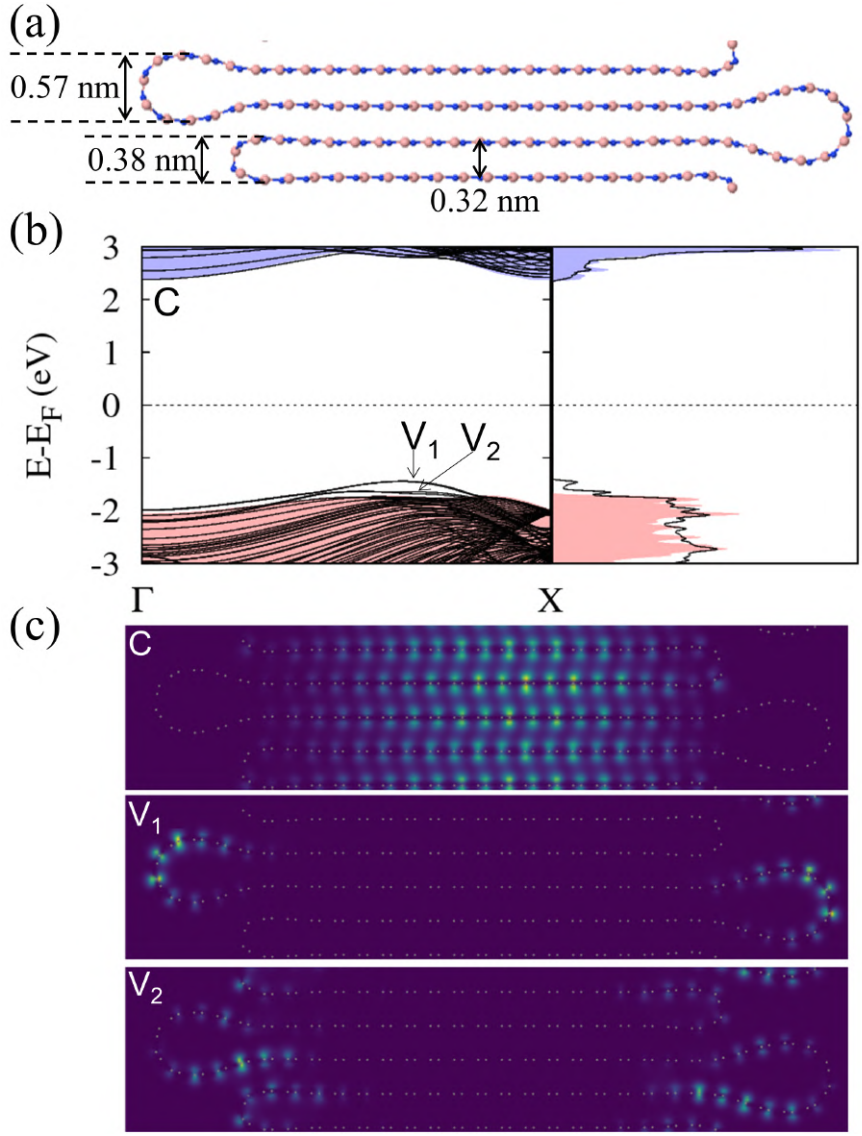

Figure 3.29: (a) Optimized structure of multiply folded hBN, showing values of main geometric parameters. (b) Electronic band structure (left) and total electronic density of states (right) of armchair folded AA′-stacked h-BN single-layer (black solid lines) and corresponding bulk AA′-stacked h-BN (filled colour). (c) Integration perpendicular to the cross-section image of the wave function square showing the top of the highest (VBM) and second-highest (VBM-1) bands at k-points V_1 and V_2 corresponding to nearly 2/3 of Γ-X path, respectively, and the bottom of the conduction band (CBM) at k-point C corresponding to Γ point. The CBM is bulk-like, while the states immediately below the Fermi level are localized at the edge cavities. Image taken from Paper II.

Table 3.6: DFT-D2 computed energy gap between VBM[edge]−(VBM−1) for armchair and (CBM+1)−CBM[edge] for zig-zag fold orientations. Taken from Paper III.

Fold Orientation	Configuration	Gap Reduction [eV]
Armchair	(n,n)	0.07
	(n,n)@$(n+5,n+5)$	0.15
	Multiply folded	0.39
Zig-zag	$(n,0)$	0.37
	$(n,0)$@$(n+8,0)$	0.63
	Multiply folded	0.68

3.4 Summary

In conclusions, we carried out a systematic large-scale density functional study in order to explore the physics of closed edges in different nanostructures, showing novel and distinct properties.
We theoretically confirmed that single-walled carbon nanotubes collapse above diameter threshold of 5.1 nm using DFT-GGA/PBE implemented with Grimme D2 scheme, in excellent agreement with the most plausible experimental result. We have demonstrated that all considered nanotubes (armchair, zig-zag, and chiral) including all sub-families become semiconducting, exhibiting the opening of a small band-gap upon collapsing. This metal-semiconductor transition is a consequence of the curvature localization which breaks the lattice symmetry. The signature of latter point is the inverse relationship between energy gap and nanotube width together with local charge effect. Both collapse threshold and different scaling rules of the energy gap for achiral nanotubes depend on the interlayer shear, a new variable introduced to the nanotube introduced by its collapse. The impact of the slight displacements between adhering layers in this tube topology is of great interest to engineer suitable band gaps for applications like interconnects.
We also confirmed the overall tendency for interlayer bonds to form prismatic dislocations between the basal planes of bulk graphite, which usually occur in highly damaged and irradiated samples. This analysis might suggest the formation of nanostructures, resembling collapsed nanotubes intercalated between carbon layers. Formation energy analysis have shown a significant preference for the symmetric zig-zag core. The corresponding electronic structure calculations exhibited the appearance of edge states at the monolayer region together with closed edges. The low-energy bands at the Fermi level strongly depend by the interlayer coupling of the bilayer-like region, while the opening of a band gap is due to symmetry breaking derived from the local curvature, analogous to collapsed nanotubes. The apparition of edge states is important to study the magnetism at the reconstructed cores (like GNRs), which are considered responsible for the magnetization usually observed in

damaged and irradiated graphite.
High pressure application in multi-walled boron nitride nanotubes leads to the formation of novel morphologies with respect to carbon family, including bamboo-like, alveolar having irregular size, and the apparition of folded edges, as observed through TEM imaging analysis. The formation of this set of novel configurations can be attributed to the fracture of polygonized internal tubes in response to the applied pressure, yielding to different arrangements. DFT-D2 energy tests revealed that collapsed SWBNNTs are energetically favored with respect to their cylindrical counterpart for a threshold diameter value of 3.0 nm. The formation of morphologies different from those of carbon case together with lower collapse cut-off diameter represent a clear signature of the ionic nature of boron and nitrogen.
The analysis of the electronic properties revealed that mechanical folding deformation in BN nanotubes decreases the band gap at the edge cavities, behaving as Type-II homojunction. Furthermore, lower band gap multi-layer nanoarches at edges may similarly act as preferential recombination sites for optical excitation, in analogous to facet edges in larger curved multi-walled nanotubes.
This study highlights the surprising aspect of how local structural deformation can induce strong changes to the physical properties of layered micro-meter sized materials at the macro-scale, suggesting close-edged systems can be promising candidates for applications, in electro-optical tuned devices and even spintronics,.

Chapter4

Raman signature of folded edges

In general, carbon occurs in a plethora of nanoforms, each with different properties depending on its own structural diversity. For this reason, Raman spectroscopy has historically played a predominant role as diagnostic tool for the precise identification and characterization of different types of carbon nanomaterials [121,157,159,281–285]. In general, Raman spectroscopy can give a large amount of information about main properties of sp^2 carbon materials, but its great advantage is the renowned sensitivity in detecting the presence of disorder and distinguishing different types of defect.
Despite available data in experiments, the computational reproduction of Raman spectrum of carbon nanostructures by *ab-initio* techniques represents an ardous task, especially in determining those induced-defect bands usually activated by second-order process and dependent by applied excitation wavelength. A powerful solution is to develop a method able to catch up Raman peaks due to the presence of disorder, taking into account any changes related to applied excitations as well.
After provided a quick introduction about main Raman features, we gauge the performance of our developed "multi-wavelength" method based on Placzek approximation on main carbon nanosystems. All the contents of this part of the current Chapter are included in a paper currently in preparation.
In addition, Raman spectra of circular and collapsed nanotubes have been recorded by our experimental colleagues of CRPP and CEMES Institutes. In paper III, on which second-half of this Chapter is based, we have proven experimentally, and confirmed theoretically that collapsing generates an intense and narrow D band, *despite the absence of any lattice disorder*. Not only that, this result can be harnessed as a basis to revisit the definition of Raman D band and all of those materials comprising structural distortion where poor carbon organization was concluded on Raman basis.

4.1 Raman spectroscopy of graphene based nanoforms

This section is divided in two parts. The first one gives theoretical background information about vibrational modes encountered in graphene. The second section deals an overview of the main findings about Raman spectroscopy of carbon-based on nanostructures with theoretical support provided by Placzek approximation.

4.1.1 Basic knowledge of Raman spectroscopy

The symmetry of a given crystalline structure serves as a basis to define its fundamental vibrational features. In the group theory framework [286], the honeycomb lattice of pristine monolayer graphene is characterized by a hexagonal symmetry which belongs to the space group P6/mmm (D_{6h})[1].

Phonon dispersion and vibrational modes. Both energy and frequency of the quantized vibrations (known as phonons with wavevector $\mathbf{q}$) in graphene can be derived in a similar way to the corresponding electronic structure. The graphene phonon dispersion [287] and associated density of states [288] are shown in Fig. 4.1(a),(b). The kind of motion to which the atoms are normally subjected generates two classes of phonon branches: acoustic (A) and optical (O). In each class, one longitudinal (L) and two transverse (T) are distinguished according to whether the atomic displacements occurs parallel or perpendicular to the wavevector direction. In addition, the transverse branches can be further classified in two sub-categories: in-plane (i) or out-of-plane (o) when the atomic displacements is in or out of the graphene plane, respectively.
The most relevant vibrational contributions come from phonons near Γ and K point, as evidenced in the phonon band structure. All phonon branches and atomic motion are depicted in Fig. 4.1(c),(d) and described as follows [289, 290]:

- At the Γ point ($q = 0$), the wavevector is isomorphic to the point group D_{6h}, to which following six modes are associated: A_{2g}, B_{2g}, E_{1u}, and E_{2g}, with double-degeneration for last two modes (see Fig. 4.1(c)). Among them, only the two E_{2g} modes represent 1^{st}-order Raman active mode of graphene.

- At the K point ($q \neq 0$) the wavevector features a symmetry which belongs to the point group D_{3h} and to which correspond the following six modes: A'_1, A'_2, E', and E'', with double-degeneration for last two modes (see Fig. 4.1(d)). All these modes are Raman active, albeit exhibiting different intensity.

Based on this information, it is possible to characterize spectroscopic bands recorded in experiments by assigning the corresponding phonon branch and atomic displacement, as we discuss in the following.

[1]Even the slightest perturbation breaks the original symmery with remarkable changes on the vibrational properties of interest.

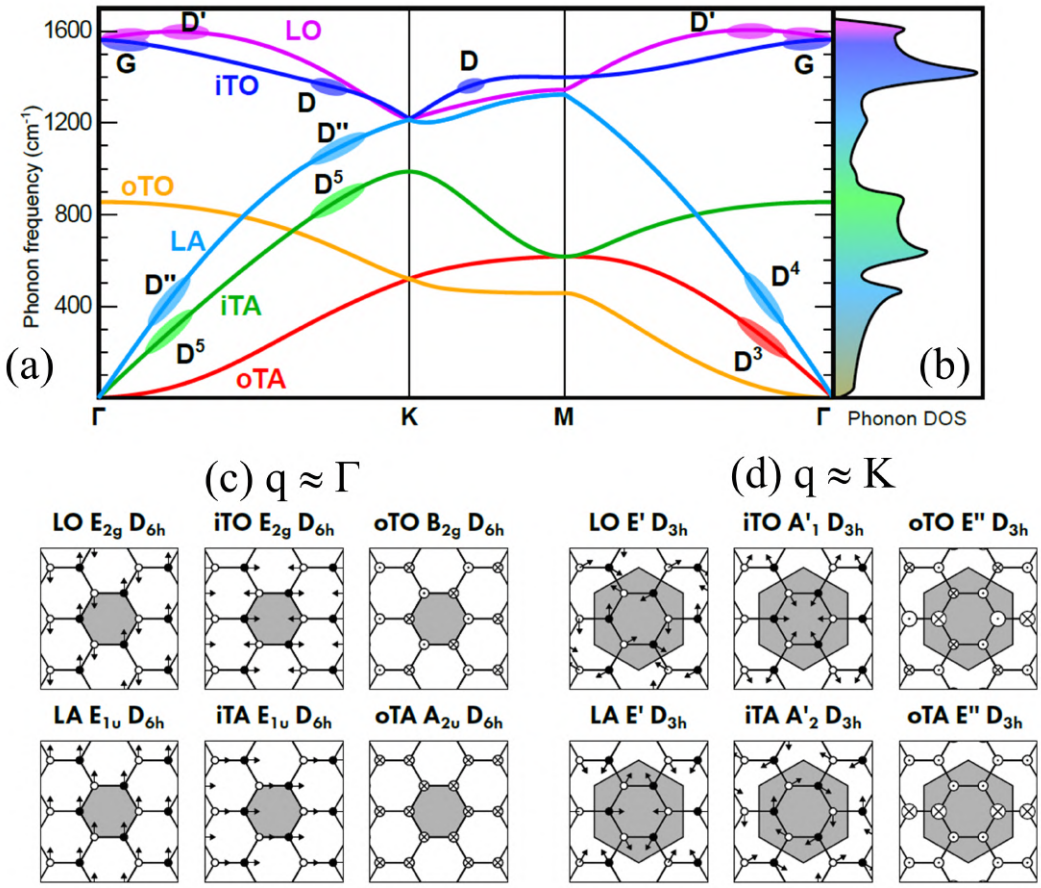

Figure 4.1: (top) Phonon (a) band structure and associated (b) density of states of pristine graphene calculated along the Γ-K-M-Γ path. The phonon branches are labeled according to their type of atomic motion. The contribution of each Raman mode at different phonon frequency is indicated by color. (bottom) Scheme of vibrational modes at wavevectors equal to (c) $q \approx \Gamma$ and (d) $q \approx K$. Each mode is indicated by the wavevector symmetry, the space group and by the type of the associated atomic displacement. Image adapted from [289, 290].

Raman scattering process. In graphene and its related nanostructures, Raman scattering processes are commonly described by perturbation theory [291]. For an n-phonon process involving $n+1$ intermediate states, we derive an $(n+2)$ order matrix element given by the following master equation:

$$\mathcal{M} = \sum_{s_0,\ldots,s_n} \frac{\langle f|\hat{H}_{em}|s_n\rangle \langle s_n|\hat{H}_{ph}|s_{n-1}\rangle \ \ldots \ \langle s_1|\hat{H}_{ph}|s_0\rangle \langle s_0|\hat{H}_{em}|i\rangle}{(\hbar\omega_L - E_n + i\Gamma_n/2)\ldots(\hbar\omega_L - E_1 + i\Gamma_1/2)(\hbar\omega_L - E_0 + i\Gamma_0/2)}, \quad (4.1)$$

where: Γ_k are decay rates of intermediate states where no phonons are present, while $\hat{H}_{em}$ and $\hat{H}_{ph}$ represent the Hamiltonians describing the interactions of electrons with

the electromagnetic field and phonons, respectively. The using of Eq. (4.1) permits to investigate all double-, triple- and even higher-order phonon modes. However, the state-of-the art of Raman for carbon reports spectra with vibration range up to $\sim$3300 cm^{-1}. This means that we can restrict our attention to just single- and double-phonon processes, according to the number of vanishing factors in the denominator of Eq. (4.1). Although there are numerous types of Raman processes occuring in graphene[2], we will examine only those covered in this thesis (see Fig. 4.2):

- G band: it belongs the iTO branch associated to the two E_{2g} vibrational modes, which correspond to the stretching of C-C bonds. This band is defined as a single-phonon process, where a non-resonant electron-hole pair is scattered by a low-wavevector phonon near Γ ($q \approx 0$)[3] (see Fig. 4.2(a)) [289, 290]. The peculiarity of this Raman feature - appearing at 1582 cm^{-1}, is the capacibility to probe any modifications of the flat graphene plane, for which its original symmetry results broken in response to external perturbations, such as strain, doping, temperature, substrate interaction and so on [121].

- D band: it belongs the iTO phonon branch corresponding to the A_1' vibrational modes near the corners of the 1^{st} Brillouin zone. This band is generated by a second-order phonon process, in which a resonant electron-hole pair is initially scattered by a phonon (with finite wavevector $q \neq 0$) from the K Dirac cone to the K' Dirac cone and then back-scattered by a defect that ensures momentum conservation (see Fig. 4.2(b),(c)) [290]. Such mechanism is mainly known in literature as double resonance process. In addition, since this scattering process occurs between two nonequivalent Dirac cones is called intervalley [282,292]. This band usually appears at around 1350 cm^{-1} for laser excitation of 2.41 eV.

- D$'$ band: the double resonance mechanism giving rise the D$'$ band in a similar way to the D one but with two relevant differences. First, it belongs the LO phonon branch associated to the E$'$ vibration modes, occurring near the center of the 1^{st} Brillouin zone. Second, its finite wavevector is much shorter than the one to the D band. This means that the resonant electron-hole pair is scattered by the phonon from one eigenstate to another belonging to the same Dirac cone rather than two distinct ones (see Fig. 4.2(d),(e)) [290]. For this reason, the scattering process here involved is called intravalley [282, 292].

[2]For a wide overview on all different Raman processes encountered in vibrational spectra of carbon nanomaterials, one can refer to A. C. Ferrari and D. M. Basko. "Raman spectroscopy as a versatile tool for studying the properties of graphene". *Nat. Nanotechnol.* **8** (2013), pp. 235-246 [282].

[3]This condition is sometimes referred also as the *fundamental Raman selection rule* and it is valid for those materials with following requirements: preserved original symmetry and nul wavevector.

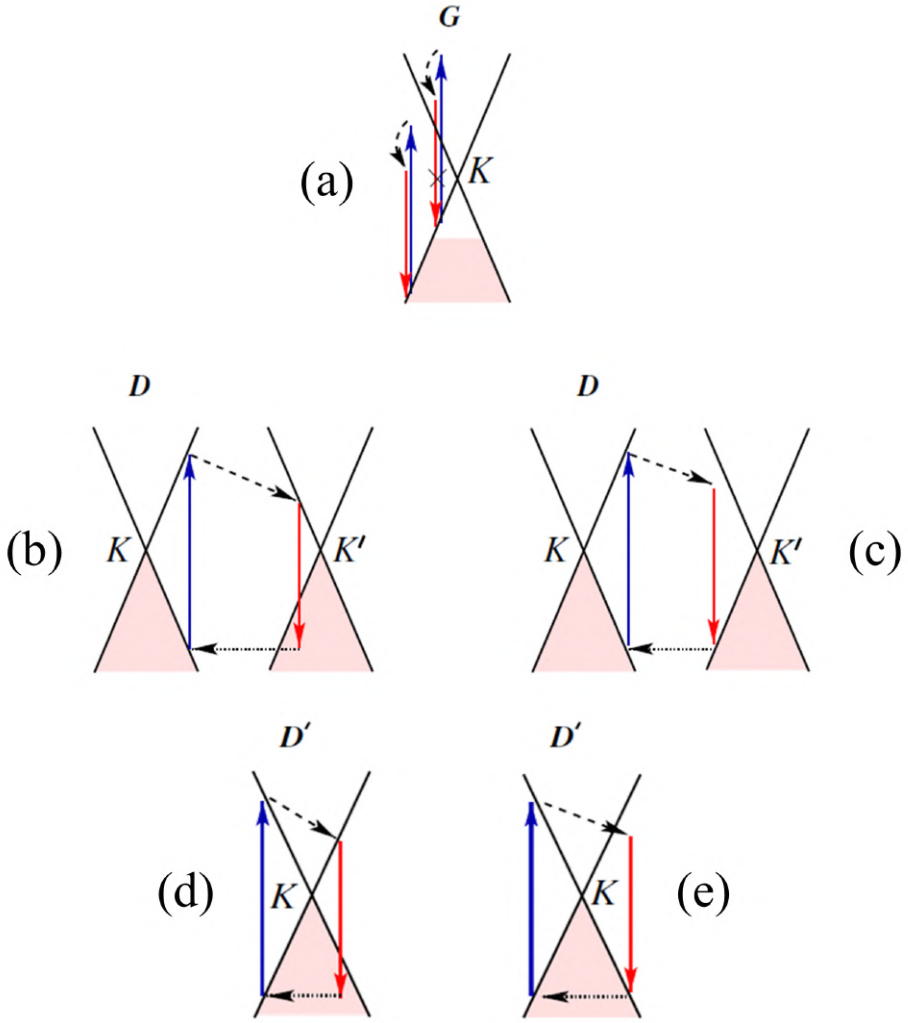

Figure 4.2: Schematic representation of Raman scattering processes in graphene which determine the (a) G band, (b,c) D band, and (d,e) D′ band. Electron dispersion is indicated by black solid lines, where shaded areas represent the occupied states. Photon absorption and emission are blue and red lines, respectively. The processes of intraband transitions accompained by phonon emission and the electron scattering on a defect are indicated by dashed and horizontal dotted lines, respectively. Image adapted from [282].

Both inter- and intravalley processes are further distinguished in outer (see Fig. 4.2(b),(d)) and inner (see Fig. 4.2(c),(e)) depending on the crossing or not of Dirac cones, respectively.

Energy laser dependence. A really intriguing feature of the Raman spectrum of graphene-based on nanostructures is their dependence of peak positions on the laser

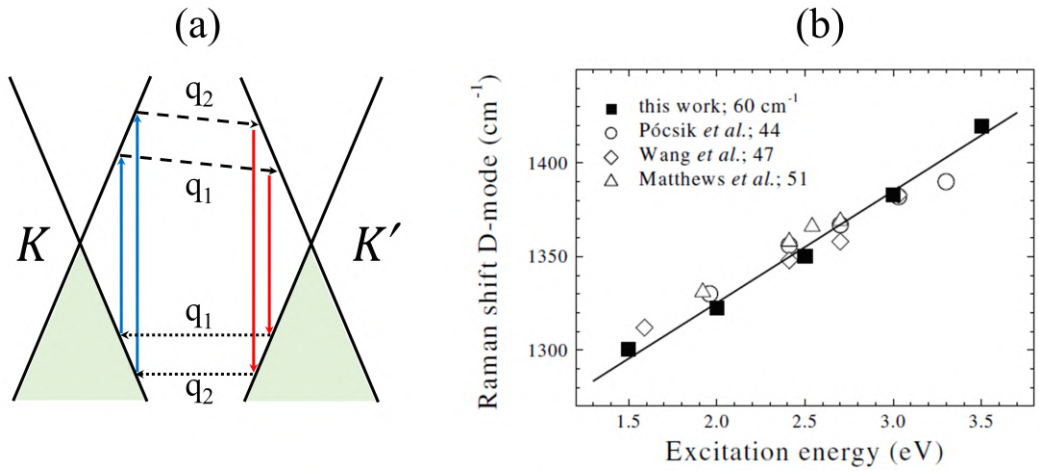

Figure 4.3: (a) Scheme of laser excitation energy dependence on scattering process for D band. (b) Measured and calculated shift of the D band as effect of laser power. The open symbols correspond to experimental data, while the closed square to the calculated phonon energies in double resonance. The line is a linear best of the theoretical values with a slope of 60 cm^{-1}, confirming that the D band activation is mediated by double resonance mechanism. Image (b) adapted from [294].

source that induces Raman scattering. Every Raman band of graphene, except G band, shows a significant dispersion of its peak position as a function of excitation laser energy E_L.

This feature is particularly strong for the disorder-induced D band. The origin of that dispersive behavior for the D band has been a focus of long discussions with various interpretations. Initially, this feature has been attributed to the dependence of k-selective rule on the electronic transition inducing the resonance [293]. In the end, Thomsen and Reich proposed a model, in which double resonance processes are responsible for this particular character [294]. In general the photon energy satisfying the double resonance condition can change by varying E_L, since the corresponding intermediate states s_k - previously introduced in Eq. (4.1), are determined for given E_L. As illustrated in scheme of Fig. 4.3(a), when the laser energy increases, the optical absorption occurs at k point away from the energy minimum of the conduction bands. Then the wavevector q that satisfies the double resonance condition becomes large and hence corresponding phonon energy $\hbar\omega_1(q_1)+\hbar\omega_2(q_2)$ changes along the phonon dispersions. It was found that the D peak position of graphitic systems exhibits a linear correlation with the incident excitation energy characterized by a slope of 60 cm^{-1}, which is in excellent agreement with experimental results referred to in Ref. [294].

Thus, the general rule is: if the Raman spectrum of a given carbon nanomaterial exhibits peaks, whose position is laser energy dependent, then they represent a distinct signature of induced disorder in the system. Both the origin of the D band

and its dispersive character can be explained by double resonance mechanism. These phenomena make Raman spectroscopy the most sensitive technique to better detect and identify disorder in sp^2 network of different carbon nanomaterials.

4.1.2 Performance of Placzek approximation

Below, we address the accuracy of the *ab-initio* method based on Placzek approximation[4] that we have implemented to a program, investigating Raman spectroscopy of main carbon nanoforms by comparison of the simulated spectra with those recorded in experiments.

Computational details. All DFT computations are made with AIMPRO code. The GGA functional by PBE formalism is used to describe the exchange-correlation effects. The vdW forces are added by Grimme D2 scheme. Wave functions are expanded in terms of Gaussian *pdpp* and *pdddp* basis sets, which give 22 and 38 independent functions in total, respectively. While hexagonal unit cells are used to contain infinite graphene sheet, fullerene (C_{60}) molecule, and circular SWCNTs, we simulated hydrogenated-edge graphene nanoribbons by orthorhombic unit cell. All structures and axial lattice vectors allowed to fully relax without any simmetry constraint. Reciprocal space is sampled by $4 \times 1 \times 1$ ($4 \times 4 \times 1$) grid mesh for nanotubes and nanoribbons (monolayer graphene) with origin at Γ point. Only fullerene molecule is relaxed using homogeneous $1 \times 1 \times 1$ k-point grid. Vacuum space is large enough (at least 20 Å) to avoid interaction with periodic replicas. Vibrational frequencies are determined by calculating energies and forces for ± 0.106 Å atomic displacements. Phonon calculations used the second derivative of the energy with respect to atomic the positions i and j, $\partial^2 E/\partial R_i R_j$, using a finite difference scheme of the derivatives from the calculated forces. The dynamical matrix is constructed as $\mathrm{E}_{ij}/(\mathrm{M}_i\mathrm{M}_j)^{0.5}$, where M_i and M_j represent the masses of the i_{th} and j_{th} atoms, respectively. After that, we displaced the equilibrium structures along the eigenvectors of each phonon mode and calculate the energy-dependent dielectric function derivative with respect to atomic displacements. To evaluate dielectric functions, we used a dense $360 \times 1 \times 1$ ($360 \times 360 \times 1$) k-point grid for nanotubes and nanoribbons (monolayer graphene). All of these calculations are carried out with high convergence tolerance for self-consistency (10^{-10} Ha). Resulting matrix elements are multiplied by phonon eigen-displacements to obtain Raman tensors. The latter components have used to determine Raman intensities. The Raman spectra of fullerene is calculated using Eq. (2.24), while those of periodic systems are obtained through Eq. (2.25), where incident and scattered light polarization are averaged in all in-plane directions. We applied a Lorentzian broadening of the peaks in all configurations.

[4]See Chapter 2 for details in Placzek approximation.

4.1.2.1 Raman features of carbon nanoforms

Fig. 4.4 shows a collection of computed Raman spectra from main types of sp^2 carbon nanoforms at an excitation energy equal to 2.3 eV. Notice that the G-band is a common feature for graphene and semiconducting zig-zag (11,0) SWCNT cases. While monolayer graphene exhibits only the G peak corresponding to the two degenerate E_{2g} modes in iTO phonon branch, in the case of nanotube this degeneracy is removed and consequently the G band is split in two sub-bands, namely G^+ and G^- at 1575 cm^{-1} and 1580 cm^{-1}, which are associated with vibrations around the circumference and along the axis of the tube, respectively. These atomic displacements resemble the E_{2g} modes in iTO and LA phonon branches, respectively. This difference between graphene and carbon nanotube can be attributed to an effect of the curvature[5]. Nonetheless, our resulting G band positions appear slightly lower than those recorded in experimental spectra.
Another distinct feature of (11,0) nanotube finds in the low frequency region, which corresponds to the radial breathing modes (RBM). In our calculations, the most intense RBM mode is located at 252 cm^{-1}, which falls within experimental range, typically between 100 and 300 cm^{-1}. The importance of this other class of vibrational modes is threefold [121]: (*i*) the determination of the nanotube diameter; (*ii*) the understanding of interactions between tubes involved in multi-walled and bundle configurations; (*iii*) the chirality dependent correlation between frequency and optical transition energies within resonance regime that reveals a great deal of information, such as σ-π hybridization and excitonic effects [121, 295].
Notice that both graphene and (11,0) carbon nanotube do not show the presence of the D band given the absence of defects, as expected. In order to better explore the D band behavior, we re-calculated the Raman spectrum of (11,0) nanotube after the introduction of a single vacancy, giving one pentagon and an octagon. Interestingly, the removal of a single atom breaks the initial tube symmetry with consequent activation of a new weak defect-induced normal mode at 1360 cm^{-1}. This result demonstrates that: although the D band is due to the intervalley double resonance process using perturbation theory, our calculation approach based on semiclassical approximation is however able to successfully simulate this point-defect induced mode.
Contrary to graphene and nanotubes, it was found that C_{60} molecule exhibits distinct Raman features. Our simulated spectrum highlights a very intense peak compared to others, which rises at 1480 cm^{-1}. This peak corresponds to the $A_g(2)$ mode and its high intensity is due to the vibronic coupling which enhances the intensity as effect of increasing laser power [296]. This band can be harnessed as a probe of the coupling between molecule and its environment. In addition, the peak at 486 cm^{-1} belongs the $A_g(1)$ mode, while all other visible modes represent the H_g modes [296].

[5]The G band splitting occurs in graphene under strain likewise.

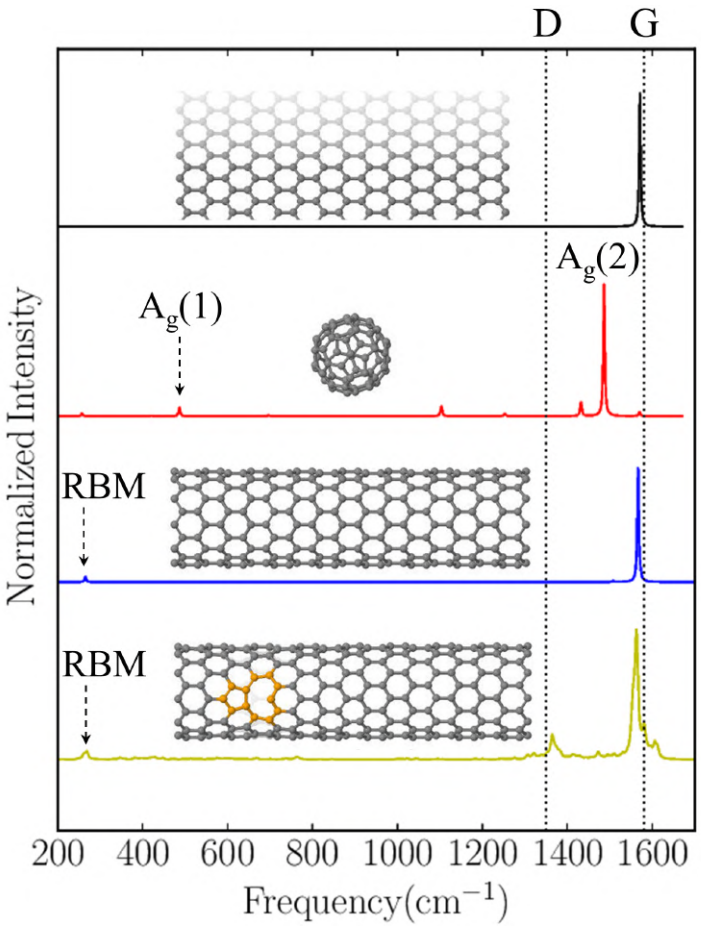

Figure 4.4: DFT-D2 calculated Raman spectra of different carbon-based on nanostructures: monolayer graphene (black solid line), fullerene (red solid line), single-walled (11,0) carbon nanotube without (blue solid line) and with (orange solid line) point defect. Insets show the geometries of examined systems. Vertical dashed lines represents positions of D and G peaks given in experiment [121]. Vertical arrows indicates uncommon weak peaks, like the RBM and $A_g(1)$ modes for nanotubes and fullerene, respectively. All spectra are simulated at excitation energy equal to 2.3 eV (538 nm).

4.1.2.2 Induced disorder by graphene edges?

Besides vacancy detection, it is known that disorder characterization depends on the specific defect into the system under analysis.
Thus, the next step is to examine the disorder induced by different defects in order to further test the robustsness and sensitivity level of our method. To this end, we made a detailed computational Raman investigation of graphene sheet with edges oriented at two different crystallographic directions: armchair and zig-zag.

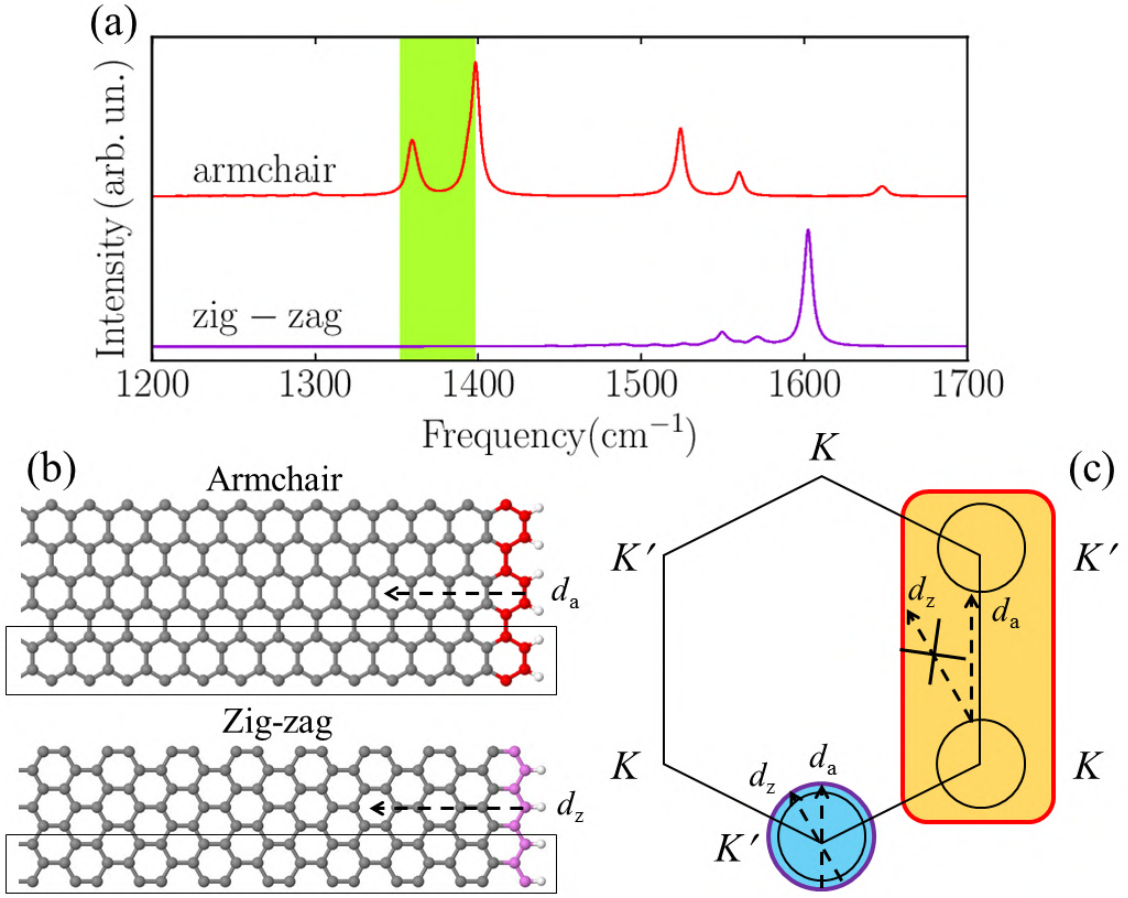

Figure 4.5: (a) DFT-D2 calculated Raman spectra of different armchair (red line) and zig-zag (purple line) GNRs. Both spectra are simulated at excitation energy equal to 2.3 eV (538 nm). Incident and scattered light polarization are averaged in the ribbons plane. Green shaded section is the region where the D band usually finds. (b) Optimized geometry of both graphene ribbons in super cell approximation, where color balls represent two atomic edge arrangements in play: armchair (red) and zig-zag (purple). The unit cell used for Raman computations is indicated by black solid rectangle. Only half width is shown here for clarity. The direction of exchanged momenta for electron back-scattered by armchair (d_a) or zig-zag (d_z) edge are represented by horizontal dashed arrow. (c) Schematic illustration of 1^{st} Brillouin zone, showing the intervalley process of the double resonance mechanism: only the exchanged momentum from armchair edges can connec two Dirac point (K and K') belonging to nonequivalent cones.

In this context a computationally convenient atomistic approach adopted to study graphene-edge related effects, is to use graphene nanoribbons. A primitive unit cell is used for the zig-zag case, while the supercell is doubled along the periodic axis for the armchair ribbon, as depicted in Fig. 4.5(b). The zig-zag GNR is 8.38 nm wide,

while the armchair one 10.55 nm.
As discussed in Chapters 1 and 3, GNRs are of particular interest since their edge orientation determines the electronic properties: while zGNRs are metallic conductors, the acGNRs show size-dependent energy gap. Thus, the following questions then arise: (1) "*Can graphene edges be considered as activation source for disorder?*" and (2) "*Is it possible to spectroscopically differentiate between these two edge arrangements in play?*".

1. Fig. 4.5(a) compares calculated Raman intensities of armchair and zig-zag ribbons. In addition to the G band, we can observe the presence of other bands. This result suggests that graphene edges can be viewed as extended (1D) defects that break lattice symmetry. Indeed, σ bonds and on-site energies of edge carbon atoms differ from those in the central region of the ribbon.

2. A closer look at the simulated Raman spectra (Fig. 4.5(a)) shows that in the ordered armchair edge there are two visible peaks at 1365 cm^{-1} and 1380 cm^{-1} within the frequency region attributed to the D band, while they are absent in the zig-zag case. This difference is a consequence of the momentum conservation [297]. We learned that the activation of the D band is mediated by intervalley process, which requires: (*i*) a defect with momentum exactly opposite to the phonon momentum and (*ii*) back-scattering. However, as illustrated in Fig. 4.5(b), the wavevector direction of electrons back-scattered is perpendicular to the edges, and thus the direction of corresponding momentum changes depending on the type of edge arrangement: armchair (d_a) and zig-zag (d_z). Fig. 4(c) represents the 1^{st} Brillouin zone of 2D graphite, showing the scheme of the intervalley process, where circles centered at the Dirac points are formed by all electron wavevectors involved in the scattering process in play. We note that the armchair d_a vector follows the K-K' path satisfying the key requirement of the intervalley process, i.e. the connection between two inequivalent Dirac cones. For the zig-zag case, we find the opposite situation, since that d_z vector is directed along K-K path and hence cannot reach the point belonging to circle centered at mirror Dirac cone. Furthermore, the circle radius defined by incident light (2.3 eV in our case) is not large enough to allow the connection required for the intervalley mechanism. This explains why we have no induced-disorder D peak in the perfect zig-zag edge, while we can obtain modes potentially attributable to the D band near ordered armchair edges. Our results are further supported by real space model developed by Casiraghi and co-workers [298].
   In order to identify the two peaks of the armchair ribbon at lower frequency region, we re-simulated its spectrum as a function of the excitation energy in 1.0-3.0 eV range (see Fig. 4.6(a)). While the first peak at 1365 cm^{-1} for 1.0 eV shows little dependence only at highest excitation energies, the position of the

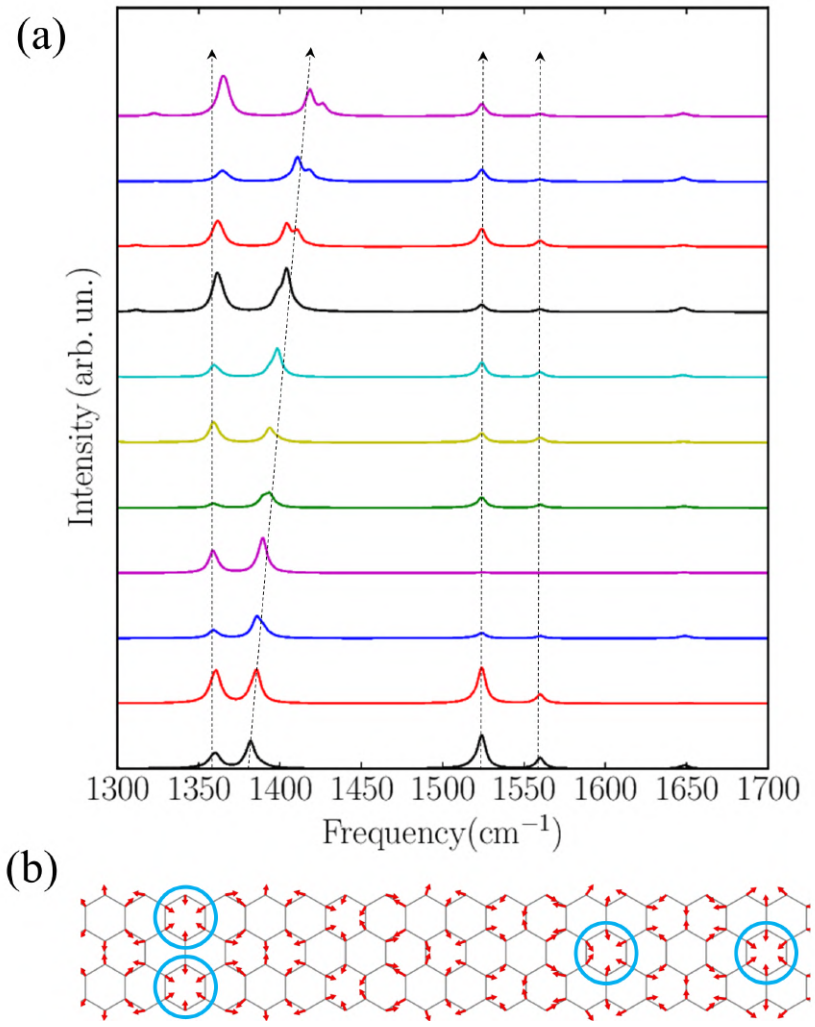

Figure 4.6: DFT-D2 calculated Raman spectra of armchair GNR by changing the excitation energy. Incident and scattered light polarization are averaged in the ribbons plane. Shifts of the peak positions are marked by dashed arrows. (b) Representation of eigen-displacements in graphene ribbon plane, where A_1' modes typical of the iTO phonon branch belonging to the point group D_{3h} are indicated by purple circles.

next one remarkably shifts towards higher frequencies by increasing the laser source. Following the logics of double resonance mechanism, our excitation energy dependent peak would correspond to the D band. In order to double-check the last statement, we plotted the atomic displacements along ribbon plane for the second peak, showing the breathing of carbon hexagons belonging to the iTO phonon branch in vicinity to the K point, which are known to participate in defect-assisted D band of graphene. Thus, although the found mode

cannot be called 'D band' properly, since our calculation approach takes no account of double resonance processes, it qualitatively exhibits the same features of the D band, i.e. dispersive character and typical atomic motion of iTO branch near Dirac point. This result refutes the conclusions of Ruffieux and colleagues, for which Placzek approximation cannot predict the laser energy dependence of disorder-induced modes [164]. The reason why their Placzek computed spectra no show any dispersion by changing the excitation energy can be attributed to ultra-narrow width of the ribbons. More importantly, our findings are in excellent agreement with recent Raman measurements made on GNRs [299, 300].

In summary, our calculation method based on semiclassical Placzek approximation using the first order derivative of polarizability is able to detect and distinguish different defects from one another. Thus, the next purpose is to apply this approach to characterize the main focus of this thesis, i.e. edge folds.

4.2 Defect-free D band of collapsed nanotubes

While self-collapse is very common in carbon nanotubes and its role in defining the ultimate electronic and transport properties has been experimentally proven, little is known about its Raman signature. In this section we report a detailed multi-wavelength Raman characterization of fully collapsed CNTs integrated by *ab initio* simulations via Placzek approximation. The goal is to unravel the distinct Raman feature of curved closed edges so we can expand our knowledge regarding defect quantification in the field of carbon nanomaterials.

4.2.1 Experimental results

Fig. 4.7(a) shows TEM image of a collection of fully collapsed carbon nanotubes (blue arrows) obtained using Choi's method [98], i.e. sonication-based on extraction of inner tubes from large-diameter MWCNTs (orange arrows) in solution[6]. Only one sample exhibits a 'partial' extraction (red arrow), having both uncollapsed (right) and collapsed (left) morphologies. The resulting values of flattened nanotube width ($W \sim 7nm$) and original MWNT diameter ($D \sim 5nm$) for latter objects are consistent with collapse deformation relation: $W \approx \pi D/2$ [98]. Our simulated TEM image shows the formation of collapsed nanotube through the extraction of large-diameter tube from multi-walled sample (see inset of Fig. 4.7(a)). This image

[6]Full explanation about sample preparation and structural characterization is reported in Supplementary Information of Paper IV: E. Picheau, A. Impellizzeri, D.V. Rybkovskiy, M. Bayle, J.-Y. Mevellec, F. Hof, H. Saadaoui, L. Noé, A. C. Torres-Dias, J.-L. Duvail, M. Monthioux, B. Humbert, P. Puech, C.P. Ewels and A. Pénicaud. "Intense Raman D band without disorder in flattened carbon nanotubes". *ACS Nano*, *accepted* (2020).

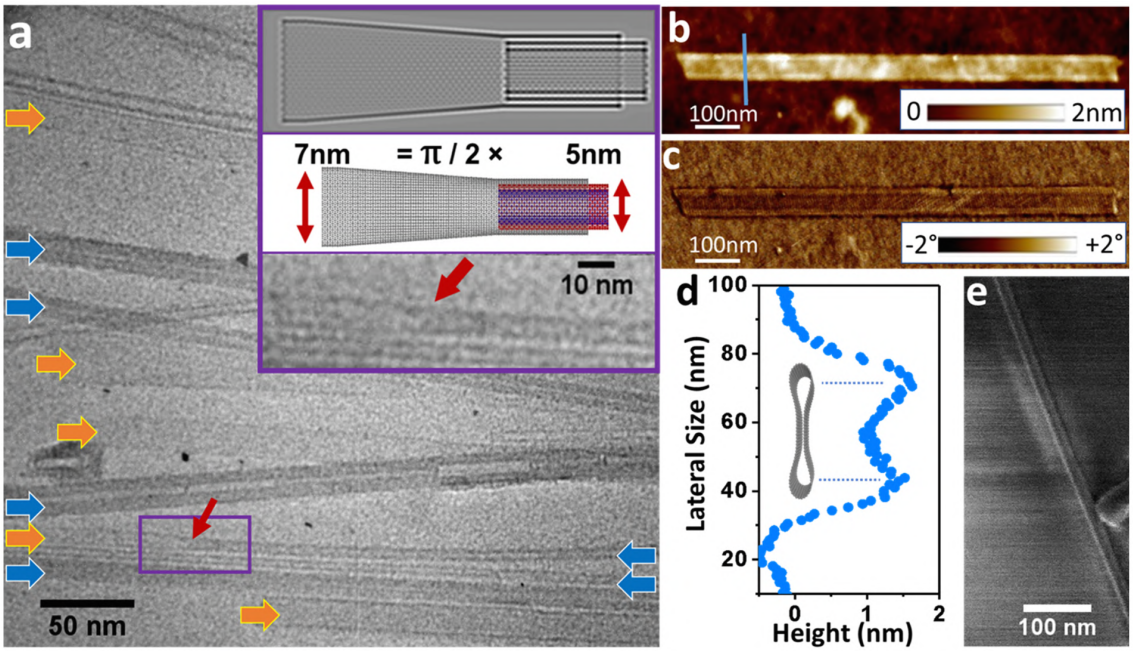

Figure 4.7: (a) TEM image showing MWCNTs (blue arrows) and FCNTs (orange) arrows operated at 100 kV voltage. The inset shows: (bottom) the collapse from a circular multi-walled tube (right) to a flattened one (left), indicated by a red arrow. (middle) AIREBO optmized representation of the extraction/sonication effect on the opened multi-walled nanotube. (top) Simulated TEM image showing collapse of outer tube after sonication. (b,c) AFM height and phase of a FCNT deposited on a substrate composed by a silicon wafer with 300 nm and SiO_2 layer. (d) AFM height profile along blue line in (b) and scheme of flattened cross-section. (e) SEM image of a FCNT on a Si wafer. Image taken from Paper III.

has been obtained using QSTEM software package [301] at 100 kV with spherical aberration 1.9 mm, defocus set to Scherzer value -97.7 Å and convergence angle of 23.5 mrad. These simulation conditions are chosen to be consistent with its own experimental counterpart. The architecture of grown flattened carbon nanotubes is further confirmed by atomic force microscopy (AFM) images in height and phase (see Fig. 4.7(b),(c)) together with longitudinal scheme provided by corresponding height profile (see Fig. 4.7(d)). Not only that, the collapsed cross-sectional shape is also visible with SEM (see Fig. 4.7(e)).
Our colleagues clearly identified two sets of chiral nanotubes with distinct circular and flattened morphology on the basis of their AFM heights: below 3 nm and above 5.8 nm, respectively (see Fig. 4.8(a)). There are three tubes in total for each set and they are labelled as follows: CNTs for multi-walled samples, while FCNTs indicates flattened ones. In addition, numbers 1, 2 and 3 are assigned to their AFM height profile.

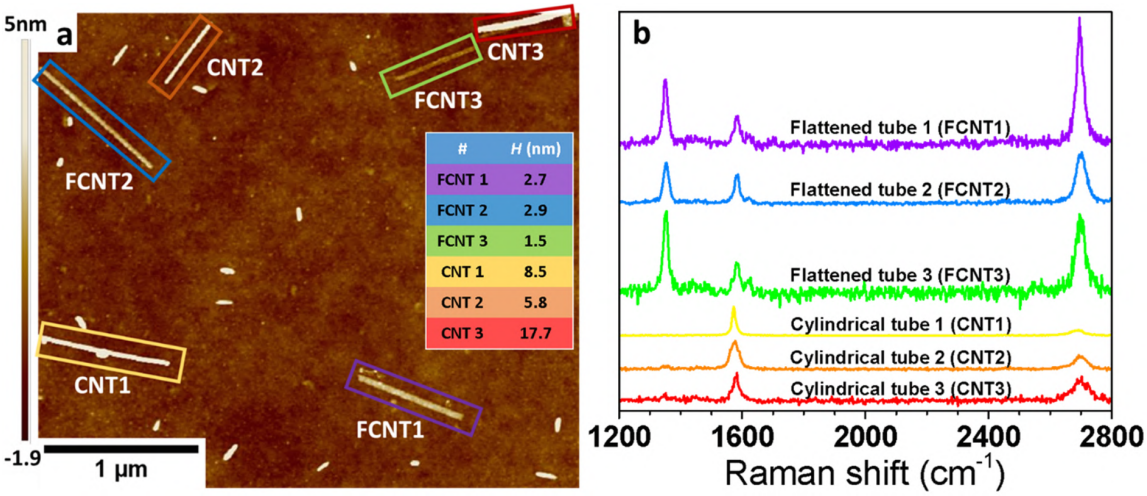

Figure 4.8: (a) AFM image of 3 circular (CNT) and 3 flattened (FCNT) nanotubes. Inset shows their respective heights H (nm). All values are recorded using a single tip. (b) Corresponding Raman spectra normalized over the G peak ($\sim$1580 cm^{-1}), recorded at 514 nm (2.41 eV) with incident light parallel to the axial axis of FCNT1. Image taken from Paper III.

We next used Raman spectroscopy to characterize the two nanotube species in play in order to highlight properties in common and others that differ (see Fig. 4.8(b)). Although the spectra of of CNTs and FCNTs are both characterized by the presence of the G ($\sim$1580 cm^{-1}) band, there are two remarkable differences:

- the assisted-defect D and D$'$ bands are nearly absent for circular nanotubes, while we can note their presence in FCNTs at $\sim$1350 cm^{-1} and $\sim$1620 cm^{-1}, respectively. In particular, the D band exhibits very high intensity.

- the 2D ($\sim$2700 cm^{-1}) band of circular tubes have much lower intensity and broader than corresponding flattened counterpart.

The absence of the induced-disorder bands in circular nanotubes is a clear evidence of their high level of purity, due to the preparation method based on arc-discharge. To be sure about the identity of the band at $\sim$1350 cm^{-1} for FCNTs, we performed multi-wavelength measurements, obtaining a linear frequency shift of $\sim$60 cm^{-1}/eV, which is typical for double resonance processes in disordered graphitic materials. Thus, the peak observed at $\sim$1350 cm^{-1} corresponds to the D band. But, we know that circular and collapsed nanotubes come from the same solution. This means that the negligible defect concentration for circular tubes is expected to be similar in collapsed samples and it is supported by the bandwidth of the D peak, which is narrow (full width half maximum $\sim$18 cm^{-1}) in comparison to more conventional defect-driven D band. Since the appearance of the latter peak in nanotubes with

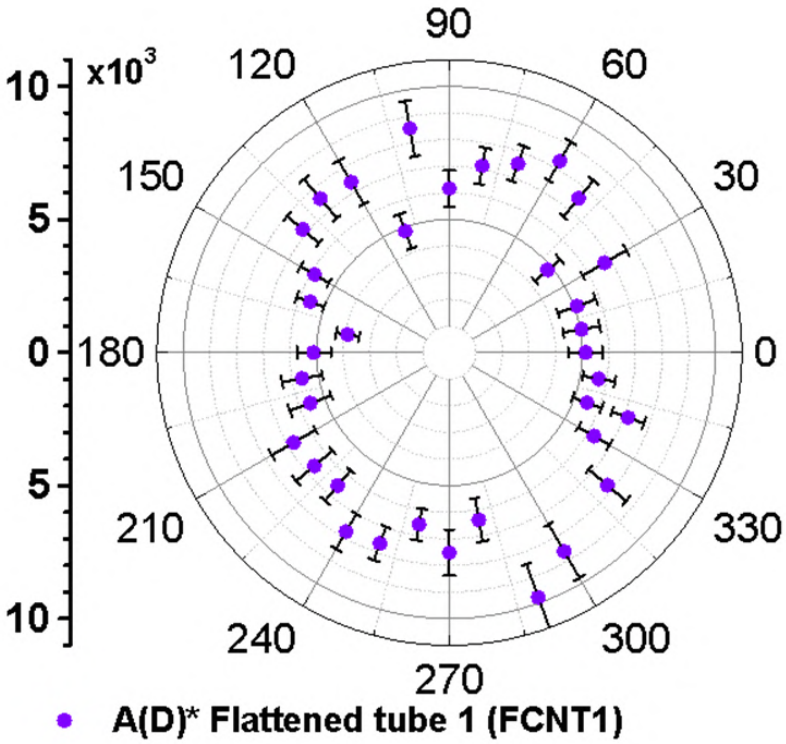

Figure 4.9: Polar plot of the D band as a function incident polarization for FCNT1 sample at 2.33 eV (532 nm). The incident light polarization is set along the 90°-270° axis, while the object is rotated of an angle α. Thus, the angle $\alpha = 0°$ corresponds to a situation where FCNT1 is orthogonal to the light polarization, while $\alpha = 90°$ represents a situation in which the tube in play is parallel to the incident light. Image taken from Paper III.

collapsed shape cannot be attributed to the presence of local structural defects, the question then arises: "*What is the activation source of this intense band in a high clean system, like collapsed nanotube?*".
A number of consistent analysis, thoroughly described in Paper III, have demonstrated the D peak activation in collapsed CNTs is due the presence of strained edge cavities:

- Fig 4.9 shows the polar plot of D band intensity for FCNT1 sample for different incident polarization at 2.33 eV (532 nm). The nanotube surface is rotated in steps of 10°, while the incident laser polarization is kept fixed along the 90°-270° axis. The D band is strongest for polarization parallel ($\alpha = 90°$) to the edge cavities ($\alpha = 90°$) and minimum for perpendicular ($\alpha = 0°$). Like GNRs, the appearance of the D band in FCNT is mediated by intervalley

process, which means that when an electron collides with the edge cavity, it must be scattered backward perpendicularly to the edge interface. This condition is reached when incident light is parallel to the cavities at $\alpha = 90°$. On the contrary, the electron back-scattering cannot be obtained when the light polarisation and the cavities are orthogonal for $\alpha = 0°$.

- Following the simple model proposed by Cançado and co-workers [302], we estimated the ratio between D and G peak intensities in order to determine the nanotube area responsible to the activation of the D band, as follows:

$$\frac{I_{\mathrm{D}}}{I_{\mathrm{G}}} = C_a \left(\frac{4r_a}{W} \right), \tag{4.2}$$

where: C_a represents a proportionality factor linking to the intensity ratio with the total fraction of this area, while r_a is the radius of the structurally disordered area caused by the local edge curvature. For the FCNT1 sample with r_a= 3 nm and W= 30 nm, we obtain $\frac{I_{\mathrm{D}}}{I_{\mathrm{G}}} = 2.2$ where $C_a \approx 5.5$. The resulting C_a value is larger than that obtained for a point defect [302], clearly showing that the whole D band for FCNTs is activated by localized curvature at the edges and does not come from any other structural defect.

These findings clearly indicate that the activation of an intense and narrow defect-free D band in Raman spectra of FCNTs is induced by scattering processes associated with edge cavities. The appearance of the D band in 'pristine' collapsed SWCNTs is confirmed by simplified atomistic model based on DFT calculations, which are described in detail in the next section.

4.2.2 DFT calculations

The key ingredient extracted from the experimental Raman investigation of collapsed carbon nanotubes is the high intensity of their D band, which is activated by the phonon assisted-electron backscattering perpendicular to the edge cavities within intervalley process. However, the full evaluation of double resonance process is currently limited to small-size systems [303], and for systems composed by hundreds of atoms like collapsed SWCNTs is inaccessible with conventional computational resources. Given promising results obtained for more standard carbon nanomaterials, calculations based on semiclassical Placzek approximation would constitute a reliable alternating approach to study the D peak activation in carbon nanotubes with collapsed shape.
We computed Raman spectra of different collapsed tubes in order to figure out how tube cavities induce the emergence of the D peak and even the possible factors that can affect its behavior such as lattice registry and substrate coupling. Both structural optimization and vibrational properties (phonons and dielectric function derivatives) of collapsed SWCNTs are calculated with the same conditions already

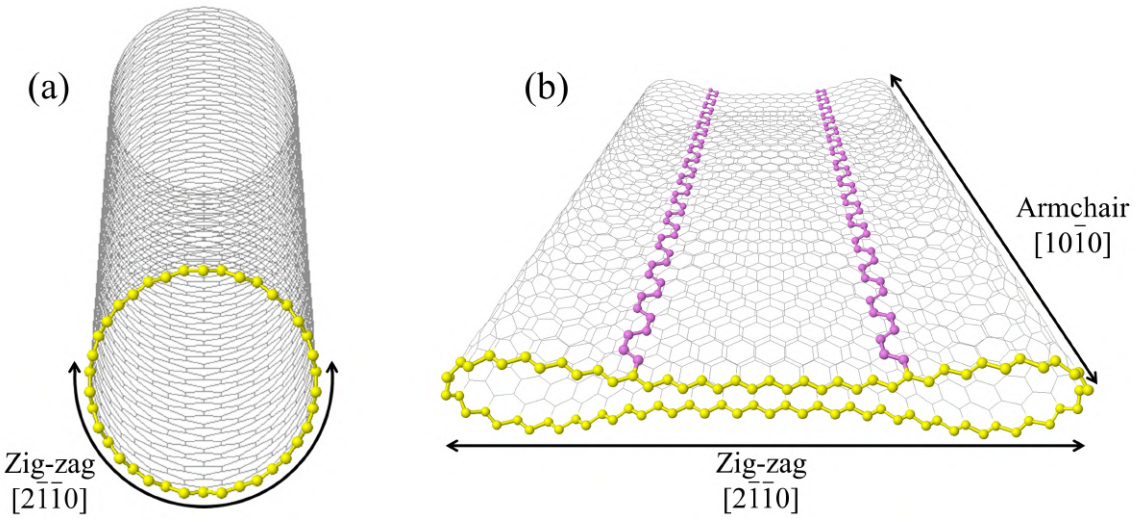

Figure 4.10: DFT-D2 optimized geometries of (yellow balls) zig-zag (a) circular and (b) collapsed CNTs, where the latter shows the (purple balls) armchair line of hybridization change as an analog of GNRs. Image taken from Paper III.

used for GNRs.
Before showing spectra of our interest, it is useful to specify a particular detail concerning the nomenclature used to label collapsed nanotube chirality which might otherwise be confusing. It is widely known that circular CNT type (zig-zag, armchair, and chiral) refers to the arrangement of carbon atoms around the tube circumference (see Fig. 4.10(a)), while GNR notation refers to the atom arrangement along the edge length. Given FCNTs are usually defined as hybrid systems between the previous two configurations, we follow the circular nanotube notation and hence, for example, a zig-zag FCNT has carbon atoms in the zig-zag orientation around its radially deformed circumference and also the armchair orientation along its length (see Fig. 4.10(b)).

4.2.2.1 Achiral collapsed nanotubes

Fig. 4.11(a) plots the Placzek Raman spectrum of AB′-stacked collapsed zig-zag (70,0) SWCNT calculated at 2.3 eV excitation energy, exhibiting interesting features. First of all, the spectrum has two main peaks at frequencies 1371 and 1564 cm^{-1}. By looking atomic displacements, we note that the peak at 1371 cm^{-1} corresponds to the A_1' modes associated with the iTO phonon branch near the K point of the 1^{st} Brillouin zone. These phonons are known to participate in the defect-induced D band of graphene [289,290]. In the case of zig-zag FCNTs, the armchair-edges can be seen as extended defects, breaking lattice symmetry and coupling these phonons to the electronic structure, resulting in the modulation of the dielectric function. The frequency of this peak is overestimated, because semi-local DFT functionals tend

to overestimates iTO phonons near the K Dirac point [304]. The high-frequency peak at 1564 cm^{-1} is associated with C-C bond stretching along the tube longitudinal axis, and is interpreted as the G band. In addition, we find a smaller peak at 1603 cm^{-1} that arises from transversal displacements, whose intensity is modulated along the circumference of the nanotube. This modulation, if considered in terms of graphene phonon structure, points out at their non-zero wavevector character. Its high frequency value, together with the above-mentioned modulation allow attribution of this peak to the iLO phonon branch at the Γ point corresponding to the D$'$ band of defective graphene.

Fig. 4.11(b) shows the Raman spectrum of AB-stacked collapsed armchair (50,50) SWCNT calculated at the same excitation energy of the previous case. The main difference, when compared to the results for the zig-zag tube is the absence of peaks in the D band region. At the same time, the Raman signal in the G band region for the armchair case is more complex, consisting of multiple peaks. The strongest peak arises from two vibrations at 1558 and 1560 cm^{-1}. The first is associated with transverse vibrations, mainly localized at the cavities of the collapsed tube, while the second consists of longitudinal vibrations coming from the flat region. The higher frequency peaks correspond to transverse vibrations with different degree of modulation and can be interpreted as D$'$ peak components.

Our results highlights that the D peak activation depends strongly on the fold orientation at the edge of collapsed nanotubes, which can be explained as follows: in FCNTs, both electronic and vibronic levels can be considered as "zone-folded" states of a perfect monolayer graphene, which allows the coupling of finite wavevector phonons of graphene with the electronic states around the K point, depending on the tube geometry. For zig-zag FCNTs the zone-folding in exact mapping in the Γ-K direction of the monolayer graphene reciprocal space to the Γ-point of the 1D FCNT cell. This permits the coupling of the iTO phonon branch with to the electrons around K and K' valleys, resembling the intervalley scattering process. Changing the chiral vector direction induces a rotation of the graphene Brillouin zone with respect to the periodic axis of the collapsed nanotube. For armchair FCNTs results in the disappearance of the D band signal, because the electron-phonon coupling between two nonequivalent valleys cannot be reached. But on the other hand, we detect the presence of the normal modes typical of the D$'$ band for both zig-zag and armchair oriented edge folds, since the iLO phonons can connect with electrons around points belonging to two equivalent Dirac cones: K-K.

These results qualitatively confirm that the D band for collapsed CNTs is caused by the symmetry breaking in the system imposed by the folded edge rather than by structural defect-induced scattering. Note only that, the fold orientation dependence of D peak activation resembles the edge-scattering selection rules previously observed for different arrangament of GNRs [297, 298]. This further demonstrates that collapsed nanotube can be recognized as an analog of closed-edges bilayer graphene ribbons [81,154], with the main exception that edge cavities of FCNTs does not cre-

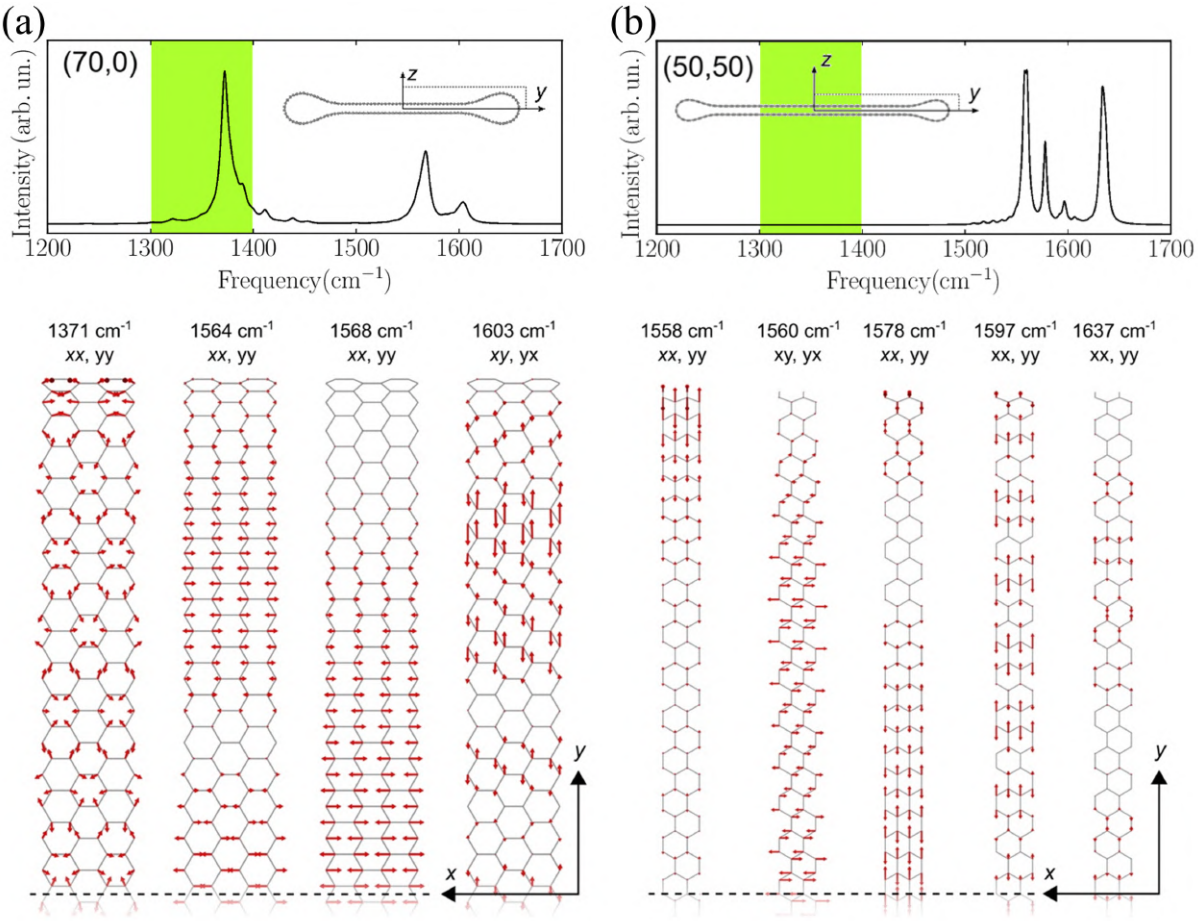

Figure 4.11: (Top) DFT-D2 calculated Raman spectra of flattened (a) AB′-stacked zig-zag (70,0) and (b) AB-stacked armchair (50,50) SWCNTs at 2.3 eV excitation energy. Incident and scattered light polarization are averaged in the nanotube plane. Green shaded section indicates the D band-frequency region. The insertions in both plots depict the cross sections of the structures under consideration, with dotted rectangle indicating the part of the system for which the eigendisplacements are shown. (Bottom) Eigendisplacements of the strongest vibrations contributing to the Raman peaks. Each is labelled with its corresponding frequency and non-zero Raman tensor components in the flattened tube plane. Only the top-half and front-face of the tubes are shown for clarity. Image taken from Paper III.

ate electronic levels (with associated scattering) around the Fermi level [244]. All of these Raman calculations have been carried out on free-standing collapsed SWCNTs neglecting the interactions with the underlying substrate. A few experimental [305] and theoretical [81, 306] works showed that the section of the cavity adhering with the substrate are subject to flattening deformation as a consequence of additional vdW interaction and charge transfer. Molecular dynamics calculations suggested

that the substrate enhances the stability of the collapsed tube [81, 306], since the resulting collapse threshold diameters are systematically lower (1.09-1.90 nm) than the value obtained for the free-standing case (∼5.1 nm) [99, 154, 244].
Given the local curvature at the edge of flattened tubes is responsible of the D peak activation, we next investigated the effects of the substrate on Raman intensities of FCNTs. Although our experimental samples have been grown on Si/SiO_2 wafer, we performed Raman computations for the collapsed (70,0) nanotube on a flat single-layer graphene substrate to simplicity[7]. In Fig. 4.12 we compare the Raman spectra of (70,0) FCNT before and after coupling with the substrate. The interaction with underlying graphene layer induces the appearance of multiple peaks within the D band-region. The eigendisplacements corresponding to the peaks at ∼1348 and ∼1372 cm^{-1} show the A_1' modes associated with iTO phonon branch near K point, which are assigned to the D band. The lower peak at ∼1313 cm^{-1} exhibits a series of normal modes, whose identities remain unclear and therefore subject to on-going investigations. The next two peaks at ∼1533 and ∼1546 cm^{-1} exhibit the E_{2g} modes corresponding to iTO phonon branch close to Γ point and recognized as the G band.

4.2.2.2 Chiral collapsed nanotubes

Our TEM and AFM imaging analysis suggest that our synthesized collapsed tubes have random chirality distribution with turbostratic stacking sequence in the central flattened zone, resembling the interlayer arrangement of a twisted bilayer graphene. Recent multi-wavelength Raman measurement performed on graphene heterostructures with different Moiré angles revealed the presence of additional peaks arising by inter- and intra-layer electron-phonon interactions [307]. Given the structural analogy with the flat middle section of FCNTs, we wondered if a few Raman peaks of our samples can be associated with angle dependent random interlayer coupling, as observed in Moiré graphene heterostructures. However, the experimental spectra never exhibit features attributed to intralayer and interlayer electron-phonon interactions. A possible explanation is that the lateral size of FCNTs is not large enough to give an observable and distinct Raman signal contrary to twisted bilayer graphene. This is a further confirmation that the Raman spectrum of collapsed nanotube is uniquely dominated by the presence of classical G band together with the cavity-induced D band.
As observed in the previous chapter, the electronic states of collapsed chiral nanotube show weak interlayer coupling, whereas it is known that achiral flattened tubes with high-symmetry stacking orders (AB or AB′) show much larger covalent interactions [154, 244], which could affect the results on Raman spectra.

[7]Given the different periodicity between graphene and Si, we would need to simulate supercells with appropriate length, which is computationally demanding for Raman computations based on DFT.

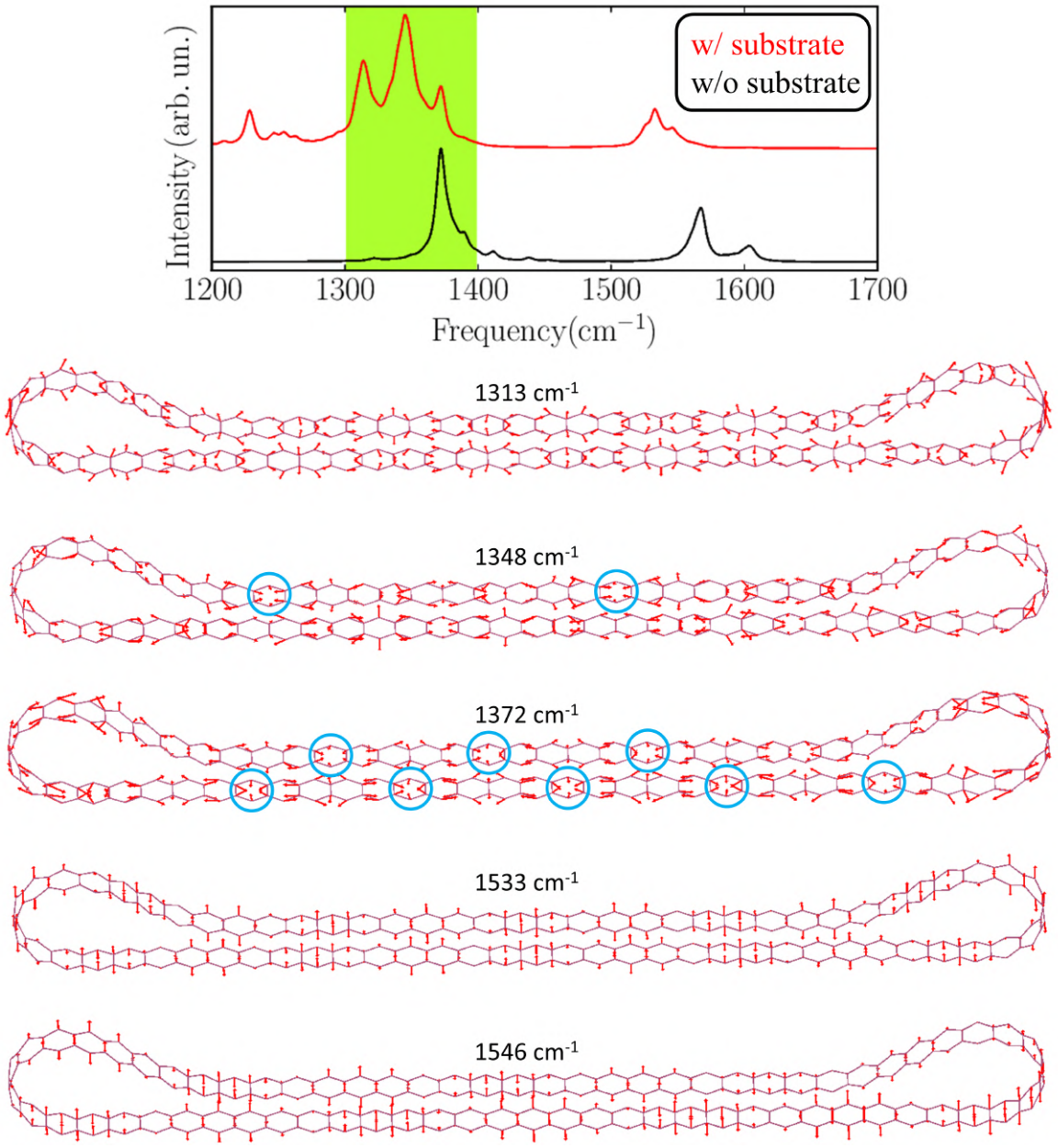

Figure 4.12: (Top) DFT-D2 calculated Raman spectra of flattened AB′-stacked zig-zag (70,0) SWCNT in free-standing (black line) and deformed after interaction with monolayer graphene substrate (red line) at 2.3 eV excitation energy. Incident and scattered light polarization are averaged in the nanotube plane. Green shaded section indicates the D band-frequency region. (Bottom) Eigendisplacements of the strongest vibrations contributing to the Raman peaks, where violet circles indicate the breathing of the hexagons resembling the iTO phonon branch of the D band. Each is labelled with its corresponding frequency in the flattened tube plane.

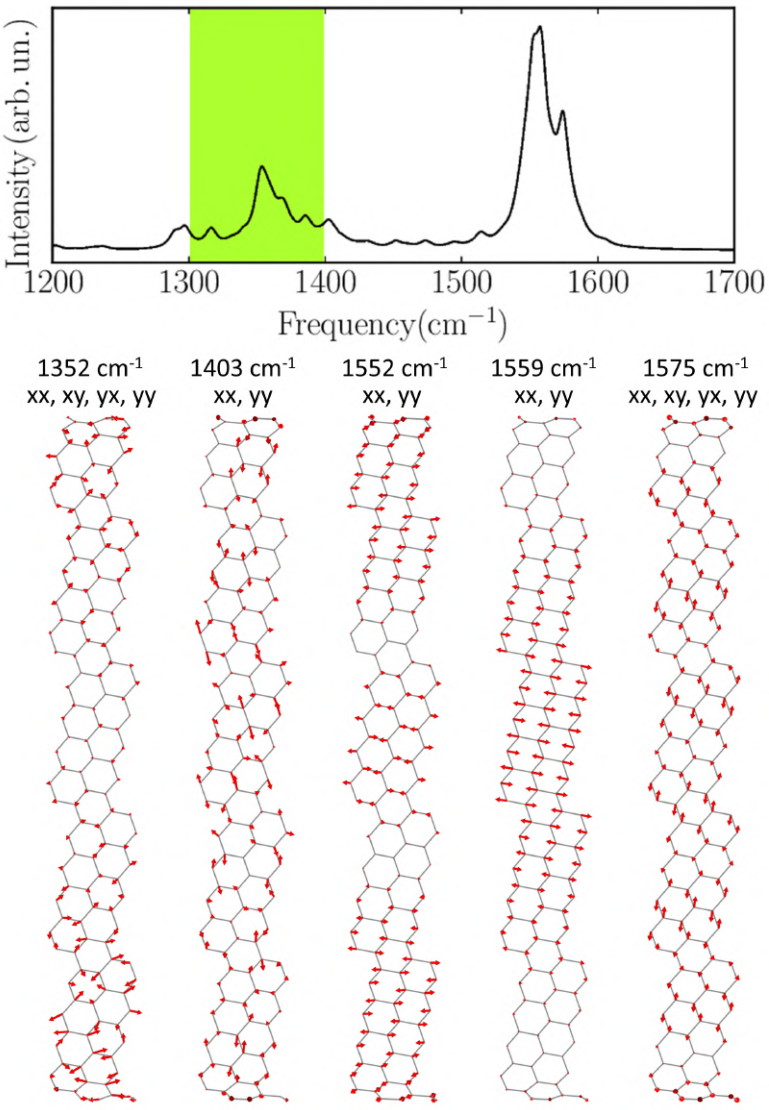

Figure 4.13: (Top) DFT-D2 calculated Raman spectra of flattened chiral (40,10) SWCNT at 2.3 eV excitation energy. Incident and scattered light polarization are averaged in the nanotube plane. Green shaded section indicates the D band-frequency region. (Bottom) Eigendisplacements of the strongest vibrations contributing to the Raman peaks. Each is labelled with its corresponding frequency and non-zero Raman tensor components in the flattened tube plane. Only the top-half and front-face of the tubes are shown for clarity. Image taken from Paper III.

In order to double-check the role of random interlayer coupling, we also calculated the Raman spectrum of a collapsed chiral (40,10) SWCNT (see Fig. 4.13), albeit its width is smaller than armchair and zig-zag cases analyzed before, since chiral tubes have longer unit cells along their periodic axis. Like the zig-zag case, we found a

normal mode at ∼1352 cm^{-1} exhibiting the typical eigendisplacements belonging to iTO phonon branch, which resemble the defect-induced D band. The D-like signal is weaker than the zig-zag case, because the Dirac cone is now being cut offset from K point. In addition, we detected two G peaks at ∼1552 cm^{-1} and ∼1559 cm^{-1}, since they are assigned to the C-C stretching modes along tube axis. In the end, the highest-frequency peak at ∼1575 cm^{-1} corresponds to the E_{2g} belonging to the iLO phonon branch around Γ point and can be interpreted as the D′ band.

4.2.3 Comparison with experiments

These simulations agree with the experimental trends. First of all, the collapsed zig-zag (70,0) nanotube shows an intense D band, wheras it is absent in the same calculation performed on its circular counterpart (see Fig. 4.14), like proven in the experimental spectra (Fig. 4.8). This demonstrates clearly how the symmetry breaking due to the presence of local curvature at the edge of flattened nanotubes represents the determining factor for the D peak activation. Second, the multi-wavelength Raman computations carried out on the collapsed (70,0) tube show a dispersive character for the D-type band signal (see Fig. 4.15(a)). The D-like band position varies linearly by increasing the excitation energy. The slope for the D-mode's excitation energy dependence calculated by our model is ∼22 cm^{-1}/eV, which is somewhat lower than experimental value (∼60 cm^{-1}/eV), as shown in Fig. 4.15(b). This quantitative difference can be attributed to the accuracy level of our semiclassical approximation, which takes no account of the description of the full double resonance process, which is accessible within the framework of the perturbation theory [282, 287, 294].
Having collected all of these experimental results with qualitatively excellent theoretical support, it is evident that the D-band is provoked in this case, not by defect scattering, but by the localised curvature at the edge of collapsed nanotubes. In detail there are a number of factors from this symmetry breaking which can contribute to the activation of the D-band signal in this context, including:

1. direction change of the electron wavepacket, as it moves around the curved edge from the top to bottom FCNT surface, resulting in an inversion of the k-vector and a switch of associated k-space valley.

2. local change in curvature at the interface between the middle bilayer-like region and the start of the edge. This involves a small out-of-plane sp^2-sp^3 rehybridisation of the carbon atoms, which can act as an electrostatic potential scattering barrier (see Fig. 4.16) [282, 297].

3. the change from bilayer to two fully decoupled separated layers as the folded edge is approached breaks the symmetry and acts as a scattering barrier, particularly in the situation where the electron wave packet in the central region is distributed across both top and bottom layers.

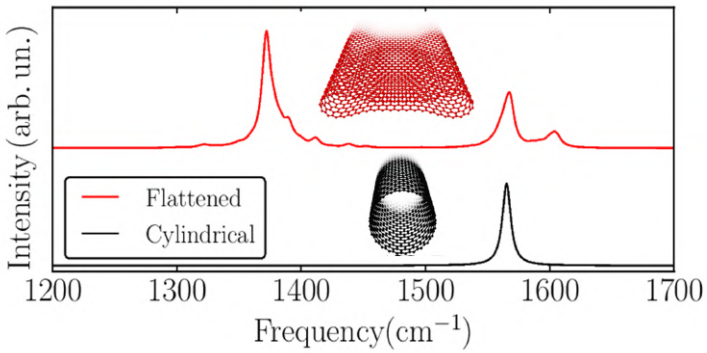

Figure 4.14: Comparison of DFT-D2 Raman spectra of zig-zag (70,0) SWCNT between (black line) circular and (red line) collapsed shape. at 2.3 eV excitation energy. Incident and scattered light polarization are averaged in the nanotube plane. Image taken from Paper III.

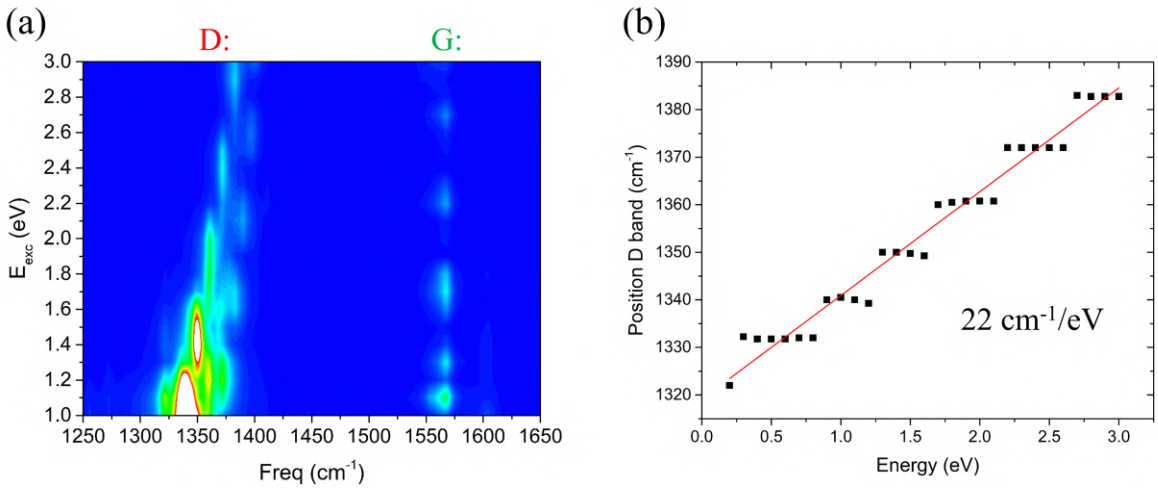

Figure 4.15: (a) Simulated Raman mapping of computed peak positions for collapsed zig-zag (70,0) SWCNT as a function of the excitation energy. It shows the high dispersive character of the D-like band, while the G peak presents a negligible shift with the laser energy. (b) Linear best-fit showing of Placzek D-type bands as a function of incident light with a slope of $\sim$22 cm^{-1}/eV, which is smaller than experimental, $\sim$60 cm^{-1}/eV, usually obtained for the double resonance activated D in more conventional carbon materials. Image (b) taken from Paper III.

However, it is either difficult or impossible to extract out exactly which of these dominates. In practise all are likely to play a part. They are all manifestations of the same structural change, namely *localisation of curvature* at the edge of the collapsed carbon nanotubes.

Figure 4.16: Curvature of collapsed carbon nanotube (top) before and (bottom) after substrate-induced deformation. The borderline of hybridization change between flat middle section and folded edges is indicated by red arrows. In this section it is expected a change of electrostatic potential, which induces the electron back-scattering process necessary to activate the D band. The highest point of edge cavities are indicated by black arrows. Image taken from Paper III. Credit: Pascal Puech.

4.3 Summary

In conclusions, we have applied a semiclassical Placzek formulation Raman theory to simulate vibrational spectra with DFT-D2 accuracy. The underlying idea of this approach is the direct relation between Raman scattered cross section and first derivative of the polarizability with respect to the vibrational coordinates. We have introduced key concepts behind Raman spectroscopy in order to better intrepret our computational results.
The Placzek approximation permitted to analyze and differentiate a wide variety of carbon nanomaterials, such as graphene, fullerene and cylindrical SWCNTs. Our proposed method has shown the activation of the disorder-induced D band for CNTs and GNRs, where both point defects and edges are responsible for the hexagonal symmetry breaking, in according to previous experimental works.
In addition, TEM and AFM imaging analysis clearly identified isolated collapsed CNTs. By comparing Raman spectra between cylindrical and collapsed tubes having a comparable negligible defect density, we have observed the absence and the presence of an intense and narrow D band, respectively. Thus, we have demonstrated that the D band represents an inherent property of collapsed nanotubes, which is due to the line of hybridisation change along edge cavities, rather than a consequence of structural defects. This results is of fundamental interest since D band intensity is historically employed to quantify the total amount of disorder in a given carbon nanomaterial, while we detected the presence of a defect-free band, which is activated by the symmetry breaking derived from the simultaneous presence of flattened sheets and ultra-smooth curved edges.

Interestingly, Raman analysis of achiral collapsed nanotubes highlighted that the appearance/disappearance of D band obeys to the same edge-scattering selection rules known from studies of different graphene edges, in analogy to nanoribbons.
This folding-induced D band serves to revisit the Raman characterization of that class of systems, whose symmetry is broken through a local change in curvature, including: folded [308, 309] and scrolled graphene [309], buckling in annealed nuclear graphite [310], platelet carbon nanofibers [311], cone-shaped graphenic polyhedral crystals [312], and so on.
Moreover, the principles behind the presented multi-wavelength method is more general and not limited to only carbon-based on systems investigated here. We will show an example of this in the next chapter by applying it to study the Raman spectra of phosphorus polychains encapsulated inside cylindrical single-walled carbon nanotubes.

Chapter5

Molecular filling in carbon nanotubes

Carbon nanotubes possess unique physical properties by themselves; meanwhile, their cylindrical cores also offer the storage of foreign materials with intriguing technological implications.
In the last two decades, it has been observed that the encapsulated materials in small-radius carbon nanotubes can show profound structural changes, resulting in novel low-dimensional nanoforms not encountered in their respective bulk form [112–118].
In this Chapter, we present a comprehensive experimental and theoretical study of encapsulated bulk phosphorus in the interior of SWCNTs. TEM imaging investigation highlighted the formation of long 1D tubular-like chains arranged in different packings, which greatly differ from initial configuration before the filling. The experimental results are obtained by our colleagues V. Koroteev, A. A. Vorfolomeeva, Lyubov Bulusheva, and A. V. Okotrub at Nikolaev Institute of Inorganic Chemistry, Novosibirsk State University (Russia), and A. Chuvilin at CIC nanoGUNE BRTA Institute (Spain). We also investigate the encapsulation of polyiodide (I) within a 1 nm diameter SWCNT, on which Paper IV is based. In addition, our colleagues at CEMES Institute of Toulouse have been observed the presence of I chains intercalated between the shells of a large-diameter MWCNT using scanning transmission electron microscopy (STEM) analysis. On the basis of the latter experimental evidence, we study the reason why iodine is thermodynamically more stable when intercalated between tube walls rather than inside innermost tube core.
In the last section of this Chapter, we propose a novel route of nanoribbon doping via filling edge cavities of collapsed SWCNTs. In this context, we will explore two kinds of edge filling: symmetric (with donor species filling both bulbs or vice-versa using acceptor species) and asymmetric (with donor groups filling one edge and acceptor groups along the other). This study paves the way to the experimental production of a single edge-filled collapsed-tube field effect transistor (FET) device.

5.1 Encapsulated phosphorus chains inside CNTs

Like carbon family, phosphorus represents one of the most abundant element on our planet. As introduced at the beginning, P exhibits a rich variety of allotrope nanostructures with different properties. The search for new allotropes of phosphorus represents a challenging task requiring advanced experimental techniques with accurate theoretical prediction. Several experimentalists around the world have found a solution using CNTs as templates and nanoreactors to synthesize and stabilize novel nanostructures [112, 313, 314], which may be metastable if viewed as free-standing. This is one of the advantages due to the smoothness of carbon nanotubes [315].
The filling of CNTs by phosphorus has been performed using melt infiltration at temperature T ∼323.15 K [316, 317] or by chemical vapour deposition for T ∼773.15 K [317, 318]. Narrow SWCNTs with diameter in the 0.6-1.1 nm range have used to offer an appealing environment for the encapsulation of white tetraphosphorus P_4 molecules. A series of TEM imaging analysis showed that P_4-chain was subject to different structural transformations depending of tube diameter. For nanotubes with diameter within 1 nm the encapsulated molecules arrange in single-stranded zig-zag chain [316] and even double-stranded zig-zag ladder [316, 317], while using SWCNT with diameter >1.5 nm displayed a range of new structures with irregular shape. Most recent TEM and STEM in the high-angle annular dark field (HAADF) images revealed another phase transition of the phosphorus allotrope from a square columnar structure to a planar zig-zag nanoribbon by increasing the diameter of carbon nanotube template from 1.4 to 4.1 nm [318]. These experimental results underline that the nanotube diameter has more profound influence on the structure of the encapsulated phosphorus respect to the synthesis conditions.
Herein, our colleagues of Novosibirsk Institute of Russia use commercial SWCNTs of the brand name TUBALL^{TM} [319] with diameter in the range 1.7-1.9 nm for the filling by red phosphorus, unravelling novel covalently bonded P structures consisted of a few chains held together by vdW interaction and aligned along the nanotube axis. The synthesized P chains will be observed by HRTEM and then characterized via Raman scattering analysis.
Fig. 4.1(a),(b) show two TEM images of P@SWCNTs, where we note the formation of triple P chain arranged in parallel into nanotube cavity. However, we could consider another potential interpretation: by rotating nanotube view, the encapsulated phosphorus would form a combination of seven chains, but arranged in such a way to seem like three chains (see Fig. 4.1(c),(d)).
Then, to detect the presence of P encapsulated inside SWCNTs and unravel its effect on the electronic properties of nanotubes, detailed Raman measurements are performed at an excitation wavelength of ∼514 nm (∼2.41 eV), as shown in Fig. 4.1(e). First of all, notice that recorded spectrum of initial sample exhibits features typical of SWCNTs, namely, RBMs, disorder-induced D band (at ∼1350 cm^{-1}), tangential G^- and G^+ bands (at ∼1576 cm^{-1} and ∼1593 cm^{-1}, respectively), and second-order

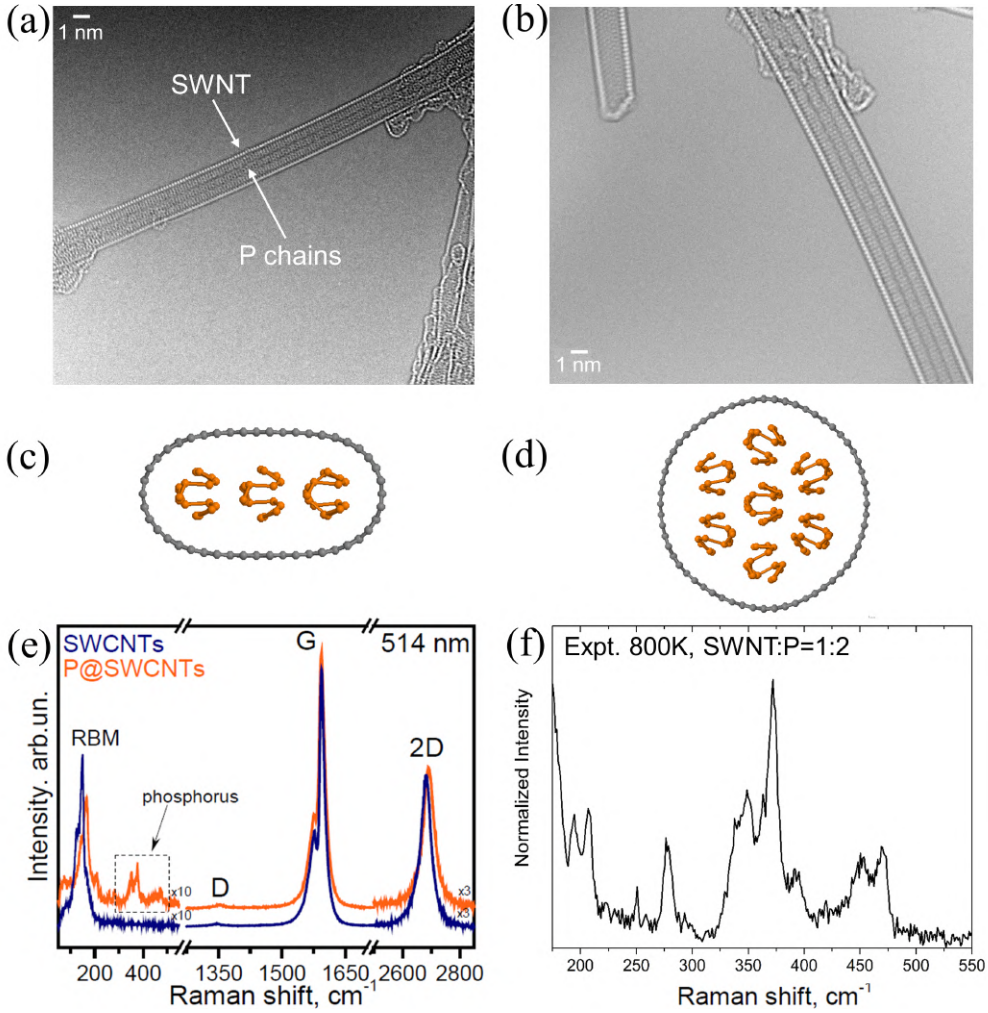

Figure 5.1: (Top) (a,b) HRTEM images of tubular phosphorus packings inside TUBALL^{TM} SWCNTs. (Middle) Optimized of possible candidates structures of P@CNTs seen in microscope imaging analysis, showing P chains arranged in either (c) three or (d) seven chains. (Bottom) (e) Raman spectrum of (red) SWCNTs and (purple) P@SWCNTs measured at 514 nm, where dashed rectangle indicated RBM signals due to the phosphorus encapsulation, whose zoom is presented in (f). The numbers near spectral lines in RBM and 2D band regions show how many times the intensity has been increased.

two-phonon 2D band (at $\sim$2640 cm^{-1}). After the phosphorus encapsulation, we note that:

- the intensity of D band is negligible like that recorded in spectrum of the unfilled nanotube. This confirms that the defect density in our samples is very low, which can be attributed to the residual of metal nanoparticles.

- Positions of G band peaks are unchanged in the spectrum that indicates an insignificant doping effect on the host nanotubes after the filling.

- Visible changes can be detected in the region of RBMs (see Fig. 4.1(f)). Phosphorus structures produce Raman signals at ∼275, 345, 377, 450 and 474 cm^{-1}. The resulting phosphorus-induced peaks nearly match violet P [320] and fibrous red P [321, 322]. Hence, we expect the formation of tubular phosphorus composed by P_5 rings. The different intensities of encapsulated chains compared to free-standing configurations may be driven by charge transfer between phosphorus and nanotubes and Coulombic screening provided by surrounding tube shell. The change of the P-P bonds bending and stretching in filled SWCNTs is related to different mutual arrangements of the crystallized chains.

5.1.1 DFT investigation of different phosphorus allotropes

From a theoretical point of view, we corroborate these experimental findings in two steps: (1) the calculation of the total energies for a plethora of P configurations using DFT, (2) after assuring the reliability of the Placzek approximation, the simulations of Raman intensities for isolated chains to figure out what P species find in the interior of nanotubes.

5.1.1.1 The stability range of phosphorus allotropes

Before turning to Raman characterization of 1D P chains, we investigate their energetic stabilities in order to detect the most stable structure, which may correspond to those observed in TEM analysis. To this end, a preliminary step is to gauge the perfomance of vdW-inclusive DFT methods on the main bulk configurations: black, red, and white. In this context, the importance to implement the different dispersion corrections is two-fold: (*i*) the vdW forces are considered responsible for keeping together the single tubular units in the crystallized packing after encapsulation [59]; (*ii*) previous theoretical analysis showed that standard GGA with no dispersion fails in the correct prediction of hierarchical scale between most common P allotropes [49].
In Table 5.1, we show the relative stability range (where the low-temperature β-white is taken as reference state) of bulk P crystals calculated with semilocal GGA-PBE including Grimme D2 and D3 schemes. The γ-form is slightly more stable than respective β-counterpart by both vdW corrections, which is in agreement with the observed phase transformations in experiment referred to in Ref. [49]. In addition, our DFT+D results on γ-white phosphorus are really close to those reported in prior literature at the same level of theory and beyond. Another general agreement is that Red-V (violet) configuration is the most stable form of red phosphorus [48, 49]. A more intricate problem is the stability of black P over red-IV and V ones, because

Table 5.1: Calculated relative energies (in meV/atom) obtained using GGA-PBE implementing various versions of van der Waals corrections for main common bulk phosphorus structures and comparison with values obtained at the same DFT level and beyond [49]. All the numbers are given with respect to β-white form.

	Our results		Ref. [49]			
	DFT+D2	DFT+D3	DFT+D2	DFT+D3	DFT+TS	RPA
Black	-198	-160	-190	-153	-140	-152
Red-IV	-191	-160	-188	-153	-152	-153
Red-V	-191	-165	-188	-160	-160	-160
γ-white	-2.4	-1	-1	-0.2	-4	-2

it changes depending on the level of calculation method. The black phosphorus is energetically favored over red species using D2 correction. In contrast, the black and red forms become almost degenerate with a little preference for the red-V phosphorus using the D3 scheme. The stability of red P over black one within DFT+D3 is consistent with DFT+TS and more sophisticated (non local) RPA calculations [49]. Our benchmark computations is in agreement with the results provided by Aykol and co-workers, concluding that red-V phosphorus can be considered as the ground state structure of the elemental phosphorus.
Having established the reliability of DFT+D3 method in describing vdW interaction in bulk phosphorus, we determine the total energies of a series of single nanorods P allotropes obtained by removing Cu and I atoms from unit cells provided by ICSD system [60] - in analogy to the experimental extraction of P nanorods from CuI matrices [59]. While the cell geometry changes after the removal of CuI matrices, the periodic lattice vector of the nanorods remains unchanged. In addition, given HRTEM showed P nanorods are arranged in packings when inside nanotubes, we calculate the total energies of groups of two, seven P chains up to bulk case. All of these energy results are summarized in the diagram of Fig. 5.2. The optimized structural parameters of nanorods in the bulk limit are shown in Table 5.2, and where available compared with prior literature at the same level of approximation. From the visualization of the energy comparison plot, we obtain the following information:

- For single-chain structures, the P2P8 is the most stable, which is composed by a sequence of covalently bonded P_5 cages. A single red-1P chain and 400984 are largely unstable due to the presence of dangling bonds;
- Among the double-chain structures, the red-2P chain is more stable than the other structures. Presumably, this happens due to a covalent bond between individual red P chains.
- In the case of 7-chain structures, a red P system cannot be constructed in an

Table 5.2: Calculated lattice parameters of the crystal phosphorus nanorods using GGA-PBE implementing various versions of van der Waals corrections and comparison with values obtained at the same DFT level [59]. The symbol β corresponds to the monoclinic angle of the unit cell.

	202051			401755			404896		
	Ref. [59]	Our results		Ref. [59]	Our results		Ref. [59]	Our results	
	D2	D2	D3	D2	D2	D3	D2	D2	D3
a_0 (Å)	9.47	9.33	9.43	12.96	12.43	12.68	7.01	6.99	7.22
b_0 (Å)	10.61	10.50	10.67	14.16	14.04	13.96	11.43	11.35	11.53
c_0 (Å)	11.25	11.16	11.22	6.48	6.66	6.78	16.64	16.51	16.50
β (°)	99.70	78.80	79.78	105.10	117.10	117.58	114.40	108.91	110.67
V_0 (Å^3)	1114.2	1073.3	1110.7	1034.3	1035.2	1064.2	1214.2	1238.6	1285.0

obvious way, since the energy stability could also depend by the mutual arrangement between chains in a given packing. Among the remaining systems, the packing composed by six P2P8P2P9 chains, connected pairwise (similar to red-2P) and a single P2P8 chain has the lowest energy.

- In the bulk limit, red-V (violet) is degenerate with another system composed by same atomic structure but different lattice vectors [323], which is labelled in the plot as red-H (H: Hittorf). These two configurations are more stable than any other P allotrope.

Although P packings composed by seven nanorods represent the lowest energy structures, it is important to point out that they may not necessarily correspond with configurations observed in our TEM analysis. This is because we have analyzed free-standing phosphorus-based systems, neglecting other possible mutual arrangements provoked by charge transfer and Coulombic interactions with surrounding carbon nanotube.
For this reason, we need to compute Raman intensities in order to differentiate all presented cases and to unravel what red P species are associated to the set of Raman signals observed in our experiments (Fig. 5.1(f)).

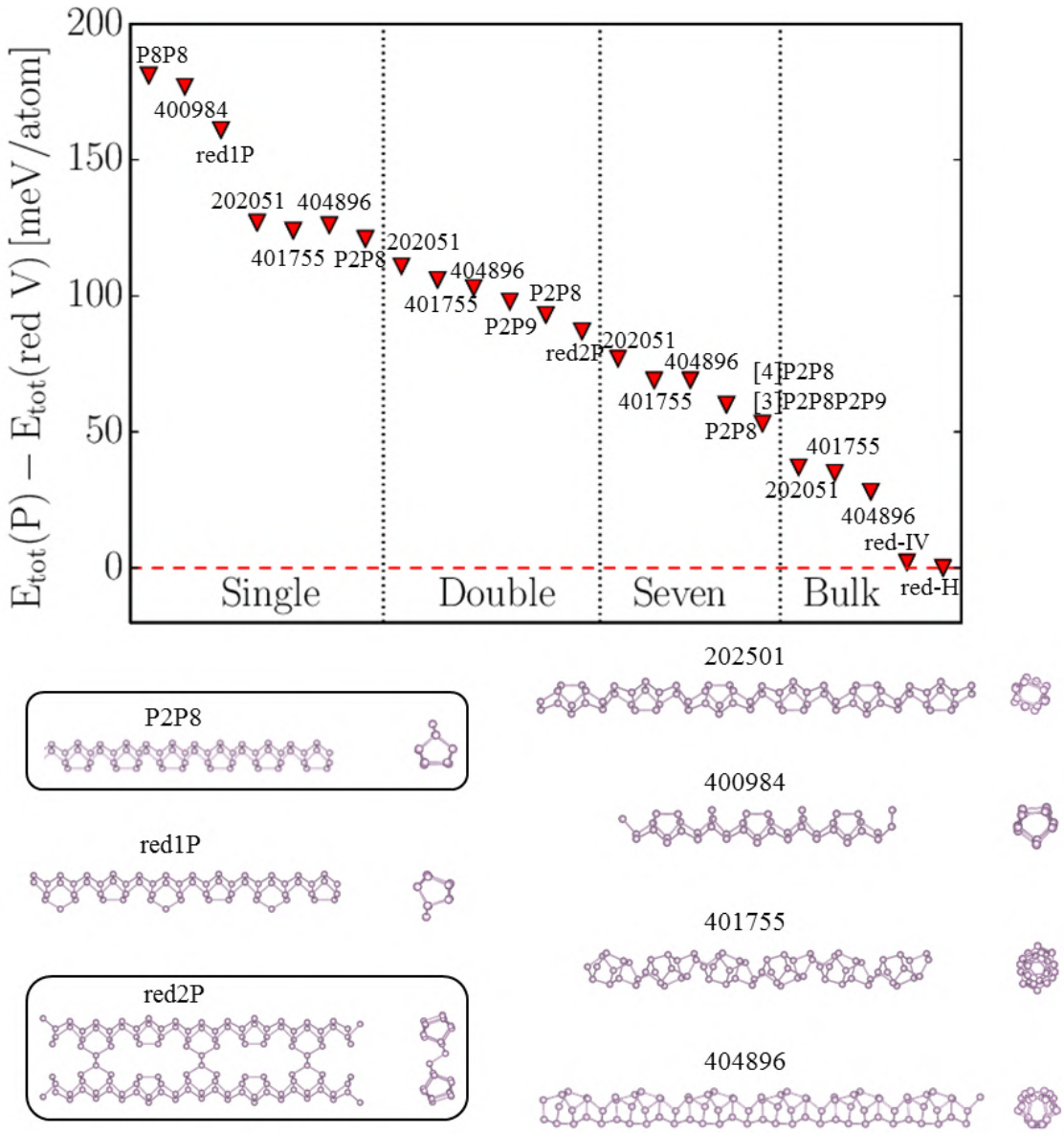

Figure 5.2: (Top) DFT-GGA+D3 calculated energy diagram showing the energy stability of phosphorus nanorods. The plot is divided in four sections, where each one indicates the total number of chains composing the unit-cell. It starts from the left with single nanorod and moving towards 2- and 7-chains up to the right with infinite number of chains or bulk packing. All the numbers are given with respect to ground-state red-V (violet) phosphorus, indicated by horizontal red dashed line. (Bottom) Optimized DFT-D3 geometries of P nanorods after removal of the CuI matrices. Lowest energy structures among single and double chains are indicated by black squares. Each is labelled with its corresponding ICSD number.

5.1.1.2 Raman signature of phosphorus nanorods

We next simulated the Raman spectra of all phosphorus configurations analyzed before via Placzek approximation. In this study, the Raman intensities have been calculated using Eq. (2.24) at an excitation energy of 2.4 eV and applying a Lorentzian broadening set to 4.0 eV in order to be consistent with the experiment.
Like previous energy test analysis, we first investigated the Raman spectra of main forms of elemental phosphorus (black, white, and red-H) using both Grimme dispersion corrections D2 and D3. The computed frequency positions of the main Raman peaks are listed in Table 5.3, which are compared with most reliable experimental results. Notice that we obtain a semi-quantitative agreement with experiments using both vdW corrections. The frequencies are slightly lower than experimental values, except for some peak of red P where we observe a frequency overestimation. However, a closer look at the table shows that: although D3 correction describes the energy stability of all configurations belonging to P family with an accuracy comparable to RPA, the D2 correction seems to provide better overall agreement about vibrational properties.
For this reason, all spectra described here are calculated using DFT-D2 scheme (see Fig. 5.3):

- black: the spectrum is characterized by the presence of three well-defined peaks at 359, 427, and 457 cm^{-1}, which are associated to the phonon modes A_g^1, B_{2g}, and A_g^2, respectively [324]. The large difference between calculated and measured frequency of the third peak may be related to the band gap underestimation by GGA-PBE functional.

- white: it exhibits one peak at 352 cm^{-1} corresponding to the bending mode E and other two at higher frequencies 455 and 594 cm^{-1}, associated with symmetric stretching modes F_2 and A_1 [325].

- red-H: the resulting spectrum can be divided in three distinct parts on the basis of the height of peak intensity [323]. In fact, the first region between 100-300 cm^{-1} exhibits signals of medium intensity. A second section lying in the range 300-340 cm^{-1} do not show any band. The third last zone is characterized by high intense peaks at 358, 364, 370, 441, and 468 cm^{-1}. The discrepancy between DFT-computed and experimental intensity height at higher frequency region is attributed to the level of accuracy of Placzek approximation [162].

Thus, our DFT-D2 simulated spectra match qualitatively the experimental counterpart, albeit with slight frequency underestimation of detected peaks. Having assessed the accuracy of the Placzek approximation combined with DFT-D2 approach for more conventional P families, we then reproduced the computational spectra of tubular phosphorus allotropes.

Table 5.3: Calculated phonon frequencies (in cm^{-1}) for the most common configurations of elemental P using GGA-PBE implementing two versions Grimme's corrections (D2 and D3) and comparison with experimental counterpart reported in prior literature: Ref. [324] for black, Ref. [325] for white, Ref. [323] and for red-H.

Allotrope	$\nu_{\text{Expt.}}$ [cm^{-1}]	$\nu_{\text{DFT-D2}}$ [cm^{-1}]	$\nu_{\text{DFT-D3}}$ [cm^{-1}]
Black	362	359	350
	437	427	429
	465	457	454
White	350	352	350
	460	455	456
	600	597	597
Red-H	205	205	200
	353	358	355
	358	364	363
	373	370	365
	446	441	442
	471	468	465

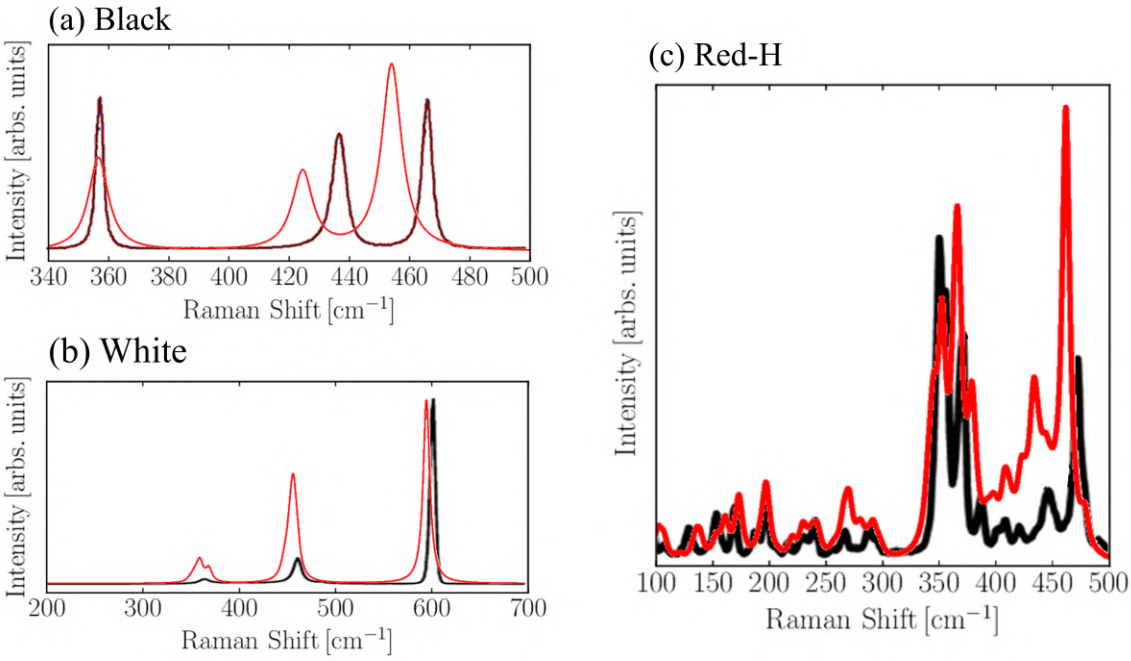

Figure 5.3: Placzek calculated Raman spectra (red lines) of main phosphorus bulk families: (a) black, (b) white, and (c) red P at excitation energy of 2.4 eV (514 nm). Black lines represent the spectra measured in experiments provided in prior literature [323–325].

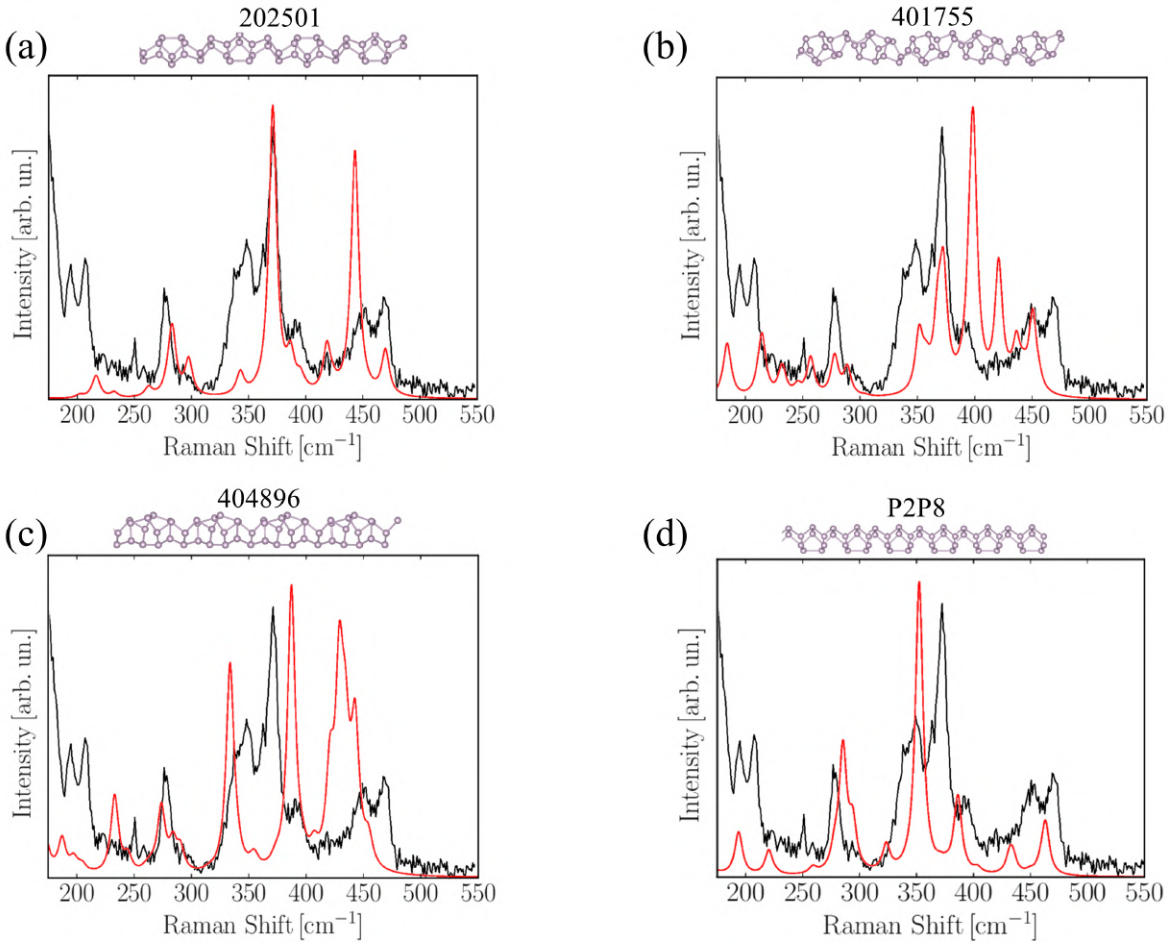

Figure 5.4: Placzek calculated Raman spectra (red lines) of single phosphorus nanorods after removal CuI matrices: (a) 202051, (b) 401755, (c) 404896, and (d) P2P8 at excitation energy of 2.4 eV (514 nm). Black lines represent the spectrum recorded in our experiments. Optimised structure of each configuration is shown above corresponding spectrum. Each is labelled with its own ICSD number.

Fig. 5.4 shows the computed Raman intensities of single P chains in comparison to measured spectra in experiments. We note that theoretical spectra of 202051, 401755, and 404896 configurations match poorly to experimental ones, while the predicted features of P2P8 chain are in good agreement with those recorded. This discrepancy is related to the fact that we are considering free-standing single chains, while TEM observation revealed the formation of dense P packings inside carbon nanotube. In fact, the reason why P2P8 chain shows better results may be due:

- The tendency to make cross-linking with neighboring chains by forming the dense packing visualized by TEM.
- Charge transfer affecting the resulting vibrational properties.

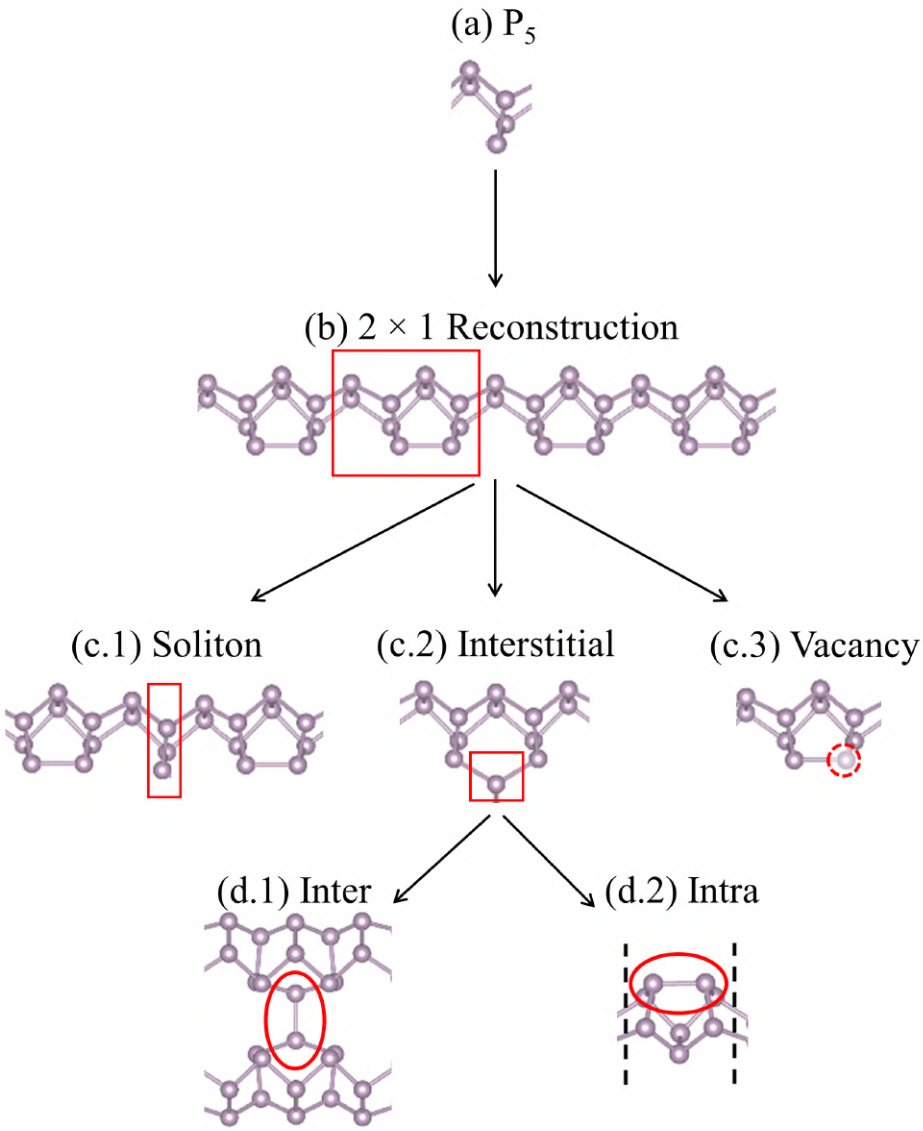

Figure 5.5: Schematic showing a proposed classification of local structure in P chains using defect and dislocation terminology, taking (a) P_5 (soliton) as the base unit along the chain: (b) 2×1 reconstruction, (c.1) unreconstructed soliton, (c.2) interstitial, (c.3) vacancy. The interstitial-type defect leads to the formation of: (d.1) inter- and (d.2) intra-chain di-interstitial.

About the cross-linking effect, its origin can be explained if we view the single chain in terms of *defects*. The proposed model is shown in Fig. 5.5 and described as follows. The single P_5 ring represents the basic structural unit having a dangling bond (with associated spin (Fig. 5.5(a)), thus, prefers to recombine in neighboring

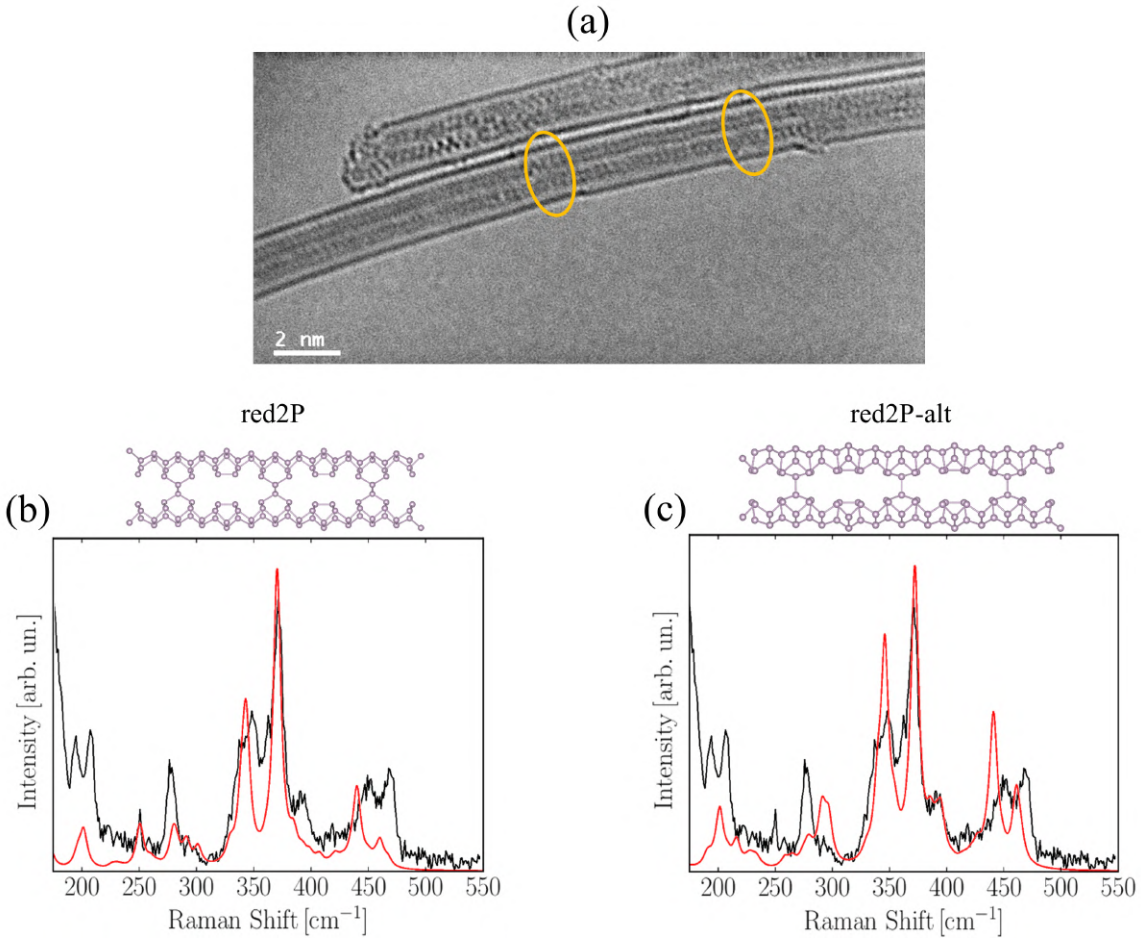

Figure 5.6: (Top) (a) HRTEM image of double phosphorus chains inside TUBALL™ SWCNT. Interchain cross-link is marked by orange circles. (Bottom) Placzek calculated Raman spectra (red lines) of two lowest energy double P chains: (b) red2P, and (c) red2P-alt at excitation energy of 2.4 eV (514 nm). Black lines represent the spectrum recorded in our experiments. Optimised structure of each configuration is shown above corresponding spectrum.

pairs leading to the formation of a 2×1 reconstruction[1] in our pristine low energy P2P8 configuration (Fig. 5.5(b)) [326]. Then, we can define various defect types:

1. The unreconstructed P_5 soliton (Fig. 5.5(c.1)). This has a dangling bond and will be highly reactive, and, we assume, highly mobile. Two of them can combine and annihilate.

2. The interstitial atom (Fig. 5.5(c.2)). Like soliton-type defect, it possesses a

[1]The proposed configuration resembles the symmetric reconstruction (2×1) of the Si(100) surface [326].

dangling bond and is reactive. It cannot easily annihilate within the chain. More interestingly, we can imagine interstitials combining into two types of di-interstitial: *inter*- (encountered in red2P chain, see Fig. 5.5(d.1)) and *intra*-chain di-interstitial (where the P_8 rings sit on the back on the chain in a pair, see Fig. 5.5(d.2)).

3. The vacancy atom (Fig. 5.5(c.3)). The P_5 cage is missing one P atom, so the two remaining neighbours rebond together.

In fact, cross-linking between two encapsulated P chains are visualized by TEM, as shown in Fig. 5.6(a). They seem to correspond with inter-chain di-interstitial type defect obtained for our optimized double P chains structures. Thus, the missing peaks in our theoretical spectra could be associated with the cross-linking formed by the interactions between phosphorus chains enclosed within the same packing. For this reason, we need to investigate the vibrational features of double phosphorus chains. In fig. 5.6(b),(c) we present the calculated Raman spectra of two lowest-energy covalently linked double chains, showing a much better agreement with experimental counterpart.
The analysis of both single- and double-chains highlights that the spectra of P2P8 and red2P configurations better reflect those measured in experiments. Now, the crucial point is to figure out how each of the two allotropes contribute in the resulting spectra. To this end, we tested a 50/50 linear combination the data of P2P8 and red2P cases, whose merged version of the spectrum is shown in Fig. 5.7. After that, we represented the eigen-displacements associated to each peak of two tubular allotropes in play (again see Fig. 5.7). We note that the peaks located at 193, 224, 285, 352, and 387 cm^{-1} come from the vibrational modes of P2P8 single nanorod, while those at 201, 251, 279, 343, 370, 440, and 460 cm^{-1} correspond to the structural motifs belonging to the double P chain. This greatly supports the initial experimental observation, for which new Raman signals are induced by the strong interaction of different P allotropes held together by forming one dense cluster.
However, our experimental TEM analysis have also shown packings composed by a number of three or even seven (depending on rotating angle view) chains inside tube nanoreactor. For this reason, we compared the recorded spectrum in experiment with the P packing composed by three P2P8P2P9 double chains together with a single P2P8, as shown in Fig. 5.8 (a). In addition, the simulated TEM (Fig. 5.8(c)) image quite matches the experimental one (Fig. 5.8(b)). Here, we used a different ratio of P2P8 and P2P9 with respect to that shown in Fig. 5.7, because it is the ratio we need to match to the TEM. But the point is that is TEM from just one tube, but the experimental Raman is an average of tubes with different diameters, so the ratio of P2P8 and P2P9 in the Raman is not going to be the same as in that one TEM image. The discrepancy between theoretical and experimental values can be explained as follows: (*i*) the computations of interacting seven chains is quite intricate, due to the additional degree of freedom of the mutual arrange-

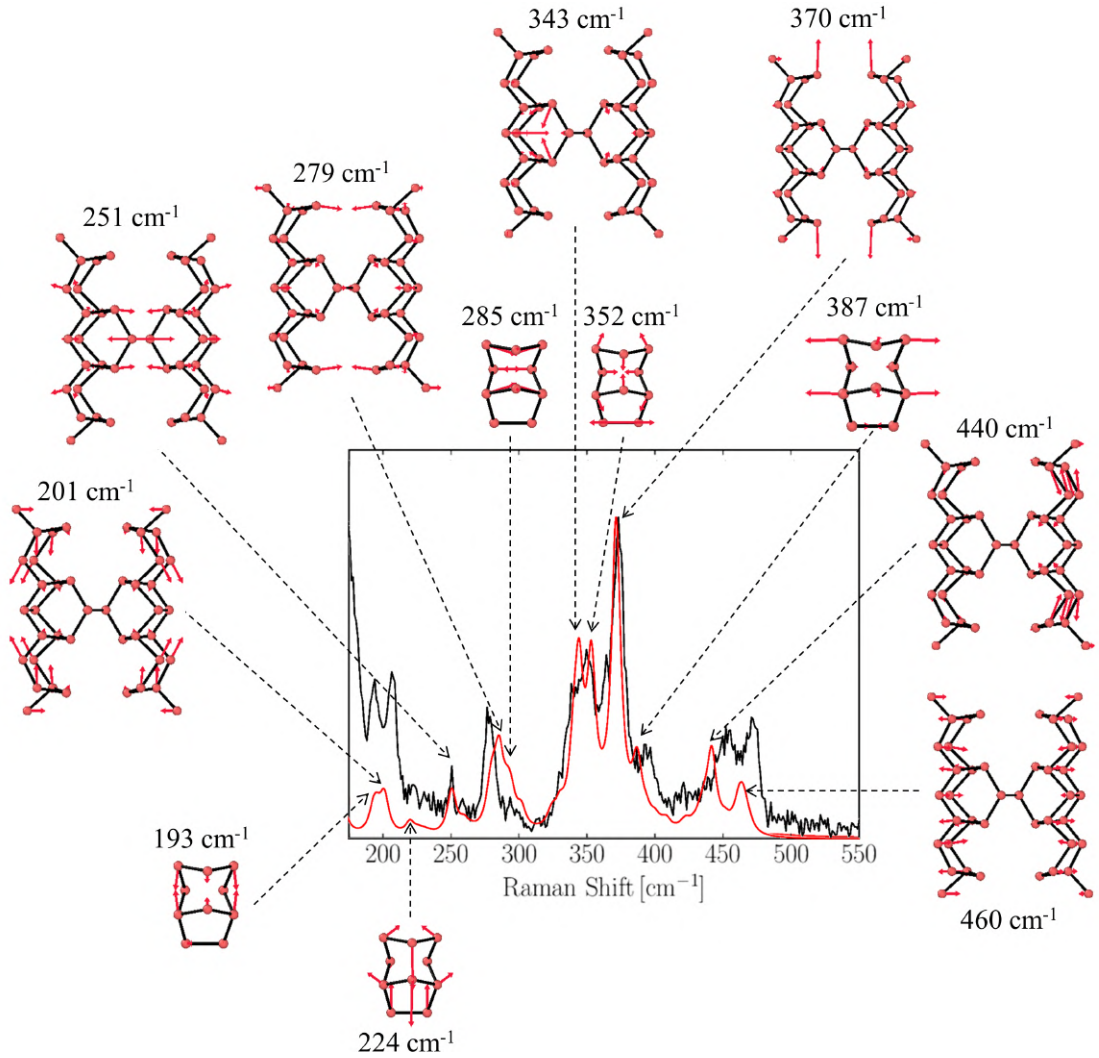

Figure 5.7: Interpolated Raman spectrum (red lines) obtained as a 50/50 linear combination of single P2P8 chain and red2P chain at excitation energy of 2.4 eV (514 nm). Black line represents the spectrum recorded in our experiments. Around the plot are depicted the optimised geometries of the structures under consideration, with eigendisplacements of the strongest vibrations contributing to the Raman peaks. Each is labelled with its corresponding frequency.

ment between single nanorods enclosed in a given packing; (*ii*) the peak frequency positions could be subject to shifts induced by charge transfer beween phosphorus-carbon nanotube.

In summary, our simulations revealed what can be the best potential candidates of red P allotropes inside nanotube, although the detection of a unique structure is quite challenging given several mechanisms in play and mentioned above. Since the energetics of these structures are quite close, it seems likely that the defect formation

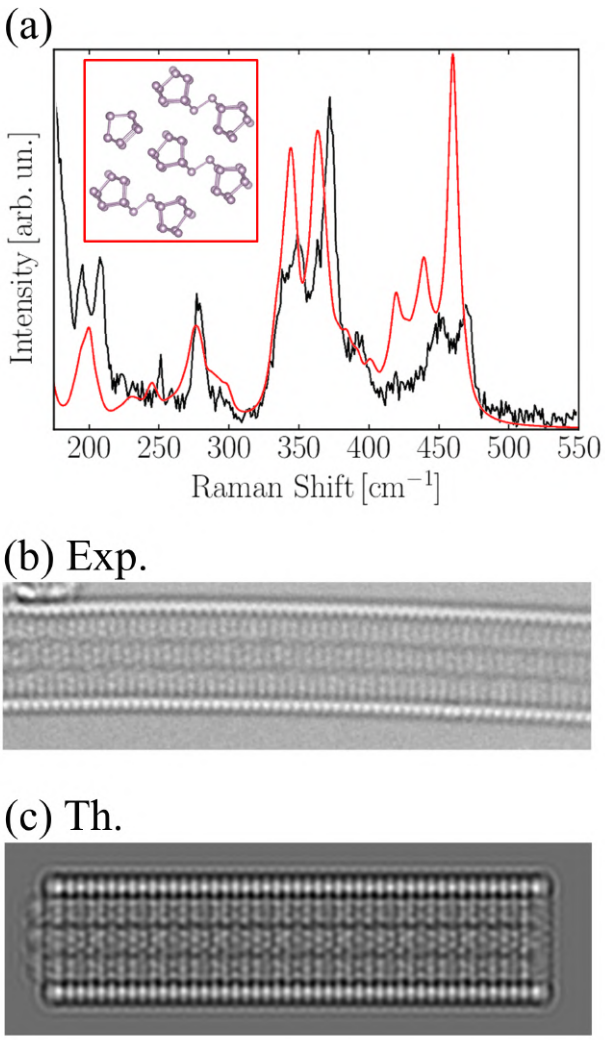

Figure 5.8: (a) Placzek calculated Raman spectra (red lines) of seven chain phosphorus composed by: three double chains plus one single P2P8 nanorod at excitation energy of 2.4 eV (514 nm). Black line represents the spectrum recorded in our experiments. The insertion in the plot depicts the cross section of P packing under consideration. (b) HRTEM image of SWCNT filled with seven P chains. (c) Corresponding simulated TEM image.

energies for intersititials (Fig. 5.2), vacancies and such like in 1D-P chain structures may be much lower than other light element nanomaterials such as graphene, in which case we would expect significant concentrations.

5.2 Iodine confinement in carbon nanotubes

Endohedral iodine filling in single- and multi-walled carbon nanotubes is of great interest fundamentally to explore the effects of p-type dopants and their techonological implications. Previous current measurements revealed that iodine-doped carbon fibers exhibit a enhanced electrical conductivity ($\sim 6.5 \pm 0.1 \times 10^6$ S $\cdot$ m^{-1}) in comparison to un-doped samples ($\sim 1.1 \times 10^6$ S $\cdot$ m^{-1}) [111]. Iodine also shows strong contrast in dark field electron microscopy [111]. DFT calculations have shown that charge transfer between nanotube and encapsulated iodine molecules (I_2) leads to the formation of polyiodide anions, exhibiting a charge transfer per atom signficantly higher than I_2 molecules used for nanotube filling [111]. Thus, the charged iodide chains are the origin of the highly efficient iodine doping in CNTs.
Control over the formation of iodine wires at the nanoscale represents a successful approach to improve nanotube perfomance, extending their range of applications in nanoelectronics [327].

5.2.1 Modelling of polyiodide structures in SWCNTs

Even more than the phosphorus family, much effort has been devoted to realize atomic 1D iodine nanowires using SWCNTs as sheaths. Iodine encapsulated in narrow tubes exhibits a rich variety of stable polymorphic structures. Raman spectroscopy of iodine-doped SWCNTs in free-standing and bundle configurations showed peaks with frequencies corresponding to I_3^-, I_5^-, and I_8^{2-} anions [328, 329]. TEM studies of I@CNTs revealed the formation of atomic arrays with complex structure depending on the nanotube diameter [330]:

- For $D \leq 1.45 \pm 0.05$ nm: single, double, and triple helical chains are successfully generated (see Fig. 5.9(a)-(c),(h)).
- For $D > 1.45 \pm 0.05$ nm: more than three chains of iodine have never been observed and they show the tendency to crystallize either in an orthorhombic structure (see Fig. 5.9(d)) or in a new form which falls outside the canonic iodine arrangements (see Fig. 5.9(f)-(h),(k)-(m)).

The prediction of stable 1D iodine geometries can represent an intricate task. For example, the helicity of encapsulated iodine chains inside silicon-carbide nanotubes was studied using a LJ potential [331]. However, the use of empirical potentials may result in insufficient accuracy, since they neglect effects such as charge transfer which could influence the resulting polyiodide geometry. To cover this point, a direct treatment of the electronic structure has to be included, which requires quantum chemical approaches, like DFT. But, the length of the nanotube lattice vector is, in general, different from that of the encapsulated iodine. Thus, we need to translate unit cells of both CNT and iodine chain in order to achieve commensurability properly for the two structures of interest. This means that the calculations

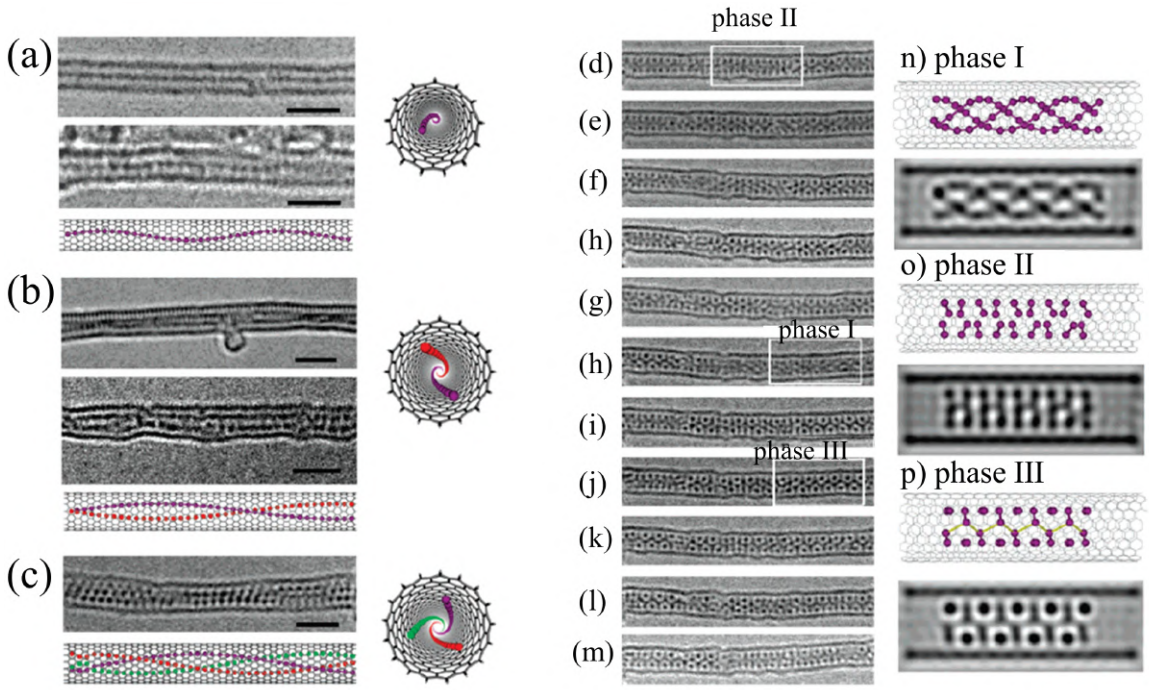

Figure 5.9: (Left) HRTEM images of different atomic iodine chains encapsulated inside SWCNTs with different diameters operated at 120 kV and their schematic illustrations in side and top view. The total number of resulting chains increases by increasing the tube diameter: (a) single, (b) double, and (c) triple chains are synthesized in tube inner cavity having diameters nearly equal to 1.05, 1,30, and 1,40 nm, respectively. (Right) Sequence of iodine arrangement inside a nanotube of 1.45 ± 0.05 nm in diameter. Three different structural phases appear during TEM observation, denoted by Phase I, II, and III. Phase I indicates the helical iodine wires, while phases II and III represent bulk crystal-like structures. Image adapted from [330].

can involve large number of atoms in the range of 100-1000 or even beyond, testing computational limits.

In order to consider the problem quantum chemically while keeping the computation time reasonable, we apply the following strategy: to generate initial geometries of the iodine as close as possible to stable iodine configurations observed in experiment so we can improve the efficiency of finding global minima. Additionally, we choose a reasonable localized-basis set within DFT implementation to speed-up calculations. In the following, we present different approaches to simulate experimentally stable structures *without* any experimetal input.

5.2.1.1 Computational details

The main computational details are described as follows.

Supercell approximation. We use a long (7 primitive cells, 29.82 Å of length) supercell of a thin (∼1.0 nm) (13,0) semiconducting nanotube with a total of 364 carbon atoms. In order to determine the preferred iodine density we performed calculations for 1 to 72 iodine atoms, encapsulated within the tube supercell.

Modelling polyiodide chains. Two different approaches are used to model initial configurations of iodine chains. In the first case, we adapted the *ab initio* random structure searching (AIRSS) method to randomly generate a large number of initial candidates for the investigated iodine [332]. Once collected all starting structures, we used a so-called fingerprint function to keep only those in which atoms are not too close together.
In the second approach we started from the almost linear iodine chain (i.e. atom positions are slightly displaced respect to periodic axis, so as to break the symmetry of the system) inside the nanotube, optimized its geometry, then compressed the atomic positions along the nanotube axis, and introduced a new iodine atom at the boundary of the unit cell in the empty space created by the compression. By applying this iterative method, we increased the iodine concentration sequentially, comparing the previous stable geometry to the next one.

Exchange-correlation functional. DFT computations are performed with AIMPRO and QUANTUM-ESPRESSO codes, using LDA and GGA-PBE coupled with Grimme D2 dispersion correction, respectively.

Basis set. Since the nanotube serves mainly as a potential well for spatial confinement and electron donor for the selected iodine chains, we fixed the positions of the carbon atoms keeping a minimum basis set for them of four contracted functions (known as, C44G*) in order to speed-up the computations during the geometry optimization of iodine. Iodine is treated using very large *dddd* basis set with 40 independent functions in total. To determine the charge transfer, we then increased the number of carbon basis functions from 4 to 38 uncontracted functions using the *pdddp* basis set.

Microscope image simulations. We performed TEM image simulations using at 120 kV with spherical aberration 0.3 mm, defocus set to the Scherzer value of 317 Å and defocus spread 38 Å. STEM image simulations have been obtained using the QSTEM software package. Simulation conditions are chosen to be consistent with experimental literature [333]. We used a HAADF detector (inner and outer radii of 55 and 195 mrad, respectively) with 30 mrad of convergence angle and applied voltage of 120 kV.

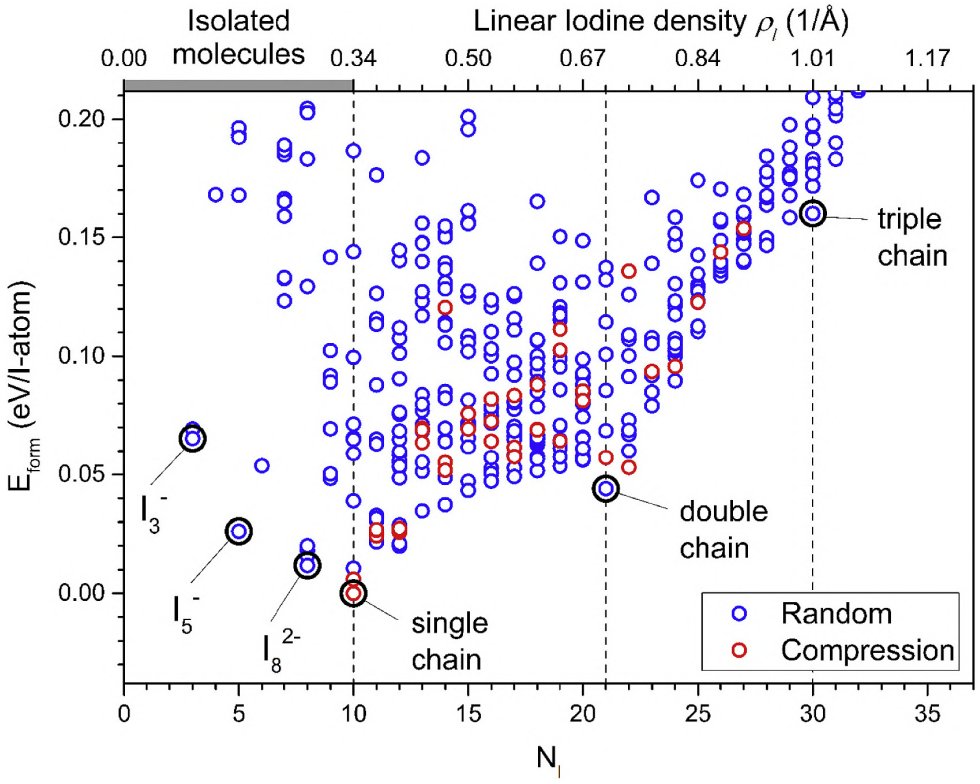

Figure 5.10: Formation energy of iodine structures within the 29.82 Å long supercell of (13,0) with the origin of the energy set to lowest I_{10}@(13,0) (single-chain) structure. x-axis shows (lower) number of iodine atoms per supercell and (upper) linear iodine density. For iodine density below 0.34 $Å^{-1}$, isolated molecules are found. Blue circles represent structures obtained by the random sampling method, red circles from the "compression" approach. Key stable structures are marked with black circles. Image taken from Paper IV. Credits: D.V. Rybkovskiy.

5.2.1.2 Polyiodide structures within a CNT

In order to select the best configurations obtained by the two structure prediction approaches described above, we compare the energetic stability of all I@(13,0) tubes with different iodine atom numbers, using the formation energy defined as follows:

$$E_{\text{form}} = \frac{(E_{\text{I@CNT}} - E_{\text{CNT}})}{N_{\text{I}}}, \tag{5.1}$$

where: $E_{\text{I@CNT}}$ is the total energy of the I@CNT system, while E_{CNT} is the energy of an empty nanotube. N_{I} is the total number of I atoms within the simulated cell. In Fig. 5.10 we map the $E_{\text{I@CNT}}$ for systems with N_{I} in the 1-37 range, where the energy zero placed at the lowest energy structure. The energy minima obtained using the random sampling and atomic chain compression approaches are indicated

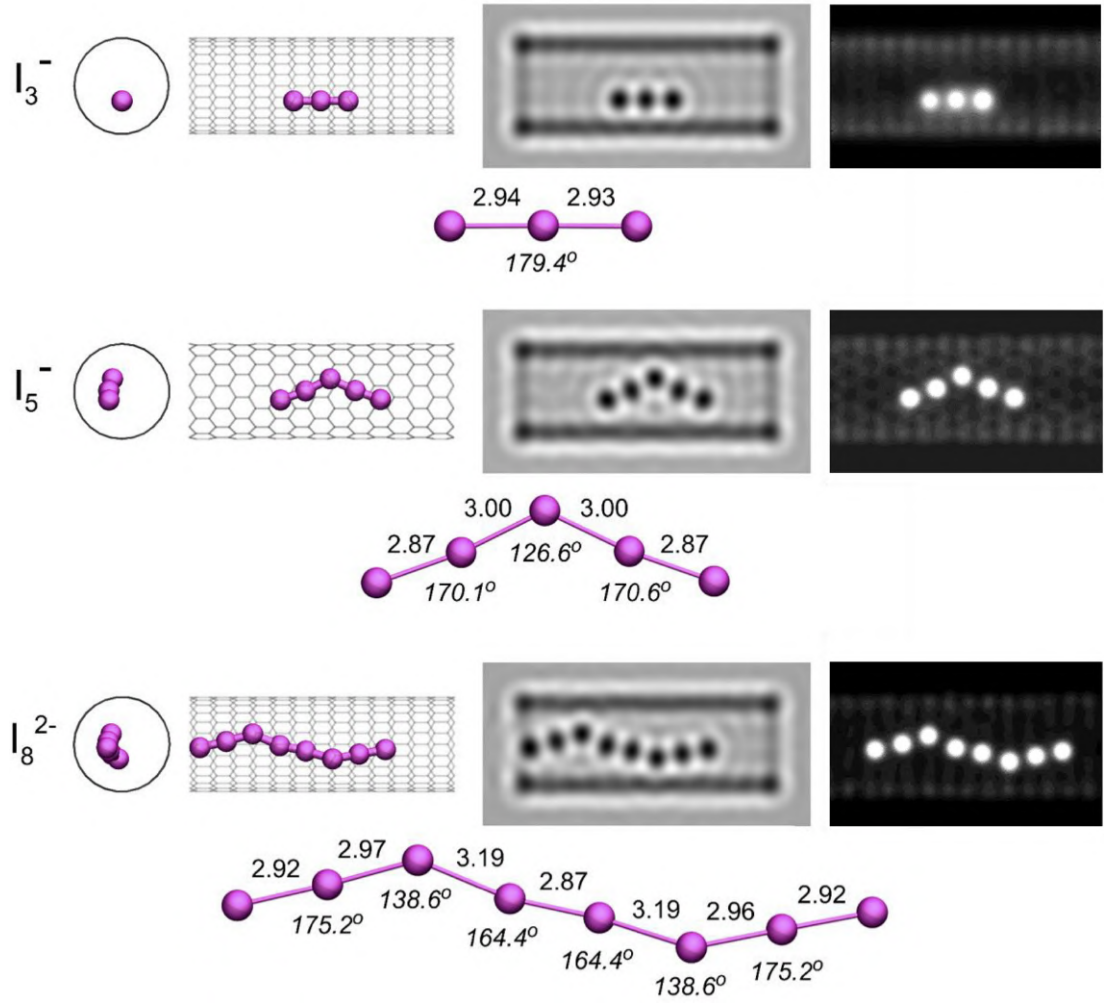

Figure 5.11: Calculated unit cells containing I_3^-@(13,0), I_5^-@(13,0), and I_8^{2-}@(13,0) with bond lengths (Å) and bond angles (°). (centre) simulated 120 kV TEM images (right) simulated 120 kV scanning-TEM high-angle angular dark field (STEM-HAADF) images. Image taken from Paper IV.

with blue and red circles, respectively. At each N_I value we consider the result with lowest E_{form}, that corresponds to the most stable configuration found via structure search algorithm. Random sampling method provides most of the formation energies, especially in the low-density region (10-21 iodine atoms). This is due to the large CNT inner-space to atomic volume ratio, which leads to a considerable amount of unexpected but stable initial structure geometries. The lowest-energy configurations of I_3^-, I_5^-, I_8^{2-} anions together with double ($N_I = 21$) and triple ($N_I = 30$) helical chains are predicted by AIRSS method. Although such a random approach is able to predict a plethora of unexpected and even stable structures, it requires a huge number of iterations to converge. For this reason, we do not obtain the lowest-

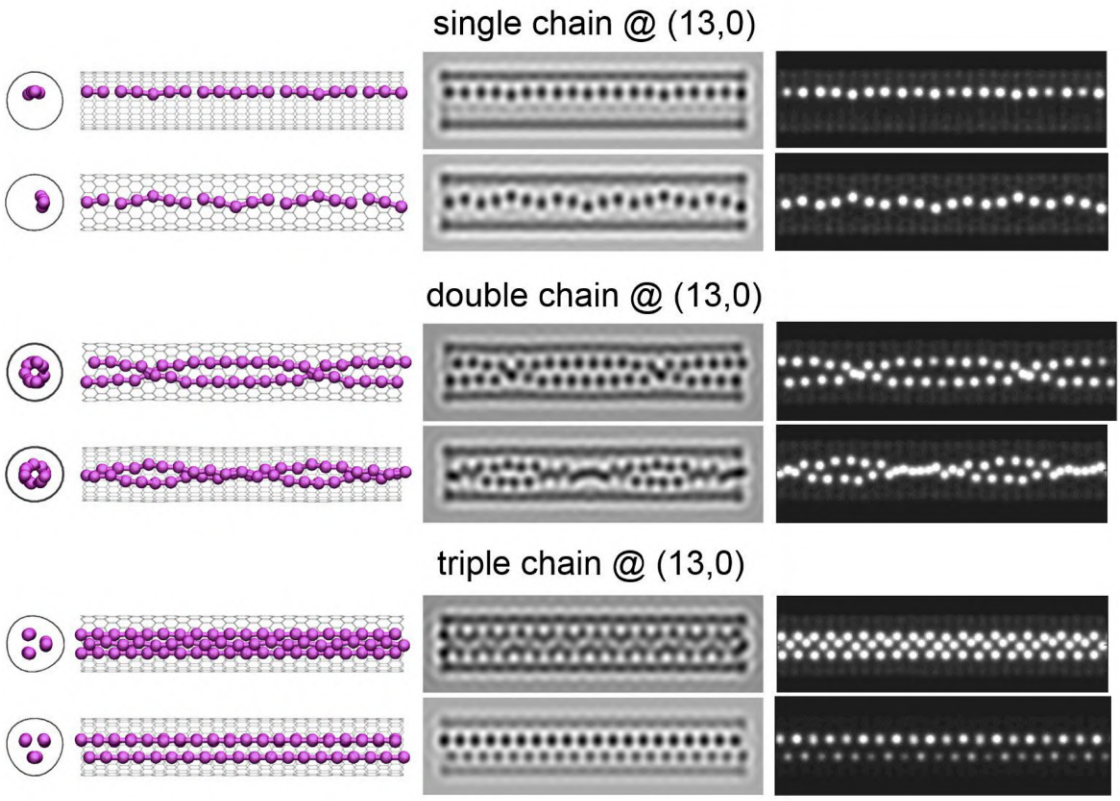

Figure 5.12: Atomic geometries of single, double, and triple chain structures, formed within the (13,0) carbon nanotube. The supercell is duplicated in order to show the perodicity of the systems and each structure is presented by two projections. (centre) simulated 120 kV TEM images. (right) simulated 120 kV STEM-HAADF images. Note the tube deformation due to the interaction within encapsulated iodine. Image taken from Paper IV.

energy configuration when the number of iodine atoms in the supercell is equal to 10. In this specific case, the compression algorithm yields the most stable single chain. All the most pronounced stuctures are highlighted in Fig. 5.10 with black circles. We note that the formation energy drops with increasing iodine concentration. This trend shows the tendency of encapsulated halogens to polymerize forming prolonged chain-like structures.

The selected optimized geometries of molecular anions (i.e. I_3^-, I_5^-, and I_8^{2-}) are depicted in Fig. 5.11 with corresponding simulated TEM and STEM-HAADF images. Besides the tendency of molecules to "stick" to the CNT inner surface due to the vdW interactions, the main geometric parameters of the polyiodides can be compared with those reported in literature. The calculated bond lengths of tri-iodide (2.93 and 2.94 Å) are in excellent agreement with average value (2.93 Å) estimated in accurate STEM-HAADF analysis [334]. The resulting bond angle of 179.4° also

lies within the range of experimental values usually seen for polyiodides [335]. Most of the bond lengths of I_5^- and I_8^{2-} anions also roughly match their experimental counterpart [335].
The Mulliken partial charges of I_3, I_5, and I_8 are 0.91, 1,06, and $1.96e^-$, respectively, which are close to the experimentally reported integer values of 1, 1, and 2. The extra-electrons, accepted from the CNT, allow the formation of additional p_{z^-} bonds and increase to the odd number of atoms within the molecule.
When there are 10 iodine atoms inside tube cell (or equivalently, the corresponding linear iodine density $\rho_I \sim$ reaches 0.34 $Å^{-1}$), the chain is long enough that the ends meet (given the chosen supercell size) and forming a single infinite chain. The resulting structure resembles a repeated sequence of V-like shaped I_5^- molecules. Higher iodine concentration ($N_I = 21$) inside the tube induces first a twist with distortion of the polyiodide chain and then the formation of a double chain to $\rho_I \sim$0.70 $Å^{-1}$.
TEM and STEM images show that the nanotube cross-section is distorted due to the repulsion between the I chains, as confirmed by the microscopy imaging analysis reported in literature [330]. By increasing again the iodine concentration ($N_I = 21$ and $\rho_I \sim$1.01 $Å^{-1}$), we witness a further phase transition to the triple helical chain. Our simulated TEM images of single, double, and triple chain configurations (see Fig. 5.12) are consistent with the experimental HRTEM stuff shown in Fig. 5.9(a)-(c) [330]. In particular, the top TEM image of our predicted triple chain is highly reminiscent of the not-well identified Phase III observed in HRTEM imaging of iodine filled CNTs (see Fig. 5.9(j),(p)) [330]. Not only that, our image simulations strongly suggest that Phases I, II and III are likely all three the same triple chain structure, but viewed at different orientations to the electron beam.
The only relevant difference between our predicted structures and experiment is the translational periodicity of the polyiodides, i.e. HRTEM images of Ref. [334] show a rather linear distribution of the single I chains, in contrast to our calculated zigzag shaped structure. We attribute this discrepancy to the lattice vector difference between CNT supercell and resulting iodine wire.
Our study demonstrates the reliability of our global optimization methods to predict stable geometries of 1D@SWCNT structures. For the molecular structures the calculated charge transfer is approximately equal to the integer charge of the corresponding molecular anions. The charge transfer on the geometry of different iodine chain structures enclosed in nanotube templates shifts the Fermi level position, suggesting high-level of p-doping as a consequence of Peierls/charge-density wave instability (see Table 5.4). This further confirms that it is possible to tune the electronic properties of carbon nanotubes manipulating the structure of confined iodine chains at the nanoscale.

Table 5.4: DFT-D2 calculated Fermi level shift (eV) in zig-zag (13,0) SWCNT filled with different polyiodide structures. Results taken from Paper IV.

I@SWCNT	
Configuration	E_F [eV]
I_3^-	0.04
I_5^-	0.05
I_8^{2-}	0.13
Single Chain	0.13
Double Chain	0.23
Triple Chain	0.19

5.2.2 Iodine intercalation in MWCNTs?

After theoretically confirming the formation of polyiodide chain structures in SWCNTs, the next question is to explore the atomic arrangement of iodine into multi-walled samples.
Raman scattering and thermogravimetric investigation have shown that MWCNTs can be effectively doped by iodine. These analysis highlights that the formation of polyiodide chains seems to occur only in the innermost tube core rather than intercalated between the graphene walls of the multi-walled sample [336]. The current state-of-the-art regarding intercalation compounds reports one study where iodine is successfully intercalated into graphite. X-ray diffraction pattern of halogenated graphite showed a large number of peaks, indicating that two carbon layers containing iodine are 0.725 nm apart [337]. This apparent discrepancy is easy to understand because for MWNTs, unlike graphite, the interlayer spacing is difficult to change given the fixed nanotube diameter.
However, our experimental colleagues at CEMES Institute have been able to provide first evidence of iodine intercalated between concentric nanotubes walls of arc-electric MWNTs by HRTEM and STEM-HAADF imaging characterization. Fig. 5.13 shows two bright (left) and dark (right) field images of I@MWCNT. The first two conclusions from microscopy analysis are: (*i*) iodine atoms seem arranged in 1D-lines, rather than 2D-planes; (*ii*) there are four lines of iodine on one side of the tube, but not in both, as evidenced by well-defined linear contrast in the dark field. Iodine lines are placed between the graphene walls. In order to achieve this, given the finite curvature of the tubes, the layers between I and CNT axis are deformed inwards, using the interior cavity space to make interlayer space available for the iodine. This means that halogenated graphene layers are not totally rigid and may

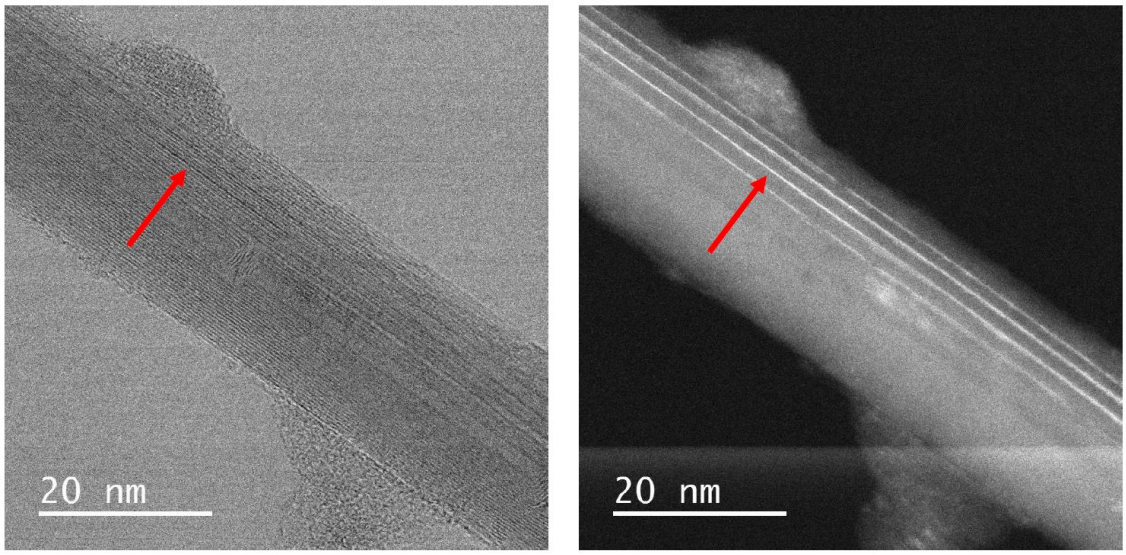

Figure 5.13: (Left) HRTEM bright and (Right) STEM dark field image of polyiodide lines intercalated between shells of a MWCNT. Images were obtained by our colleagues of CEMES Institute. Credits: A. C. Torres-Dias and M. Monthioux.

undergo limited expansion or contraction (see Fig. 5.14). To ensure the validity of this model, we need to understand why iodine chains prefer intercalate between nanotube walls, rather than inside the smallest interior carbon cavity.
For this reason, we compared the energetic stability (ΔE_{tot}) for a set of cylindrical zig-zag double-walled CNTs when iodine find inside innermost walls and between graphene sheets by DFT-D2 scheme. In these calculations, the iodine stabilization is investigated by varying a couple of geometric parameters: the inner nanotube diameter (D_{inn}) and the inter-wall distance (d_{int}). The aim is to unravel the key parameter for which iodine become stable when inserted between concentric tubes. Fig. 5.15 shows the total energy difference between DWCNTs with iodine encapsulated into the smallest nanotubes and intercalated between tube layers. The main conclusions from this series of calculations are: (*i*) the energy stability is largely independent by nanotube diameter, while it is strongly sensitive to slight variations of inter-wall spacing; (*ii*) the $\Delta E_{\text{tot}} < 0$ for (n,0)@(n+10,0) DWCNTs, whose distance between carbon layers containing iodine is 0.681 nm. These results can be summarized in the following scheme:

$$\Delta E_{\text{tot}} = \begin{cases} > 0, & (n,0)@(n+8,0) \\ > 0, & (n,0)@(n+9,0) \\ < 0, & (n,0)@(n+10,0) \end{cases} . \tag{5.2}$$

While iodine prefers to sit between graphene layers due to charge transfer and increased vdW interaction, when the layers are too close together the lack of space

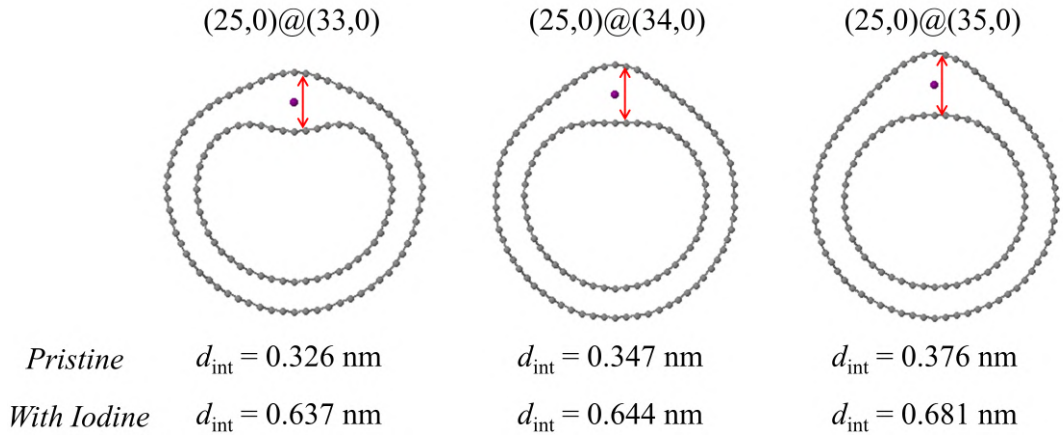

Figure 5.14: DFT-D2 optimized geometries of a set of three I@DWCNTs, keeping the same internal tube and increasing the diameter of the external one. Optimized interwall spacing values of DWCNTs without (first row) and with (second row) intercalated halogens (indicated with red arrows) are given below.

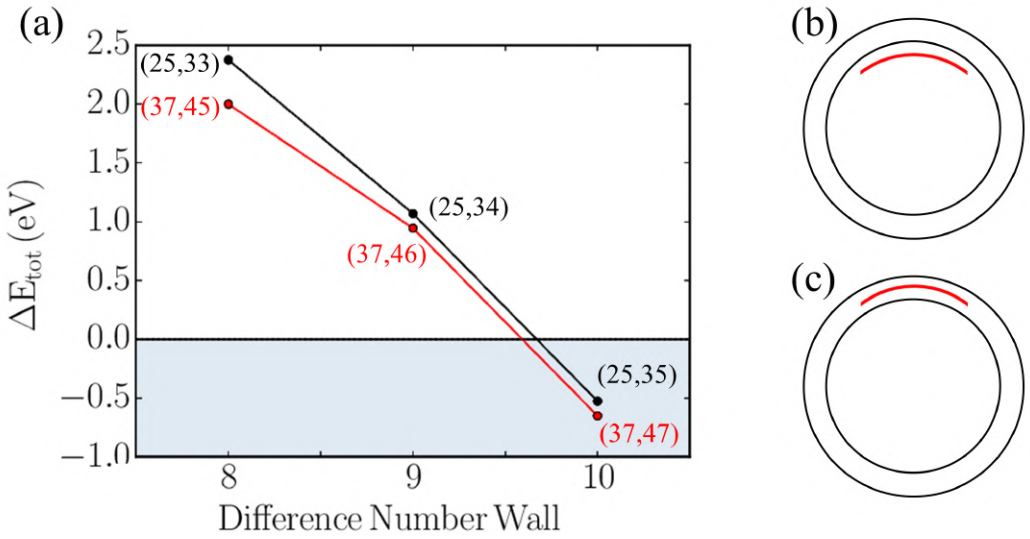

Figure 5.15: (a) DFT-D2 calculated total energy difference between I@DWCNTs configurations shown in (b) and (c) by changing the interwall spacing. Color line indicates diameter of internal tube: 2.00 nm with black and 2.95 nm with red. Each point is marked with first chiral index of every tube, i.e. (n_1,n_2) means $(n_1,0)@(n_2,0)$. Magenta shaded section indicates the region where iodine is stabilized between graphene layers as shown in (c). Corresponding cross-section of MWCNT (black) filled with iodine (red) are illustrated next to the energy plot.

renders this endothermic. These results show that such insertion is only exothermic once there is a $(n,0)@(n+10,0)$ relation between two neighbouring nanotubes.

This relation means the interlayer spacing before insertion of iodine is considerably larger than the conventional interlayer spacing expected for MWNTs of 0.344 nm (i.e. 0.376 nm). However, we have a potential explanation for where this additional space may be coming from. As the tubes are created during arc-electric process they are formed at very high temperatures, above 2000 K, and due to thermal expansion, the equilibrium interlayer spacing at these temperatures is much higher than at room temperature, and may be as much as 0.4 nm [338]. Thus, we think that arc-electric MWNTs form with larger interlayer spacings and then during cooling this will result in asymmetric buckling, similar to that seen in Fig. 5.14. The Iodine is then able to enter into the cavities formed by this buckling. If this theory is correct, we have another example where localised buckling of carbon layers again results in fascinating interaction with intercalated species. We are currently developing this theory with our experimental colleagues.
This finding would be extremely interesting, since it implies that arc-electric MWNTs are not in general fully spherical in shape, and may help explain microscopic observations of differing interlayer spacing which is sometimes variously ascribed to facetting (polygonisation), and/or local scroll formation [339].

5.3 Selective edge filling of collapsed SWCNTs

The unique architecture in collapsed SWCNTs results in two enlarged cavities along the flattened edges. It is possible to fill these regions with other materials, using procedures developed to fill conventional carbon nanotubes.
The pioneering work of edge filling has been published by Zettl and co-workers. They showed that C_{60} introduced in solution with folded graphene layers spontaneously arranges forming an array of aligned C_{60} molecules along the inside edge of the fold, due to the increased interlayer spacing and available volume [214]. More recently the synthesis of C_{60}@collapsed CNTs has been successfully achieved by Choi's method [98, 340, 341].
These experimental findings confirm the possibility of producing a novel class of hybrid carbon nanomaterials based on local edge filling of collapsed CNTs. Besides TEM characterization, no other different type of analysis has been done to unravel the effective impact of these molecules on the main properties of FCNTs. The purpose of this section are essentially: (*i*) to explore the influence of other materials on the self-collapse behavior of SWCNTs; (*ii*) since we learned that the intrinsic electronic structure of collapsed CNTs differs from that of circular ones, we expect that changes due to the inserted molecules will be different from those encountered in more conventional carbon nanostructures. In particular, if we hope to use collapsed tubes as nanoribbons, filling edge could provide an unusual and useful way to dope these ribbons. This suggestion was at the heart of the EdgeFiller project.

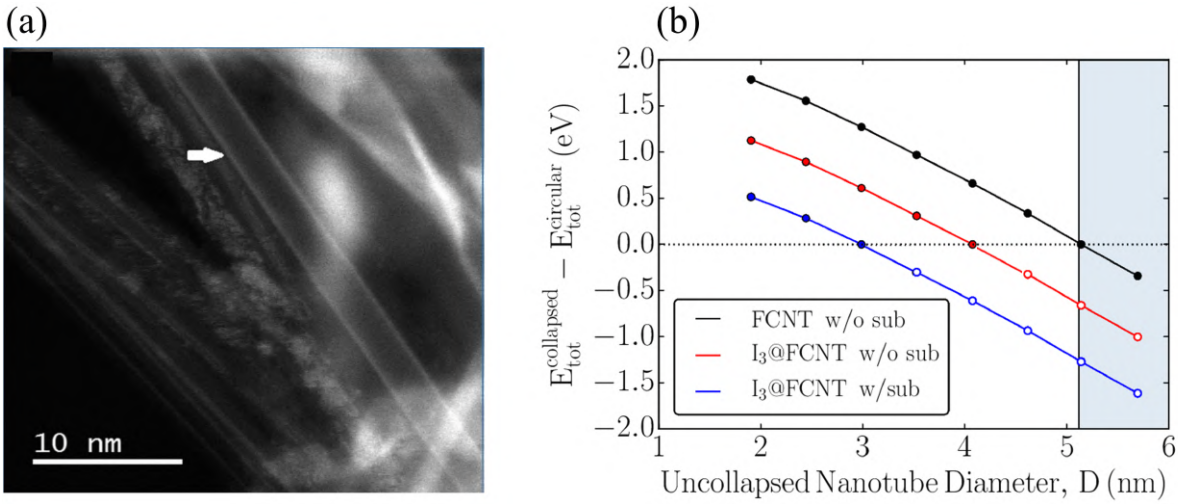

Figure 5.16: (a) STEM-HAADF image of I@DWCNTs operated at 120 kV. (b) DFT-D2 calculated total energy difference between AB-stacked collapsed ($E_{\text{tot}}^{\text{collapsed}}$) and circular ($E_{\text{tot}}^{\text{circular}}$) armchair ($n$,$n$) SWCNTs versus uncollapsed tube diameter D. Black line indicates free-standing collapsed CNTs, while red and blue lines represent I_3@cavity filled collapsed nanotubes without and with graphene substrate, respectively. Filled circles represent actually calculated points, while empty circles are those presumably expected. The intersection point at $\Delta E_{tot} = 0.0$ eV represents the threshold diameter for isolated nanotubes to collapse. Shaded section indicates diameters for which collapse is observed experimentally [99]. Image (a) adapted from [342].

5.3.1 Favored self-collapse of nanotube via edge filling

We have confirmed in Section 3.1 that free-standing SWCNTs spontaneously collapse for a diameter value of ∼5.1 nm. Interestingly, such flattened deformation can be favored by 'external' contributions, such as interaction with neighboring tubes in bundling (∼4.6 nm) [66] or the coupling with underlying substrate (1.09-1.90 nm) [99, 154, 244].
Only recently, our colleagues at CEMES Institute of Toulouse accidentally observed I@filled collapsed DWCNTs by STEM [342]. Dark field contrast highlighted how encapsulated iodine is stabilized in 1D almost linear chains along edge cavities. Notably the distance between the iodine bands implies that the resulting diameter (or width) is lower than free-standing value 5.1 nm. This result suggests another way to favour tube collapse by 'internal' edge filling (see Fig. 5.16(a)).
To corroborate this point from a computational point of view, we determined the collapse threshold of armchair I_3^-@SWCNTs in AB-stacking by calculating the total energy difference between collapsed and circular configurations (see Fig. 5.16(b)). Unlike un-filled case, we quadrupled the unit-cell along the periodic lattice vector in

order to have bond lenght (0.297 nm) and molecule spacing (0.365 nm) consistent with those observed in cylindrical samples by STEM analysis [334]. By inserting a repeated sequence of tri-iodide (characterized by a charge transfer of $0.91e^-$, as reported in Section 5.2) inside each edge cavity, collapsed filled nanotubes are stable for a lower diameter value of 4.07 nm than un-filled case. This is a direct consequence of the influence of encapsulated halogen on the energy balance defined in Eq. (1.1). While the vdW terms remains unchanged, the curvature-induced strain energy is modified by charge transfer and Coulomb interactions between molecules and nanotubes, as follows:

$$\Delta E' = W_{\mathrm{vdW}} E_{\mathrm{vdW}} - E'_{\mathrm{strain}}, \tag{5.3}$$

$$E'_{\mathrm{strain}} = E_{\mathrm{transfer}}(\mathrm{I}^- + \mathrm{CNT}^+) + E_{\mathrm{coul}}(\mathrm{I}^- + \mathrm{CNT}^+) \tag{5.4}$$

The charge transferred per iodine has a repulsive effect versus surrounding positively charged carbon atoms, resulting in an enlargement of cavity size from 0.878 to 0.901 nm. Despite the iodine favours the flattening deformation for nanotubes, the resulting collapse threshold is somewhat larger than estimated experimental value ($\sim$2.5 nm). By looking ADF image, again, we can note that nanotubes are not free-standing but arranged in bundles. In order to take into account this additional effect, we coupled I_3@SWCNTs with one flat carbon substrate and re-calculated the energy stability. The collapse threshold diameter further shifts towards 2.98 nm, which is approaching to the experimental counterpart.
This calculation shows a key difference between SWNT filling and edge cavity filling in collapsed tubes. Unlike SWNTs, the cavity size is not fixed, and can adjust to best fit the encapsulated species.

5.3.2 Perspectives of controlled amphoteric doping?

We next tune the electronic properties of collapsed SWCNT by encapsulation of organic molecules inside each edge cavity. In Fig. 5.17, we show the electronic band structures of armchair (26,26) FCNT, whose both edge cavities are filled with a channel of tetrathiafulvalene (TTF) molecules in one case (Fig. 5.17(a)) and with tetracyano-p-quinodimethane (TCNQ) molecules in the other one (Fig. 5.17(b)). These are chosen because they are well known organic donors and acceptors, respectively. From the visualization of these electronic structure, we can note: (*i*) the apparition of two overlapping flat localized states representing the molecule inserted within each cavity; (*ii*) the shift of the low-energy bands below and above E_{F} for TTF and TCNQ molecules, respectively; (*iii*) the calculated Mulliken charge transferred per molecule is +0.150 and -0.322e^- for TTF and TCNQ molecules, almost identical with those obtained in circular nanotubes using same level of theory [343]. Thus, we have shown theoretically for the first time that the semiconducting collapsed SWCNTs can be amphoterically *n*- and *p*-doped in a controlled way by encapsulated TTF and TCNQ molecules, respectively. Along with the advantage of

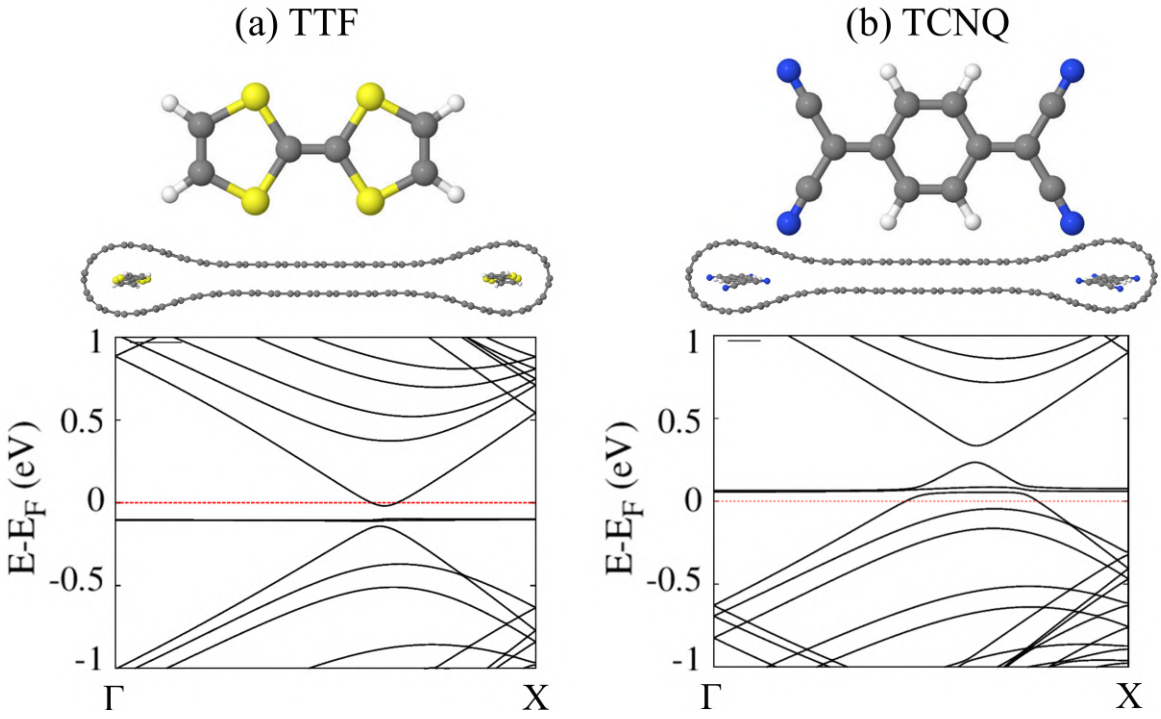

Figure 5.17: DFT-D2 calculated electronic band structures of (26,26) collapsed SWCNT filled with a channel of molecules of either (a) TTF, $C_6S_4H_4$, an acceptor, or (b) TCNQ, $C_{12}N_4H_4$, an organic donor. Coloured balls indicate different atom species: carbon is grey, hydrogen is white, sulphur is yellow, and nitrogen is blue. Horizontal red line represents the position of the Fermi level. Molecule atomic structures and cross-section of filled FCNTs are illustrated above each plot.

synthesis simplicity, this novel class of hybrid carbon nanomaterials could be promising candidates to overcome the performance limit of cylindrical SWCNT-based on devices for molecular electronics [343, 344].

5.4 Summary

In this Chapter, we have compared the energy stability of a plenty of phosphorus configurations, finding that black P is not the ubiquitous ground state, but is degenerate with red-V structure. Then, we explored the transition from 3D-bulk to 1D-phase of red P after it is encapsulated within SWCNTs through TEM imaging analysis and Raman characterization. We simulated the Raman spectra of single-, double- and seven-P chains using first order Placzek-based method within DFT-D2 accuracy level, already used in Chapter 4. Our results seem to suggest that low-frequency P signals recorded in the experiment correspond to packings composed by different weights of P2P8 and P2P9 chains. These two chains types can be seen

as defective variants of each other, in the sense that two parallel chains of P2P8 are not interlinked, whereas two parallel chains of P2P9 show the same overall structure but with interstitial phosphorus pairs crosslinking between the chains. This study revealed the formation of novel allotropes of phosphorus using carbon nanotubes as templates from an experimental and theoretical point of view.

Thereafter we systematically investigated the tendency for confined iodine atoms inside SWCNTs to polymerize in chain-like structures using random structure searching and compression methods. By increasing iodine concentration, we observe a sequence of phase transitions from single, then double-helical up to triple chain configuration. The single chain obtained by compression approach was found the most stable case and taken as reference state. Charge transfer and Fermi energy shift have proven that polyiodide ions are the dominant dopants, which is enough to explain the enhancement of nanotube conductivity observed in prior literature. The methods proposed in this study make it possible to interpret the experimental data about filled CNTs even though the amount of information is very limited.

It was also found that 1D iodine filling of highly crystalline MWCNTs results in the intercalation of iodine between concentric nanotube walls. This filling mechanism is favored by thermal interlayer expansion between tube core at high temperatures, which induce buckling deformation. Our DFT-D2 calculations demonstrated that intercalated iodine is mainly dependent by the inter-wall spacing between tube walls and is stabilized for a value of 0.681 nm, which is somewhat smaller that obtained in the case of graphite (0.725 nm). We suggest such a mechanism may also applicable for other small charge transfer complex intercalants such as bromine.

Finally, we presented a novel approach to obtain stable collapsed carbon nanotubes at diameters lower than 5.1 nm by filling their cavities with other materials like iodine, as evidenced by STEM-ADF characterization. More surprisingly, the local edge filling can tune the electronic properties of the overall collapsed tubes obtaining n- and p-doped semiconductors depending on the encapsulated material. This stimulates the interest in fabricating filled FCNTs for electronic device applications, replacing more conventional circular CNTs and GNRs.

Chapter6

Conclusions and future perspectives

6.1 Conclusions

In this thesis we have explored the physics of local folding and filling in different nanomaterials. For every considered system we have tried to choose the state-of-the art computational DFT approach which is best suited to investigate the properties of interest with compromise between efficiency and accuracy.
First of all, we have confirmed that free-standing circular single-walled carbon nanotubes are not stabilized above a diameter of ∼5.1 nm. Instead, they collapse with dogbone-like cross-section. A major impact of the local curvature at the edge of collapsed CNTs is the metal-semiconductor transition regardless of their original character while circular, which is experimentally confirmed by transport measurements reported in literature. More interestingly, we further unraveled that both threshold collapse and energy bands close to the E_F depend on two parameters: the original nanotube chirality and the interlayer registry dependence between facing layers of the flat middle region. The knowledge of the effects due to the slight displacements between two layers and the tube topology is a crucial issue to control the experimental conditions of the formation of collapsed carbon nanotubes of desired energy gap, which can be measured by STM and STS. A detailed comparative analysis permitted to highlight the main difference between bilayer graphene nanoribbons and collapsed carbon nanotubes: while the first system is characterized by the presence of edge states - which usually act as scattering centers deteriorating their performance based on the width, they are absent in the second case. This confirms their promise for potential use in nanocarbon electronics, for example as interconnects.
We then perfomed extensive DFT-D2 analysis of the prismatic core in graphite with different arrangements based on graphene zig-zag edges. Our calculations suggested that the formation of interlayer bonds results in a reduction of out-of-plane axis,

which may have relevant implications for the physics of highly irradiated graphite, where the formation of prismatic sheets could represent an important driven of dimensional change. Spin-averaged electronic structure calculations revealed the apparition of stacked-dependent band gap similar to collapsed CNTs, but with the presence of edge states due to the prismatic core in a similar manner to graphene nanotube and nanoribbon edges. This opens the interest of investigate the magnetic coupling between cores, which could be responsible to the magnetic properties of damaged and irradiated graphene [345].

It was experimentally observed that high pressure application on multi-walled boron nitride nanotubes leads to the formation of rare morphologies, including folded edges. For this purpose, we modelled collapsed single- and double-walled BNNTs both in free-standing and bundle mode and even multiply folded BN. Unlike the carbon case, electronic band structures of collapsed BNNTs exhibit additional states associated with edge cavities, which lead to the band gap reduction of the overall system in comparison with infinite flat configuration with no folding. This kind of systems behave as type-II semiconducting junctions with significant consequences on the optical spectroscopy. Lower band gaps at edges may act as preferential trapping and recombination sites for optical excitations. The understanding of folding role in BN systems could pave the way towards novel opportunities in the design of electro-optical devices.

We have implemented a method to reproduce the Raman spectra of carbon nanomaterials at different wavelengths and polarizations based on semiclassical first order Placzek approximation combined with DFT accuracy. Thanks to the simple formulation of this calculation approach, we are able to investigate Raman features of large-size collapsed SWCNTs, obtaining a narrow intense D band in absence of structural defects. The enormous importance of this result can be harnessed to revisit the Raman spectroscopy of that class of carbon nanomaterials, where D band activation is related to the symmetry breaking induced by the local curvature, rather than defects.

Applications of Placzek-based on multiwavelength approach that we have implemented are not limited to carbon. We demonstrate that it can be applied to simulate the Raman signals induced by phosphorus encapsulated inside SWCNTs. We have shown that new peaks are essentially due to a mixed combination of different red P chains held together by vdW interaction. This result in accordance to corresponding experimental Raman characterization provides reliable evidence of phase transition of P encapsulated inside narrow nanospace.

By using different structure prediction algorithms coupled with DFT, we have generated different polyiodide structures within the inner cavity of narrow SWCNTs, from simple molecular anions to more complex chain-like structures. On the basis of very recent STEM-ADF images, it was also demonstrated that polyiodide structures can be stabilized between carbon shells of a MWCNT, when the inter-wall separation distance containing the intercalant agent is nearly equal to 0.681 nm. We suggest

such spacing may occur due to thermal contraction after tube formation.
Finally, we have shown that flattening deformation of carbon nanotube is favoured by the encapsulation of molecules channels inside each edge cavity. This exploration culminated with the proposal of novel nanoribbon doping technique via edge cavity filling of collapsed nanotubes using as representative examples, TTF and TCNQ molecules. This implies a considerable advancement about the transport performance of CNT-based on devices driven by molecular electronics.

6.2 Future perspectives

The topics presented in this thesis are proofs of principle. Thus, there is plenty of room for improvements. Here we discuss some interesting perspective for each topic covered here.
In Chapter 3, we showed that the radial collapse deformation makes all achiral nanotubes semiconducting. However, chirality control during synthesis of large diameter tubes is not yet possible and therefore the synthesized dogbone-like nanotubes are supposed to be chiral. This means that the central flat region resembles twisted bilayer graphene. This structural analogy could pave the way to interesting aspects, which have not been reported to date. For example, previous experiments have demonstrated that for a twisting angle of around 1.1°, the entire infinite bilayer graphene becomes superconducting [224]. We expect that for different chiralities, and hence rotational angles in the bilayer-like region would lead to the formation of so-called semiconducting *Moiré collapsed nanotubes*. Such a control on the overlapping flat layers may culminate with the emergence of new optical and magnetic properties, which would make collapsed CNTs promising candidates in other fields, like optoelectronics, photothermoelectronics, and so on.
Regarding the investigation of prismatic edge dislocations, two potential aspects deserve attention: (*i*) Given the strong analogy with GNRs, one might well wonder what can be the magnetic configurations of the reconstructed cores. The effect of magnetic ordering between pairs of prismatic cores are of great interest in order to explain the magnetization usually exhibited by damaged and highly irradiated graphite [345]. For this reason a detailed spin polarized DFT analysis is required. (*ii*) While literature is rich about prismatic cores in carbon, little is known about hBN. Only one publication reported clear TEM evidence of Y-form dislocations in boron nitride belt samples [346]. The knowledge of the effects due to this mechanical deformation could reveal novel interesting properties of BN systems.
Thereafter we found that folded hBN exhibits a higher valence band maximum (lower conduction band minimum) with consequent gap reduction compared to infinite flat system. This implies that if there is any holes (electrons) in the BN, they will go immediately to the fold and be trapped there. So, it will form a 1D line that will trap holes or electrons depending on fold orientation. This result opens the fol-

lowing possibility: if there is a negatively charged halogen (Br and I) or positively charged alkali metals (K and Cs) on the surface of hBN, with a $+/-1$ compensating hole/electron in the BN, the molecules should migrate on the surface to lie above the folds. Therefore, we could expect to see the molecules lining up along these folds. In addition, in the case of folded bulk hBN, we would imagine it would be very favourable for molecules to intercalate along the cavities, which would have the bonus of making the fold conductive. About it, we have encouraging preliminary results from our colleagues in Nikolaev Institute of Inorganic Chemistry (Novosibirsk, Russia) suggesting halogen-treated BN indeed becomes conducting.
In Chapter 4, we showed that collapsed SWCNTs represent one clear example of how the D band is not related to the presence of structural defects, but it is really due to the symmetry breaking induced by local curvature. In order to verify the existence of an intense defect-free D band, it would be interesting to carry out additional experiments and DFT calculations on other locally deformed carbon nanomaterials, such as wrinkled, rippled and crumpled graphene [347]. First order Placzek approximation showed reliable efficiency in the computational Raman characterization of carbon nanomaterials. Howerver, it is not able to catch important aspects, like excitation energy-dependent peak and even multiple vibrational excitations. To this end, it may be worth implementing a more advanced calculation approach based on the Albrecht approximation, which is known to provide results in good agreement with experimental spectra recorded in the resonance regime [162].
In Chapter 5, we showed that TEM studies combined with experimental and computational Raman spectra highlighted the formation of 1D red P chains inside carbon nanotubes. Given its versatility, it would be curious to explore other possible stable arrangements for encapsulated P - like helical chains [348], depending on preparation procedure, applied electron beam, or atomic concentration.
Since single layer phosphorene can be obtained by exfoliating bulk black phosphorus, we might wonder if phosphorene nanotube can undergo the radial collapse deformation, like carbon and boron nitride counterparts. Presumably, collapse radius will likely be much higher because it is not a flat sheet structure, which is so hard to curve.
We also presented a novel suggestion to obtain nanotube with controlled doping states by encapsulating one array of molecules inside each edge cavities. Naturally, edge-doped collapsed SWCNTs have many intrinsic advantages over more conventional GNRs, including: the smooth edge structure results in uniform ribbon width and avoids scattering at functionalised edges, charge carrier doping can be introduced uniformly along the ribbon length, the dopant materials are environmentally protected. Since edge cavity filling is a field largely unexplored, there is a wide variety of materials to test. At the moment, we have early collaborations starting on following cases:

- ionic liquids: once confined into nanospaces they tend to arrange in equally charges ion pairs as a consequence of Coulombic interaction of opposite sign

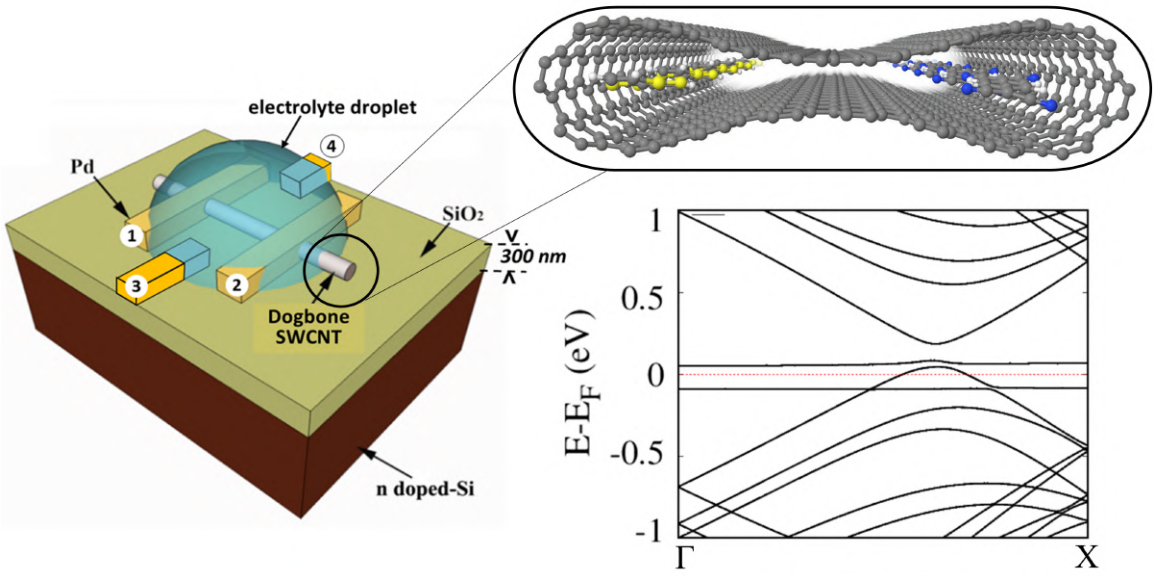

Figure 6.1: (Left) Schematic representation of FET model composed by TTF-TCNQ@SWCNT. (Right) Collapsed cross-section of filled carbon nanotube with DFT-D2 computed electronic band structure showed below.

with the carbon materials sheaths, but this can vary in interesting and largely unexplored ways if other factors such as π-stacking and vdW interaction become energetically comparable with the Coulombic interaction [349]. Presumably, each cavity of collapsed nanotubes can be viewed as a promising template to host combinations of paired anions-cations (in collaboration with A. Marie, J. Le Bideau and B. Humbert, IMN Institute of Nantes).

- superconducting oxides and sulphides: our experimental colleagues have promising preliminary results suggesting superconducting phases for ternaries inside narrow nanotubes (i.e. 1.2-1.7 nm of diameter). Since the diameter of edge cavities can be easily deformed upon encapsulation of foreign materials, it might be possible to obtain something similar in edge cavity filling and then investigate the interesting dimensional effects on the critical temperature (in collaboration with Jeremy Sloan, Warwick University).

We have analyzed the doping effect derived by symmetric doping. More interestingly, given the presence of two cavities, we could propose a 'mixed' doping filling one side with donor species (TTF) and the other one by acceptor species (TCNQ), as shown in Fig. 6.1. The reason why we might expect the asymmetric filling is: when they make crystals of TTF and TCNQ they stack into columns via π-stacking, and we have stacks of TTF and neighbouring stacks of TCNQ, rather

than mixed stacks [350]. So we might hope something similar, getting a stack of TTF in one side of the collapsed nanotube and a stack of TCNQ in the other. For this reason, we can propose the production of a single edge-filled collapsed-tube field-effect transistor device with controllable doping regime driven by encapsulated molecular arrays inside edge cavities. Following this direction, it would be also possible to use ferro- and anti-ferromagnetic dopants or molecular magnets, for which edge doped collapsed tube could be promising spin conductors.
Additionally, it would be intriguing to explore the possibilities of directing filling via external stimuli, such as lateral electric fields via gates, or using a back-gate beneath the substrate.

Bibliography

[1] G. Aad et al. "Observation of a new particle in the search for the standard model Higgs boson with the ATLAS detector at the LHC". *Phys. Lett. B* **716** (2012), pp. 1-29.

[2] S. Chatrchyan et al. "Observation of a new boson at a mass of 125 GeV with the CMS experiment at the LHC". *Phys. Lett. B* **716** (2012), pp. 30-61.

[3] K. Chang. "NASA Mars 2020 Rover gets a landing site: A crater that contained a lake - The rover will search the Jezero crater and delta for the chemical building blocks of life and other signs of past microbes". *The New York Times* (2018).

[4] F. Arute et al. "Quantum supremacy using a programmable superconducting processor". *Nature* **574** (2019), pp. 505-510.

[5] A. C. Ferrari et al. "Science and tecnology roadmap for graphene, related two-dimensional crystals, and hybrid systems". *Nanoscale* **7** (2015), pp. 4598-4810.

[6] K. S. Novoselov, A. K. Geim, S. V. Morozov, D. Jiang, Y. Zhang, S. V. Dubonos, I. V. Grigorieva, and A. A. Firsov. "Electric Field Effect in Atomically Thin Carbon Films". *Science* **306** (2004), pp. 666-669.

[7] A. K. Geim and K. S. Novoselov. "The rise of graphene". *Nat. Mater.* **6** (2007), pp. 183-191.

[8] W. F. McDonough and S.-s. Sun. "The composition of the Earth". *Chem. Geol.* **120** (1995), pp. 223-253.

[9] P. R. Wallace. "The band theory of graphite". *Phys. Rev.* **71** (1947), p. 622.

[10] K. S. Novoselov, A. K. Geim, S. V. Morozov, D. Jiang, M. I. Katsnelson, I. V. Grigorieva, S. V. Dubonos, and A. A. Firsov. "Two-dimensional gas of massless Dirac fermions in graphene". *Nature* **438** (2005), pp. 197-200.

[11] L. E. F. Foa Torres, S. Roche, and J.-C. Charlier. *Introduction to Graphene-Based Nanomaterials: from electronic structure to quantum transport.* Cambridge University Press, New York, 2014.

[12] P. E. Allain and J. N. Fuchs. "Klein tunneling in graphene: optics with massless electrons". *Eur. Phys. J. B* **83** (2011), p. 301.

[13] R. R. Nair, P. Blake, A. N. Grigorenko, K. S. Novoselov, T. J. Booth, T. Stauber, N. M. R. Peres, and A. K. Geim. "Fine structure constant defines visual transparency of graphene". *Science* **320** (2008), p. 1308.

[14] N. N. Rosli, M. A. Ibrahim, N. Ahmad Ludin, M. A. Mat Teridi, and K. Sopian. "A review of graphene based transparent conducting films for use in solar photovoltaic applications". *Renewable Sustainable Energy Rev.* **99** (2019), pp. 83-99.

[15] M. Terrones et al. "Graphene and graphite nanoribbons: Morphology, properties, synthesis, defect and applications". *Nano Today* **5** (2010), pp. 351-372.

[16] H. W. Kroto, J. Health, S. C. O' Brien, R. F. Curl, and R. F. Smalley. "C_{60}: Buckminsterfullerene". *Nature* **318** (1985), pp. 162-163.

[17] S. Iijima. "Helical microtubules of graphitic carbon". *Nature* **354** (1991), pp. 56-58.

[18] R. Saito, G. Dresselhaus, M. S. Dresselhaus. *Physical Properties of Carbon Nanotubes*. World Scientific, 1998.

[19] J.-C. Charlier, X. Blase, and S. Roche. "Electronic and transport properties of nanotubes". *Rev. Mod. Phys.* **76** (2007), p. 677.

[20] R. Rao et al. "Carbon nanotubes and related nanomaterials: critical advances and challenges for synthesis toward mainstream commercial applications". *ACS Nano* **12** (2018), pp. 11756-11784.

[21] R. Lv, E. Cruz-Silva, and M. Terrones. "Building complex hybrid carbon architectures by covalent interconnections: graphene-nanotube hybrids and more". *ACS Nano* **8** (2014), pp. 4061-4069.

[22] L. Yang, C.-H. Park, Y.-W. Son, M. L. Cohen, and S. G. Louie. "Quasiparticle energies and band gaps in graphene nanorribbons". *Phys. Rev. Lett.* **99** (2007), p. 186801.

[23] X. Li, X. Wang, L. Zhang, S. Lee, and H. Dai. "Chemically derived, ultrasmooth graphene nanoribbon semiconductors". *Science* **319** (2008), pp.1229-1232.

[24] F. Banhart, J. Kotakoski, and A. V. Krasheninnikov. "Structural defects in graphene". *ACS Nano* **5** (2011), pp. 26-41.

[25] H. Murayama and T. Taneda. "A novel form of filamentous graphite". *Nature* **345** (1990), 791-793.

[26] J. Campos-Delgado et al. "Thermal stability of CVD-grown graphene nanoribbons: defect annealing and loop formation. *Chem. Phys. Lett.* **469** (2009), pp. 177-182.

[27] X. Yang, X. Dou, A. Rouhanipour, L. Zhi, H. J. Räder, and K. Müllen. "Two-dimensional graphene nanoribbons". *J. Am. Chem. Soc.* **130** (2008), pp. 4216-4217.

[28] J. Cai, P. Ruffieux, R. Jaafar, M. Bieri, T. Braun, S. Blankenburg, M. Muoth, A. P. Seitsonen, M. Saleh, X. Feng, K. Müllen, and R. Fasel. "Atomically precise bottom-up fabrication of graphene nanoribbons". *Nature* **466** (2011), pp. 470-473.

[29] M. Terrones. "Sharpening the chemical scissors to unzip carbon nanotubes: crystalline graphene nanoribbons". *ACS Nano* **4** (2010), pp. 1775-1781.

[30] X. Jia, J. Campos-Delgado, M. Terrones, V. Meunier and M. S. Dresselhaus. "Graphene edges: a review of their fabrication and characterization". *Nanoscale* **3** (2011), pp. 86-95.

[31] R. S. Pease. "Crystal structure of boron nitride". *Nature* **165** (1950), pp. 722-733.

[32] C. Lee, Q. Li, W. Kalb, X.-Z. Liu, H. Berger, R. W. Carpick, and J. Hone. "Frictional characteristics of atomically thin sheets". *Science* **328** (2010), pp. 76-80.

[33] J. H. Warner, M. H. Rümmeli, A. Bachmatiuk, and B. Büchner. "Atomic resolution imaging and topography of boron nitride sheets produced by chemical exfoliation". *ACS Nano* **4** (2010), pp. 1299-1304.

[34] N. G. Chopra, R. J. Lyuken, K. Cherrey, V. H. Crespi, M. L. Cohen, S. G. Louie, and A. Zettl. "Boron nitride nanotubes". *Science* **269** (1995), pp. 966-967.

[35] H Zeng, C. Zhi, Z. Zhang, X. Wei, X. Wang, W. Guo, Y. Bando, and D. Goldberg. "White graphenes: boron nitride nanoribbons via boron nitride nanotube unwrapping". *Nano Lett.* **10** (2010), pp. 5049-5065.

[36] R. Arenal, O. Stéphan, M. Kociak, D. Taverna, A. Loiseau, and C. Colliex "Electron energy loss spectroscopy measurements of the optical gaps on individual boron nitride single-walled and multiwalled nanotubes". *Phys. Rev. Lett.* **95** (2005), pp. 127601-4.

[37] L. Li, L. H. Li, Y. Chen, X. J. Dai, P. R. Lamb, B.-M. Cheng, M.-Y. Lin, and X. Liu. "High-quality boron nitride nanoribbons: unzipping during nanotube synthesis". *Angew. Chem.* **125** (2013), pp. 4306-4310.

[38] D. Goldberg, Y. Bando, Y. Huang, T. Terao, M. Mitome, C. Tang, and C. Zhi. "Boron nitride nanotubes and nanosheets". *ACS Nano* **4** (2010), pp. 2979-2993.

[39] C. R. Dean, A. F. Young, I. Meric, C. Lee, L. Wang, S. Sorgenfrei, K. Watanabe, T. Taniguchi, P. Kim, K. L. Shepard, and J. Hone. "Boron nitride substrate for high-quality graphene electronics". *Nat. Nanotech.* **5** (2010), pp. 722-726.

[40] M. Yankowitz, Q. Ma, P. Jarillo-Herrero, and B. J. LeRoy. "van der Waals heterostructures combining graphene and hexagonal boron nitride". *Nat. Rev. Phys.* **1** (2019), pp. 112-125.

[41] J. Wang, F. Ma, and M. Sun. "Graphene, hexagonal boron nitride, and their heterostructures: properties and applications". *RSC Adv.* **7** (2017), pp. 16801-16822.

[42] K. S. Novoselov, A. Mishchenko, A. Carvalho, and A. H. Castro Neto. "2D materials and van der Waals heterostrutctures". *Science* **353** (2016), pp. 9439-11.

[43] K. Watanabe, T. Taniguchi, and H. Kanda. "Direct-bandgap properties and evidence for ultraviolet lasing of hexagonal boron nitride single crystals". *Nat. Mater.* **3** (2004), pp. 404-409.

[44] J. Furthmüller, J. Hafner, and G. Kresse. "*Ab initio* calculations of the structural and electronic properties of carbon and boron nitride using ultrasoft pseudopotentials". *Phys. Rev. B* **50** (1994), p. 15606.

[45] X. Blase, A. Rubio, S. G. Louie, and M. L. Cohen. "Quasi-particle band structure of bulk hexagonal boron nitride and related systems". *Phys. Rev. B* **51** (1995), pp. 6868-6875.

[46] G. Cassabois, P. Valvin, and B. Gil. "Hexagonal boron nitride is an indirect bandgap semiconductor". *Nat. Photon.* **10** (2016), pp. 262-266.

[47] Y. Nanishi. "The birth of the blue LED". *Nat. Photon.* **8** (2014), pp. 884-886. Nobel Prize in Physics.

[48] M. E. Schlensiger. "The thermodynamics properties of phosphorus and solid binary phosphides". *Chem. Rev.* **102** (2002), pp. 4267-4301.

[49] M. Aykol, J. W. Doak, and C. Wolverton. "Phosphorus allotropes: stability of black versus red-phophorus re-examined by means of the van der Waals inclusive density functional method". *Phys. Rev. B* **95** (2017), p. 214115.

[50] A. Simon, H. Borrmann, and J. Horakh. "On the polymorphism of white phosphorus". *Chem. Ber.* **130** (1997), pp. 1235-1240.

[51] P. W. Bridgman. "Two new modifications of phosphorus". *J. Am. Chem. Soc.* **36** (1914), pp. 1344-1363.

[52] Y. Xu, Z. Shi, X. Shi, K. Zhang, and H. Zhang. "Recent progress in black phosphorus and black phosphorus-analogue materials: properties, synthesis and applications". *Nanoscale* **11** (2019), pp. 14491-14527.

[53] H. Liu, A. T. Neal, Z. Zhu, Z. Luo, X. Xu, D. Tománek, and P. D. Ye. "Phosphorene: An unexplored 2D semiconductor with a high hole mobility". *ACS Nano* **8** (2014), pp. 4033-4041.

[54] W. L. Roth, T. W. DeWitt, and A. J. Smith. "Polymorfism of red phosphorus". *J. Am. Chem. Soc.* **69** (1967), pp. 2881-2885.

[55] C. C. Stephenson, R. L. Potter, T. G. Maple, and J. C. Morrow. "The thermodynamics properties of elementary phosphorus The heat capacities of two crystalline modifications of red phosphorus, of α and β white phosphorus, and a black phosphorus from 15 to 300 K". *J. Chem. Thermodynamics* **1** (1969), pp. 59-76.

[56] M. Ruck, D. Hoppe, B. Wahl, P. Simon, Y. Wang, and G. Seifert. "Fibrous red phosphorus". *Angew. Chemie - Int. Ed.* **44** (2005), pp. 7616-7619.

[57] S. Böcker and M. Häser. "Covalent structure of phosphorus: a comprehensive theoretical study". *Z. Anorg. Allg. Chem.* **621** (1995), pp. 258-286.

[58] A. Pfitzner, M. F. Bräu, J. Zweck, G. Brunklaus, and H. Eckert. "Phosphorus nanorods - two allotropic modifications of a long-known element". *Angew. Chemie - Int. Ed.* **116** (2004), pp. 4324-4327; *Angew. Chemie - Int. Ed.* **43** (2004), pp. 4228-4231.

[59] F. Bachhuber, J. v. Appen, R. Dronskowski, P. Schmidt, T. Nilges, A. Pfitzner, and R. Weihrich. "The extended stability range of phosphorus allotropes". *Angew. Chemie - Int. Ed.* **53** (2014), pp. 11629-11633.

[60] A. Belsky, M. Hellenbrandt, V. L. Karen, and P. Luksch. "New developments in the Inorganic Crystal Structure Database (ICSD): accessibility in support of materials research and design". *Acta Cryst.* **B58** (2002), pp. 364-369.

[61] K. Momma and F. Izumi. "*VESTA 3* for three-dimensional visualization of crystal, volumetric and morphology data". *J. Appl. Cryst.* **44** (2011), pp. 1272-1276.

[62] https://en.wikipedia.org/wiki/Phosphorus.

[63] V. Barone, O. Hod, and G. E. Scuseria. "Electronic structure and stability of semiconducting graphene nanoribbons". *Nano Lett.* **6** (2006), pp. 2748-2754.

[64] P. Wagner, C. P. Ewels, J.-J. Adjizian, L. Magaud, P. Pochet, S. Roche, A. Lopez-Bezanilla, V. V. Ivanovskaya, A. Yaya, M. Rayson, P. Briddon, and B. Humbert. "Band gap engineering via edge-functionalization of graphene nanoribbons". *J. Phys. Chem. C* **117** (2013), pp. 26790-26796.

[65] N. G. Chopra, L. X. Benedict, V. H. Crespi, M. L. Cohen, S. G. Louie, and A. Zettl. "Fully collapsed carbon nanotubes". *Nature* **377** (1995), pp. 135-138.

[66] M. Motta, A. Moisala, I. A. Kinloch, and A. H. Windle. "High performance fibres from 'Dog bone' carbon nanotubes". *Adv. Mater.* **19** (2007), pp. 3721-3726.

[67] T. Hertel, R. E. Walkup, and P. Avouris. "Deformation of carbon nanotubes by surface van der waals forces". *Phys. Rev. B* **58** (1998), pp. 13870-13873.

[68] J. Tersoff and R. S. Ruoff. "Structural properties of a carbon-nanotube crystal". *Phys. Rev. Lett.* **73** (1994), pp. 676-679.

[69] M.-F. Yu, O. Lourie, M. J. Dyer, K. Moloni, T. F. Kelly, R. S. Ruoff. "Strength and breaking mechanism of multiwalled carbon nanotubes under tensile load". *Science* **287** (2000), pp. 637-640.

[70] B. I. Yakobson, M. P. Campbell, C. J. Brabec, J. Bernholc. "High strain rate fracture and C-chain unraveling in carbon nanotubes". *Comput. Mat. Sci.* **8** (1997), pp.341-348.

[71] J. A. Elliott, J. K. W. Sandler, A. H. Windle, R. J. Young, and M. S. P. Shaffer. "Collapse of single-wall carbon nanotubes is diameter dependent". *Phys. Rev. Lett.* **92** (2004), pp. 095501-4.

[72] M.-F. Yu, M. J. Dyer, J. Chen, D. Qian, K. Liu, and R. S. Ruoff. "Locked twist in multiwalled carbon-nanotube ribbons". *Phys. Rev. B* **64** (2001), pp. 241403(R)-4.

[73] H. R. Barzegar, A. Yan, S. Coh, E. Gracia-Espino, C. Ojeda-Aristizabal, G. Dunn, M. L. Cohen, S. G. Louie, T. Wågberg, and A. Zettl. "Spontaneous twisting of a collapsed carbon nanotube". *Nano Res.* **10** (2017), pp. 1942-1949.

[74] C.-H. Kiang, W. A. Goddard, III, R. Beyers, and D. S. Bethune. "Structural modification of single-layer carbon nanotubes with an electron beam". *J. Phys. Chem.* **100** (1996), 3749-3752.

[75] N. G. Chopra, F. M. Ross, and A. Zettl. "Collapsing carbon nanotubes with an electron beam". *Chem. Phys. Lett.* **256** (1996), pp. 241-245.

[76] V. H. Crespi, N. G. Chopra, M. L. Cohen, A. Zettl, and S. G. Louie. "Anisotropic electron-beam damage and the collapse of carbon nanotubes". *Phys. Rev. B* **54** (1996), pp. 5927-5931.

[77] Y. B. Li, B. Q. Wei, J. Liang, Q. Yu, and D. H. Wu. "Transformation of carbon nanotubes to nanoparticles by ball milling process". *Carbon* **37** (1999), pp. 493-497.

[78] Z. Kónya, J. Zhu, K. Niesz, D. Mehn, and I. Kiricsi. "End morphology of ball milled carbon nanotubes". *Carbon* **42** (2004), pp. 2001-2008.

[79] T. Chang and Z. Guo. "Temperature-induced reversible dominoes in carbon nanotubes". *Nano Lett.* **10** (2010), pp. 3490-3493.

[80] M.-F. Yu, T. Kowalewski, and R. S. Ruoff. "Structural analysis of collapsed, and twisted and collapsed, multiwalled carbon nanotubes by atomic force microscopy. *Phys. Rev. Lett.* **86** (2001), pp. 87-90.

[81] C. Zhang, K. Bets, S. S. Lee, Z. Sun, F. Mirri, V. L. Colvin, B. I. Yakobson, J. M. Tour, and R. H. Hauge."Closed-edged graphene nanoribbons from large-diameter collapsed nanotubes". *ACS Nano* **6** (2012), pp. 6023-6032.

[82] H. R. Gutiérrez, U. J. Kim, J. P. Kim, and P. C. Eklund. "Thermal conversion of bundled carbon nanotubes into graphitic ribbons". *Nano Lett.* **5** (2005), pp. 2195-2201.

[83] X. H. Zhong, R. Wang, L. B. Liu, M. Kang, Y. Y. Wen, F. Hou, J. M. Feng, and Y. L. Li. "Structures and characterizations of bundles of collapsed double-walled carbon nanotubes". *Nanotechnology* **23** (2012), pp. 1-5.

[84] A. L. Aguiar, E. B. Barros, R. B. Capaz, A. G. Souza Filho, P. T. C. Freire, J. Mendes Filho, D. Machon, Ch. Caillier, Y. A. Kim, H. Muramatsu, M. Endo, and A. San-Miguel. "Pressure-induced collapse in double-walled carbon nanotubes: chemical and mechanical screening effects". *J. Phys. Chem. C* **115** (2011), pp. 5378-5384.

[85] F. Balima, S. Le Floch, C. Adessi, T. F. T. Cerqueira, N. Blanchard, R. Arenal, A. Brûlet, M. A. L. Marques, S. Botti, and A. San-Miguel. "Radial collapse of carbon nanotubes for conductivity optimized polymer composites". *Carbon* **106** (2016), pp. 64-73.

[86] A. C. Torres-Dias, T. F. T. Cerqueira, W. Cui, M. A. L. Marques, S. Botti, D. Machon, M. A. Hartmann, Y. Sun, D. J. Dunstan, and A. San-Miguel. "From mesoscale to nanoscale mechanics in single-walled carbon nanotubes". *Carbon* **123** (2017), pp. 145-150.

[87] R. S. Alencar, W. Cui, A. C. Torres-Dias, T. F. T. Cerqueira, S. Botti, M. A. L. Marques, O. P. Ferreira, Ch. Laurent, A. Weibel, D. Machon, D. J. Dunstan,

A. G. Souza Filho, and A. San-Miguel. "Pressure-induced radial collapse in few-wall carbon nanotubes: a combined theoretical and experimental study". *Carbon* **125** (2017), pp. 429-436.

[88] Y. Q. Zhu, T. Sekine, T. Kobayashi, E. Takazawa, M. Terrones, and H. Terrones. "Collapsing carbon nanotubes and diamond formation under shock waves". *Chem. Phys. Lett.* **287** (1998), pp. 689-693.

[89] O. Lourie, D. M. Cox, and H. D. Wagner. "Buckling and collapse of embedded carbon nanotubes". *Phys. Rev. Lett.* **81** (1998), pp. 1638-1641.

[90] C.-H. Kiang. "Growth of large-diameter single-walled carbon nanotubes". *J. Phys. Chem. A* **104** (2000), pp. 2454-2456.

[91] A. C. Torres-Dias, S. Cambré, W. Wenseleers, D. Machon, and A. San-Miguel. "Chirality-dependent mechanical response of empty and water-filled single-wall carbon nanotubes at high pressure". *Carbon* **95** (2015), pp. 442-451.

[92] S. Lebedkin, P. Schweiss, B. Renker, S. Malik, F. Hennrich, M. Neumaier, C. Stoermer, and M. M. Kappes. "Single-wall carbon nanotubes with diameters approaching 6 nm obtained by laser vaporization". *Carbon* **40** (2002), pp. 417-423.

[93] S. Liu, J. Yue, and R. J. Wehmschulte. "Large tick flattened carbon nanotubes". *Nano Lett.* **2** (2002), pp. 1439-1442.

[94] J. Campos-Delgado et al. "Bulk production of a new form of sp^2 carbon: crystalline graphene nanoribbons". *Nano Lett.* **8** (2008), pp. 2773-2778.

[95] J. Campos-Delgado, Y. A. Kim, T. Hayashi, A. Morelos-Gómez, M. Hofmann, H. Muramatsu, M. Endo, H. Terrones, R. D. Shull, M. S. Dresselhaus, and M. Terrones. "Thermal stability studies of CVD-grown graphene nanoribbons: Defect annealing and loop formation". *Chem. Phys. Lett.* **469** (2009), pp. 177-182.

[96] M. Endo, Y. A. Kim, T. Hayashi, T. Yanagisawa, H. Muramatsu, M. Ezaka, H. Terrones, M. Terrones, and M. S. Dresselhaus. "Microstructural changes induced in "stacked cup" carbon nanofibers by heat treatment". *Carbon* **41** (2003), pp. 1941-1947.

[97] L. Jiao, X. Wang, G. Diankov, H. Wang and H. Dai. "Facile synthesis of high-quality graphene nanoribbons". *Nat. Nanotech.* **5** (2010), pp. 321-325.

[98] D. H. Choi, Q. Wang, Y. Azuma, Y. Majima, J. H. Warner, Y. Miyata, H. Shinohara, and R. Kitaura. "Fabrication and characterization of fully flattened carbon nanotubes: A new graphene nanoribbon analogue". *Sci. Rep.* **3** (2013).

[99] M. He, J. Dong, K. Zang, F. Ding, H. Jiang, A. Loiseau, J. Lehtonen, and E. I. Kauppinen. "Precise determination of the threshold diameter for a single-walled carbon nanotubes to collapse". *ACS Nano* **8** (2014), pp. 9657-9663.

[100] L. Ci, R. Vajtai, and P. M. Ajayan. "Vertically aligned large-diameter double-walled carbon nanotubes arrays having ultralow density". *J. Phys. Chem. C* **111** (2007), pp. 9077-9080.

[101] C. L. Cheung, A. Kurtz, H. Park, and C. M. Lieber. "Diameter-controlled synthesis of carbon nanotubes". *J. Phys. Chem. B* **106** (2002), pp. 2429-2433.

[102] N. T. Alvarez, F. Ling, C. L. Pint, J. T. Mayo, E. Z. Fisher, J. M. Tour, V. L. Colvin, and R. H. Hauge. "Uniform large diameter carbon nanotubes in vertical arrays from premade near-monodisperse nanoparticles". *Chem. Mater.* **23** (2011), pp. 3466-3475.

[103] L. Xie, H. Wang, C. Jin, X. Wang, L. Jiao, K. Suenaga, and H. Dai. "Graphene nanoribbons from unzipped carbon nanotubes: atomic structure, Raman spectroscopy, and electrical properties". *J. Am. Chem. Soc.* **133** (2011), pp. 10394-10397.

[104] W. J. Yu, S. H. Chae, D. Perello, S. Y. Lee, G. H. Han, M. Yun, and Y. H. Lee. "Synthesis of edge-closed graphene ribbons with enhanced conductivity". *ACS Nano* **4** (2010), pp. 5480-5486.

[105] L. C. Nistor, G. Van Tendeloo, and G. Dinca. "Crystallographic aspects related to the high pressure-high temperature phase transformation of boron nitride". *Philosophical Magazine* **85** (2005), pp. 1145-1158.

[106] S. K. Jang, J. Youn, Y. J. Song, and S. Lee. "Synthesis and characterization of hexagonal boron nitride as a gate dielectric". *Sci. Rep.* **6** (2016), pp. 1-9.

[107] J. S. Lee, S. H. Choi, S. J. Yun, Y. I. Kim, S. Boandoh, J.-H. Park, B. G. Shin, H. Ko, S. H. Lee, Y.-M. Kim, Y. H. Lee, K. K. Kim, and S. M. Kim. "Wafer-scale single-crystal hexagonal boron nitride film via self-collimated grain formation". *Science* **362** (2018), pp. 817-821.

[108] R. Singh, G. Kalita, R. D. Mahyavanshi, S. Adhikari, H. Uchida, M. Tanemura, M. Umeno, and T. Kawahara. "Low temperature wafer-scale synthesis of hexagonal boron nitride by microwave assisted surface wave plasma chemical vapour deposition". *AIP Advances* **9** (2019), p. 035043.

[109] C. Collazo-Davila, E. Bengu, C. Leslie, and L. D. Marks. "Formation of BN nanoarches: Possibly the key to cubic boron nitride film growth". *Appl. Phys. Lett.* **712** (1998), pp. 314-316.

[110] M. Monthioux. "Filling single-wall carbon nanotubes". *Carbon* **40** (2002), pp. 1809-1823.

[111] A. Zubair, D. Tristant, C. Nie, D. E. Tsentalovich, R. J. Headrick, M. Pasquali, J. Kono, V. Meunier, E. Flahaut, M. Monthioux, I. C. Gerber, and P. Puech. "Charged iodide in chains behind the highly efficient iodine doping in carbon nanotubes". *Phys. Rev. Mat.* **1** (2017), pp. 064002-7.

[112] R. R. Meyer, J. Sloan, R. E. Durin-Borkowski, A. I. Kirkland, M. C. Novotny, S. R. Bailey, J. L. Hutchison, and M. L. H. Green. "Discrete atom imaging of one-dimensional crystals formed within single-walled carbon nanotubes". *Science* **289** (2000), pp. 1324-1326.

[113] J. Sloan, A. I. Kirkland, J.L. Hutchison, and M. L. H. Green. "Integral atomic layer architectures of 1D crystals inserted into single walled carbon nanotubes". *Chem. Commun.* **318** (2002), pp. 1319-1332.

[114] J. Sloan, S. Friedrichs, R. R. Meyer, A. I. Kirkland, J. L. Hutchison, and M. L. H. Green. "Structural changes induced in nanocrystals of binary compounds confined within single walled carbon nanotubes: a brief review". *Inorg. Chim. Acta.* **330** (2002), pp. 1-12.

[115] A. A. Eliseev, N. S. Falaleev, N. I. Verbitskiy, A. A. Volykhov, L. V. Yashina, A. S. Kumskov, V. G. Zhigalina, A. L. Vasiliev, A. V. Lukashin, J. Sloan, and N. A. Kiselev. "Size-dependent structure relations between nanotubes and encapsulated nanocrystals". *Nano Lett.* **17** (2017), pp. 805-810.

[116] A. Vasylenko, S. Marks, J. M. Wynn, P. V. C. Medeiros, Q. M. Ramasse, A. J. Morris, J. Sloan, and D. Quigley. "Electronic structure control of sub-nanometer 1D SnTe *via* nanostructuring within single-walled carbon nanotubes". *ACS Nano* **12** (2018), pp. 6023-6031.

[117] R. Senga, H.-P. Komsa, Z. Liu, K. Hirose-Takai, A. V. Krasheninnikov, and K. Suenaga. "Atomic structure and dynamic behaviour of truly one-dimensional ionic chains inside carbon nanotubes". *Nat. Mater.* **13** (2014), pp. 1050-1054.

[118] A. Chuvilin, E. Bichoutskaia, M. C. Gimenez-Lopez, T. W. Chamberlain, G. A. Rance, N. Kuganathan, J. Biskupek, U. Kaiser, and A. N. Khlobystov. "Self-assembly of a sulfur-terminated graphene nanoribbon within a single-walled carbon nanotube". *Nat. Mater.* **10** (2011), pp. 687-692.

[119] C. J. Pickard and R. J. Needs. "*Ab initio* random structure searching". *J. Phys.: Condens. Matter.* **23** (2011), pp. 053201-23.

[120] T. S. Hofer and S. P. de Visser. "Editorial: Quantum mechanical/molecular mechanical approaches for the investigation of chemical systems - Recent developments and advanced applications". *Frontiers in Chemistry* **6** (2018), p. 357.

[121] M. S. Dresselhaus, A. Jorio, M. Hofmann, G. Dresselhaus, and R. Saito. "Perspectives on carbon nanotubes and graphene Raman spectroscopy". *Nano Lett.* **10** (2010), 751-758.

[122] P. Hohenberg and W. Kohn. "Inhomogeneus electron gas". *Phys. Rev.* **136** (1964), p. B864.

[123] W. Kohn and L. J. Sham. "Self-Consistent equations including exchange and correlation effects". *Phys. Rev.* **140** (1965), p. A1133.

[124] D. S. Sholl and J. A. Steckel. *Density functional theory-A pratical introduction.* John Wiley & Sons, 2009.

[125] D. Hartree. "The calculations of atomic structures". *Report on Progress in Physics* **11** (1947), p. 305.

[126] A. D. Becke. "Perspective: Fifty years of density-functional theory in chemical physics". *J. Chem. Phys.* **140** (2014), p. 18A301.

[127] R. M. Martin. *Electronic Structure: Basic Theory and Pratical Methods.* Cambridge University Press, 2004.

[128] S. Mohr, L. E. Ratcliff, L. Genovese, D. Caliste, P. Boulanger, S. Goedecker, and T. Deutsch. "Accurate and efficient linear scaling DFT calculations with universal applicability". *Phys. Chem. Chem. Phys.* **17** (2015), p. 31360.

[129] F. Jensen. *Introduction to computational chemistry.* Wiley: Chichester, 2007.

[130] E. Engel and R. M. Dreizler. *Density Functional Theory: An Advanced Course.* Springer & Business Media, 2011.

[131] P. A. M. Dirac. "Note on exchange phenomena in the Thomas atom". *Mathematical Proceedings of the Cambridge Philosophical Society* **26** (1930), pp. 376-385.

[132] E. Teller. "On the stability of molecules in the Thomas-Fermi theory". *Rev. Mod. Phys.* **34** (1962), pp. 627-631.

[133] J. C. Slater. "A simplification of the Hartee-Fock method". *Phys. Rev.* **81** (1951), pp. 385-390.

[134] F. Nogueira, A. Castro, and M. A. L. Marques. *A Tutorial on Density Functional Theory, A Primer in Density Functional Theory*, Lecture Notes in Physics 620, Springer, Berlin, 2003, pp. 218-256.

[135] M. J. Rayson and P. R. Briddon. "Rapid iterative method for electronic-structure eigenproblems using localised basis functions". *Comput. Phys. Commun.* **178** (2008), pp. 128-134.

[136] M. J. Rayson and P. R. Briddon. "Highly efficient method for Kohn-Sham density functional calculations of 500-1000 atom systems". *Phys. Rev. B* **80** (2009), p. 205104.

[137] M. J. Rayson. "Rapid filtration algorithm to construct a minimal basis on the fly from a primitive Gaussian basis". *Comput. Phys. Commun.* **181** (2010), pp. 1051-1056.

[138] *AIMPRO Community web pages.* https://www.aimpro.ncl.ac.uk/restricted.

[139] P. Giannozzi, et al. "Advanced capabilities for materials with Quantum ESPRESSO". *J. Phys.: Condens. Matter.* **29** (2017), p. 465901.

[140] https://www.quantum-espresso.org.

[141] J. Perdew, K. Burke, and M. Ernzerhof, "Generalized Gradient Approximation Made Simple". *Phys. Rev. Lett.* **77** (1996), p. 3865.

[142] S. Grimme. "Semiempirical GGA-type density functional constructed with a long-range dispersion correction". *J. Comput. Chem.* **25** (2006), p. 1787.

[143] S. Grimme, J. Antony, S. Ehrlich, and H. Krieg. "A consistent and accurate *ab initio* parametrization of density functional dispersion correction (DFT-D) for the 94 elements H-Pu". *J. Chem. Phys.* **132** (2010), p. 154101.

[144] S. Grimme, S. Ehrlich, and L. Goergik. "Effect of the damping function in dispersion corrected density functional theory". *J. Comput. Chem.* **32** (2011), pp. 1456-1465.

[145] J. P. Perdew and M. Levy. "Physical content of the exact Kohn-Sham orbital energies: band gaps and derivative discontinues". *Phys. Rev. Lett.* **51** (1983), p. 1884.

[146] J. Heyd, G. E. Scuseria, and M. Ernzerhof. "Hybrid functionals based on a screened Coulomb potential". *J. Chem. Phys.* **124** (2006), p. 219906.

[147] P. Borlido, T. Aull, A. W. Huran, F. Tran, M. A. L. Marques, and S. Botti. "Large-scale benchmark of exchange-correlation functionals for the determination of electronic band gaps of solids". *J. Chem. Theory. Comput.* **15** (2019), pp. 5069-5079.

[148] A. V. Krukaku, O. A. Vydrov, A. F. Izmaylov, and G. E. Scuseria. "Influence of the exchange screening parameter on the performance of screened hybrid functionals". *J. Chem. Phys.* **125** (2006), p. 224106.

[149] P. Deák, E. Khorasani, M. Lorke, M. Farzalipour-Tabriz, B. Aradi, and T. Frauenheim. "Defect calculations with hybrid functionals in layered compounds and in slab models". *Phys. Rev. B* **100** (2019), p. 235304.

[150] J. P. Goss, M. J. Shaw, and P. R. Briddon. *Theory of Defects and Semiconductors*, Topics in Applied Physics **104** (Berlin, Heideberg) 2007, pp. 69-94.

[151] M. I. Heggie, G. L. Haffenden, C. D. Latham, and T. Trevethan "The Stone-Wales transformation: from fullerene to graphite, from radiation damage to heat capacity". *Philos. Trans. R. Soc. A* **374** (2016), pp.1-13.

[152] R. Zacharia, H. Ulbricht, and T. Hertel. "Interlayer cohesive energy of graphite from thermal desorption of polyaromatic hydrocarbons". *Phys. Rev. B* **69** (2004), p. 155406.

[153] E. Mostaani, N. D. Drummond, and V. I. Fal'ko. "Quantum Monte Carlo calculation of the binding energy of bilayer graphene." *Phys. Rev. Lett.* **115** (2015), p. 115501.

[154] M. Hasegawa, K. Nishidate, and N. Yoshimoto. "Collapsed armchair single-walled carbon nanotubes: as an analogue of closed-edged bilayer graphene nanoribbons". *Phys. Rev. B* **92** (2015), p. 245429.

[155] S. Lebègue, J. Harl, T. Gould, J. G. Àngyàn, G. Kresse, and J. F. Dobson. "Cohesive properties and asymptotics of the dispersion interaction in graphite by the random phase approximation". *Phys. Rev. Lett.* **105** (2010), p. 196401.

[156] D. A. Long. *The Raman Effect: A Unified Treatment of the Theory of Raman Scattering by Molecules*; John Wiley & Sons Ltd: Baffins Lane, Chichester, West Sussex PO19 1UD, England, 2002.

[157] J. R. Ferraro, K. Nakamoto, and C. W. Brown. *Introductory Raman Spectroscopy*; (Second Edition); Elsevier Inc.: 2003.

[158] D. Porezag and M. R. Pederson. "Infrared intensities and Raman scattering activities within density-functional theory". *Phys. Rev. B* **54** (1996), pp. 7830-7836.

[159] A. Merlen, J. J. Buijnsters, and Cedric Pardanaud. "A guide to and review of the use of multiwalength Raman spectroscopy for characterizing defective aromatic carbon solids: from graphene to amorphous carbons". *Coatings* **7** (2017), pp. 1-55.

[160] H. A. Kramers and W. Heisenberg. Über die Streuung von Strahlung durch Atome. *Zeitschrift f̈r Physik* **31** (1925), pp. 681-708.

[161] P. A. M. Dirac. "The Quantum Theory of Dispersion". *Proc. R. Soc. London, Ser. A* **114** (1927), pp. 710-728.

[162] M. Walter and M. Moseler. "Ab Initio Wavelength-Dependent Raman Spectra: Placzek Approximation and Beyond". *J. Chem. Theory Comput.* **16** (2020), pp. 576-586.

[163] S.-Y. Lee. "Placzek-type polarizability tensors for Raman and resonance Raman scattering". *J. Chem. Phys.* **78** (1983), pp. 723-734.

[164] G. Borin Barin et al. "Surface-synthesized graphene nanoribbons for room temperature switching devices: substrate transfer and ex situ characterization". *ACS Appl. Nano Mater.* **2** (2019), pp. 2184-2192 (cit on Supp. Inf.)

[165] A. C. Albrecht. "On the Theory of Raman Intensities". *J. Chem. Phys.* **34** (1961), pp. 1476-1484.

[166] J. Guthmuller. "Comparison of simplified sum-over-state expressions to calculate resonance Raman intensities including Franck-Condon and Herzberg-Teller effects". *J. Chem. Phys.* **144** (2016), p. 064106.

[167] D. W. Brenner. "Empirical potential for hydrocarbons for use in simulating the chemical vapour deposition of diamond films". *Phys. Rev. B* **46** (1992) p. 1948.

[168] D. H. Robertson, D. W. Brenner, and C. T. White. "On the way to fullerenes: molecular dynamics study of the curling and closure of graphitic ribbons". *J. Phys. Chem.* **96** (1992) pp. 6133-6135.

[169] J. N. Gosli and F. H. Ree. "Liquid-liquid phase transformation in carbon". *Phys. Rev. Lett.* **82** (1999) pp. 4659.

[170] Z. D. Sha, P. S. Branicio, Q. X. Pei, V. Sorkin, and Y. W. Zhang. "A modified Tersoff potential for pure and hydrogenated diamond-like carbon". *Comput. Mat. Sc.* **67** (2013), pp. 146-150.

[171] C. de Tomas, I. Suarez-Martinez, and N. A. Marks. "Graphitization of amorphous carbons: A comparative study of interatomic potentials". *Carbon* **109** (2016), pp. 681-693.

[172] X. Han, F. Xu, S. Duan, H. Zhan, Y. Gu and G. Liu. "A novel super-elastic carbon nanofiber with cup-stacked carbon nanocones and a screw dislocation". *Carbon* **154** (2019), pp. 98-107.

[173] C.-D. Wu, T.-H. Fang, and C.-Y. Chan. "A molecular dynamics simulation of the mechanical characteristics of a C_{60}-filled carbon nanotubes under nanoindentation using various carbon nanotube tips". *Carbon* **49** (2011), pp. 2053-2061.

[174] Yuman thesis. "title". PhD thesis. Institut des Matériaux Jean Rouxel, Université de Nantes, 2019.

[175] J.-W. Jiang and H. S. Park. "A Gaussian treatment for the friction issue of Lennard-Jones potential in layered materials: Applications to friction between graphene, MoS_2, and black phosphorus". *J. Appl. Phys.* **117** (2015), p. 124304.

[176] J. Tersoff. "New empirical approach for the structure and energy of covalent systems". *Phys. Rev. B* **37** (1988), p. 6991.

[177] G. C. Abell. "Empirical chemical pseudopotential theory of molecular and metallic bonding". *Phys. Rev. B* **31** (1985), p. 6184.

[178] D. W. Brenner, O. A. Shenderova, J. A. Harrison, S. J. Stuart, B. Ni, and S. B. Sinnott. "A second-generation reactive empirical bons order (REBO) potential energy expression for hydrocarbons". *J. Phys.: Condens. Matter* **14** (2002), pp. 783-802.

[179] S. J. Stuart, A. B. Tutein, and J. A. Harrison. "A reactive potential for hydrocarbons with intermolecular interactions". *J. Chem. Phys.* **112** (2000), p. 6472.

[180] S. Plimpton. "Fast parallel algorithms for short-range molecular dynamics". *J. Comput. Phys.* **117** (1995), pp. 1-19.

[181] A. Hashimoto, K. Suenaga, A. Gloter, K. Urita, and S. Iijima. "Direct evidence for atomic defects in graphene layers". *Nature* **430** (2004), pp. 870-873.

[182] O. Zhou, R. M. Fleming, D. W. Murphy, C. H. Chen, R. C. Haddon, A. P. Ramirez, and S. H. Glarum. "Defects in carbon nanostructures". *Science* **263** (1994), pp. 1744-1747.

[183] Y. Fan, B. R. Goldsmith, and P. G. Collins. "Identifying and counting point defects in carbon nanotubes". *Nat. Mater.* **4** (2005), pp. 906-911.

[184] K. Suenaga, H. Wakabayashi, M. Koshino, Y. Sato, K. Urita, and S. iijima. "Imaging active topological defects in carbon nanotubes". *Nat. Nanotech.* **2** (2007), pp. 358-360.

[185] C. Jin, F. Lin, K. Suenaga, and S. Iijima. "Fabrication of a freestanding boron nitride single layer and its defect assignments". *Phys. Rev. Lett.* **102** (2009), pp. 195501-4.

[186] Y. Liu, X. Zou and B. I. Yakobson. "Dislocations and grain boundaries in two-dimensional boron nitride". *ACS Nano* **6** (2012), pp. 7053-7058.

[187] Y. Lin and J. W. Connell. "Advances in 2D boron nitride nanostructures: nanosheets, nanoribbons, nanomeshes, and hybrids with graphene". *Nanoscale* **4** (2012), pp. 6908-6939.

[188] V. V. Ivanovskaya, P. Wagner, A. Zobelli, I. Suarez-Martinez, A. Yaya, and C. P. Ewels. "Graphene edge structure: Folding, scrolling, tubing, rippling and twisting" (2012), pp.75-85. In: L. Ottaviano and V. Morandi (eds) *GraphITA 2011*, Carbon Nanostructures. Springer, Berling, Heidelberg.

[189] G. Wang, Z. Dai, J. Xiao, S. Feng, C. Weng, L. Li, Z. Xu, R. Huang, and Z. Zhang. "Bending of multilayer van der Waals materials". *Phys. Rev. Lett.* **123** (2019), pp. 116101-7.

[190] J. A. Elliott, J. K. W. Sandler, A. H. Windle, R. J. Young, and M. S. P. Shaffer. "Collapse of single-wall carbon nanotube is diameter dependent". *Phys. Rev. Lett.* **92** (2004), pp. 095501-4.

[191] X. H. Zhang, Z. F. Liu, and X. G. Gong. Comment on "Collapse of single-wall carbon nanotube is diameter dependent". *Phys. Rev. Lett.* **93** (2004), pp. 149601-1.

[192] B. Liu, M.-F. Yu, and Y. Huang. "Role of lattice registry in the full collapse and twist formation of carbon nanotubes". *Phys. Rev. B* **70** (2004), pp. 161402(R)-4.

[193] M. He, J. Dong, H. Wang, H. Xue, Q. Wu, B. Xin, W. Gao, X. He, J. Yu, H. Sun, F. Ding, and J. Zhang. "Advance in closed-edged graphene nanoribbon: property investigation and structure fabrication". *Small* **15** (2019), pp. 1804473-19.

[194] H. J. Liu and K. Cho. "A molecular dynamics study of round and flattened carbon nanotube structures". *Appl. Phys. Lett.* **85** (2004), pp. 807-809.

[195] T. Tang, A. Jagota, C.-Y. Hui, and N. Glassmaker. "Collapse of single-walled carbon nanotubes". *J. Appl. Phys.* **97** (2005), pp. 074310-6.

[196] G. Gao, T. Çagin, and W. A. Goddard III. "Energetics, structure, mechanical and vibrational properties of single-walled carbon nanotubes". *Nanotechnology* **9** (1998), pp. 184-191.

[197] L. X. Benedict, V. H. Crespi, N. G. Chopra, A. Zettle, M. L. Cohen, and S. G. Louie. "Microscopic determination of the interlayer binding energy in graphite". *Chem. Phys. Lett.* **286** (1998), pp. 490-496.

[198] P. Zhang and V. H. Crespi. "Nucleation of carbon nanotubes without pentagonal rings". *Phys. Rev. Lett.* **83** (1999), pp. 1791-1794.

[199] W. Lu, T.-W. Chou, and B.-S. Kim. "Radial deformation and its related energy variations of single-walled carbon nanotubes". *Phys. Rev. B* **83** (2011), pp. 134113-8; **84** (2011), pp. 059901-8(E).

[200] J. Xiao, B. Liu, Y. Huang, J. Zuo, K.-C. Hwang, and M.-F. Yu. "Collapse and stability of single- and multi-wall carbon nanotubes". *Nanotechnology* **18** (2007), pp. 395703-7.

[201] J. Liu. "Explicit solutions for a SWCNT collapse". *Arch. Appl. Mech.* **82** (2012), pp. 767-776.

[202] S. Zhang, R. Khare, T. Belytschko, K. J. Hsia, S. L. Mielke, and G. C. Schatz. "Transition states and minimum energy pathways for the collapse of carbon nanotubes". *Phys. Rev. B* **73** (2006), pp.075423-7.

[203] X. Meng, B. Zhang, H. Li, F. Li, Z. Kang, M. Li, and Y. Chen. "A theoretical analysis on self-collapsing of nanotubes". *Int. J. Solids Struct.* **160** (2019), pp. 51-58.

[204] M. Hasegawa and K. Nishidate. "Radial deformation and stability of single-wall carbon nanotubes under hydrostatic pressure". *Phys. Rev. B* **74** (2006), pp. 115401-10.

[205] K. Nishidate and M. Hasegawa. "Deformation and transfer doping of a single-walled carbon nanotube adsorbed on metallic substrate". *Phys. Rev. B* **81** (2010), pp. 125414-12.

[206] I. V. Lebedeva, A. V. Lebedev, A. M. Popov, and A. A. Knizhinik."Comparison of performance of van der Waals-corrected functionals for interlayer interaction in graphene and bilayer graphene". *Comput. Mat. Sc.* **128** (2017), pp. 45-58.

[207] L. Spanu, S. Sorella, and G. Galli. "Nature and strength of interlayer binding in graphite". *Phys. Rev. Lett.* **103** (2009), pp. 196401-4.

[208] H. Shin, J. Kim, H. Lee, O. Heinonen, A. Benali, and Y. Kwon. "Nature of interlayer binding and stacking of *sp*-sp^2 hybridized carbon layers: A quantum monte carlo study". *J. Chem. Theory Comput.* **13** (2017), pp. 5639-5646.

[209] W.-J. Yin, Y.-E. Xie, L.-M. Liu, Y.-P. Chen, R.-Z. Wang, X.-L. Wei, J.-X. Zhong, and L. Lau. "Atomic structure and electronic properties of folded graphene nanoribbons: A first-principles study". *J. Appl. Phys.* **113** (2013), pp. 173506-6.

[210] D. Zhan, L. Liu, Y. N. Xu, Z. H. Ni, J. X. Yan, C. Zao and Z. X. Shen. "Low temperature edge dynamics of AB-stacked bilayer graphene: Naturally favored closed zigzag edges". *Sci. Rep.* **1** (2011), pp. 1-5.

[211] D. Sheppard, R. Terrell, and G. Henkelmen. "Optimization methods for finding minimum energy paths". *J. Chem. Phys.* **128** (2008), pp. 134106-10.

[212] J. K. Lee, J.-G. Kim, K. P. S. S. Hembram, Y.-I. Kim, B.-K. Min, Y. Park, J.-K. Lee, D. J. Moon, W. See, S.-G. Lee, and P. John. "The nature of metastable AA′ Graphite: Low dimensional nano- and single-crystalline forms". *Sci. Rep.* **6** (2016), pp. 39624-8.

[213] M. Aoki and H. Amawashi. "Dependence of band structures on stacking and field in layered graphene". *Solid State Commun* **142** (2007), pp.123-127.

[214] K. Kim, Z. Lee, B. D. Malone, K. T. Chan, B. Alemán, W. Regan, W. Gannett, M. F. Crommie, M. L. Cohen, and A. Zettl. "Multiply folded graphene". *Phys. Rev. B* **83** (2011), pp. 245433-8.

[215] C. E. Giusca, Y. Tison, and S. R. Silva. "Atomic and electronic structure in collapsed carbon nanotubes evidenced by scanning tunnelling microscopy". *Phys. Rev. B* **76** (2007), pp. 035429-6.

[216] C. E. Giusca, Y. Tison, and S. R. P. Silva. "Evidence for metal-semiconductor transitions in twisted and collapsed double-walled carbon nanotubes by scanning tunneling microscopy". *Nano Lett.* **8** (2008), pp. 3350-3356.

[217] C. Gómez-Navarro, J. J. Sáenz, and J. Gómez-Herrero. "Conductance oscillations in squashed carbon nanotubes". *Phys. Rev. Lett.* **96** (2006), pp. 076803-4.

[218] M. P. Lima, A. Fazzio, and A. J. R. da Silva. "Edge effects in bilayer graphene nanoribbons: *Ab initio* total-energy density functional theory calculations". *Phys. Rev. B* **79** (2009), pp. 153401-4.

[219] E. V. Castro, K. S. Novoselov, S. V. Morozov, N. M. R. Peres, J. M. B. Lopes dos Santos, J. Nilsson, F. Guinea, A. K. Geim, and A. H. Castro Neto. "Biased bilayer graphene: semiconductor with a gap tunable by the electric field effect". *Phys. Rev. Lett.* **99** (2007), pp. 216802-5.

[220] L. G. Bulusheva, A. V. Okotrub, D. A. Romanov, and D. Tomanek. "Electronic structure of *(n,0)* zigzag carbon nanotubes: cluster and crystal approach". *J. Phys. Chem. A* **102** (1998), pp. 975-981.

[221] Y.-W. Son, M. L. Cohen, and S. G. Louie. "Energy gaps in graphene nanoribbons". *Phys. Rev. Lett.* **97** (2006), pp. 216803-4. Erratum: *Phys. Rev. Lett.* **98** (2007), pp. 089901-4.

[222] K.-T. Lam and G. Liang. "An *ab initio* on energy gap of bilayer graphene nanoribbons with armchair edges". *Appl. Phys. Lett.* **92** (2008), pp. 223106-3.

[223] M. Boldoni, A. Sgamellotti, and F. Mercuri. "Electronic properties and stability of graphene nanoribbons: An interpretation based on Clar sextet theory". *Chem. Phys. Lett.* **464** (2008), pp. 202-207.

[224] J. Wang, X. Mu, L. Wang, and M. Sun. "Properties and applications of new superlattice: twisted bilayer graphene". *Mater. Today Phys.* **9** (2019), pp. 100099-16.

[225] H. C. Po, L. Zou, A. Vishwanath, and T. Senthil. "Origin of Mott insulating behavior and superconductivity in twisted bilayer graphene". *Phys. Rev. X* **8** (2018), pp. 0311089.

[226] M. Ochi, M. Koshino and K. Kuroki. "Possible correlated insulating states in magic-angle twisted bilayer graphene under strongly competiting interactions". *Phys. Rev. B* **98** (2018), pp. 081102.

[227] Y. Cao, V. Fatemi, S. Fang, K. Watanabe, T. Taniguchi, E. Kaxiras, P. Jarillo-Herrero. "Unconventional superconductivity in magic-angle graphene superlattice". *Nature* **556** 2018, pp. 43-50.

[228] C.-J. Park, Y.-H. Kim, and K. J. Chang. "Band-gap modification by radial deformation in carbon nanotubes". *Phys. Rev. B* **60** (1999), pp. 10656.

[229] S. Y. Zhou, G.-H. Gweon, A. V. Federov, P. N. First, W. A. de Heer, D.-H. Lee, F. Guinea, A. H. Castro Neto, and A. Lanzara. "Substrate-induced bandgap opening in epitaxial graphene". *Nat. Mater.* **6** (2007), pp. 770-775.

[230] H. Mehrez, A. Svizhenko, M. P. Anantram, M. Elstner, and T. Frauenheim. "Analysis of band-gap formation in squashed armchair carbon nanotubes". *Phys. Rev. B* **71** (2005), pp. 155421-7.

[231] J.-Q. Lu, J. Wu, W. Duan, F. Liu, B.-F. Zhu, and B.-L. Gu. "Metal-to-semiconductor transition in squashed armchair carbon nanotubes". *Phys. Rev. Lett.* **90** (2003), pp. 156601-4.

[232] R. S. Mulliken."Electronic population analysis on LCAO-MO molecular wave functions. IV. Bonding and and antibonding in LCAO and valence-bond theories". *J. Chem. Phys.* **23** (1955), pp. 2343-2346.

[233] Z. Wu, J. B. Neaton, and J. C. Grossman. "Charge separation via strain in silicon nanowires". *Nano Lett.* **9** (2009), pp. 2418-2422.

[234] T. Nakanishi and T. Ando. "Effective-mass theory of collapsed carbon nanotubes". *Phys. Rev. B* **91** (2015), pp. 155420-16.

[235] J. Oostinga, H. Heersche, X. Liu, A. Morpurgo, and L. Vandersypen. "Gate-induced insulating state in bilayer graphene devices". *Nat. Mater.* **7** (2008), pp. 151-157.

[236] Y. Zhang, T.-T. Tang, C. Girit, Z. Hao, M. Martin, A. Zettl, M. Crommie, Y. Shen, and F. Wang. "Direct observation of a widely tunable bandgap in bilayer graphene". *Nature* **459** (2009), pp. 820-823.

[237] P. J. Ouseph. "Observation of prismatic dislocation loops in graphite by scanning tunnelling microscope". *Phys. Stat. Sol. (a)* **169** (1998), pp. 25-32.

[238] I. Suarez-Martinez, G. Savini, G. Haffenden, J.-M. Campanera, and M. I. Heggie. "Dislocations of Burgers vector $c/2$ in graphite". *Phys. Stat. Sol. (c)* **4** (2007), pp. 2958-2962.

[239] F. Atamny, A. Baiker, and R. Schlögl. "Atomic resolution of defects in graphite studied by STM". *J. Anal. Chem.* **358** (1997), pp. 344-348.

[240] C. Karthik, J. Kane, D. P . Butt, W. E. Windes, and R. Ubic. "In situ transmission electron microscopy of electron-beam induced damage process in nuclear grade graphite". *J. Nucl. Mater.* **412** (2011), pp. 321-326.

[241] R. Krishna, J. Wade, A. N. Jones, M. Lasithiotakis, P. M. Mummery, B. J. Marsden. "An understanding of lattice strain, defects and disorder in nuclear graphite". *Carbon* **124** (2017), pp. 314-333.

[242] J.-Y. Huang, F. Ding, K. Jiao, and B. I. Yakobson. "Self-templated growth of carbon-nanotube walls at high temperature". *Small* **3** (2007), pp. 1735-1739.

[243] S. Dai, Y. Xiang, and D. J. Srolovitz. "Structure and energetics of interlayer dislocations in bilayer graphene". *Phys. Rev. B* **93** (2016), pp. 085410-9.

[244] A. Impellizzeri, P. Briddon, and C. P. Ewels. "Stacking- and chirality-dependent collapse of single-walled carbon nanotubes: A large-scale density-functional study". *Phys. Rev. B* **100** (2019), pp. 115410-17.

[245] Y.-W. Son, M. L. Cohen, and S. G. Louie. "Half-metallic graphene nanoribbons". *Nature* **444** (2006), pp. 347-349.

[246] V. V. Ivanovskaya, A. Zobelli, P. Wagner, M. I. Heggie, P. R. Briddon, M. J. Rayson, and C. P. Ewels. "Low-energy termination of graphene edges via the formation of narrow nanotubes". *Phys. Rev. Lett.* **107** (2011), pp. 065502-4.

[247] Y. Liao, Z. Chen, J. W. Connell, C. C. Fay, C. Park, J.-W. Kim, and Y. Lin. "Chemical sharpening, shortening, and unzipping of boron nitride nanotubes". *Adv. Funct. Mater.* **24** (2014), pp. 4497-4506.

[248] D. Kim, H. Muramatsu, and Y. A. Kim. "Hydrolitic unzipping of boron nitride nanotubes in nitric acid". *Nanoscale Res. Lett.* **12** (2017), pp. 1-5.

[249] A. Fathalizadeh, T. Pham, W. Mickelson, and A. Zettl. "Scaled synthesis of boron nitride nanotubes, nanoribbons, and nanocooons using direct feedstock injection into an extended-pressure, inductively-coupled thermal plasma". *Nano Lett.* **14** (2014), pp. 4881-4886.

[250] T. Xu, Y. Zhou, X. Tan, K. Yin, L. He, F. Banhart, and L. Sun. "Creating the smallest BN nanotube from bilayer h-BN". *Adv. Funct. Mater.* **27** (2017), pp. 1603897-7.

[251] C. Tang, Y. Bando, G. Shen, C. Zhi and D. Goldberg. "Single-source precursor for chemical vapour deposition of collapsed boron nitride nanotubes". *Nanotechnology* **17** (2006), pp. 5882-5888.

[252] C. Tang, Y. Bando, T. Sato, and K. Kurashima. "A novel precursor for synthesis of pure boron nitride nanotubes". *Chem. Commun.* (2002), pp. 1290-1291.

[253] C. Zhi, Y. Bando, C. Tan, and D. Golberg. "Effective precursor for high yield synthesis of pure BN nanotubes". *Solid State Commun.* **135** (2005), pp. 67-70.

[254] A. T. Matveev, K. L. Firestein, A. E. Steinman, A. M. Kovalskii, O. I. Lebedev, D. V. Shtansky, and D.Goldberg. "Boron nitride nanotube growth via boron oxide assisted chemical vapour transport-deposition process using $LiNO_3$ as a promoter". *Nano Research* **8** (2015), pp. 2063-2072.

[255] E. Cannuccia, B. Monserrat, and C. Attaccalite. "Theory of phonon-assisted luminescence in solids: Application to hexagonal boron nitride". *Phys. Rev. B* **99** (2019), pp. 081109-6.

[256] F. Paleari, H. P. C. Miranda, A. Molina-Sánchez, and L. Wirtz. "Exciton-phonon coupling in the ultraviolet absorption and emission spectra of bulk hexagonal boron nitride". *Phys. Rev. Lett.* **122** (2019), pp. 187401-4.

[257] R. Bourrellier, M. Amato, L. H. Galvao Tizei, C. Giorgietti, A. Gloter, M. I. Heggie, K. March, O. Stephán, L. Reining, M. Kociak, and A. Zobelli. "Nanometric resolved luminescence in h-BN flakes: excitons and stacking order". *ACS Photonics* **1** (2014), pp. 857-862.

[258] L. Schué, I. Stenger, F. Fossard, A. Loiseau, and J. Barjon. "Characterization methods dedicated to nanometer-thick hBN layers". *2D Mater.* **4** (2016), pp. 015028-22.

[259] G. Cassabois, P. Valvin, and B. Gil. "Intervalley scattering in hexagonal boron nitride". *Phys. Rev. B* **93** (2016), pp. 035207.

[260] A. Celik-Aktas, J.-M. Zuo, J. F. Stubbins, C. Tang, and Y. Bando. "Double-helix structure in multiwall boron nitride nanotubes". *Acta Cryst. A* **61** (2005), pp. 533-541.

[261] A. Pierret, H. Nong, F. Fossard, B. Attal-Trétout, Y. Xue, D. Golberg, J. Barjon, and A. Loiseau. "Role of structural defects in the ultraviolet luminescence of multiwall boron nitride nanotubes". *J. Appl. Phys.* **118** (2015), pp. 234307-8.

[262] I. Leven, R. Guerra, A. Vanossi, E. Tosatti, and O. Hod. "Multiwalled nanotube faceting unravelled". *Nat. Nanotechnol.* **11** (2016), pp. 1082-1086.

[263] S.M. Kim, A. Hsu, M.H. Park, S.H. Chae, S.J. Yun, J.S. Lee, D.-H. Cho, W. Fang, C. Lee, T. Palacios, M. Dresselhaus, K.K. Kim, Y.H. Lee, and J. Kong. "Synthesis of large-area multilayer hexagonal boron nitride for high material performance". *Nat. Commun.* **6** (2015), pp. 8662-11.

[264] S. M. Gilbert, T. Pham, M. Dogan, S. Oh, B. Shevitski, G. Schumm, S. Liu, P. Ercius, S. Aloni, M. L. Cohen, and A. Zettl. "Alternative stacking in hexagonal boron nitride". *2D Mater.* **6** (2019), pp. 021006-9.

[265] G. Constantinescu, A. Kuc, and T. Heine. "Stacking in bulk and bilayer hexagonal boron nitride". *Phys. Rev. Lett.* **111** (2013), pp. 036104-5.

[266] O. Arroyo-Gascón, R. Fernández-Perea, E. Suárez Morell, C. Cabrillo and L. Chico. "One-dimensional Moiré superlattices and flat bands in collapsed chiral carbon nanotubes". *Nano Lett.* (2020).

[267] L. Xian, D. M. Kennes, N. Tancogne-Dejean, M. Altarelli, and A. Rubio. "Multiflat bands and strong correlations in twisted bilayer boron nitride: doping-induced correlated insulator and superconductor". *Nano Lett.* **19** (2019), pp. 4934-4940.

[268] N. Marom, J. Bernstein, J. Garel, A. Tkatchenko, E. Joselevich, L. Kronik, and O. Hod. "Stacking and registry effects in layered materials: the case of hexagonal boron nitride". *Phys. Rev. Lett.* **105** (2010), pp. 046801-4.

[269] F. Zheng, G. Zhou, S. Hao, and W. Duan. "Structural characterizations and electronic properties of boron nitride nanotube crystalline bundles". *J. Chem. Phys.* **123** (2005), pp. 124716-5.

[270] D. Goldberg, Y. Bando, C. Tang, and C. Zhi. "Boron nitride nanotubes". *Adv. Mater.* **19** (2007), pp. 2413-2432.

[271] M. Zheng, C. Ke, I.-T. Bae, C. Park, M. W. Smith, and K. Jordan. "Radial elasticity of multi-walled boron nitride nanotubes". *Nanotechnology* **23** (2012), pp. 095703-10.

[272] K. A. Mengle and E. Kioupakis. "Impact of the stacking sequence on the bandgap and luminescence properties of bulk, bilayer, and monolayer hexagonal boror nitride". *APL Mater.* **7** (2019), pp. 021106-6.

[273] Y. Fujimoto and S. Saito. "Band engineering and relative stabilities of hexagonal boron nitride bilayer under biaxial strain". *Phys. Rev. B* **94** (2016), pp. 245427-6.

[274] R. M. Ribeiro and N. M. R. Peres. "Stability of boron nitride bilayers: Ground-state energies, interlayer distances, and thight-binding description". *Phys. Rev. B* **83** (2011), pp. 235312-6.

[275] D. Wickramaratne, L. Weston, and C. G. Van de Walle. "Monolayer to bulk properties of hexagonal boron nitride". *J. Phys. Chem. C* **122** (2018), pp. 25524-25529.

[276] M. L. Hu, Z. Yu, J. L. Yin, C. X. Zhang, and L. Z. Sun. "A DFT-LDA study of electronic and optical properties of hexagonal boron nitride under uniaxial strain". *Comput. Mater. Sci.* **54** (2012), pp. 165-169.

[277] M. E. Turiansky, A. Alkauskas, L. C. Bassett, and C. G. Van de Walle. "Dangling bonds in hexagonal boron nitride as single-photon emitters". *Phys. Rev. Lett.* **123** (2019), pp. 127401-6.

[278] K. H. Khoo, M. S. C. Mazzoni, and S. G. Louie. "Tuning the electronic properties of boron nitride nanotubes with transverse electric fields: A giant dc Stark effect". *Phys. Rev. B(R)* **69** (2004), pp. 201401 (4 pp.).

[279] Z. Zhang and W. Guo. "Energy-gap modulation of BN ribbons by transverse electric fields: First-principle calculations". *Phys. Rev. B* **77** (2008), pp. 075403 (5 pp.).

[280] J. Qi, X. Qian, L. Qi, J. Feng, D. Shi, and J. Li. "Strain-engineering of band gaps in piezoelectric boron nitride nanoribbons". *Nano Lett.* **12** (2012), pp. 1224-1228.

[281] R. Saito, M. Hofmann, G. Dresselhaus, A. Jorio, and M. S. Dresselhaus. "Raman spectroscopy of graphene and carbon nanotubes". *Adv. Phys.* **60** (2011), pp. 413-550.

[282] A. C. Ferrari and D. M. Basko. "Raman spectroscopy as a versatile tool for studying the properties of graphene". *Nat. Nanotechnol.* **8** (2013), pp. 235-246.

[283] M. S. Dresselhaus, G. Dresselhaus, R. Saito, and A. Jorio. "A Raman spectroscopy of carbon nanotubes", *Phys. Rep.* **409** (2005), pp. 47-99.

[284] M. S. Dresselhaus and G. Dresselhaus. *Science of Fullerenes and Carbon Nanotubes.* Academic Press: San Diego, CA, 1996.

[285] C. Casiraghi and D. Prezzi. "Raman spectroscopy of graphene nanoribbons: A review." (2017). In: L. Ottaviano and V. Morandi (eds) *GraphITA*, Carbon Nanostructures. Springer, Cham.

[286] M. S. Dresselhaus, G. Dresselhaus, and A. Jorio. *Group Theory: Application to the Physics of Condensed Matter.* Springer-Verlag, 2008.

[287] P. Venezuela, M. Lazzeri, and F. Mauri. "Theory of double-resonant Raman spectra in graphene: Intensity and line shape of defect-induced and two-phonon bands". *Phys. Rev. B* **84** (2011), pp. 035433 (28 pp.).

[288] W. A. Diery, E. A. Moujaes, and R. W. Nunes. "Nature of localized phonon modes of tilt grain boundaries in graphene". *Carbon* **140** (2018), pp. 250-258.

[289] A. Jorio, L. G. Cançado, and L. M. Malard. "Vibrations in Graphene". (2017). In: P. Avouris, T. F. Heinz and T. Low (eds) *2D Materials*, Cambridge University Press: Cambridge.

[290] A. Armano and S. Agnello. "Two-dimensional carbon: A review of synthesis methods, and electronic, optical, and vibrational properties of single-layer graphene". *C–J. Carbon Res.* **5** (2019), pp. 1-37.

[291] P. Yu and M. Cardona. *Fundamentals of Semiconductors.* Springer, 2005.

[292] R. Saito, A. Jorio, A. G. Souza Filho, G. Dresselhaus, M. S. Dresselhaus, and M. A. Pimenta. "Probing phonon dispersion relations of graphite by double resonance Raman scattering". *Phys. Rev. Lett.* **88** (2001), pp. 027401 (5 pp.).

[293] I. Pócsik, M. Hundhausen, M. Koós, and L. Ley. "Origin of the D peak in the Raman spectrum of microcrystalline graphite". *J. Non-Cryst. Solids* **227-230** (1998), 1083-1086.

[294] C. Thomsen and S. Reich. "Double resonant Raman scattering in graphite". *Phys. Rev. Lett.* **85** (2000), pp. 5214-5217.

[295] K. Sato, R. Saito, A. R. T. Nugraha, and S. Maruyama. "Excitonic effects on radial breathing mode intensity of single wall carbon nanotubes". *Chem. Phys. Lett.* **497** (2010), pp. 94-98.

[296] M. Matus, H. Kuzmany, and W. Kratschmer. "Resonance Raman scattering and electronic transitions in C_{60}". *Solid State Commun.* **80** (1991), pp. 839-842.

[297] L. G. Cançado, M. A. Pimenta, B. R. A. Neves, M. S. S. Dantas, and A. Jorio. "Influence of the atomic structure on the Raman spectra of graphite edges". *Phys. Rev. Lett.* **93** (2004), 247401 (4 pp.).

[298] C. Casiraghi, A. Hartuschuh, H. Qian, S. Piscanec, C. Georgi, A. Fasoli, K. S. Novoselov, D. M. Basko, and A. C. Ferrari. "Raman spectroscopy of graphene edges". *Nano Lett.* **9** (2009), pp. 1433-1441.

[299] R. Nishinakagawa, K. Matsuda, T. Arai, A. Sawada, and T. Terashima. "Raman spectroscopy investigations of chemically derived zigzag edge graphene nanoribbons". *AIP Advances* **3** (2013), 092111 (5 pp.).

[300] D. Rizzo, D. Prezzi, A. Ruini, V. Nagyte, A. Keerthi, A. Narita, U. Beser, F. Xu, Y. Mei, X. Feng, K. Müllen, E. Molinari, and C. Casiraghi. "Multi-wavelength Raman spectroscopy of ultranarrow nanoribbons made by solution-mediated bottom-up approach". *Phys. Rev. B* **100** (2019), 045406 (12 pp.).

[301] C. Koch. PhD thesis. Arizona State University (2002).

[302] L. G. Cançado, A. Jorio, E. H. Martins Ferreira, F. Stavale, C. A. Achete, R. B. Capaz, M. V. O. Moutinho, A. Lombardo, T. S. Kulmala, and A. C. Ferrari. "Quantifying defects in graphene via Raman spectroscopy at different excitation energies". *Nano Lett.* **11** (2011), pp. 3190-3196.

[303] A. Torche, F. Mauri, J.-C. Charlier, and M. Calandra. "First-principles determination of the Raman fingerprint of rhombohedral graphite". *Phys. Rev. Mater.* **1** (2017), 041001 (18 pp.).

[304] S. Reichardt and L. Wirtz. "Raman spectroscopy of graphene" (2017). In: R. Binder (ed) *Optical Properties of Graphene*, World Scientific, chap. 3, pp. 85-132.

[305] M.F. Yu, M. J. Dyer, and R. S. Ruoff. "Structure and mechanical flexibility of carbon nanotube ribbons: An atomic-force microscopy study". *J. Appl. Phys.* **89** (2001), pp. 4554-4557.

[306] X. Yuan and Y. Wang. "Radial deformation of single-walled carbon nanotubes adhered to solid substrates and variations of energy: Atomistic simulations and continuum analysis". *Int. J. Solids Struct.* **144-145** (2018), pp. 145-149.

[307] G. S. N. Eliel, M. V. O. Moutinho, A. C. Gadelha, A. Righi, L. C. Campos, H. B. Ribeiro, P.-W. Chiu, K. Watanabe, T. Taniguchi, P. Puech, M. Paillet, T. Michel, P. Venezuela, and M. A. Pimenta. "Intralayer and interlayer electron-phonon interactions in twisted graphene heterostructures". *Nat. Commun.* **9** (2018), pp. 1-8.

[308] A. K. Gupta, C. Nisoli, P. E. Lammert, V. H. Crespi, and P. C. Eklund. "Curvature-induced D-band Raman scattering in folded graphene". *J. Phys. Condens. Matter.* **22** (2010), 334205 (6 pp).

[309] R. Podila, R. Rao, R. Tsuchikawa, M. Ishigami, and A. M. Rao. "Raman spectroscopy of folded and scrolled graphene". *ACS Nano* **6** (2012), pp. 5784-5790.

[310] M. I. Heggie, I. Suarez-Martinez, C. Davidson, and G. Haffenden. "Buckle, ruck and tuck: A proposed new model for the response of graphite to neutron irradiation". *J. Nucl. Mater.* **413** (2011), pp. 150-155.

[311] S. H. Yoon, S. Lim, S. Hong, W. Qiao, D. D. Whitehurst, I. Mochida, B. An, and K. Yokogawa. "A conceptual model for the structure of catalytically grown carbon nano-fibers". *Carbon* **43** (2005), pp. 1828-1838.

[312] Y. Saito and T. Arima "Features of vapor-grown cone-shaped graphitic whiskers deposited in the cavities of wood cells". *Carbon* **45** (2007), pp. 248-255.

[313] J. Zhang, Y. Feng, H. Ishiwata, Y. Miyata, R. Kitaura, J. E. P. Dahl, R. M. K. Carlson, H. Shinohara, and D. Tománek. "Synthesis and transfomation of linear adamantane assemblies inside carbon nanotubes". *ACS Nano* **6** (2012), pp. 8674-8683.

[314] T. W. Chamberlain, J. Biskupek, G. A. Rance, A. Chuvilin, T. J. Alexander, E. Bichoutskaia, U. Kaiser, and A. N. Khlobystov. "Size, structure, and helical twist of graphene nanoribbons controlled by confinement in carbon nanotubes". *ACS Nano* **6** (2012), pp. 3943-3953.

[315] J. H. Spencer, J. M. Nesbitt, H. Trewhitt, R. J. Kashtiban, G. Bell, V. G. Ivanov, E. Faulques, J. Sloan, and D. C. Smith. "Raman spectroscopy of optical transitions and vibrational energies of ∼1nm HgTe extreme nanowires within single walled carbon nanotubes". *ACS Nano* **8** (2014), pp. 9044-9052.

[316] M. Hart, E. R. White, J. Chen, C. M. McGilvery, C. J. Pickard, A. Michaelides, A. Sella, M. S. P. Shaffer, and C. G. Salzmann. "Encapsulation and polymerization of white phosphorus inside single-walled carbon nanotubes". *Angew. Chem. Int. Ed.* **56** (2017), pp. 8144-8148.

[317] M. Hart, J. Chen, A. Michaelides, A. Sella, M. S. P. Shaffer, and C. G. Salzmann. "One-dimensional pnictogen allotropes inside single-wall carbon nanotubes". *Inorg. Chem.* **58** (2019), pp. 15216-15224.

[318] J. Zhang, C. Fu, S. Song, H. Du, D. Zhao, H. Huang, L. Zhang, J. Guan, Y. Zhang, X. Zhao, C. Ma, C.-L. Jia, and D. Tománek. "Changing the phosphorus allotrope from a square columnar structure to a planar zigzag nanoribbon by increasing the diameter of carbon nanotube nanoreactors". *Nano Lett.* **20** (2020), pp. 1280-1285.

[319] A. J. Clancy, E. R. White, H. H. Tay, H. C. Yau, and M. S. P. Shaffer. "Systematic comparison of conventional and reductive single-walled carbon nanotube purifications". *Carbon* **108** (2016), pp. 423-432.

[320] L. Zhang, H. Huang, B. Zhang, M. Gu, D. Zhao, X. Zhao, L. Li, J. Zhou, K. Wu, Y. Cheng, and J. Zhang. "Structure and properties of violet phosphorus and its phosphorene exfoliation". *Angew. Chem. Int. Ed.* **59** (2020), pp. 1074-1080.

[321] R. A. L. Winchester, M. Whitby, and M. S. P. Shaffer. "Synthesis of pure phosphorus nanostructures". *Angew. Chem. Int. Ed.* **48** (2009), pp. 3616-3621.

[322] P. E. M. Amaral, D. C. Hall Jr., R. Pai, J. E. Król, V. Kalra, G. D. Ehrlich, and H.-F. Ji. "Fibrous phosphorus quantum dots for cell imaging". *ACS Appl. Nano Mater.* **3** (2020), pp. 752-759.

[323] L. Zhang, H. Huang, B. Zhang, M. Gu, D. Zhao, X. Zhao, L. Li, J. Zhou, K. Wu, Y. Cheng, and J. Zhang. "Structure and properties of violet phosphorus and its phosphorene exfoliation". *Angew. Chem. Int. Ed.* **132** (2020), pp. 1090-1096.

[324] S. R. Suryawanshi, M. A. More, and D. J. Late. "Laser exfoliation of 2D black phosphorus nanosheets and their application as a field emitter". *RCS Adv.* **6** (2016), pp. 112103 (6 pp).

[325] E. N. Rissi, E. Soignard, K. A. McKiernan, C. J. Benmore, and J. L. Yarger. "Pressure-induced crystallization of amorphous red phosphorus". *Solid State Commun.* **152** (2012), pp. 390-394.

[326] A. Ramstad, G. Brocks, and P. J. Kelly. "Theoretical study of the Si(100) surface reconstruction". *Phys. Rev. B* **51** (1994), 14504 (21 pp).

[327] Y. Zhao, J. Wei, R. Vajtai, P. M. Ajayan, and E. V. Barrera. "Iodine doped carbon nanotube cables exceeding specific electrical conductivity of metals". *Sci. Rep.* **1** (2011), pp. 1-5.

[328] L. Alvarez, J.-L. Bantignies, R. Le Parc, R. Aznar, J.-L. Sauvajol, A. Merlen, D. Machon, and A. San Miguel. "High-pressure behavior of polyiodides confined into single-walled carbon nanotubes: A Raman study". *Phys. Rev. B* **82** (2010), 205403 (8 pp).

[329] A.A. Tonkikh, E. D. Obraztsova, E. A. Obraztsova, A. V. Belkin, and A. S. Pozharov. "Optical spectroscopy of iodine-doped single-wall carbon nanotubes of different diameter". *Phys. Status Solidi B* **249** (2012), pp. 2454-2459.

[330] L. Guan, K. Suenaga, Z. Shi, Z. Gu, S. Iijima. "Polymorphic structures of iodine and their phase transition in confined nanospace". *Nano Lett.* **7** (2007), pp. 1532-1535.

[331] Z. Yao, C.-J. Liu, Y. Li, X.-D. Jing, and Q. Yuan. "Helicity analysis of single, double, and triple helical iodine chains inside single-walled silicon carbide nanotubes". *Can. J. Phys.* **97** (2017), pp. 731-737.

[332] C. J. Pickard and R. J. Needs. "*Ab initio* random structure searching". *J. Phys.: Condens. Matter.* **23** (2011), 053201 (23 pp).

[333] R. Arenal, K. March, C. P. Ewels, X. Rocquefelte, M. Krociak, A. Loiseau, and O. Stéphan. "Atomic configuration of nitrogen-doped single-walled carbon nanotubes". *Nano Lett.* **14** (2014), pp. 5509-5516.

[334] H. P. Komsa, R. Senga, K. Suenaga, and A. V. Krasheninnikov. "Structural distortions and charge density waves in iodine chains encapsulated inside carbon nanotubes". *Nano Lett.* **17** (2017), pp. 3694-3700.

[335] P. H. Svensson and L. Kloo. "Synthesis, structure, and bonding in polyiodide and metal iodide-iodine systems". *Chem. Rev.* **103** (2003), pp. 1649-1684.

[336] W. Zhou, S. Xie, L. Sun, D. Tang, Y. Li, Z. Liu, L. Ci, X. Zou, G. Wang, P. Tan, X. Dong, B. Xu, and B. Zhao. "Raman scattering and themogravimetric analysis of iodine-doped multiwall carbon nanotubes". *Appl. Phys. Lett.* **80** (2002), pp. 2553-2555.

[337] C.-C. Hung and D. Kucera. "Graphite intercalation compound with iodine as the major intercalate". *Carbon* **32** (1994), pp. 1441-1448.

[338] B. Kelly. *Physics of Graphite.* Springer Netherlands, 1981.

[339] S. Amelinckx, D. Bernaerts, X. B. Zhang, G. Van Tendeloo, and J. Van Landuyt. "A structure model and growth mechanism for multishell carbon nanotubes". *Science* **267** (1995), pp. 1334-1338.

[340] H. R. Barzegar, E. Gracia-Espino, A. Yan, C. Ojeda-Aristizabal, G. Dunn, T. Wagberg, and A. Zettl. "C_{60}/Collapsed carbon nanotube hybrids: A variant of peapods". *Nano Lett.* **15** (2015), pp. 829-834.

[341] Q. Wang, R. Kitaura, Y. Yamamoto, S. Arai, and H. Shinohara. "Synthesis and TEM structural characterization of C_{60}-flattened CNT nanopeapods". *Nano Research* **7** (2014), pp. 1843-1848.

[342] C. Nie, A. Galibert, B. Soula, L. Datas, J. Sloan, E. Flahaut, and M. Monthioux. "The unexpected complexity of filling double-wall carbon nanotubes with Nickel (and Iodine) 1-D nanocrystals". *IEEE Trans. Nanotechnol.* **16** (2017), pp. 759-766.

[343] J. Liu, S. Nagase, D. Yu, H. Xe, R. Han, Z. Gao, S. Zhang. and L. Peng. "Amphoteric and controllable doping of carbon nanotubes by encapsulation of organic and organometallic molecules". *Phys. Rev. Lett.* **93** (2004), 116804 (4 pp).

[344] T. Takenobu, T. Takano, M. Shiraishi, Y. Murakami, M. Ata, H. Kataura, Y. Achiba, and Y. Iwasa. "Stable and controlled amphoteric doping by encapsulation of organic molecules inside carbon nanotubes". *Nat. Mater.* **2** (2003), pp. 683-688.

[345] T. L. Makarova, A. L. Shelankov, I. T. Serenkov, V. I. Sakharov, and D. W. Boukhvalov. "Anisotropic magnetism of graphite irradiated with medium-energy hydrogen and helium ions". *Phys. Rev. B* **83** (2011), 085417 (8 pp).

[346] Q. Weng, X. Wang, C. Zhi, Y. Bando, and D. Goldberg. "Boron nitride porous microbelts for hydrogen storage". *ACS Nano* **7** (2013), pp. 1558-1565.

[347] S. Deng and V. Berry. "Wrinkled, rippled and crumpled graphene: an overview of formation mechanism, electronic properties, and applications". *Mater. Today* **19** (2016), pp. 197-212.

[348] D. Liu, J. Jang, and D. Tománek. "Unusually stable helical coil allotrope of phosphorus". *Nano Lett.* **16** (2016), pp. 7865-7869.

[349] R. Futamura, T. Iiyama, Y. Takashi, Y. Gogotsi, M. J. Biggs, M. Salanne, J. Ségalini, P. Simon and K. Kaneko. "Partial breaking of the Coulombic ordering of ionic liquids confined in carbon nanopores". *Nat. Mater.* **16** (2017), pp. 1225-1232.

[350] S. Yasuzuka and K. Murata. "Recent progress in high-pressure studies on organic conductors". *Sci. Technol. Adv. Mater.* **10** (2009), 024307 (15 pp).

UNIVERSITE MATIERE BRETAGNE MOLECULES LOIRE ET MATERIAUX

UNIVERSITÉ DE NANTES

Titre : Modélisation à l'échelle atomique du pliage et du remplissage dans des nanostructures 2D

Mots clés : Graphène, Nitrure de bore, Pliage, Remplissage, Théorie Fonctionnelle de la Densité, Approximation de Placzek

Résumé : Cette thèse explore les implications de la courbure locale dans les nanomatériaux basés sur les couches de carbone et de nitrure de bore, en utilisant principalement la théorie fonctionnelle de la densité (DFT) avec des fonctions semi-locales et hybrides. Les nanotubes de carbone et de nitrure de bore ne sont pas stables au-dessus d'un certain diamètre mais s'effondrent spontanément. Des phénomènes électroniques fascinants peuvent apparaître dans ces nanosystèmes déformés radialement, tels qu'une transition métal-semiconducteur pour le carbone, et une réduction du gap électronique dans le hBN isolant. Je compare ces phénomènes à la structure et aux propriétés électroniques des dislocations prismatiques des bords du graphite massif. La "bande D" en spectroscopie Raman est généralement attribuée à des défauts ponctuels. Je démontre ici que sa présence intense dans des nanotubes de carbone propres et effondrés est plutôt liée à la rupture de symétrie induite par la localisation de la courbure le long du bord effondré.
Des éléments tels que l'iode et le phosphore peuvent être encapsulés à l'intérieur de nanotubes de carbone ou dans les cavités du bord des tubes effondrés, formant des chaînes de type 1D dont les structures peuvent ne pas exister si elles sont considérées comme autonomes, et facilitant l'effondrement des nanotubes par transfert de charge. Je propose une méthode simple et efficace basée sur la DFT, la mécanique quantique et l'approximation semi-classique de Placzek pour caractériser les caractéristiques Raman de grands systèmes tels que les nanotubes effondrés et les chaînes de phosphore avec une grande précision. Ces résultats démontrent comment des déformations locales peuvent modifier complètement les propriétés des nanomatériaux, les poussant vers des applications nouvelles et inattendues.

Title: Atomic-Scale Modelling of Folding and Filling in 2D Nanostructures

Keywords: Graphene, Boron Nitride, Folding, Filling, Density Functional Theory, Placzek Approximation

Abstract: This thesis explores the implications of local curvature in layered carbon and boron-nitride nanomaterials, using primarily density functional theory with semi-local and hybrid functionals. Carbon and boron-nitride nanotubes are not stable above a certain diameter but spontaneously collapse. Fascinating electronic phenomena can emerge in these radially deformed nanosystems, such as a metal-semiconductor transition for carbon, and gap reduction in the case of insulating hBN. I compare this with the structure and electronic properties of prismatic edge dislocations in bulk graphite. The so-called “D-band” in Raman spectroscopy is typically assigned to point defects, I demonstrate here that its intense presence in clean collapsed carbon nanotubes is instead related to symmetry breaking induced by localization of curvature along the collapsed edge.
Elements such as iodine and phosphorus can be encapsulated inside carbon nanotubes or the edge cavities of collapsed tubes, forming 1D-like chains whose structures may not exist if considered free-standing, and facilitating nanotube collapse through charge transfer. I propose a simple and efficient method based on quantum mechanical DFT and semiclassical Placzek approximation to characterize the Raman features of large systems such as collapsed nanotubes and phosphorus chains with high accuracy. These results demonstrate how local deformations can completely modify the properties of nanomaterials, pushing them towards novel and unexpected applications.